

ANLEC Project 7-1110-0101

Geochemical and Geomechanical Testing of Near Wellbore CO₂
Injectivity Improvement

Final Report

G.K.W. Dawson^a, D. Biddle^b, S.M. Farquhar^a, J. Gao^a, S.D. Golding^a, X. Jiang^b, R. Keck^b,
C. Khan^b, A.C.K. Law^{a,b}, Q. Li^c, J. K. Pearce^a, V. Rudolph^b, A. Watson^a and H. Xing^a

^aSchool of Earth Sciences, The University of Queensland, QLD 4072, Australia

^bSchool of Chemical Engineering, The University of Queensland, QLD 4072,
Australia

^cEnvironmental Engineering, Griffith University, Nathan, QLD 4111, Australia

E-mail addresses: g.dawson@uq.edu.au (G.K.W. Dawson);
s.golding1@uq.edu.au (S.D. Golding)

October 2014



**THE UNIVERSITY
OF QUEENSLAND**
AUSTRALIA

Geochemical and Geomechanical Testing of Near Wellbore CO₂ Injectivity Improvement

The authors wish to acknowledge financial assistance provided through Australian National Low Emissions Coal Research and Development (ANLEC R&D). ANLEC R&D is supported by Australian Coal Association Low Emissions Technology Limited and the Australian Government through the Clean Energy Initiative.

Executive Summary

This project encompassed three key parts aimed at supporting Australian CO₂ geosequestration field demonstration and commercial projects: 1) geochemical reaction investigations of the CO₂-H₂O-rock system of target host formations, identifying changes to mineralogy, porosity and permeability, with leading-edge tools and methodology; 2) measurement of the anisotropic mechanical properties and permeability of samples, investigating dynamic changes as a result of geochemical reactions; and 3) advancing development of physicochemical and numerical models, to replicate the lab findings of fluid and mass transport, for application at different spatial and time scales. Lab experiments were conducted on archived and fresh cores from the target formations of the Wandoan CCS project in the Surat Basin, Queensland and Berea Sandstone supplied by ANLEC for the purpose of benchmarking of permeability results across related ANLEC projects. Additionally, our team has collaborated with ANLEC project 7-0311-0128 that characterised the Surat cores using 3D Digital Core Analysis (DCA) and automated quantitative mineral mapping (QEMSCAN).

The Surat core samples were taken from a stacked reservoir-seal sequence. The Upper Triassic to Lower Jurassic Precipice Sandstone is the potential CO₂ storage reservoir, with the overlying Lower to Middle Jurassic Evergreen Formation acting as the primary seal. The Middle Jurassic Hutton Sandstone is a secondary seal above the Evergreen Formation and also in some areas of the basin a potential reservoir in its own right. The primary seal formation comprises a stacked sequence of variably baffled to impermeable units so is it is unlikely that CO₂ injected into the Precipice Sandstone would be able to completely penetrate it. However, samples of Hutton Sandstone were included in the work program to investigate its behaviour if it were exposed to CO₂-rich fluids in the event of CO₂ leakage or was used as a CO₂ storage reservoir.

Rock samples were reacted with water or brine and CO₂ in batch and continuous flow mode under simulated *in situ* conditions. For most samples, the conditions of 60°C and 12 MPa were used to simulate conditions in the northern part of the Surat Basin, Australia. The fluids were sampled over a period of about 16 or 28 days for Chinchilla 4 samples and West Wandoan 1 samples, respectively. Berea Sandstone samples were reacted at 50°C and 10 MPa for 10 days that were the conditions chosen for the Berea Round Robin experiments. The short reaction times were chosen to represent conditions expected near an injection wellbore during initial flooding with CO₂. Fluids from the geochemical experiments were sampled periodically and analysed for major and trace elements to infer CO₂-water-rock interactions. These data were related to changes to pre-experiment sample mineralogy and texture, as observed using SEM-EDS, QEMSCAN and X-ray micro-CT. Kinetic geochemical modelling of sampled fluids obtained during the CO₂-water-rock experiments was

Geochemical and Geomechanical Testing of Near Wellbore CO₂ Injectivity Improvement

conducted for selected aqueous major and minor elements and successfully reproduced the general trends observed in aqueous geochemistry.

In batch reactor mode, the majority of major and minor elements showed an overall increase in concentration relative to initial water chemistry, indicating dissolution and possibly desorption of material into the fluid phase with decreasing pH. Carbonates were observed to rapidly dissolve in the early stages of the experiments, whereas silicate minerals followed a more gradual, linear dissolution trend. These dissolution and desorption processes are highly dependent on initial host rock mineralogy, with less reactive samples showing little change in mineralogy. The continuous flow reactor experiments tended towards high sample reactivity initially, as shown by the incremental water chemistry, followed by a gradual overall decline in dissolved element concentrations. This may indicate reaction of predominantly fine material early on followed by reaction of lower surface area material. Carbonates, sulphates and reactive silicates such as chloritised biotite contributed the most to changes in reaction water chemistry, as demonstrated by comparison of SEM images taken before and after reactions. The behaviour of the carbonate and other cements as well as fines observed are major factors governing rock response to CO₂ geosequestration.

Porosity of sister samples was determined before and after reaction using Hg-intrusion and showed that <1 % up to >4 % by volume of minerals is readily soluble in brine saturated with CO₂ at reservoir conditions. The heterogeneous nature of the coarser-grained samples means that an undefined proportion of any difference in porosity may be due to natural pore size variation between samples. Nevertheless, an increase in porosity will lead to a corresponding increase in permeability as additional space is opened for flow. This was confirmed by the permeability measurements that showed a significant increase in permeability post reaction for the calcite cemented sandstones generally, and the 40 mm cubes largely independent of mineralogy or lithology. The response of the 40mm cubes to flushing with a CO₂ saturated fluid in the continuous flow reactor may indicate that formerly cemented pores, as well as barrier layers of fines were breached.

Geomechanical tests provided the basis for stress – permeability relationships to be described. The reservoir material is under natural overburden and tectonic lateral stresses and an overpressure is applied in order to drive injection fluid into the subsurface. This overpressure increases the internal interstitial (pore) pressure and consequently reduces the net stress, increasing the permeability. This behaviour needs to be defined in order to predict injectivity dynamics correctly. Further, once characterised, the permeability-stress relationships allow unstressed permeability measurements to be scaled to stressed permeabilities. The measured strains experienced by the samples tested are quite small, and yet the permeability was still quite sensitive to any increase in stress applied irrespective of the general composition of the samples. This in turn implies that small components

Geochemical and Geomechanical Testing of Near Wellbore CO₂ Injectivity Improvement

within the samples, be these pore throats or fine particles, may be what is most affected by the applied stress prior to any geochemical reactions taking place. However, changes in sample strain response following geochemical reactor experiments reflect both physical (e.g. mobilisation) and chemical (dissolution/precipitation) effects on fines material, as well as changes in components such as pore-filling carbonate cement and acid-reactive aluminosilicate framework grains.

The experimental and kinetic geochemical modelling studies indicate that the injection of CO₂ into water bearing reservoirs will reduce the formation water pH and cause dissolution of some minerals. Although the models indicated that some precipitation may have also taken place during the experiments, this was far outweighed by the dissolution reactions. This increases the porosity in the critical near wellbore zone which in turn improves permeability and increases the CO₂ injectivity. Near wellbore modelling using very conservative simplifying assumptions showed a substantial improvement in injectivity in more reactive lithologies; starting with an initial porosity of 21%, the injection rate increases by about 10% for each 1% increase in porosity. More significant increases in permeability are associated with a lower initial porosity provided there is sufficient permeability to allow fluid access. By comparing cases where the dissolution improvement is not accounted for with ones where it is, the economic consequences of using the higher injectivity for either: (i) reducing the number of injection wells that are necessary for a given CO₂ injection rate (thus resulting in capital cost savings), or (ii) with a fixed number of wells reducing the injection pressure necessary to infiltrate a given rate of CO₂ (reducing compression capital and operating costs), have been determined. Reducing the compression requirements leads to the better economic outcome; for the cases considered a saving in the order of 50c per ton of CO₂ injected or some 2 million dollars per year for a CCS project storing some 4 Mtpa of CO₂ is predicted. More comprehensive dynamic modelling will push these predicted results to even bigger (more realistic) savings.

Regarding pore-scale modelling that seeks to track more closely the actual physical transport through the porous media, the in-house extended LBM (XLBM) modelling provides a useful tool for understanding the fluid flow and local changes to the flow architecture at the mesoscale including the porosity change with calcite dissolution and feedback impacts on fluid flow. It provides insights regarding the impact of detailed heterogeneity and matrix properties on the fluid flow, the flow flux with respect to different sample sizes, and illuminates sample size effects on digitally derived permeability. Once a representative scale is established that provides reliable and representative transport calculations (e.g. directional permeability) for upscaling, detailed pore-scale modelling leads to average characteristic parameters suitable for input for the next size scale of modelling. While the general concepts by which this upscaling may be done are known, the detailed mechanics of carrying it out require further work.

Contents

Executive Summary	3
Index of figures.....	9
Index of tables.....	15
1. Introduction	18
2. Experimental Methods	21
2.1. Batch and Continuous Flow Reactors.....	21
2.1.1. Batch Reactors	21
2.1.2. Continuous Flow Reactor	22
2.2. SEM-EDS.....	23
2.3. QEMSCAN and X-ray Micro-CT Scanning.....	23
2.4. Water Chemistry	24
2.5. Porosity, Permeability and Geomechanical Apparatus	24
2.5.1. Unstressed Permeameter	26
2.5.2. True Triaxial Cell Stress/Strain Permeameter.....	29
3. Rock Sample Characterisation	30
3.1. Sample Selection.....	30
3.2. X-ray Diffraction (XRD) Analysis.....	34
3.3. Standard Petrography.....	35
3.3.1. Precipice Sandstone	35
3.3.2. Evergreen Formation	38
3.3.3. Hutton Sandstone	42
3.3.4. Berea Sandstone	44
3.4. General SEM-EDS Surveys.....	45
3.4.1. Precipice Sandstone	45
3.4.2. Evergreen Formation	49
3.4.3. Hutton Sandstone	52
3.4.4. Berea Sandstone	54
4. Experimental Results	56
4.1. SEM-EDS Analysis Pre and Post Reaction.....	56
4.1.1. Precipice Sandstone	56
4.1.2. Evergreen Formation	57
4.1.3. Hutton Sandstone	60
4.1.4. Berea Sandstone	61
4.2. QEMSCAN Mineralogy and X-ray Micro-CT Results.....	61
4.2.1. Precipice Sandstone	61

Geochemical and Geomechanical Testing of Near Wellbore CO₂ Injectivity Improvement

4.2.2.	Evergreen Formation	65
4.2.3.	Hutton Sandstone	67
4.3.	Batch Reactor Water Chemistry Results	68
4.3.1.	Precipice Sandstone	68
4.3.2.	Evergreen Formation	70
4.3.3.	Hutton Sandstone	74
4.3.4.	Berea Sandstone	77
4.4.	Continuous Flow Reactor Water Chemistry Results	77
4.4.1.	Precipice Sandstone	77
4.4.2.	Evergreen Formation	78
4.4.3.	Berea Sandstone.....	81
4.5.	Porosity and Permeability Results	82
4.5.1.	Porosity	82
4.5.2.	Permeability	84
4.6.	Geomechanical Testing.....	91
4.6.1.	Precipice Sandstone	91
4.6.2.	Evergreen Formation	91
4.6.3.	Berea Sandstone	92
5.	Discussion of Experimental Results	94
5.1.	Sample Mineralogy	94
5.2.	Batch and Continuous Flow Reactor Geochemistry	95
5.3.	Porosity and Permeability.....	96
5.4.	Geomechanical Testing.....	97
6.	Modelling Methods and Results	98
6.1.	Geochemical Modelling	98
6.1.1.	Modelling Methodology.....	98
6.1.2.	Geochemical Modelling Results	98
6.2.	Mesoscale Lattice Boltzmann Modelling	107
6.2.1.	Reconstruction of Digital Porous Media from X-ray Micro-CT/QEMSCAN Images	109
6.2.2.	Simulation Results and Discussion.....	109
6.3.	Near Wellbore Reservoir Modelling	121
6.3.1.	Summary	121
6.3.2.	Introduction.....	122
6.3.3.	Reservoir Simulation Model	123
6.3.4.	Results and Discussion.....	124
7.	Discussion of Modelling Results – Outcomes and Significance	129
8.	Recommendations for Future Work.....	130
9.	Acknowledgments.....	134

10. References	135
APPENDIX A – Reservoir Model Details	141
Geological Model	141
Fluid and Rock Properties	141
Well Properties.....	143
APPENDIX B – Economic Evaluation Details	144
Cost of CO ₂ Compression	144
Cost of CO ₂ Transportation	145
Cost of CO ₂ Injection	145

Index of figures

Figure 2.1-1: Illustration of Parr reactor showing thermoplastic liner, and rock samples immersed in water or brine.	22
Figure 2.1-2: Schematic of continuous flow reactor.	23
Figure 2.5-1: Directional permeability of a sedimentary rock.....	25
Figure 2.5-2: The wide brine permeability range measured perpendicular to bedding (through ply) using a sequence of different concentrations of NaCl solutions for single 15 mm cube samples of a) Berea Sandstone and b) WW1 Upper Precipice Sandstone. These samples were not pre-soaked in test solution prior to each measurement and the resultant occurrences of disequilibrium between clay swelling response and brine concentration are circled on these plots, that are modified after Keck <i>et al.</i> (2013).	25
Figure 2.5-3: Low pressure permeameter (drawing not to scale).....	26
Figure 2.5-4: The custom-built True Triaxial Stress Cell Permeater (TTSCP).....	29
Figure 3.1-1: Photographs of the Chinchilla 4 samples used in this study.	31
Figure 3.1-2: Photographs of the West Wandoan 1 samples used in the batch reactor experiments.	31
Figure 3.3-1: Chin4-1192-Precipice poorly sorted quartzose sandstone with blue staining indicating open porosity (0), x25 magnification a) Plain polarized light view (PPL) and b) Cross polarized light view (XPL). The scale bar is 100 micrometres.	36
Figure 3.3-2: WW1-1165-Precipice. Calcite (Ca) cement-supported framework grains, with a thin band of clay (cly) and oxide (ox) minerals, x50 a) PPL and b) XPL.	36
Figure 3.3-3: Photograph of sample WW1-1165-Precipice thin section showing an iron oxide micro-lamination.	37
Figure 3.3-4: WW1-1165-Precipice a) Feldspar grains, bottom left grain almost entirely replaced with clay minerals, central grain undergoing replacement with calcite congruent with twinning, XPL x100; b) Partially altered pyrite (Py) amongst quartz grains, reflected light view (RL) x200.	37
Figure 3.3-5: WW1-1217-Precipice a) Quartz overgrowth and 120° contacts, XPL x5; b) Concave-convex contact and undulose extinction, XPL x50.	38
Figure 3.3-6: WW1-1217-Precipice a) Clay-altered feldspar grain (F) and unmineralized pore space, XPL x10; b) Euhedral sulphide crystal partially altered (S), RL x200.	38
Figure 3.3-7: Chin4-1138-Evergreen. Poorly sorted fine- to medium-grained, matrix supported feldspatholithic wacke, x25 a) PPL and b) XPL. The scale bar is 100 micrometres.	39
Figure 3.3-8: Chin4-897-Evergreen carbonaceous shale, a) PPL x25 and b) XPL x50. The scale bar is 100 micrometres.	39
Figure 3.3-9: WW1-981-Evergreen. a) Photograph of thin section showing interlamination of sandstone and carbonaceous siltstone; b) Partly altered biotite (B), XPL x100.	40
Figure 3.3-10: WW1-1043-Evergreen. a) Rare pyroxene crystals (Pyr) amongst quartz, XPL x50; b) Plagioclase (Plag) amongst quartz.	40

Figure 3.3-11: WW1-1056-Evergreen. Photograph of thin section showing Fe-oxide precipitation, predominantly from biotite alteration, along sand layer boundaries.41

Figure 3.3-12: WW1-1056-Evergreen x100 a) PPL, feldspar framework partially and entirely replaced with clay minerals (F, centre), and b) XPL, abundant calcite cement visible between grains (Ca).....41

Figure 3.3-13: WW1-1056-Evergreen. Biotite almost entirely replaced by chlorite (centre). PPL, x100.....42

Figure 3.3-14: Chin4-868-Hutton: poorly sorted fine- to medium-grained lithic matrix-supported sandstone with minor carbonate cement, x50 a) PPL and b) XPL. The scale bar is 100 micrometres.....42

Figure 3.3-15: Chin4-799-Hutton. Poorly sorted medium to very coarse-grained calcite-cemented sandstone, x50 a) PPL and b) XPL. The scale bar is 100 micrometres.43

Figure 3.3-16: WW1-800-Hutton XPL x100 a) Partially altered microcline feldspar with tartan twinning (m-F), calcite cement (Cal) and quartz (Q), XPL x10; b) Partially altered plagioclase (Plag), calcite cement, quartz; c) Carbonate cement (multi-coloured) amongst quartz grains, XPL x5; d) Polycrystalline (p-Q) and monocrystalline quartz grains, calcite cement mixed with clay (Cal/clay).44

Figure 3.3-17: WW1-800-Hutton. Photograph of thin section showing discontinuous layers and isolated pieces of coal within this calcite-cemented quartzose sandstone.44

Figure 3.3-18: Berea Sandstone a) Muscovite flake between both monocrystalline and polycrystalline quartz grains, XPL x200; b) Hematite cement (red) visible in photograph of thin section.45

Figure 3.4-1: Chin4-1192-Precipice a) SEM electron backscatter image, quartz with minor pore-occluding kaolin; b) Dickite (large crystals, 1), lesser kaolinite (small crystals, 2) and trace pyrite (3).....46

Figure 3.4-2: WW1 upper Precipice Sandstone; Dickite (a, b) fills some pore space. Ti-rich altered aluminosilicates with remnant Fe and K occur (c, d) as well as primary Ti oxide +/- Fe (white) (e, f).47

Figure 3.4-3: WW1 Upper Precipice Sandstone a),b) K and lesser Na sulphate and minor phosphate (1) coating kaolin (2) between quartz grains (3); c),d) Muscovite flakes (4) amidst K(Na)-sulphates (5) and kaolin (6) between quartz grains (7).48

Figure 3.4-4: WW1 Lower Precipice Sandstone a),b) K(Na)-sulphate and lesser carbonate (both white and intermixed) were most abundant within this sample (WW1-1217-Precipice).48

Figure 3.4-5: Chin4-1138-Evergreen a) (Nd, Ce, La)-monazite (1) with qualitative EDS spectra shown below image, (Fe, Mg)-chlorite (2), chloritised biotite, colloidal silica and kaolin (3), quartz (4); b) Oxyphlogopite (5) with qualitative EDS spectra shown below image, phlogopite (6), K-feldspar (7), quartz (8), kaolin (9).....49

Figure 3.4-6: Chin4-1138-Evergreen a) (Ca,Mg)-Fe-aluminosilicate surrounded by degraded K-feldspar; b) (Ca,Mg)-Fe-aluminosilicate (1), K-feldspar (2) and kaolin-replaced remnant K-feldspar (3). EDS spectra and semi-quantitative analysis of the (Ca,Mg)-Fe-aluminosilicates shown below images.50

Figure 3.4-7: Fe-chlorite altered biotite group minerals in a) WW1-1043-Evergreen with EDS spectra in (b); c) WW1-981-Evergreen with EDS spectra in (b).....51

Figure 3.4-8: WW1-1056-Evergreen. a) Sphalerite and minor chalcopyrite (both white) amongst illite and other clays between quartz grains; b) EDS spectra of the sulphides and near-by minerals.....52

Figure 3.4-9: Chin4-897-Evergreen coalified organic matter (1) and muscovite, oxyphlogopite, and biotite mica flakes (2) are the largest common constituents of this sample.52

Figure 3.4-10: Chin4-868-Hutton a) Altered phlogopite containing small crystals of anatase and vermiculite/smectite (1), degraded muscovite (2), K-feldspar (3), Kaolin (4), quartz (5); b) Network of iron oxide crystals (1), Fe-chlorite (2), K-feldspar (3), Quartz (4).53

Figure 3.4-11: a) Chin4-799-Hutton. Euhedral (REE, U)-monazite (1) within calcite (2) cemented quartzose (3) sandstone; b) WW1-799-Hutton. (REE)-monazite with minor pyrite (1) in strongly calcite (2) cemented quartzose (3) sandstone.53

Figure 3.4-12: a) Chin4-799-Hutton. Calcium phosphate (1), calcite cement (2) and quartz (3); b) WW1-800-Hutton. Layer of coal pieces (1) in calcite (2) cemented quartzose (3) sandstone.....54

Figure 3.4-13: Berea Sandstone a) K-feldspar (1), kaolin (2), quartz (3); b) K-feldspar (1), perthitic K-feldspar (2), quartz (3).....54

Figure 3.4-14: Berea Sandstone a) Vermiculite and chlorite (1), degraded K-feldspar (2), quartz (3); b) Ankerite (1), quartz (2).55

Figure 4.1-1: WW1 Upper Precipice Sandstone rutile (1), kaolin (2), and quartz (3) pre (a) and post (b) batch reaction. Although there has been some physical movement of clay fines, the clays did not show evidence of any significant chemical dissolution.....56

Figure 4.1-2: WW1 Lower Precipice Sandstone; (a) K-Na-sulphates (1) on and between quartz grains pre batch reactor experiment (2); (b) the sulphate minerals were removed during batch reaction.57

Figure 4.1-3: Chin4-897-Evergreen a) Clay altered mica (1), phlogopite (2), muscovite (3), kaolin altered K-feldspar (4), albite (5), rutile (6), zircon (7), quartz and kaolin (8); b) little obvious change occurred to these specific minerals after reaction with CO₂-water.....57

Figure 4.1-4: WW1-1043-Evergreen; Illite and fine grains of oxyphlogopite (1) between quartz grains (2) pre (a) and post reaction (b) showing little change.58

Figure 4.1-5: WW1-1056-Evergreen Ca-phosphate grain pre (a) and post (b) batch reaction showing only minor surficial changes.58

Figure 4.1-6: Chin4-897-Evergreen a) Biotite, chlorite and siderite (1); phlogopite (2), perthitic K-feldspar (3); b) siderite dissolved leaving behind remnants of the chloritised biotite framework in which it occurred (4).58

Figure 4.1-7: WW1-1043-Evergreen calcite (1) and clays (2) between quartz grains (3) pre (a) and post reaction (b); WW1-1056-Evergreen calcite (4), quartz (5), and zircon (6) grains pre (c, e) and post (d, f) reaction, with clays sometimes exposed by loss of calcite (e.g. 7 in f).59

Figure 4.1-8: Chin4-799-Hutton, top of reacted sample a) Calcite cement (1) in between quartz grains (2) and minor others such as K-feldspar (3); b) Remnant calcite cement (4) and new pore-space that was previously cemented (5); c) Sample WW1-800-Hutton, base of reacted sample. Partially reacted calcite (6) remaining between quartz grains (7) was commonly observed.60

Figure 4.1-9: Berea Sandstone; Siderite and haematite (white) between quartz grains (grey) pre (a) and post (b) CO₂-brine exposure.61

Figure 4.2-1: Vertical plane images from high resolution 3D μ CT tomograms of WW1 sub-plugs before reaction a) 1217-Precipice (WC14a), b) 1165-Precipice (WC11a), c) 1056-Evergreen (WC9a), d) 1043-Evergreen (WC8a), e) 981-Evergreen (WC3a), f) 800-Hutton (WC15a). Source: Golab et al. (2014), used with permission.63

Figure 4.2-2: Registered tomogram images of WW1-1043-Evergreen sub-plug slice, a) Pre-reaction, b) post-reaction, c) difference image (dark areas = loss of material) , d) QEMSCAN after reaction with mineral key shown. Source: Golab et al. (2014), used with permission. ..66

Figure 4.3-1: WW1 Upper Precipice incremental water chemistry results for batch reactor experiment.....69

Figure 4.3-2: WW1 Lower Precipice incremental water chemistry results for batch reactor experiment.....69

Figure 4.3-3: Chinchilla 4 Upper Precipice incremental water chemistry results for batch reactor experiment.70

Figure 4.3-4: WW1 Upper Evergreen incremental water chemistry results for batch reactor experiment.....71

Figure 4.3-5: WW1 Lower Evergreen lithic sandstone incremental water chemistry results for batch reactor experiment.....72

Figure 4.3-6: WW1 calcite cemented Lower Evergreen sandstone incremental water chemistry results for batch reactor experiment.....73

Figure 4.3-7: Chinchilla 4 Lower Evergreen sandstone incremental water chemistry results for batch reactor experiment.73

Figure 4.3-8: Chinchilla 4 Upper Evergreen interlaminated siltstone and sandstone sample incremental water chemistry results for batch reactor experiment.74

Figure 4.3-9: WW1 calcite cemented Hutton Sandstone sample incremental water chemistry results for batch reactor experiment.....75

Figure 4.3-10: Chinchilla 4 calcite cemented Hutton Sandstone sample incremental water chemistry results for batch reactor experiment.....76

Figure 4.3-11: Chinchilla 4 lithic Hutton Sandstone sample incremental water chemistry results for batch reactor experiment.....76

Figure 4.3-12: Berea Sandstone sample incremental water chemistry results for batch reactor experiment.....77

Figure 4.4-1: WW1-1211-Precipice incremental chemistry results for continuous flow reactor experiment.....78

Figure 4.4-2: WW1-1056-Evergreen; reddish-brown colloidal material settling-out shortly after fluid sampling.....80

Figure 4.4-3: Incremental water chemistry for continuous flow reactor experiment with calcite cemented WW1-1056-Evergreen.80

Figure 4.4-4: a) Hot glue injected into the joints between the sample and the sample holder insert foamed in response to exposure to supercritical CO₂ increasing the seal efficiency; b) the heat-shrink wrap around the sample remained firmly in place during the experiment, with

the sample largely intact apart from a small sliver of rock that split off the base during removal from the chamber.81

Figure 4.4-5: Major (a, b) and minor (c, d) elements measured within incremental fluid samples for the continuous flow reaction of Berea Sandstone sample B1.82

Figure 4.5-1: Unreacted WW1-1211-Precipice (WC20) permeability vs stress.87

Figure 4.5-2 :WW1-1043-Evergreen N₂ permeability vs stress; all three orientations pre-reaction and vertical post reaction.88

Figure 4.5-3: WW1-1056-Evergreen N₂ permeability vs stress a) pre exposure to scCO₂ saturated water during continuous flow reactor experiment; b) post exposure to scCO₂ saturated water.89

Figure 4.5-4: a) Berea Sandstone permeability vs stress; b) Conceptual cartoon of fines creation during stressing.90

Figure 4.6-1: Directional stress-microstrain of WW1-1211-Precipice pre- and post-reaction.91

Figure 4.6-2: Directional stress-microstrain of WW1-1056-Evergreen pre- and post-reaction.92

Figure 4.6-3: Directional stress-microstrain of WW1-1043-Evergreen pre- and post-reaction.92

Figure 4.6-4: Directional stress-microstrain of Berea Sandstone cube B1 pre- and post-reaction.93

Figure 6.1-1: Geochemical modelling results for WW1-1165-Precipice batch reactor experiment.99

Figure 6.1-2: Geochemical modelling results for WW1-1217-Precipice batch reactor experiment.100

Figure 6.1-3: Geochemical modelling results for WW1-981-Evergreen batch reactor experiment.102

Figure 6.1-4: Geochemical modelling results for WW1-1043-Evergreen batch reactor experiment.103

Figure 6.1-5: Geochemical modelling results for WW1-1056-Evergreen calcite cemented sandstone batch reactor experiment.105

Figure 6.1-6: Geochemical modelling results for WW1-800-Hutton calcite cemented sandstone batch reactor experiment.106

Figure 6.2-1: Multiple approaches for computational fluid dynamics with their preferred range of applicability (Raabe, 2004).108

Figure 6.2-2: (a) Scan of a real porous medium section (315 × 295); (b) reconstructed digital structure, which has some slight variations compared to the original (e.g. features circled).109

Figure 6.2-3: Fluid flow route with (a) impermeable aggregates and (b) permeable geomaterials; velocity profile of fluid flow with (c) impermeable aggregates and (d) permeable geomaterials; velocity profile (e) detached from (c), and velocity profile (f) detached from (d).110

Figure 6.2-4: A thin section of porous medium involving multiple geomaterials shown in different colors (pore - red, lithic fragments - green, weathered feldspars - blue, quartz -

black). The vertical black lines at $x = 23, 72$ and 172 indicate cross-section lines to be studied.111

Figure 6.2-5: Outcrop of multiple geomaterials (thick black lines indicate surfaces of geomaterials), and velocity distribution of the fluid flow (arrows and length indicate the velocity direction and size, respectively)..... 112

Figure 6.2-6: Outcrop of multiple geomaterials (thick black lines indicate surfaces of geomaterials), and velocity magnitude field with contours (contour step = 50). 112

Figure 6.3-1: Plume dispersion for case 1 after 2 years of injection 125

Figure 6.3-2: Injection rates for different porosities and permeabilities. 126

Index of tables

Table 3.1-1: Chinchilla 4 Sample Summary.....	32
Table 3.1-2: West Wandoan 1 Sample Summary.....	33
Table 3.2-1: Chinchilla 4 qualitative X-ray diffraction analysis of bulk-rock powder and oriented clay fraction, listed in order of most to least abundant.....	35
Table 3.2-2: WW1 whole rock semi-quantitative XRD results, listed in order of most to least abundant.....	35
Table 4.2-1: Resolved mineral and porosity components from 3D tomogram segmentation of Chin-4 sub-plugs pre- and post CO ₂ -water-rock reactions (vol. %)......	62
Table 4.2-2: Mineral assays (area %) of Chin-4 samples derived from QEMSCAN microanalysis of polished sections from sub-plugs pre- and post- CO ₂ -water-rock reactions.	62
Table 4.2-3: Resolved mineral and porosity components from 3D tomogram segmentation of WW-1 sub-plugs pre- CO ₂ -brine-rock reactions (vol. %). Resolved porosity indicates pores that are larger than the elemental volume for a tomogram, i.e. 1 voxel (3D pixel) in size.	64
Table 4.2-4: Comparative mineral assays, as area percentages, of WW-1 sub-plug polished sections measured by QEMSCAN pre and post CO ₂ -brine-rock reactions.....	64
Table 4.5-1: Porosity of sister samples pre- and post- reaction tested using Hg-intrusion.	83
Table 4.5-2: Unstressed WW1 15 mm samples N ₂ permeability pre and post reaction (mD) ¹	84
Table 4.5-3: N ₂ permeability (unstressed) of WW1 unreacted Precipice Sandstone samples (mD).	85
Table 4.5-4: WW1-1211-Precipice (40 mm) N ₂ (unstressed) permeability improvement following reaction.	86
Table 4.5-5: WW1-1043-Evergreen 40 mm cube sample unstressed N ₂ permeability (mD) .	88
Table 4.5-6: Directional permeability of the 40mm Berea Sandstone cube samples (unstressed, N ₂).	90
Table 6.2-1: Example of voxel resolution effects on the modelled directional permeability.	120

Geochemical and Geomechanical Testing of Near Wellbore CO₂ Injectivity Improvement

Glossary of Minerals

Name		Formula	Other notes
Amphibole		Quite variable, an example is Ca ₂ (Mg,Fe) ₅ Si ₈ O ₂₂ (OH) ₂ (actinolite)	Rare in sediments, highly reactive
Carbonates	Ankerite	Ca(Fe,Mg,Mn)(CO ₃) ₂	(Pure ankerite has no Mg; this is rare in nature)
	Bronshedtite	Na-Fe-PO ₄ CO ₃	
	Calcite	CaCO ₃	Sometimes contains significant Mn &/or Mg
	Dolomite	CaMg(CO ₃) ₂	Often contains some Fe
	Siderite	FeCO ₃	
	Soda ash	Na ₂ CO ₃	
	Strontianite	SrCO ₃	
	Rhodochrosite	MnCO ₃	
	Witherite	BaCO ₃	
Clays	Kaolin	Dickite	Al ₂ Si ₂ O ₅ (OH) ₄
		Kaolinite	Al ₂ Si ₂ O ₅ (OH) ₄
	Illite		(K,H ₃ O)(Al,Mg,Fe) ₂ (Si,Al) ₄ O ₁₀ [(OH) ₂ ·(H ₂ O)]
	Smectite	Montmorillonite	(Na,Ca) _{0.33} (Al,Mg) ₂ (Si ₄ O ₁₀)(OH) ₂ ·nH ₂ O
		Nontronite	(Ca _{0.5} ,Na) _{0.3} Fe ³⁺ ₂ (Si,Al) ₄ O ₁₀ (OH) ₂ ·nH ₂ O
		Saponite	Ca _{0.25} (Mg,Fe) ₃ (Si,Al) ₄ O ₁₀ (OH) ₂ ·n(H ₂ O)
	Vermiculite		(Mg ⁺² ,Fe ⁺² ,Fe ⁺³) ₃ [(AlSi) ₄ O ₁₀](OH) ₂ ·4H ₂ O
Chlorites	Chamosite		(Fe ²⁺ ,Mg) ₅ Al(AlSi ₃ O ₁₀)(OH) ₈
	Clinochlore		(Mg,Fe) ₃ (Si,Al) ₄ O ₁₀ (OH) ₂ ·(Mg,Fe) ₃ (OH) ₆
Feldspars	(Alkali/Potassic)	Microcline	KAlSi ₃ O ₈
		Orthoclase	KAlSi ₃ O ₈
		Perthitic K-feldspar	Minor Na within KAlSi ₃ O ₈
		Sanidine	K(AlSi ₃ O ₈)
	Plagioclase	Albite (Ab)	NaAlSi ₃ O ₈
		Oligoclase	90-70% Ab, 10-30% An
		Andesine	70-50% Ab, 30-50% An
		Labradorite	50-30% Ab, 50-70% An
		Bytownite	30-10% Ab, 70-90% An
		Anorthite (An)	CaAl ₂ Si ₂ O ₈
Garnet		X ₃ Y ₂ (SiO ₄) ₃ where X commonly can be Fe, Mg, Mn, or Ca and Y can be Al, Cr, or Fe	
Hydroxide	Dawsonite		NaAlCO ₃ (OH) ₂
	Gibbsite		γ-Al(OH) ₃

Geochemical and Geomechanical Testing of Near Wellbore CO₂ Injectivity Improvement

Name		Formula	Other notes	
Micas	Biotite	Eastonite	$KMg_2Al_3Si_2O_{10}(OH)_2$	
		Oxyphlogopite	$K(Mg,Ti,Fe)_3[(Si,Al)_4O_{10}](O,F)_2$	Ti-phlogopite
		Phlogopite	$KMg_3AlSi_3O_{10}(F,OH)_2$	
		Siderophyllite	$KFe^{2+}_2Al(Al_2Si_2)O_{10}(F,OH)_2$	
		Glaucosite	$(K,Na)(Fe^{3+},Al,Mg)_2(Si,Al)_4O_{10}(OH)_2$	
	(Potassic)	Muscovite	$KAl_2(AlSi_3O_{10})(F,OH)_2$	
		Sericite	As for muscovite	Fine-grained muscovite
Oxides	Hematite	$\alpha-Fe_2O_3$		
	Anatase	TiO_2		
	Rutile	TiO_2		
Oxy-hydroxide	Boehmite	$\gamma-AlO(OH)$		
	Diaspore	$\alpha-AlO(OH)$		
	Lepidocrocite	$\gamma-FeO(OH)$		
	Quartz	SiO_2	Chalcedony is intergrown microcrystalline quartz & moganite (also SiO_2)	
Phosphates	Apatite	$Ca_5(PO_4)_3(F,Cl,OH)$		
	Crandallite	$CaAl_3(PO_4)_2(OH)_5 \cdot H_2O$		
	Monazite	$(Ce,La)PO_4$		
Sulfides	Chalcopyrite	$CuFeS_2$		
	Galena	PbS		
	Pyrite	FeS_2		
	Pyrrhotite	$Fe_{1-x}S$ (x = 0 to 0.2)		
	Sphalerite	$(Zn,Fe)S$		
Sulfates	Anhydrite	$CaSO_4$		
	Arcanite	K_2SO_4		
	Barite	$BaSO_4$		
	Celestine	$SrSO_4$		
	Cyanochroite	$K_2Cu(SO_4)_2 \cdot 6(H_2O)$	Hydrated K-Cu-sulphate	
	Gypsum	$CaSO \cdot 2H_2O$		
	Jarosite	$KFe_3(SO_4)_2(OH)_6$	Hydrated K-Fe-sulphate	
	Mirabilite	$Na_2SO_4 \cdot 10H_2O$		
	Natrojarosite	$(K,Na)Fe^{3+}_3(SO_4)_2(OH)_6$	Hydrated Na-K-Fe-sulphate	
	Zircon	$ZrSiO_4$		

1. Introduction

This report presents the results of ANLEC Project 7-1110-0101 that investigated changes in reservoir properties in the near wellbore region as a result of geochemical reactions. This will affect injectivity and storage capacity, as well as the number of wells required for CO₂ storage projects. This project is part of a group of related ANLEC projects supporting Australian CO₂ sequestration demonstration and commercial projects.

The near wellbore area is critical for CO₂ injection into deep geological formations as most of the resistance to flow occurs in this region. Any changes to the permeability in this region can have significant economic impact in terms of well utilisation efficiency and compression costs. In the far field, away from the well, the affected reservoir is much larger and changes to permeability through blocking or enhancement have relatively low impact, though they can still affect the direction of CO₂ plumes over longer time scales.

Injected supercritical CO₂ displaces the formation water ahead of it, and the CO₂ and water, being mutually soluble, create a mixing zone that grades from pure water at the leading edge to pure CO₂ at the trailing edge. The CO₂-water mixture has a relatively low pH, due to formation of carbonic acid, which varies according to the concentration profile across the mixing zone and may induce dissolution of reactive minerals in the host rock. This is a favourable process that potentially creates new porosity and permeability in the near wellbore region and is a form of acid stimulation similar to that practised by the oil and gas industry on low permeability formations or scaled-up wells. Further out in the reservoir, and potentially at the interface with the seal rock, temperature and pressure conditions change as does the degree of fluid pH-buffering, leading to changes in solubility and thus precipitation of some of the previously solubilised minerals, somewhat reducing porosity and permeability. This precipitation leads to favourable mineral trapping of the CO₂.

In this project, the geochemical, rock mechanical and petrophysical effects of supercritical CO₂ (scCO₂) injection on a targeted storage system in the Surat Basin, Queensland, Australia, were investigated using experimental reactions at simulated basin conditions. Samples from a potential CO₂ reservoir, the Precipice Sandstone, and from two overlying formations, the Evergreen Formation (potential seal) and Hutton Sandstone (overlying aquifer), were sourced from the Geological Survey of Queensland stratigraphic drill core Chinchilla 4 and the recently drilled West Wandoan 1 borehole. Samples of an international standard, quarried Berea Sandstone were also provided by ANLEC for the purpose of experimental procedure testing and benchmarking of results across related ANLEC projects. The inclusion of samples of formations other than the target reservoir in this work program allowed investigation of the response of a wide range of lithologies to CO₂ exposure.

Geochemical and Geomechanical Testing of Near Wellbore CO₂ Injectivity Improvement

The project workflow is based around five major aspects: 1) detailed characterisation of selected rock samples; 2) geochemical testing of sample responses to both static and dynamic reaction with carbonic acid under simulated *in situ* CO₂ geosequestration conditions; 3) permeability studies of the samples before and after reaction with carbonic acid; 4) geomechanical testing of samples before and after carbonic acid treatment; and 5) detailed modelling of CO₂ geosequestration behaviour at both the pore and near-well scales, coupled where possible with experimental data.

Detailed characterisation has involved the use of techniques such as the Hylogger tool at the core scale, and standard petrography, X-ray diffraction analysis (XRD), scanning electron microscopy with energy-dispersive spectrometry (SEM-EDS), QEMSCAN, 3D X-ray micro-computed tomography (X-ray micro-CT), N₂ gas and brine permeability, He pycnometry and mercury porosimetry for selected rock samples before and after geochemical experiments where possible (Dawson et al., 2013; Dawson et al., 2014; Farquhar et al., 2013; Farquhar et al., 2014). The fluids of geochemical experiments were sampled periodically and analysed for major and trace elements to infer CO₂-water-rock interactions. These data were related to changes to pre-experiment sample mineralogy and texture, as observed using SEM-EDS, QEMSCAN and micro-CT. Kinetic geochemical modelling of sampled fluids obtained during the CO₂-water-rock experiments was conducted for selected aqueous major and minor elements and successfully reproduced the general trends observed in aqueous geochemistry, allowing identification and verification of dissolving or precipitating minerals.

For mesoscale modelling of fundamental fluid flow dynamics in geometrically complex, pore-scale porous media (sandstones), the conventional lattice Boltzmann method (LBM) has been extended to describe the heterogeneous porous media where each composition on the lattice grid has its own hydraulic property. This also includes the reconstruction of digital 2D/3D reservoir rock samples from registered X-ray micro-CT and QEMSCAN images of core sub-plugs from the Chinchilla 4 well, which have been translated into a high-resolution lattice for LBM flow simulations. The model is implemented as an in-house extended LBM code (XLBM), and benchmarked through comparison with existing analytical solutions. We have also developed an effective pore scale reactive transport computational model based on the in-house parallel XLBM, which describes the geochemical reactions of both solute ion transport and solid phase CaCO₃ dissolution in CO₂-saturated water as well as their effects on the velocity fields of fluid flow during the CO₂ injection process. This includes the porosity change with calcite dissolution and feedback impacts on fluid flow, and it has been validated against experimental results for a calcite-cemented Hutton Sandstone sample.

The large-scale simulation model is based on conditions relevant to the Wandoan carbon storage project in the Surat Basin, Queensland, and aims to better quantify the dynamic injectivity and real storage volumes as they evolve over time during CO₂ geosequestration. The commercial software

tool GEM, from the Computer Modelling Group (CMG), has been used for the simulation. This software is based on the finite element method, populated with parameters derived from the experiments and informed by the mesoscale LBM model. We examined the cases where (i) CO₂ injection has limited effect on the porosity or permeability of the injection zone (set at a total porosity value of 21%); (ii) porosity increases modestly (to 22 and 23%); and (iii) where there is a higher degree of interaction and dissolution (to 24 and 25%). For the interaction cases, we applied the porosity (and hence permeability) increase only in the immediate completion zone yet nevertheless demonstrated a significant increase in injectivity and storage capacity for more reactive lithologies.

2. Experimental Methods

2.1. Batch and Continuous Flow Reactors

2.1.1. Batch Reactors

Batch experiments were performed using unstirred Parr® reactors (250ml, N4651, Parr) with custom-built thermoplastic vessel liners, sample holders and a dip tube assembly (Figure 2.1-1), with a fully contained piped emergency pressure relief set-up (Pearce et al., 2014). Pressure and temperature monitoring, and control and safety shutoff systems were incorporated through a dedicated Labview program, and the hardware was also configured so that any electrical faults would result in system shutdown. Vessels were maintained at $60 \pm 1^\circ\text{C}$ with heating jackets and thermostats (B-200-2, Cynebar), and vessel pressure monitored with pressure transducers (4-20 mA; 40.0 MPa, GEM, ECEFast).

Deoxygenated Milli-Q water or brine was added to the reactor, with the rock samples (SEM sample, porosity/permeability cube, X-ray micro-CT sub-plug) suspended in a thermoplastic basket immersed in the fluid. Vessels were purged of residual air with a low pressure N₂ flush. A Teledyne ISCO syringe pump (500HP) was used to pressurise vessels to 12.0 ± 0.5 MPa, initially with N₂ gas. Following an initial baseline water – rock reaction period, water samples were obtained, and N₂ gas subsequently replaced with pure food grade CO₂ (Coregas) using the syringe pump, and without exposing the internal system to the atmosphere. For most samples, the conditions of 60°C and 12 MPa were used to simulate conditions in part of the Surat Basin, Australia.

The fluids were sampled over a period of about 16 or 28 days for Chinchilla 4 samples and West Wandoan 1 samples respectively, before terminating the experiment and collecting the residual fluids and solids. Berea Sandstone samples were reacted at 50 °C and 10 MPa at the conditions chosen for the Berea Round Robin experiments, for 10 days in 1% NaCl, with further details in Dawson et al. (2014). The short reaction time was chosen to represent conditions expected near an injection wellbore during initial flooding with CO₂ (or mixed gas). In this region gas-acidified groundwater is expected to be displaced by a gas-dominated phase thus terminating the main aqueous reactions (e.g. André et al., 2011).

Deoxygenated pure water, 1.5 g/L NaCl, 1.5 g/L KCl, 1 wt% NaCl solution, or 1 wt% KCl solution was added to the reactors depending upon which rock samples were being reacted. The Chinchilla 4 sample experiments used 70 mL of pure MQ water, except for Chin4-1138-Evergreen where 1 wt% KCl was used to prevent ion exchange and swelling of clays (detailed in Farquhar et al. (2014)). Subsequent West Wandoan 1 samples were reacted with 100 mL of 1.5 g/L NaCl brine, except for WW1-1056-Evergreen (1 wt% KCl), and WW1-800-Hutton (1.5 g/L KCl). Berea Sandstone was

reacted with 100 ml of 1 wt% NaCl as this was shown during separate testing to be above the critical salt concentration for this sample (Keck et al., 2013). Blank tests were also conducted without rock material, which verified that any cation contamination from corrosion of the reaction vessel was below the level detected from rock reactions. All vessel liners and samplers were cleaned by soaking in nitric acid and Milli-Q water after use, and the reactor itself cleaned twice between experimental runs with a supercritical CO₂ – water mixture.

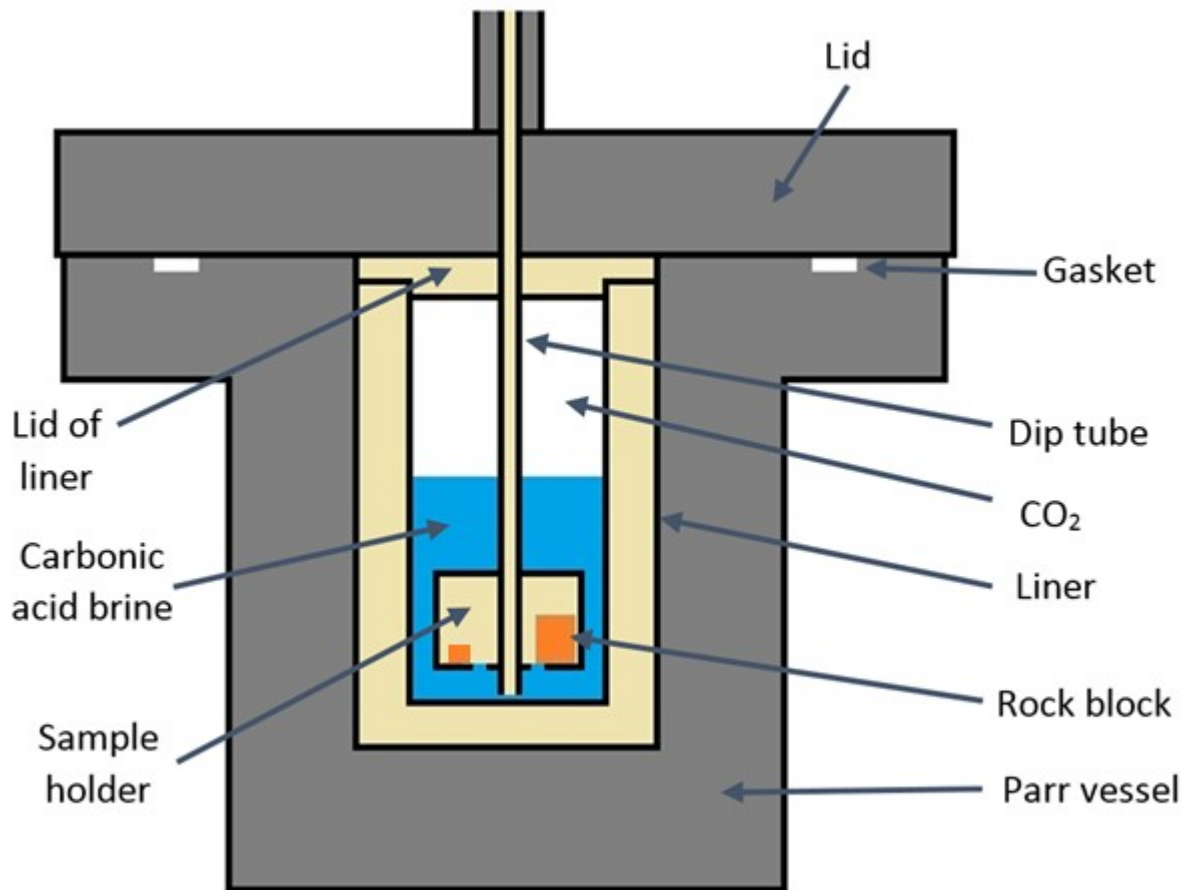


Figure 2.1-1: Illustration of Parr reactor showing thermoplastic liner, and rock samples immersed in water or brine.

2.1.2. Continuous Flow Reactor

The 40 mm cube samples were reacted orientated vertically, i.e. fluid flow perpendicular to bedding layers, in a system in which a mixture of supercritical CO₂ and water could be passed continuously through the samples (Figure 2.1-2). Reverse osmosis treated water was pumped into the system with CO₂ at a pressure of 12 MPa at 60 °C. Saline water could not be safely pumped with the current stainless-steel narrow-piped system; however, it was able to be added directly to the head of the sample chamber in order to test sample response to changes in salinity. It was not possible to precisely set the CO₂-water mixture flow-rate; rather, this was done indirectly through a

combination of setting the level of the water reservoir, the water pump flow-rate used to top-up the water reservoir, the pressure of CO₂ pumped into the system, and the degree of restriction upon the tap at the fluid outlet. Hence, it was not possible to quantify dynamic permeability with the present system. Permeability was therefore measured pre and post reaction with separate systems. For safety reasons, the reactor was operated only during lab hours with pressure shut-in overnight and on weekends.

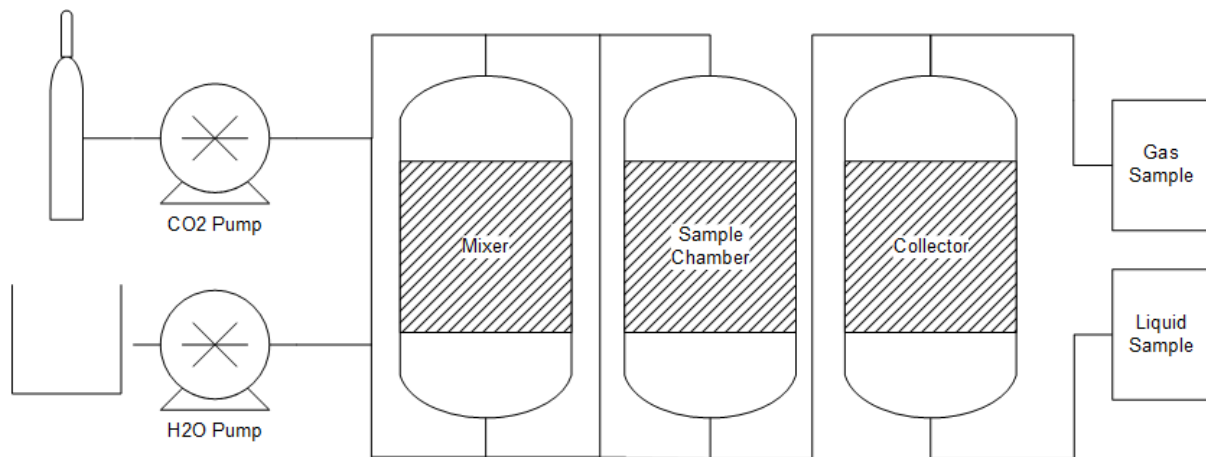


Figure 2.1-2: Schematic of continuous flow reactor.

2.2. SEM-EDS

SEM-EDS was performed pre and post reaction on rock cube surfaces using a JEOL6460 environmental SEM with low vacuum capability. For semi-quantitative EDS spot analyses 1000x magnification was used, which equates to an area of electron beam-sample surface interaction of roughly 3 micrometres. Quantitative EDS analysis was not possible due to surface roughness. The brightness and contrast of SEM backscatter electron images give an indication of compositional differences within the samples, with brighter regions corresponding to heavier elements, and different minerals appearing as different shades of grey. However, surface charging and topography effects also contribute to image brightness and so visual appearance of the images can only be used as an approximate guide as to the different minerals present within the samples.

2.3. QEMSCAN and X-ray Micro-CT Scanning

Suitable sections of core were selected and sub-plugs cut from the Chinchilla 4 and West Wandoan 1 core samples. Sub-plugs were reacted in addition to cubes, with pre and post reaction analyses performed by FEI – Lithicon Digital Rock Services. X-ray micro CT was performed to visualise and characterise pore networks and determine porosity within resolution (above ~ 2 µm). QEMSCAN (automated SEM) was also performed pre and post-reaction on separate polished slices from the end of the sub-plug to determine the major mineral components present.

2.4. Water Chemistry

The solution chemistry of the geochemical reactors was periodically analysed during the course of the experiments to monitor reaction progress. Sampled aliquots (~ 2 millilitres) were diluted and preserved with 2% v/v HNO₃ prior to analysis. An Inductively Coupled Plasma Optical Emission Spectrometer (ICP-OES, Perkin Elmer Optima 3300 DV ICP-OES, 3 σ detection limit of 0.001 mg L⁻¹) with an error of ~ 5% was used to measure elemental concentrations of aqueous species in the experiment waters. Solution pH and conductivity was also measured *ex situ* immediately upon sampling, using a TPS WP81 meter and probes with an error of ± 0.01 .

2.5. Porosity, Permeability and Geomechanical Apparatus

To assess potential changes in porosity due to geochemical reactor experiments, sister samples were produced for each test. For the three sister samples batch reacted during each of those experiments (SEM sample, X-ray micro-CT plug, and porosity/permeability cube), unreacted offcuts were kept aside for comparative tests of density, porosity, and permeability. The continuous flow reactor experiments used 40 mm cubes of sample material directly related to batch reactor samples. For core samples these were cut vertically adjacent to each other, whereas the Berea 15 mm and 40 mm cubes obtained were all horizontal sister samples. The unstressed N₂ permeability was measured for cube face orientations (Figure 2.5-1) of all samples prior to and following both batch and continuous flow reactor experiments (Section 2.5.1.2), with water permeability only measured for 15 mm cubes (Section 2.5.1.3). Water permeability was not measured for the 40 mm cubes so as to limit the number of variables affecting the stressed N₂ gas permeability and geomechanical testing done on these samples pre and post continuous flow reaction with a mixture of scCO₂ and water.

The order and conditions under which specific tests were done for each sample are integral to interpretation of the results. Firstly, mass and He-density were measured for each sister sample set. The virgin N₂ permeability (unstressed) of the 15 mm cubes was tested prior to water permeability. It was necessary to first soak the samples in water of salt composition used during batch reactions for at least a day prior to testing water permeability. This was to ensure that the swelling response of clays within the accessible porosity of the samples was stabilised sufficiently to not change during the actual water permeability test (Figure 2.5-2). This procedure was used for both the unreacted cubes and the batch reaction permeability cubes.

Geochemical and Geomechanical Testing of Near Wellbore CO₂ Injectivity Improvement

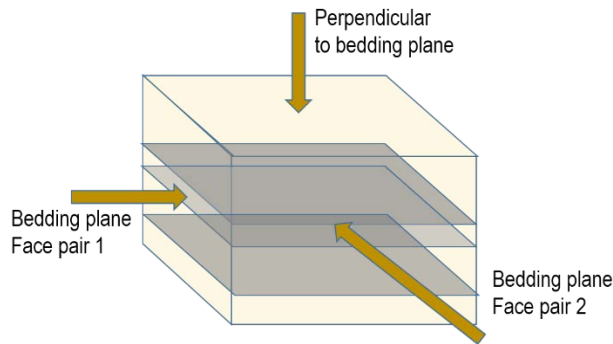
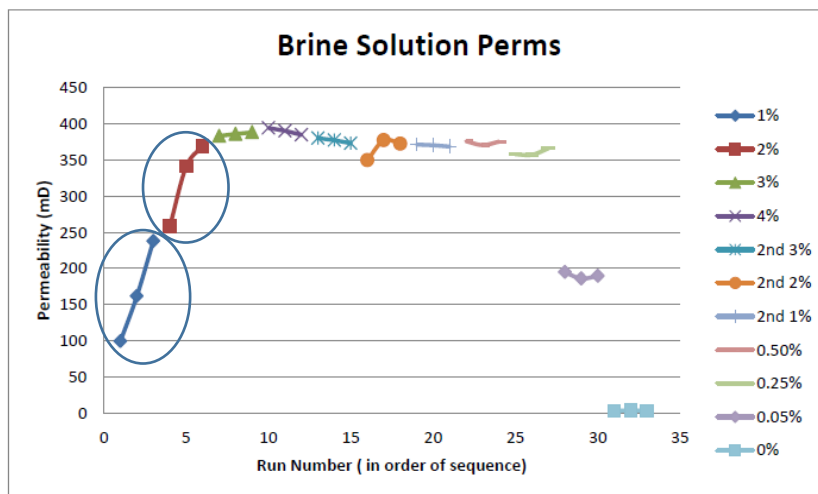
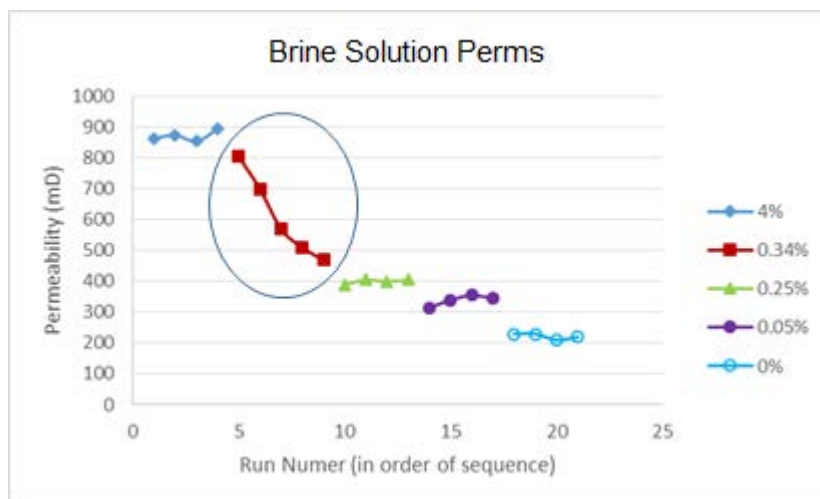


Figure 2.5-1: Directional permeability of a sedimentary rock

a



b



Post reaction, permeability (using brine with the same salt composition as test fluid) was remeasured using the still-wet reacted 15 mm permeability cubes prior to oven drying and subsequent retesting of the N₂ permeability. The reacted samples were then used for testing of post-reaction density and porosity. Following reaction the 40 mm cube samples were oven dried prior to testing of the post reaction unstressed N₂ permeability for all three face orientations. These samples were then retested for stressed N₂ permeability and triaxial strain response (Section 2.5.2).

2.5.1. Unstressed Permeameter

This custom-built equipment (Figure 2.5-3) can measure oriented gas or water permeability for 15 mm and 40 mm cube samples, as well as cylindrical sample shapes not tested for this project. Gas permeability of all three cube orientations (Figure 2.5-1) was measured using N₂ gas. Liquid test fluids included pure water, 1.5 g/L NaCl, 1.5 g/L KCl, 10 g/L NaCl, and 10 g/L KCl.

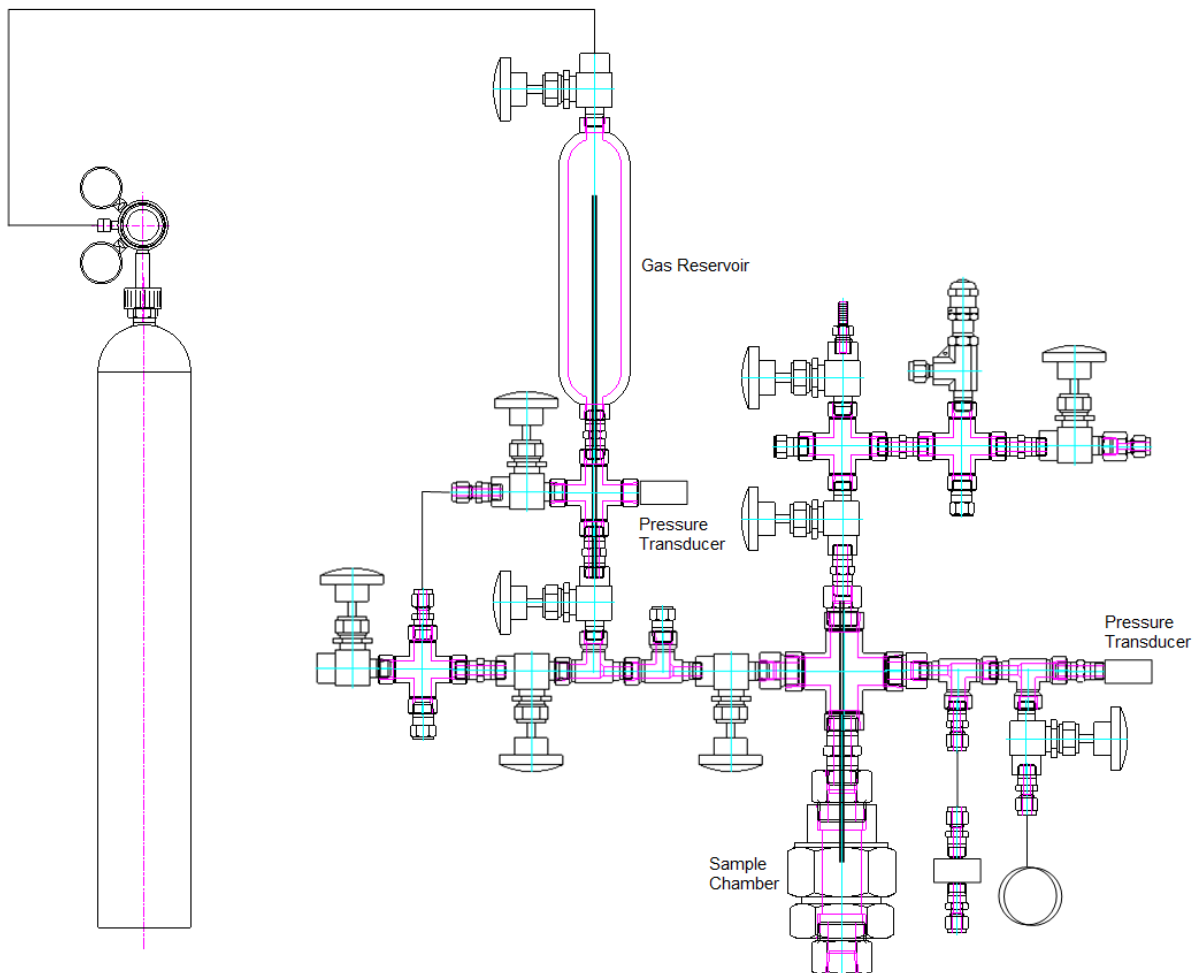


Figure 2.5-3: Low pressure permeameter (drawing not to scale).

2.5.1.1. Theory

For a compressible gas, fluid expansion affects the permeability measurement. However, for these experiments, it was assumed that the gas permeation through the samples is an isothermal process and that the fluid flow is laminar, and the ideal gas law applied. Throughout this report experimentally-determined permeability of the samples for different fluids are calculated by using the empirical Darcy law (Darcy, 1856). From the experimental work the normalised pressure drop and fractional flow rate for each test were used in the permeability calculation (Eq. 2.5-1).

$$Q = \frac{kA(\Delta p)}{\mu L} \quad (\text{Eq. 2.5-1})$$

Where Q is the flow rate of the fluid, k is permeability, A is the cross-sectional area of the rock sample, Δp is the pressure difference between the inlet fluid pressure and outlet fluid pressure, μ is viscosity of fluid, and L is the length of the sample.

To obtain water permeability, equation 1 was rearranged to give k based upon measured average water flow rate for given pressure drops across each sample over time. Though the liquid permeability of a sample could be obtained from measuring the discharge rate of fluid under a certain pressure gradient, accurate measurements of gas flow rate can be difficult to obtain, thus time was measured instead. Accordingly, a method initially developed by (Brace et al., 1968) was adopted. The fundamental equations for this measurement are:

$$(p_i - p_f) = \Delta p \left[\left(\frac{v_2}{v_1} \right) + v_2 \right] e^{-at} \quad (\text{Eq. 2.5-2})$$

$$a = \left(\frac{Ak}{\mu ZL} \right) \left(\frac{1}{v_1} + \frac{1}{v_2} \right) \quad (\text{Eq. 2.5-3})$$

Where A is cross sectional area of the sample, L is length of the sample, v_1 and v_2 are volumes of reservoirs 1 and 2 respectively, $p_i - p_f$ is difference between inlet fluid pressure and outlet fluid pressure, Δp is step change of pressure in reservoir at $t=0$, Z is compressibility and μ is viscosity of the fluid. The natural logarithm of both sides of equation 2.5-2 was taken, which gives:

$$\ln(p_i - p_f) = -at + \ln(\Delta p) \left(\frac{v_2}{v_1} + v_2 \right) \quad (\text{Eq. 2.5-4})$$

Where the slope (a) is obtained from plotting $\ln(p_i - p_f)$ against t.

Permeability can then be calculated.

2.5.1.2. Unstressed gas permeability measurement procedure

Both 15 mm and 40 mm cubes were tested with N₂ gas using the custom-built “unstressed permeameter” using the following procedure:

- 1- Polyolefin heat shrink was used to jacket the sample, with the test face-pair left exposed.
- 2- The covered sample was put into a cylindrical steel container. For 15 mm cube samples, hot glue was used to fill the gap between covered sample and steel container prior to insertion into the permeability apparatus. The 40 mm samples were inserted into the triaxial cell normally used in the stressed-permeameter, and this was then attached to the base of the unstressed permeameter apparatus.
- 3- After the desired initial pressure was set, the valve was opened to allow gas flow. The difference between the inlet fluid pressure and outlet fluid pressure was logged every 1 second. Up to twenty-two replicate measurements of permeability were recorded per cube face-pair.
- 4- $\ln(p_i - p_f)$ versus time was plotted, and the slope of the linear portion was obtained from the plot to use in equation 2 for gas permeability calculation.
- 5- Steps 1-4 were repeated for each cube face-pair.

2.5.1.3. Unstressed water permeability measurement procedure

Synthetic brine was used, in which the solutes were 1 wt% sodium chloride (NaCl), 1.5 g/L NaCl, or 1.5 g/L KCl. The lower half of the apparatus was removed and left open to the atmosphere. A balance with a beaker was placed beneath the lower opening of the sample cell. Exactly 100 mL of water was introduced to the top of the apparatus, with the initial pressure of that section set to 100 kPa(g) using N₂. The pressure drop over time due to water draining through the sample and out of the apparatus was recorded by LabView software, and the incremental weight increase due to water entering the beaker was recorded by the balance. These two data sets were then combined and manipulated to produce graphs of liquid permeability over elapsed experimental time.

Permeability for samples was measured over the same defined range of Δp before and after experiments in order to help ensure that the separate measurements would be as comparable as possible. The Δp range was chosen on the basis of steady-state flow, for all samples. Non-linear phenomena such as pore liquid/gas displacement were minimised by ensuring that samples were pre-soaked in solution of the same composition used for the tests. As for gas tests, permeability was calculated using the empirical Darcy Law.

2.5.2. True Triaxial Cell Stress/Strain Permeameter

The 40 mm cube samples were tested in a custom-built True Triaxial Stress Cell Permeater (TTSCP-rig (Massarotto et al., 2010)). This apparatus (Figure 2.5-4) can be used to measure gas permeability under stressed conditions. For these tests, strain gauges were mounted to three of the cube faces (one for each orientation) and the sample fitted with a polyurethane gasket. The sample was then placed within the true triaxial stress cell and sealed within the rig. Pressure on each face was increased isotropically in 1.0 MPa increments up to 23 MPa; this equates roughly to the equivalent confining pressure of up to 1000 m depth. For each step, the sample was held at the stressed condition for 10 minutes to fully relax, before moving to the next measurement point. Following testing the strain gauges were removed and the samples moved to the flow reactor for pressure leaching with CO₂-saturated water. After reaction, strain gauges were remounted to the same prepared points on each face that had been tested pre-reaction and the stress-strain measurements done again in the TTSCP apparatus.



Figure 2.5-4: The custom-built True Triaxial Stress Cell Permeater (TTSCP).

3. Rock Sample Characterisation

3.1. Sample Selection

Samples were obtained from cores GSQ Chinchilla 4 (Figure 3.1-1 and Table 3.1-1) and West Wandoan 1 (Figure 3.1-2 and Table 3.1-2) that were drilled in the Surat Basin of Queensland, Australia. Samples of Berea Sandstone from a quarry in the USA were also included in the work program to help test the permeability and rock mechanics apparatus and procedures, and also to act as a benchmark against other petroleum-industry related studies that have used Berea Sandstone as a standard test material. The Surat core samples were taken from a stacked reservoir-seal sequence. The Upper Triassic to Lower Jurassic Precipice Sandstone is the potential CO₂-storage reservoir with the overlying Lower to Middle Jurassic Evergreen Formation acting as the primary seal. The Middle Jurassic Hutton Sandstone is a secondary seal and also in some areas of the basin is a potential sub-reservoir in its own right. The Middle Jurassic Walloon Coal Measures system and other overlying units act as additional seals above. The primary seal formation contains a stacked sequence of largely impermeable units so it is unlikely that CO₂ injected into the Precipice Sandstone would be able to completely penetrate it. However, samples of Hutton Sandstone were included in the work program to investigate its behaviour if it were exposed to CO₂-rich fluids in the event of CO₂ leakage, or if it was utilised as a sub-reservoir for CO₂ storage. Furthermore, the study of lithologies other than that of the primary quartzose sandstone reservoir extends the applicability of this report to lower quality potential reservoirs that may be considered for CO₂ geosequestration in the future.

Initially samples were taken from curated GSQ Core Chinchilla 4 (Chin4), which has been used in a number of ANLEC, CO2CRC, Geological Survey of Queensland and other studies regarding carbon sequestration potential within the Surat Basin (e.g. Dixon et al., 2010; Farquhar et al., 2013; Farquhar et al., 2014; Grigorescu, 2011a, b; Hodgkinson and Grigorescu, 2012; Hodgkinson et al., 2010; Horner et al., 2014; Pearce et al., 2014). One sample was chosen from the quartzose Precipice Sandstone, two from the Evergreen Formation (lithic argillaceous sandstone and arenaceous shale), and two samples from the Hutton Sandstone (lithic sandstone and calcite cemented quartzose sandstone). Subsequently, fresh samples were taken from the newly drilled core West Wandoan 1 (WW1); three samples of the Precipice Sandstone, three from the Evergreen Formation (calcite cemented quartzose sandstone, lithic argillaceous sandstone, interlaminated mudstone and sandstone), and one from the Hutton Sandstone (calcite cemented quartzose sandstone).

Geochemical and Geomechanical Testing of Near Wellbore CO₂ Injectivity Improvement

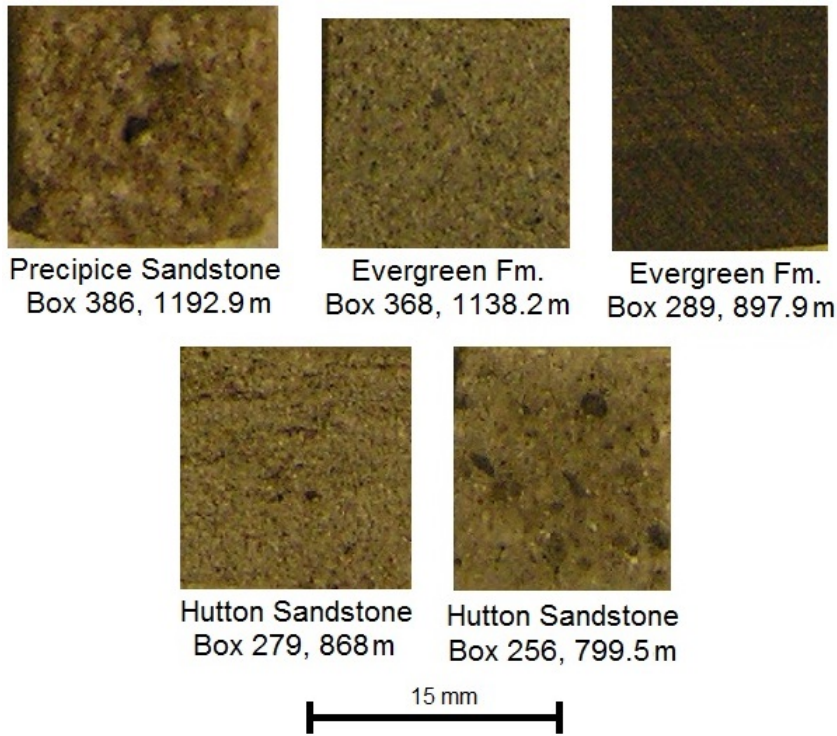


Figure 3.1-1: Photographs of the Chinchilla 4 samples used in this study.

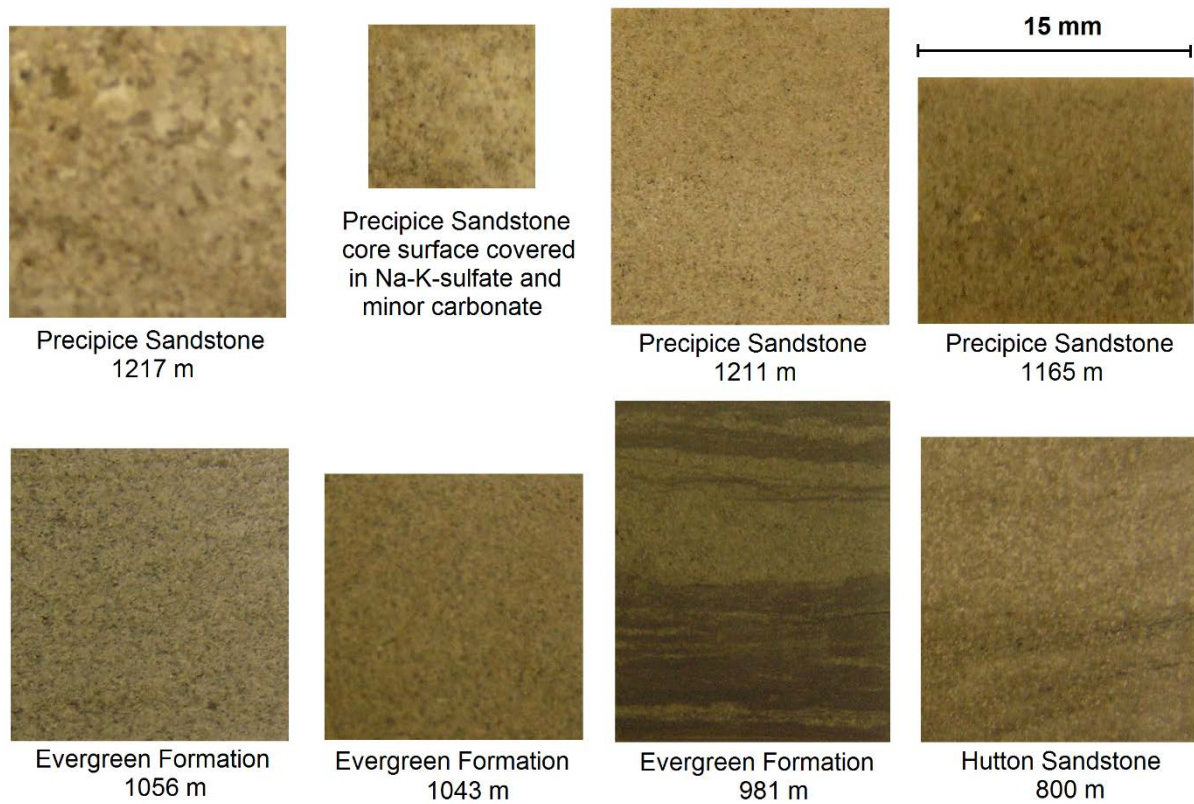


Figure 3.1-2: Photographs of the West Wandoan 1 samples used in the batch reactor experiments.

Geochemical and Geomechanical Testing of Near Wellbore CO₂ Injectivity Improvement

Table 3.1-1: Chinchilla 4 Sample Summary

UQ sample name	FEI-Lithicon aka Digital Core name	Formation and Depth (m)	Hand Sample Descriptions	Grainsize
Chin4-1192-Precipice	ANLEC_5_Chin1192	(Upper) Precipice Sandstone, 1192.9 m.	Pebbly, poorly sorted, medium to very coarse-grained, very porous quartzose sandstone with minor clay matrix. Low angle cross-bedding, foresets (cm-scale) fining up from basal conglomerate.	0.25–2 mm, with some pebbles up to 5 mm.
Chin4-1138-Evergreen	ANLEC_5_Chin1138	(Lower) Evergreen Formation, 1138.2 m.	Moderately- to poorly-sorted, fine to medium-grained, clay-rich micaceous sandstone with common carbonaceous stringers and minor carbonate cement.	0.125-0.5 mm.
Chin4-897-Evergreen	ANLEC_5_Chin897	(Upper) Evergreen Formation, 897.9 m.	Interlaminated to lenticular carbonaceous siltstone and very fine-grained sandstone.	Siltstone layers; mostly <62 µm. Very fine sand layers; 62-125 µm.
Chin4-868-Hutton	ANLEC_5_Chin867	(Lower) Hutton Sandstone, 868 m.	Well-sorted, medium-grained, clayey micaceous and lithic-rich sandstone with subparallel laminated cross-bedding. Common carbonaceous lamellae.	0.25-0.5 mm.
Chin4-799-Hutton	ANLEC_5_Chin799	(Upper) Hutton Sandstone, 799.5 m.	Pebbly very poorly sorted very fine- to coarse-grained calcite cemented quartzose sandstone with minor clay matrix. Massive to low angle cross-bedding.	62 µm – 2 mm, with some 5 mm pebbles.

Geochemical and Geomechanical Testing of Near Wellbore CO₂ Injectivity Improvement

Table 3.1-2: West Wandoan 1 Sample Summary

UQ sample name	FEI-Lithicon aka Digital Core name	Formation and Depth (m)	Hand Sample Descriptions	Grainsize
WW1-1217-Precipice	ANLEC_5_WW1WC14_a	(Lower) Precipice Sandstone, 1217.48-1217.55	Pebbly moderately sorted interbedded medium to very coarse grained quartz arenite, with sodium-potassium sulphate salts and kaolin (dickite and kaolinite) clays partly occluding pore spaces.	In dominant coarse-very coarse sand layers; 0.5-2 mm with some 4 mm pebbles. In medium sand layers; 0.25-0.5 mm.
WW1-1211-Precipice	ANLEC_5_WW1WC20 (tested as substitute for WC11 and WC14 40 mm cubes only)	(Lower) Precipice Sandstone, 1211.65-1211.75	Well sorted fine grained quartz arenite, with sodium-potassium sulphate salts and kaolin partly occluding pore spaces.	0.125-0.25 mm.
WW1-1165-Precipice	ANLEC_5_WW1WC11_a	(Upper) Precipice Sandstone, 1165.44-1165.52	Moderately sorted fine to coarse grained quartz arenite, with minor kaolin partly occluding some pore spaces. Hand sample shows cross-bedding.	0.35-0.75 mm.
WW1-1056-Evergreen	ANLEC_5_WW1WC9_a	(Lower) Evergreen Formation, 1056.10-1056.19	Moderately well sorted calcite cemented fine to medium grained sandstone.	0.125-0.5 mm.
WW1-1043-Evergreen	ANLEC_5_WW1WC8_a	(Lower) Evergreen Formation, 1043.70-1043.77	Moderately well sorted fine to medium grained sandstone with clay matrix.	0.125-0.5 mm.
WW1-981-Evergreen	ANLEC_5_WW1WC3_a	(Upper) Evergreen Formation, 981.24-981.31	Interbedded and interlaminated black carbonaceous silty mudstone and very fine sandstone.	Silty mudstone layers; mostly <3.9 µm with some grains 3.9-62 µm. Very fine sand layers; 62-125 µm.
WW1-800-Hutton	ANLEC_5_WW1WC15_a	Hutton Sandstone, 800.70-800.85	Well sorted calcite cemented fine sandstone with intermittent very fine laminations of coalified organic matter.	0.125-0.25 mm.

Originally only two samples had been selected from the WW1 Precipice, but one split during courier transport and the other failed while being cut into a 40 mm cube so a replacement was chosen (WW1-1211-Precipice). WW1-981-Evergreen also split whilst being cut. Adjacent core sections of the friable Precipice and fissile Evergreen samples (SEM samples, 15 mm cubes and X-ray micro-CT sub-plugs) were still tested in batch reactors.

Two sister sample sets of Berea Sandstone were obtained from ANLEC – three 40 mm cubes (B1, B2, B3) and four 15 mm cubes (A1, A2, A3, A4). This material is a fine grained, well sorted quartzose sandstone with minor K and Na-Ca-feldspars, Fe-Ca-Mg-Mn-carbonate cements, degraded micas and chlorite/smectite/kaolinite occluding some pore spaces. Very thin (sub-millimetre) laminations of clays rarely occurred between some sand bedding layers in the samples, with regions of samples occasionally being carbonate cemented.

3.2. X-ray Diffraction (XRD) Analysis

Unreacted off-cuts of the core segments used for geochemistry experiments were crushed for XRD analysis. Broadly similar minerals were present in the Chinchilla 4 (Table 3.2-1) and West Wandoan 1 (Table 3.2-2) samples, although Ca-rich plagioclase was more commonly observed in WW1 samples than for Chin-4. The minor/trace minerals did vary somewhat, but were present in quantities at or below the analytical detection limit for the XRD-technique (~ 5%). Some diagnostic peaks were therefore missing and so identification is less certain than for the major and moderate minerals.

In addition to standard whole-rock samples, a scraping of the millimetres-thick white powder covering much of the lower surface of the tray-stored WW1 Precipice core was also tested; it appeared to be salts that precipitated from pore-water slowly draining out of the core as it sat in the core-trays. The white powder, in addition to quartz introduced during scraping of the core, was found by XRD analysis to be predominantly a mixture of Na-K-sulphate minerals with minor carbonates, kaolin, and possibly phosphate. It is possible that some of the K-component especially may have been derived from drilling mud, but K is also naturally present in most groundwater and dissolved sulphate was not a component of the drilling fluid used.

Table 3.2-1: Chinchilla 4 qualitative X-ray diffraction analysis of bulk-rock powder and oriented clay fraction, listed in order of most to least abundant.

Sample	Major	Moderate	Minor / ± trace
Chin4-1192-Precipice	Quartz	Kaolin	Smectite, muscovite, illite
Chin4-1138-Evergreen	Quartz, K-feldspar, albite	Smectite, kaolin, chlorite, calcite, ankerite	Muscovite, biotite
Chin4-897-Evergreen	Quartz, albite	Kaolin, chlorite, muscovite, siderite	Smectite, illite ± Anatase
Chin4-868-Hutton	Quartz, albite, kaolin, Fe-chlorite	K-feldspar, muscovite	Chlorite-smectite, ankerite, anatase
Chin4-799-Hutton	Quartz, calcite	Kaolin, chlorite, albite, K-feldspar,	Smectite, glauconite, illite

Table 3.2-2: WW1 whole rock semi-quantitative XRD results, listed in order of most to least abundant.

Sample	Major (>20%)	Moderate (5-20%)	Minor (<5%)
WW1-1217-Precipice	Quartz	Orthoclase, muscovite/illite	Dickite, kaolinite, rhodochrosite
White powder on Lower Precipice core surface	Quartz	K-Na-sulphates	Bronstedite (Na-Fe-PO ₄ CO ₃), jarosite, kaolin, cyanochroite (hydrated K-Cu-sulphate), Mg-calcite
WW1-1165-Precipice	Quartz	N/A	Kaolin
WW1-1056-Evergreen	Ca-Na-plagioclase, quartz	Muscovite/illite, calcite, orthoclase	Kaolin, smectite/chlorite, dolomite
WW1-1043-Evergreen	Quartz, Ca-Na-plagioclase	Muscovite/illite, orthoclase, smectite/chlorite	Lepidocrocite, kaolin, calcite
WW1-981-Evergreen	Quartz, Ca-Na-plagioclase	Muscovite/illite, orthoclase, kaolin	Calcite
WW1-800-Hutton	Quartz, calcite	Albite, Ca-Na-plagioclase, muscovite/illite, kaolin	Orthoclase, biotite

3.3. Standard Petrography

Mineral and textural observations were made via optical microscopy of thin sections (see also Farquhar *et al.*, 2013 for more details about Chinchilla 4 samples). Detailed descriptions are given for each sample, including images of key features observed. The feldspar and lithic fragment percentages given in QFL statistics presented for the WW1 samples do not account for grains fully replaced by clays (and so no longer reliably identifiable as once having been feldspars or lithic fragments); rather, these and other “grains” completely replaced by clay have been counted as “pseudo-matrix”, which is accounted for in the cement-matrix ratios given for those samples.

3.3.1. Precipice Sandstone

Sample Chin4-1192-Precipice

This is a poorly sorted, fine- to very coarse-grained quartz arenite. Grains are angular to subrounded with moderate sphericity (Figure 3.3-1). Point to tangential contacts form a grain-supported fabric, with some triple junction and suturing interpreted to have been formed via partial quartz grain dissolution and authigenic quartz overgrowth during compaction. Quartz grains frequently show evidence of embayment, possibly resulting from the removal of significant amounts of quartz

overgrowths by a further stage of grain dissolution. The sample contains enhanced intergranular porosity, with oversized pores from near to complete dissolution of feldspars. Partial porosity-infilling of interstitial kaolin matrix is common, with frequent pore-throat lining by clays.

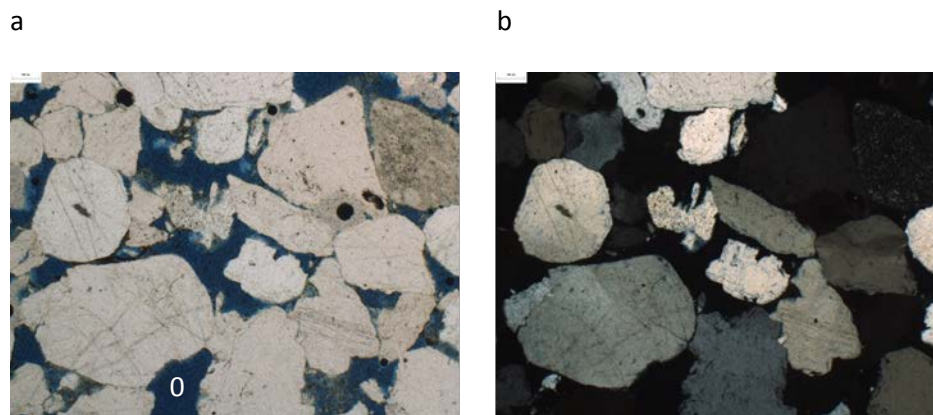


Figure 3.3-1: Chin4-1192-Precipice poorly sorted quartzose sandstone with blue staining indicating open porosity (0), x25 magnification a) Plain polarized light view (PPL) and b) Cross polarized light view (XPL). The scale bar is 100 micrometres.

Sample WW1-1165-Precipice

This is a moderately sorted, fine- to coarse-grained, sporadically calcite cemented sandstone (Figure 3.3-2), and with patchy clay matrix and rare micro-laminations of oxide cement (Figure 3.3-3). Q:F:L – 70:16:14 and cement-matrix ratio 31:19. The majority of the quartz grains are angular to subrounded and monocrystalline with parallel extinction, though some have undulose extinction and polycrystalline (probably metamorphic) grains were also observed. The feldspars have largely undergone allomorphic replacement either with clay minerals or calcite, which has commonly replaced the original mineral congruent with twinning (Figure 3.3-4a). Lithic fragments are mainly volcanic with some metamorphic. Biotite flakes and pyrite are uncommon (Figure 3.3-4b), with rare amphibole fragments also observed.

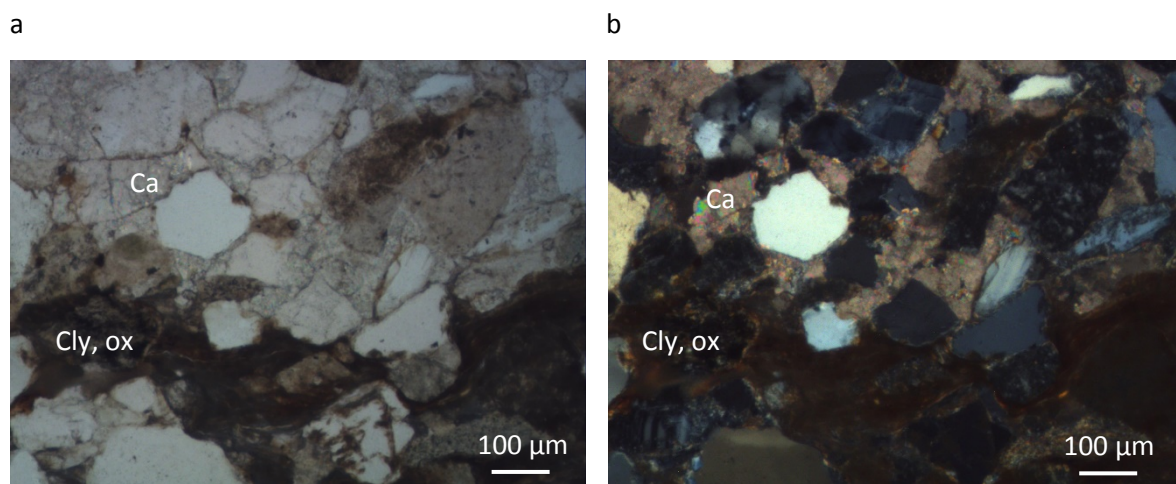


Figure 3.3-2: WW1-1165-Precipice. Calcite (Ca) cement-supported framework grains, with a thin band of clay (cly) and oxide (ox) minerals, x50 a) PPL and b) XPL.



Figure 3.3-3: Photograph of sample WW1-1165-Precipice thin section showing an iron oxide micro-lamination.

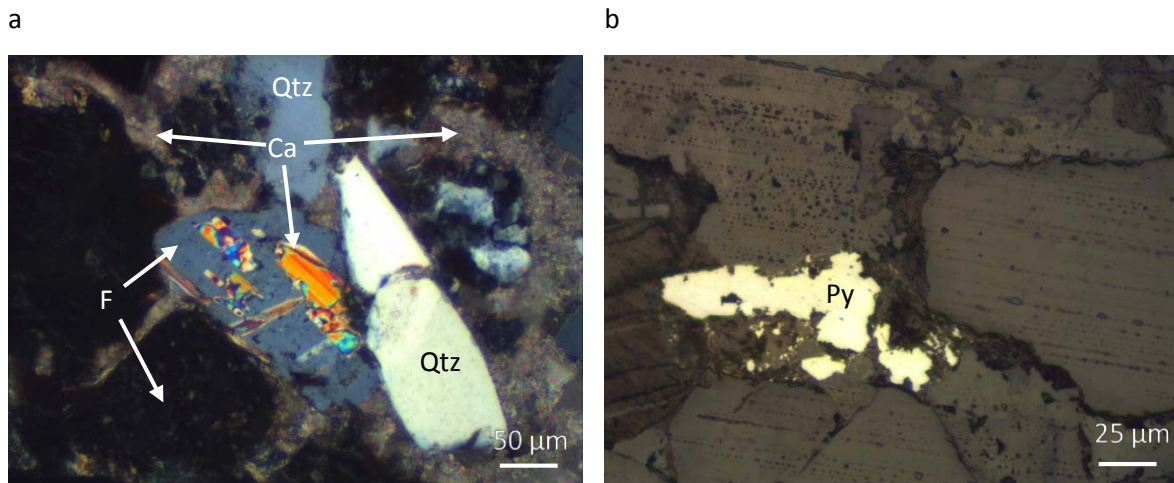


Figure 3.3-4: WW1-1165-Precipice a) Feldspar grains, bottom left grain almost entirely replaced with clay minerals, central grain undergoing replacement with calcite congruent with twinning, XPL x100; b) Partially altered pyrite (Py) amongst quartz grains, reflected light view (RL) x200.

Sample WW1-1217-Precipice

This is a moderately sorted, pebbly, medium- to very coarse-grained quartz arkose with rare clay pore-fill. The sample predominantly comprises medium to high sphericity, subangular to well-rounded and slightly bedding-aligned quartz grains (99%), about 10% of which were polycrystalline and a further 20% had undulose rather than the more common parallel extinction. The quartz shows many signs of compaction including overgrowths, 120° contacts, concave-convex contacts, and suturing (Figure 3.3-5). Clay-replaced feldspar grains were rarely observed (Figure 3.3-6a). Euhedral partially altered sulphide crystals are also present (Figure 3.3-6b), with these potentially being a source of minor iron oxide cement observed in some Precipice samples.

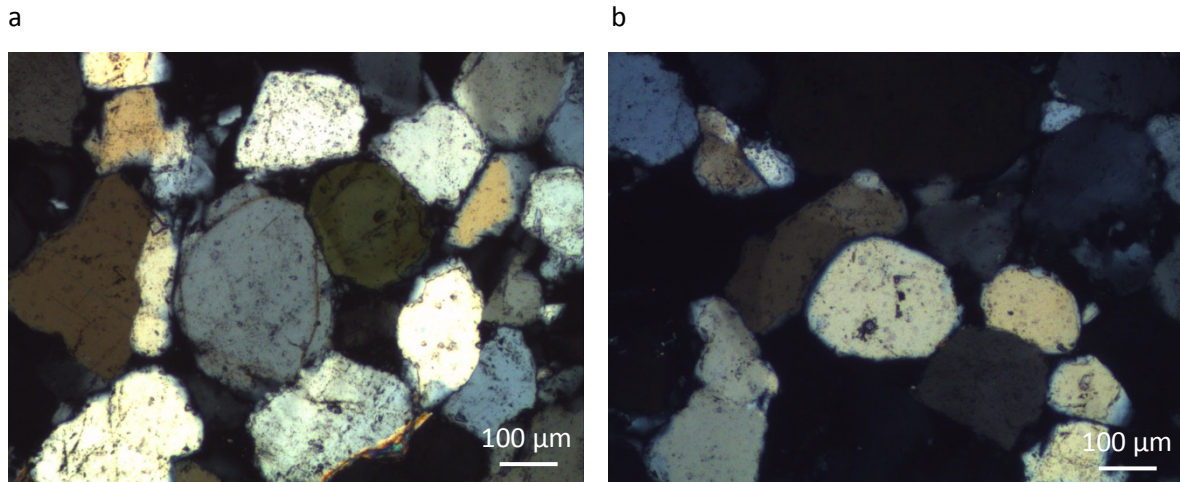


Figure 3.3-5: WW1-1217-Precipice a) Quartz overgrowth and 120° contacts, XPL x5; b) Concave-convex contact and undulose extinction, XPL x50.

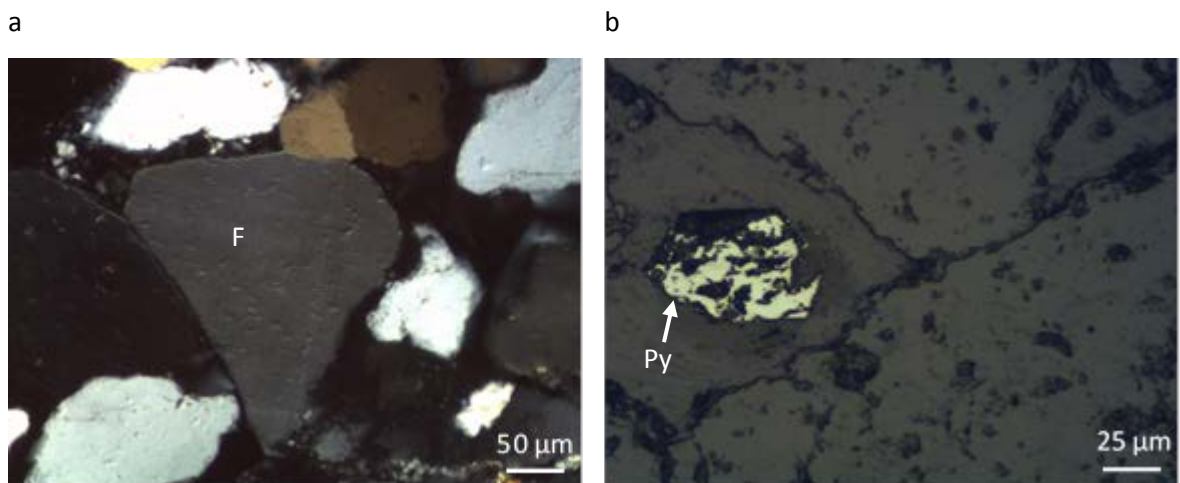


Figure 3.3-6: WW1-1217-Precipice a) Clay-altered feldspar grain (F) and unmineralized pore space, XPL x10; b) Euhedral sulphide crystal partially altered (S), RL x200.

3.3.2. Evergreen Formation

This formation contains a spectrum of stacked lithological units ranging from “dirty” sandstones to mudstones.

Sample Chin4-1138-Evergreen

This is a matrix-supported lithic wacke, with feldspars, muscovite, phlogopite and biotite, commonly showing alteration to clay minerals (Figure 3.3-7). Quartz is subangular to subrounded with low to moderate sphericity. Mudstone (?) lithics form some of the interstitial matrix from compaction of labile grains. Some organic material, with minor iron-bearing minerals (possibly hematite?) also occurs, along with minor partial carbonate (calcite and siderite) cementation.

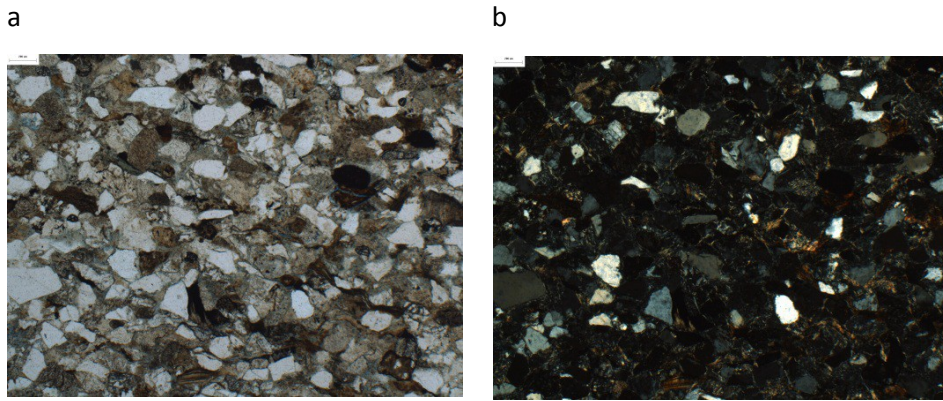


Figure 3.3-7: Chin4-1138-Evergreen. Poorly sorted fine- to medium-grained, matrix supported feldspatholithic wacke, x25 a) PPL and b) XPL. The scale bar is 100 micrometres.

Sample Chin4-897-Evergreen

This is a moderately laminated arenaceous shale consisting of a clay-rich matrix with angular, low-sphericity, silt-sized monocrystalline quartz grains, layer-parallel preferentially-oriented detrital muscovite and phlogopite flakes and lesser biotite (Figure 3.3-8). Lenses of micaceous, poorly sorted, matrix-supported fine-grained to silty subfeldspathic sandstone occur sporadically.

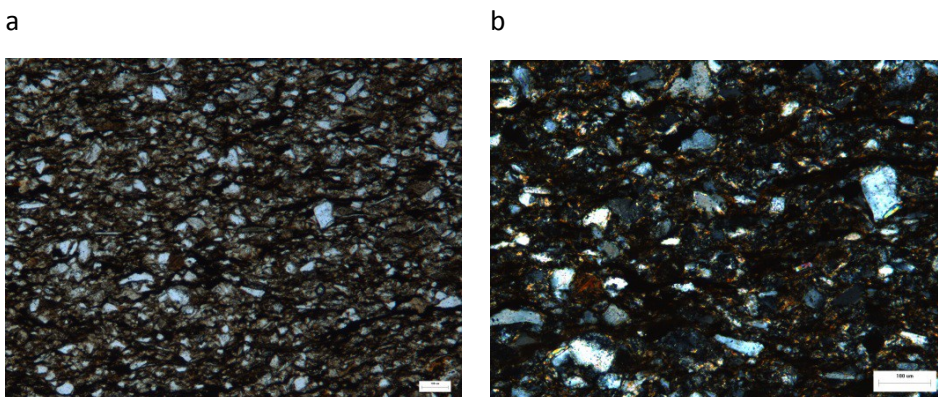


Figure 3.3-8: Chin4-897-Evergreen carbonaceous shale, a) PPL x25 and b) XPL x50. The scale bar is 100 micrometres.

Sample WW1-981-Evergreen

This is an interlaminated to discontinuous, lenticular, very fine-grained sandstone and black carbonaceous siltstone (Figure 3.3-9). The sandstone is clay matrix supported containing quartz, feldspars, biotite, lithic fragments, pyrite, chalcopyrite, some organic laminations, minor carbonate cement, and microscopic fractures mineralised with oxides. In sandstone; Q:F:L – 76:12:12. The predominantly angular, low sphericity sand grains have some alignment along bedding and undulose extinction is common. Sand grains and mica flakes occur scattered within the siltstone layers.

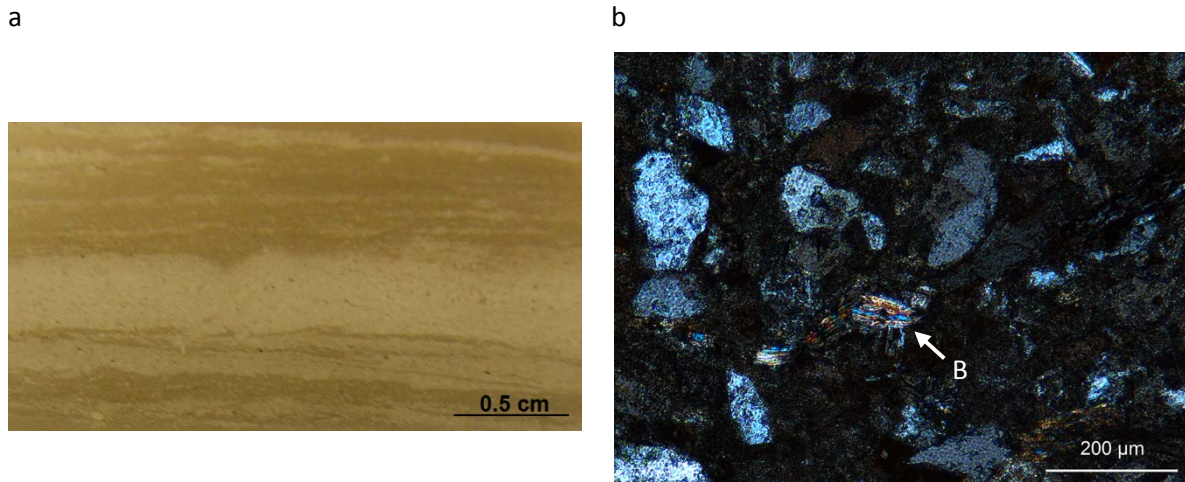


Figure 3.3-9: WW1-981-Evergreen. a) Photograph of thin section showing interlamination of sandstone and carbonaceous siltstone; b) Partly altered biotite (B), XPL x100.

Sample WW1-1043-Evergreen

This is a moderately-well sorted, clay matrix-supported, fine- to medium-grained sandstone with some layer parallel oxide staining. Q:F:L – 50:26:24 and cement-matrix ratio 7:18. The monocrystalline quartz grains have either parallel or undulose extinction and some polycrystalline quartz is present. Grains are angular to subangular, with medium sphericity and slightly aligned along cross laminations. Some feldspars have been partly replaced by calcite along twinning and cleavage surfaces. Both metamorphic- and volcano-lithic fragments, clay altered plagioclase and K- feldspar, minor micas, oxidised sulphides, rare chlorite, unaltered amphibole and garnets are present (Figure 3.3-10).

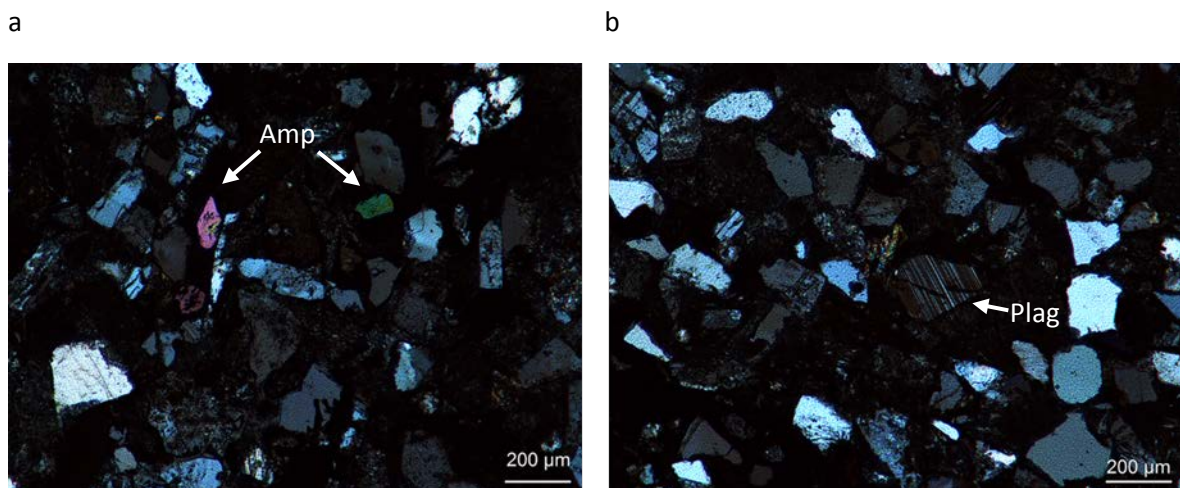


Figure 3.3-10: WW1-1043-Evergreen. a) Rare amphibole crystals (Amp) amongst quartz, XPL x50; b) Plagioclase (Plag) amongst quartz.

Sample WW1-1056-Evergreen

This is a moderately-well sorted, fine- to medium-grained lithic sandstone with highly abundant calcite cement and patchy clay matrix, cross laminated with biotite alteration and oxide precipitation along lamination boundaries (Figure 3.3-11). Q:F:L – 62:10:28 and cement-matrix ratio 19:6. Quartz grains are angular to subrounded, with low to moderate sphericity, with monocrystalline quartz having either parallel or undulose extinction and polycrystalline quartz also present. Most feldspar grains show partial to near-complete allomorphic replacement with clays and calcite (Figure 3.3-12), and biotite flakes altering to chlorite (in addition to more common oxide alteration) were also observed (Figure 3.3-13). Schistose clasts containing partially altered mica, and volcanolithic fragments are present. Large sulphide crystals up to 0.5 mm diameter that have undergone near-complete oxide alteration and rare garnets are also present.



Figure 3.3-11: WW1-1056-Evergreen. Photograph of thin section showing Fe-oxide precipitation, predominantly from biotite alteration, along sand layer boundaries.

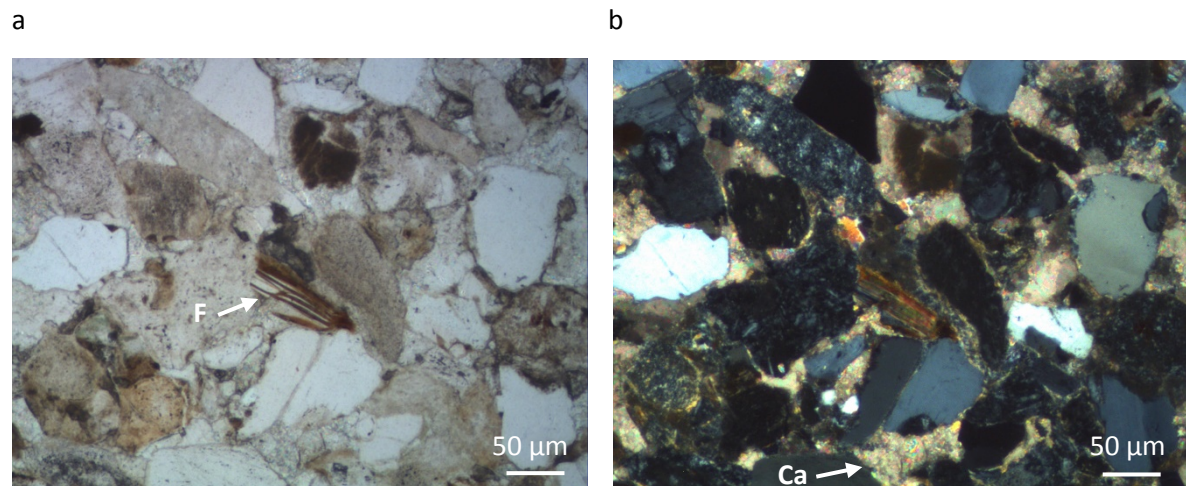


Figure 3.3-12: WW1-1056-Evergreen x100 a) PPL, feldspar framework partially and entirely replaced with clay minerals (F, centre), and b) XPL, abundant calcite cement visible between grains (Ca).

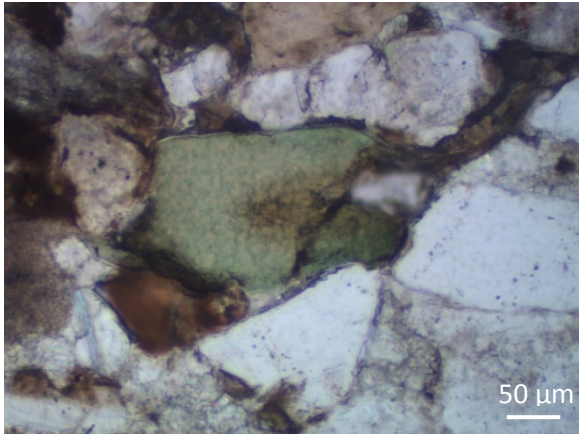


Figure 3.3-13: WW1-1056-Evergreen. Biotite almost entirely replaced by chlorite (centre). PPL, x100.

3.3.3. Hutton Sandstone Sample Chin4-868-Hutton

This is a clay-rich matrix-supported lithic wacke, with angular to subangular monocrystalline quartz grains, chloritized detrital biotite flakes, metamorphic (fine grained muscovite schist) and volcanolithic fragments, and minor carbonate cement (Figure 3.3-14). Significant reduction of porosity is attributed to mechanical compaction of lithics and detrital mica flakes, and the formation of microstylolites. Hematite occurs as a grain-coating, sometimes absent from grain contact points but frequently within microstylolitic suturing of quartz grains. Authigenic quartz overgrowths were occasionally noted with hematite-rich rims.

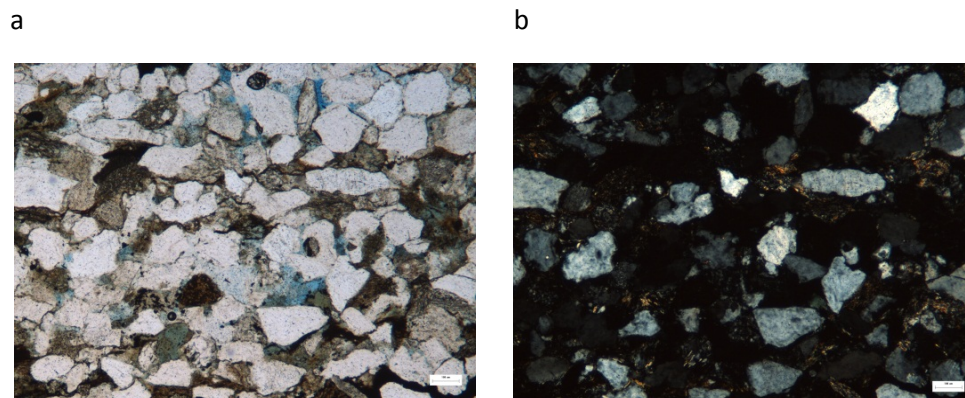


Figure 3.3-14: Chin4-868-Hutton: poorly sorted fine- to medium-grained lithic matrix-supported sandstone with minor carbonate cement, x50 a) PPL and b) XPL. The scale bar is 100 micrometres.

Sample Chin4-799-Hutton

Grain-supported quartz arenite with abundant calcite cement (Figure 3.3-15). Quartz grains are predominantly heavily embayed, monocrystalline and subrounded, with lesser polycrystalline (metamorphic) quartzite and chert grains. Minor detrital biotite and feldspar (microcline and albite), including skeletal and honeycombed (kaolin-replaced) feldspars, were observed. Partial porosity infilling by kaolin is largely obscured by younger calcite cementation of pores. Quartz grains show evidence of pressure solution and commonly show authigenic quartz overgrowths.

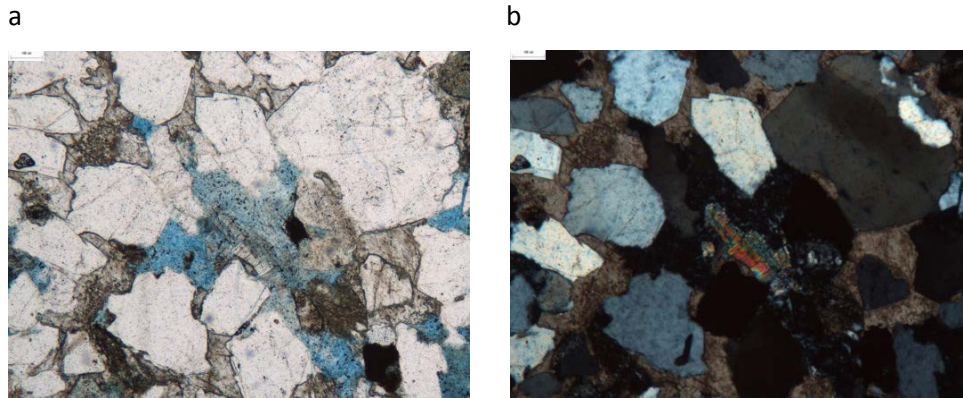


Figure 3.3-15: Chin4-799-Hutton. Poorly sorted medium to very coarse-grained calcite-cemented sandstone, x50 a) PPL and b) XPL. The scale bar is 100 micrometres.

Sample WW1-800-Hutton

This is a well-sorted quartzose sandstone with abundant calcite cement (Figure 3.3-16a) that is continuously extinct over > 2 mm in section. Q:F:L – 88:4:8 and cement-matrix ratio 9:1. Quartz has low to moderate sphericity and is angular to subrounded with both parallel and undulose extinction, and some polycrystalline clasts (Figure 3.3-16b). Feldspar grains are often twinned (Figure 3.3-16c,d) and sometimes partially replaced by calcite. Minor biotite partially altered to chlorite, and highly altered pyrite and possibly pyrrhotite grains are present. Coal is present as sporadic discontinuous layers and isolated grains (Figure 3.3-17).

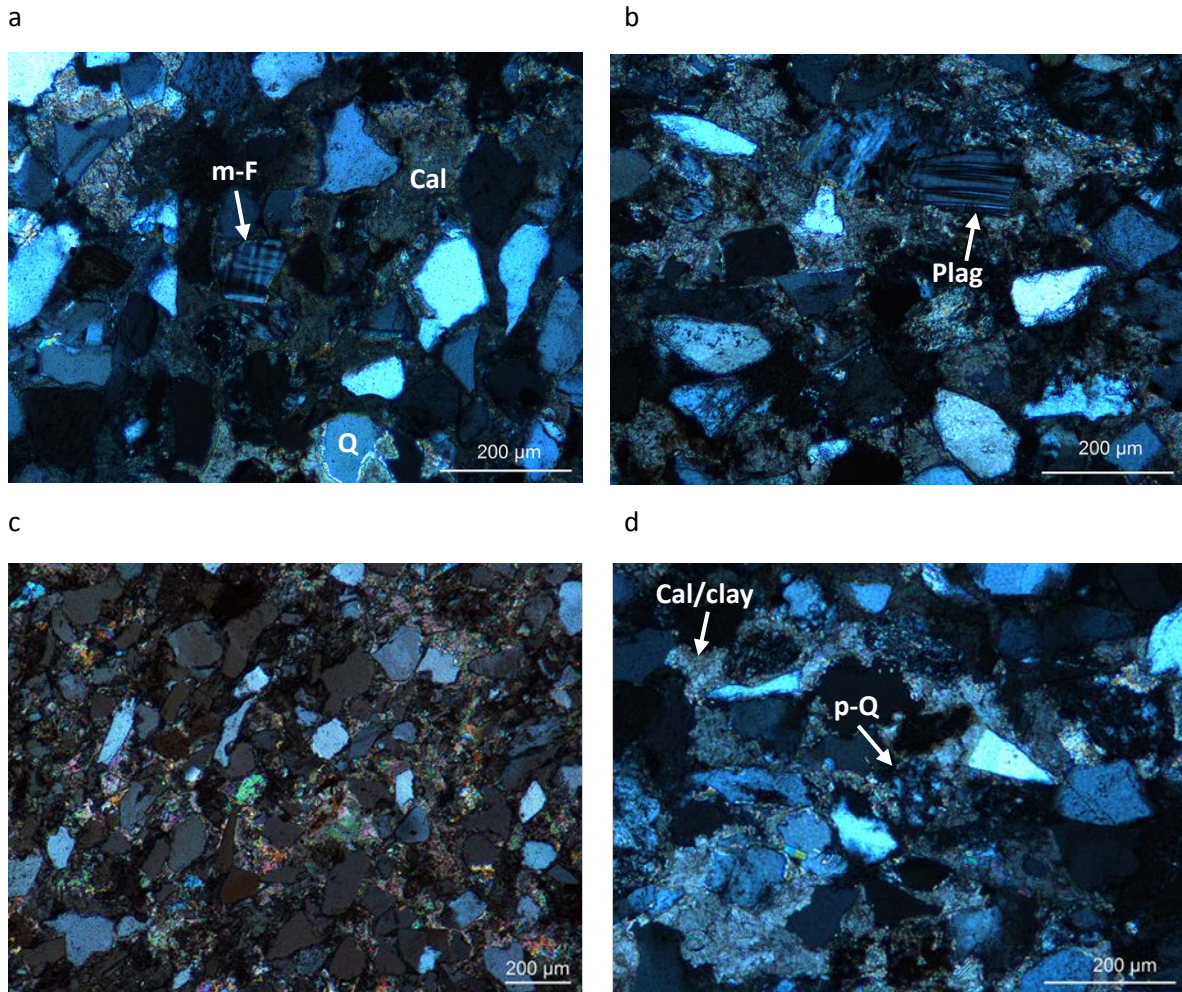


Figure 3.3-16: WW1-800-Hutton XPL x100 a) Partially altered microcline feldspar with tartan twinning (m-F), calcite cement (Cal) and quartz (Q), XPL x10; b) Partially altered plagioclase (Plag), calcite cement, quartz; c) Carbonate cement (multi-coloured) amongst quartz grains, XPL x5; d) Polycrystalline (p-Q) and monocrystalline quartz grains, calcite cement mixed with clay (Cal/clay).



Figure 3.3-17: WW1-800-Hutton. Photograph of thin section showing discontinuous layers and isolated pieces of coal within this calcite-cemented quartzose sandstone.

3.3.4. Berea Sandstone

This is a well-sorted, fine-grained quartzose sandstone containing a few percent mica flakes (Figure 3.3-18a) as well as heavily altered lithic fragments and rare shattered feldspar grains. Q:F:L – 86:4:10 and cement-matrix ratio 2:1. Quartz has low to moderate sphericity and is angular to subrounded

with both parallel and undulose extinction, and some polycrystalline clasts. Hematite (Figure 3.3-18b) and clays as well as carbonate cements occlude some of the porosity.

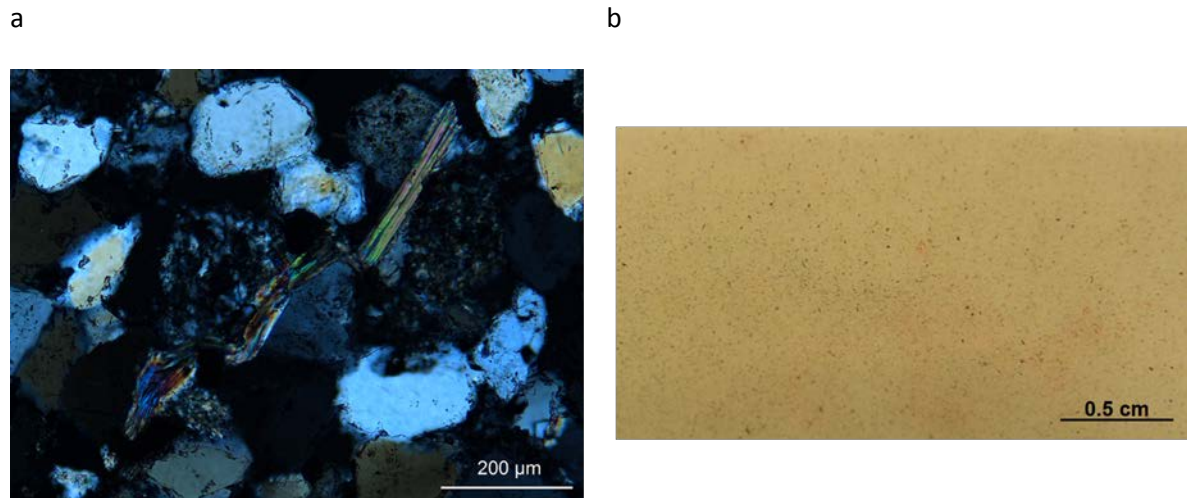


Figure 3.3-18: Berea Sandstone a) Muscovite flake between both monocrystalline and polycrystalline quartz grains, XPL x200; b) Hematite cement (red) visible in photograph of thin section.

3.4. General SEM-EDS Surveys

SEM analysis allowed a finer-scale investigation of the type and textural context of minerals present within the samples than was possible with XRD or standard petrography alone. The presence of minerals indicated by XRD or standard petrography was able to be confirmed or clarified. Additional minerals not otherwise detected were also shown to be present.

3.4.1. Precipice Sandstone

The predominantly quartzose Precipice samples commonly contained partially pore filling kaolin, as well as sporadic zircon, rutile, REE-monazite, muscovite, biotite, and framboidal microscopic (microbial?) crystals of various sulphide minerals. SEM identified both dickite and kaolinite (e.g. Figure 3.4-1), in addition to the poorly crystallised and potentially amorphous material of kaolin-like composition reported in Farquhar et al. (2013). The distinctive crystal morphology of dickite was used to distinguish it from kaolinite, and the crystal-stacking and other growth patterns observed indicate that the dickite is authigenic, having formed *in situ* most likely during alteration of depositional kaolinite by migrating acidic fluids of elevated temperature (e.g. Galán and Ferrell, 2013). Such alteration could also be responsible for the presence of the poorly-crystallised kaolinite previously reported.

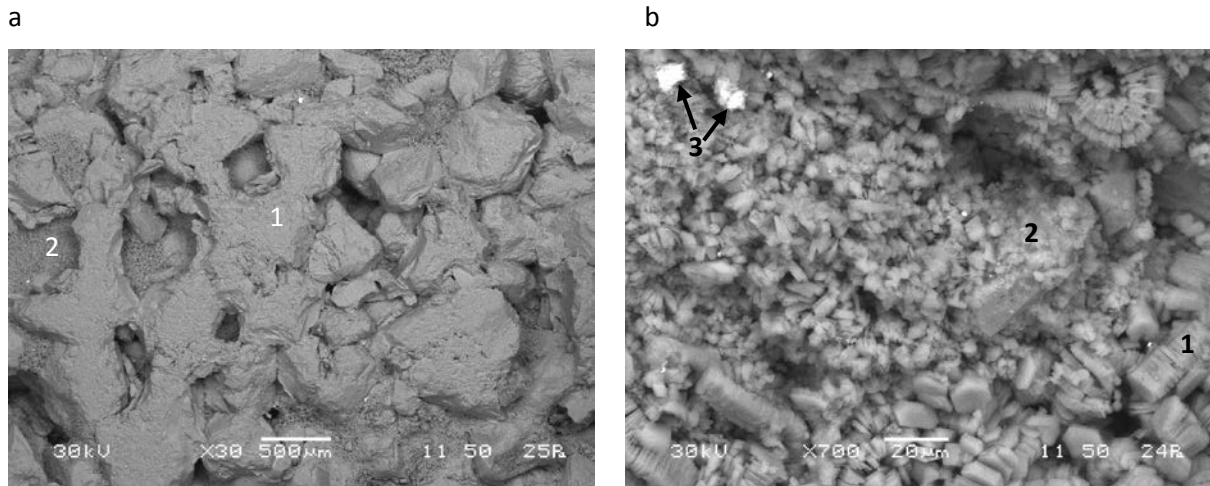
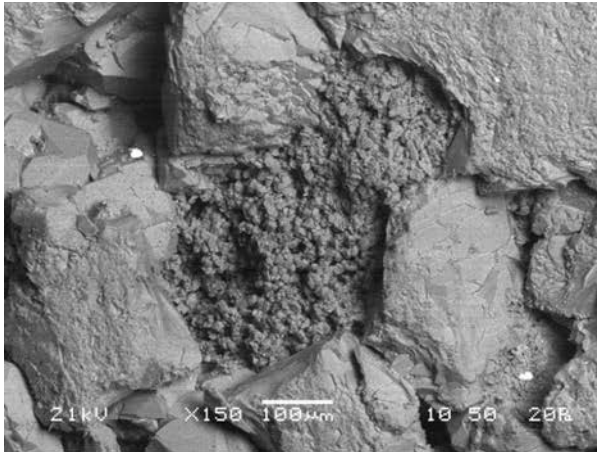


Figure 3.4-1: Chin4-1192-Precipice a) SEM electron backscatter image, quartz with minor pore-occluding kaolin; b) Dickite (large crystals, 1), lesser kaolinite (small crystals, 2) and trace pyrite (3).

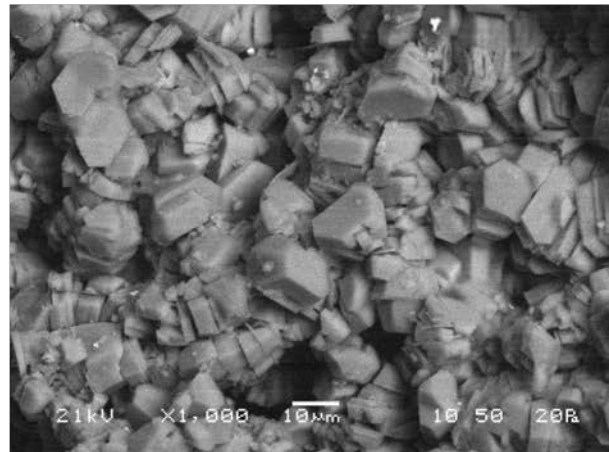
Further evidence of fluid alteration was observed in the West Wandoan 1 Precipice samples. They also contain well-developed dickite as well as remnant heavily altered aluminosilicates (Figure 3.4-2). Unlike the Chinchilla 4 sample, the WW1 samples have K-sulphate minerals, with lesser Na-sulphate and Na-carbonate, either coating grains or blocking pore space (Figure 3.4-3 and 3.4-4). That the SEM survey found K-sulphate in greater abundance than Na-sulphate was contrary to XRD analysis of a related sample which found Na-sulphate to be more abundant. Regardless, these types of sulphates and carbonate are highly soluble in water, so their continued presence within the samples following sample preparation suggests that the *in situ* pore water must have been supersaturated with sulphate, and to a lesser extent carbonate anions.

Geochemical and Geomechanical Testing of Near Wellbore CO₂ Injectivity Improvement

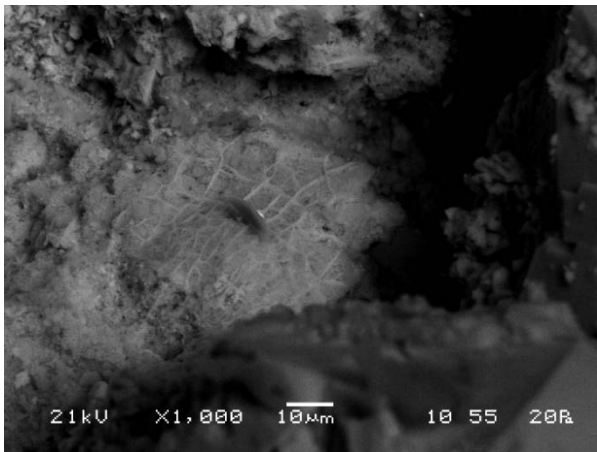
a



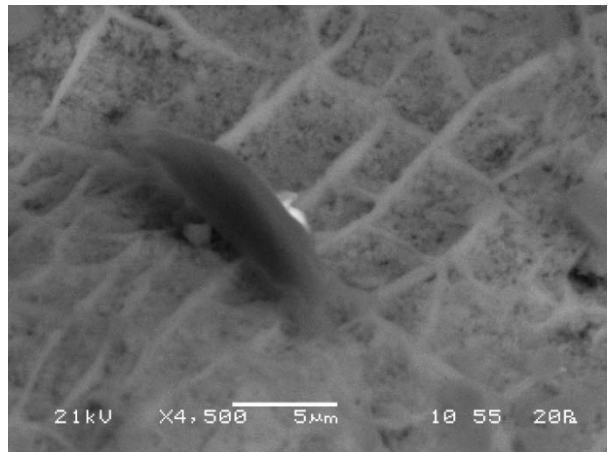
b



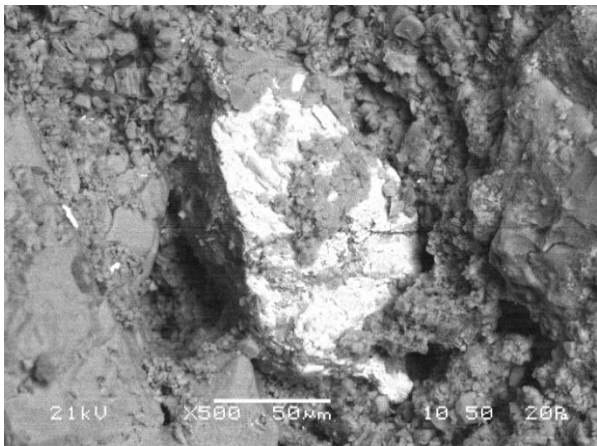
c



d



e



f

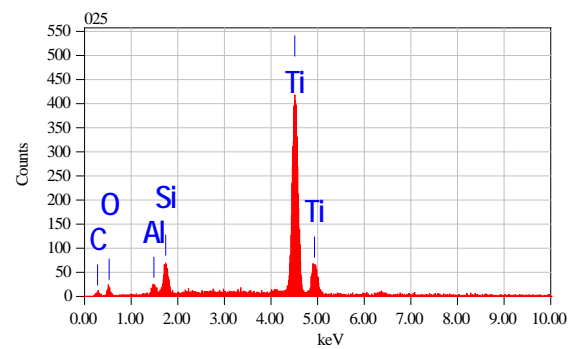


Figure 3.4-2: WW1 upper Precipice Sandstone; Dickite (a, b) fills some pore space. Ti-rich altered aluminosilicates with remnant Fe and K occur (c, d) as well as primary Ti oxide +/- Fe (white) (e, f).

Geochemical and Geomechanical Testing of Near Wellbore CO₂ Injectivity Improvement

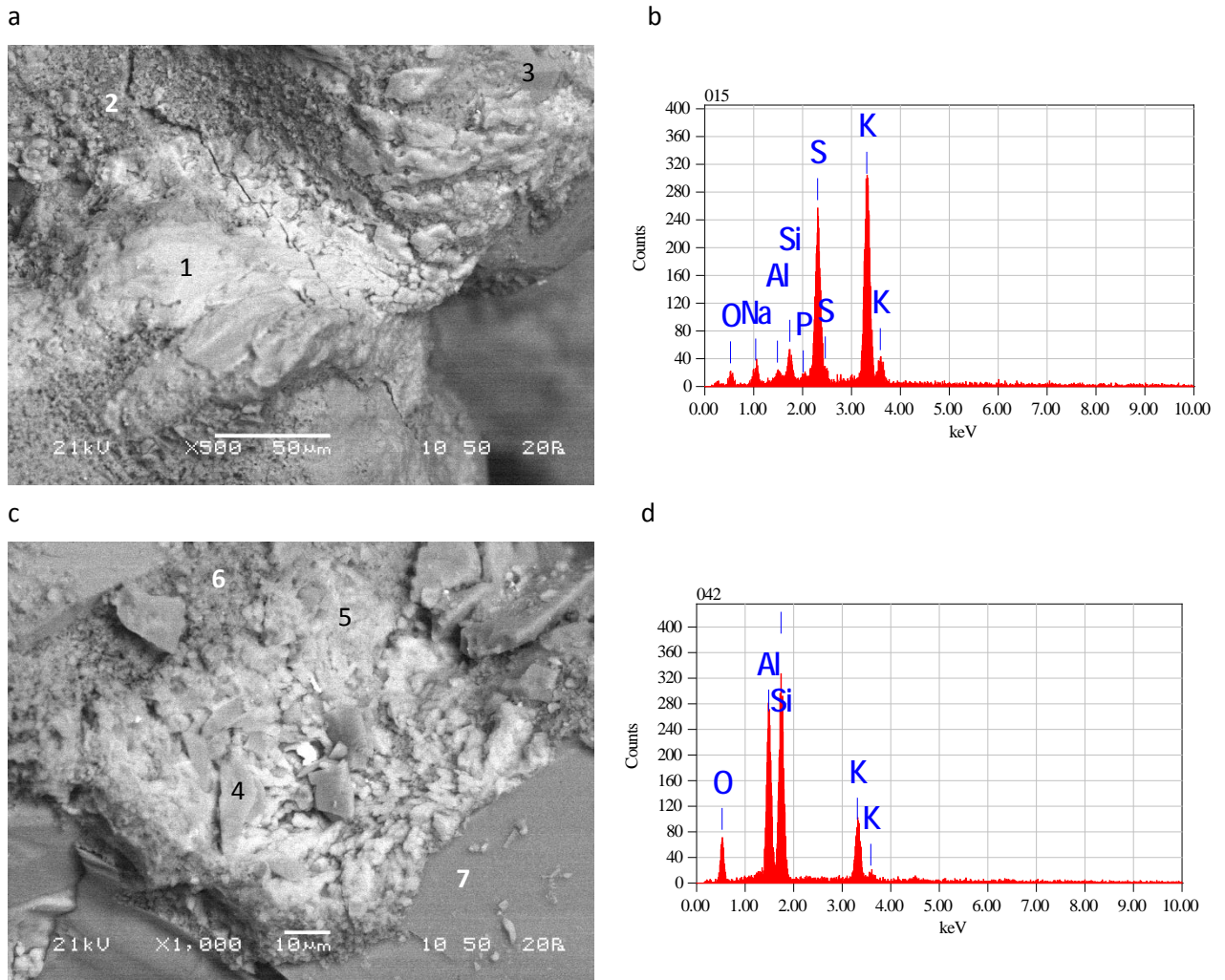


Figure 3.4-3: WW1 Upper Precipice Sandstone a),b) K and lesser Na sulphate and minor phosphate (1) coating kaolin (2) between quartz grains (3); c),d) Muscovite flakes (4) amidst K(Na)-sulphates (5) and kaolin (6) between quartz grains (7).

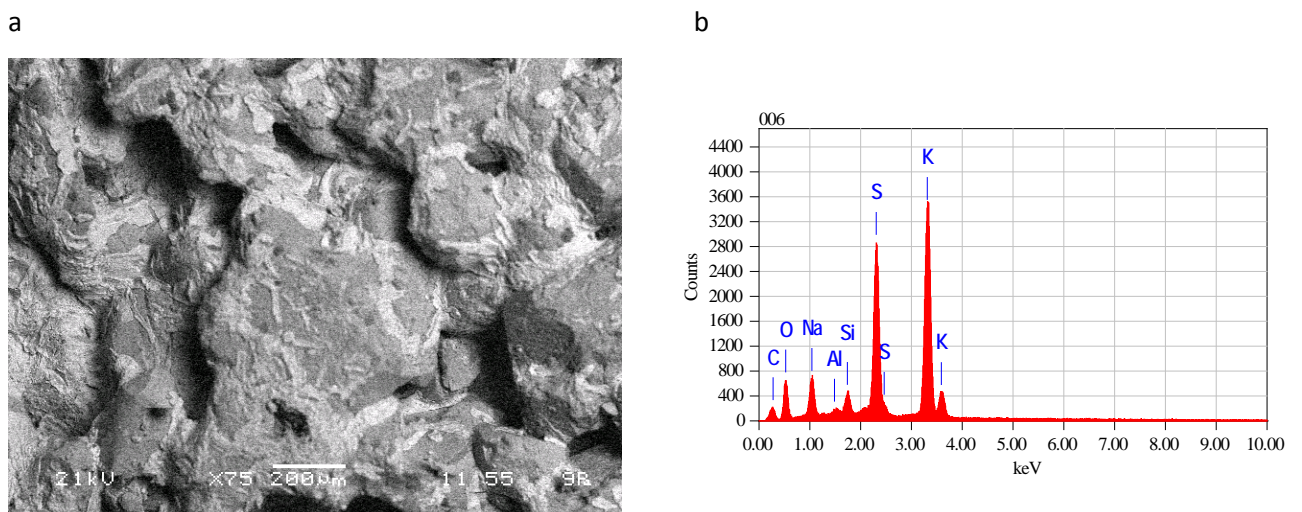


Figure 3.4-4: WW1 Lower Precipice Sandstone a),b) K(Na)-sulphate and lesser carbonate (both white and intermixed) were most abundant within this sample (WW1-1217-Precipice).

3.4.2. Evergreen Formation

The large variety of mineral and lithic grains observed in standard petrography were explored in finer detail using SEM. Mineral grains generally tended to be less altered in the shale samples than the sandstone, although unaltered examples of many minerals still also occurred within the sandstones. Crystals of rare earth element (REE)-bearing monazite were frequently observed in Evergreen Formation samples (e.g. Figure 3.4-5a), and more rarely calcium phosphate. Albite, sanidine, and Ca-Na-plagioclase (the latter more commonly for WW1 than Chin-4) occur along with unaltered flakes of oxyphlogopite (Figure 3.4-5b), a pneumatolitic titanium-bearing mica formed via high temperature magmatic gas alteration of alkali basalt, implying that deposition occurred relatively close to an eroding volcanic sediment source. The entire muscovite-phlogopite-biotite spectrum of micas appears to be present. Grains of a Ca-Mg ferrous aluminosilicate, most likely a type of amphibole, were also commonly observed (e.g. Figure 3.4-6).

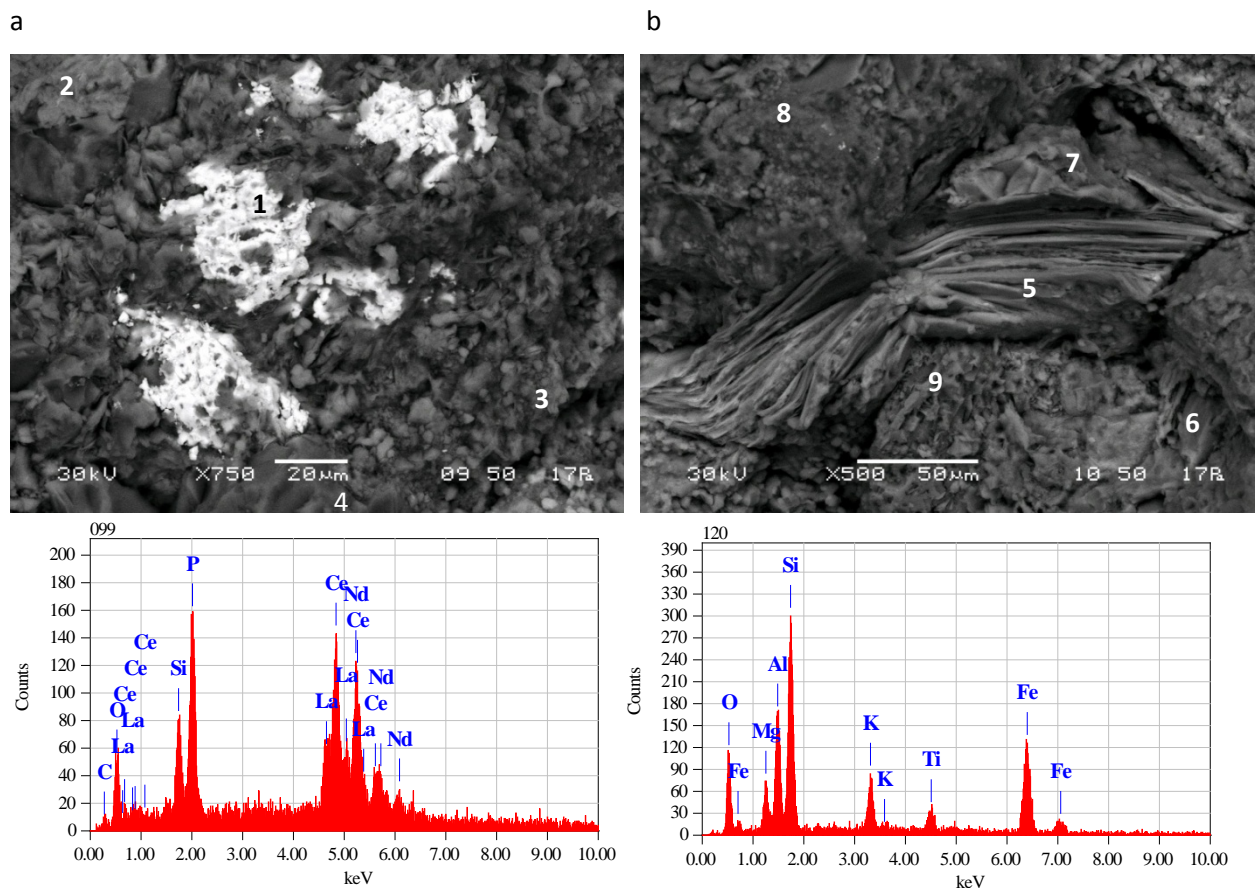
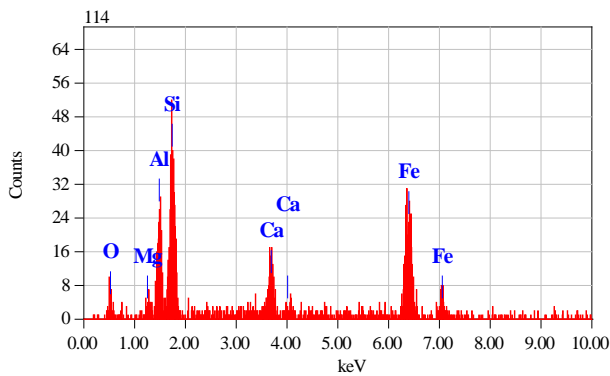
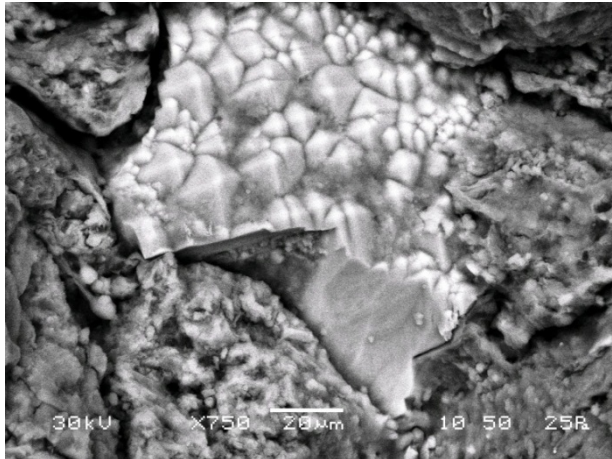


Figure 3.4-5: Chin4-1138-Evergreen a) (Nd, Ce, La)-monazite (1) with qualitative EDS spectra shown below image, (Fe, Mg)-chlorite (2), chloritised biotite, colloidal silica and kaolin (3), quartz (4); b) Oxyphlogopite (5) with qualitative EDS spectra shown below image, phlogopite (6), K-feldspar (7), quartz (8), kaolin (9).

Geochemical and Geomechanical Testing of Near Wellbore CO₂ Injectivity Improvement

a

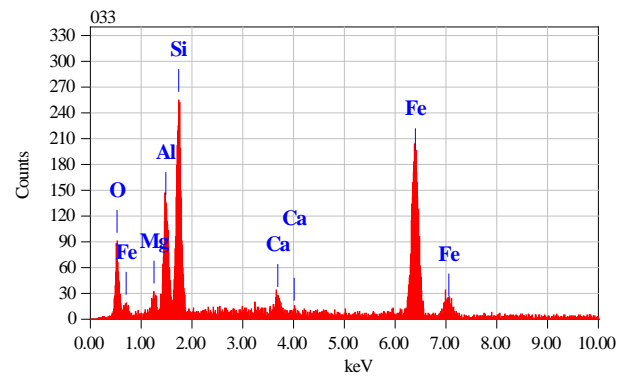
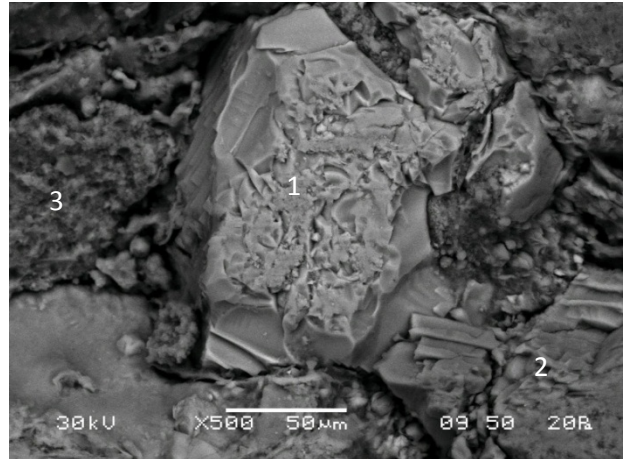


ZAF Method Standardless Quantitative Analysis

Fitting Coefficient : 0.6267

Element	(keV)	Mass%	Error%	Atom%
O K	0.525	20.74	1.02	36.07
Mg K*	1.253	2.78	0.48	3.18
Al K	1.486	17.44	0.39	17.98
Si K	1.739	23.83	0.43	23.60
Ca K	3.690	8.26	0.33	5.73
Fe K	6.398	26.96	0.55	13.43
Total		100.00		100.00

b



ZAF Method Standardless Quantitative Analysis

Fitting Coefficient : 0.4611

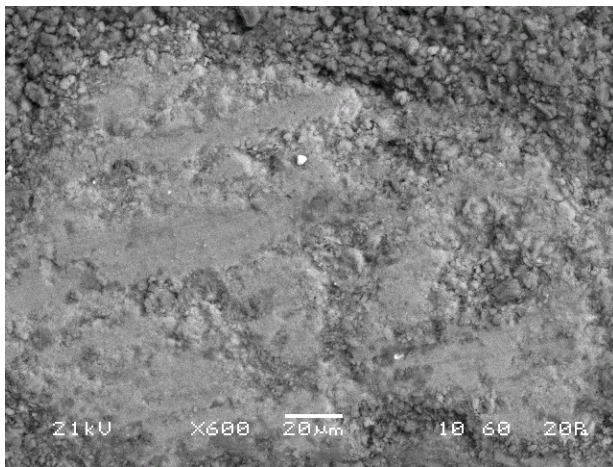
Element	(keV)	Mass%	Error%	Atom%
O K	0.525	25.24	0.52	43.47
Mg K	1.253	3.40	0.41	3.86
Al K	1.486	12.23	0.33	12.49
Si K	1.739	21.94	0.32	21.52
Ca K	3.690	1.62	0.24	1.11
Fe K	6.398	35.57	0.39	17.55
Total		100.00		100.00

Figure 3.4-6: Chin4-1138-Evergreen a) (Ca,Mg)-Fe-aluminosilicate surrounded by degraded K-feldspar; b) (Ca,Mg)-Fe-aluminosilicate (1), K-feldspar (2) and kaolin-replaced remnant K-feldspar (3). EDS spectra and semi-quantitative analysis of the (Ca,Mg)-Fe-aluminosilicates shown below images.

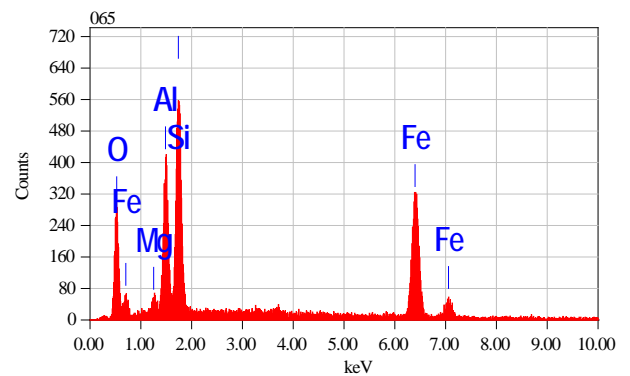
Geochemical and Geomechanical Testing of Near Wellbore CO₂ Injectivity Improvement

Altered and thus likely older cratonic felsic minerals such as K-feldspar, perthite and lithic fragments of both regional metamorphic and granitic rocks are also present in abundance. The rock matrix is comprised partly of various primary grain micro-fragments but mainly alteration products such as vermiculite, smectite, kaolinite and chlorite, particularly chloritised biotite (e.g. Figure 3.4-7). Other minerals observed include rutile, zircon, barite, galena, sphalerite (Figure 3.4-8), rhodochrosite, anatase, siderite and ankerite, the latter three being most commonly associated with alteration of Ti-phlogopite/biotite. Coal particles and micro-laminations are present in both samples, but most commonly in the shaley laminations (Figure 3.4-9).

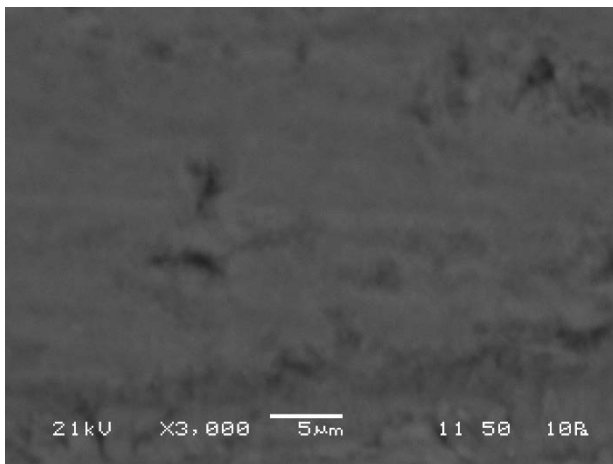
a



b



c



d

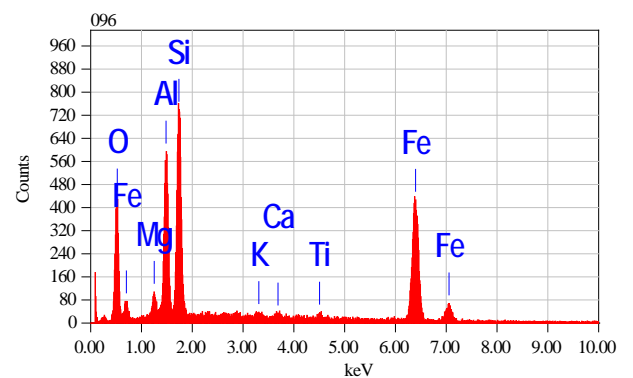


Figure 3.4-7: Fe-chlorite altered biotite group minerals in a) WW1-1043-Evergreen with EDS spectra in (b); c) WW1-981-Evergreen with EDS spectra in (b).

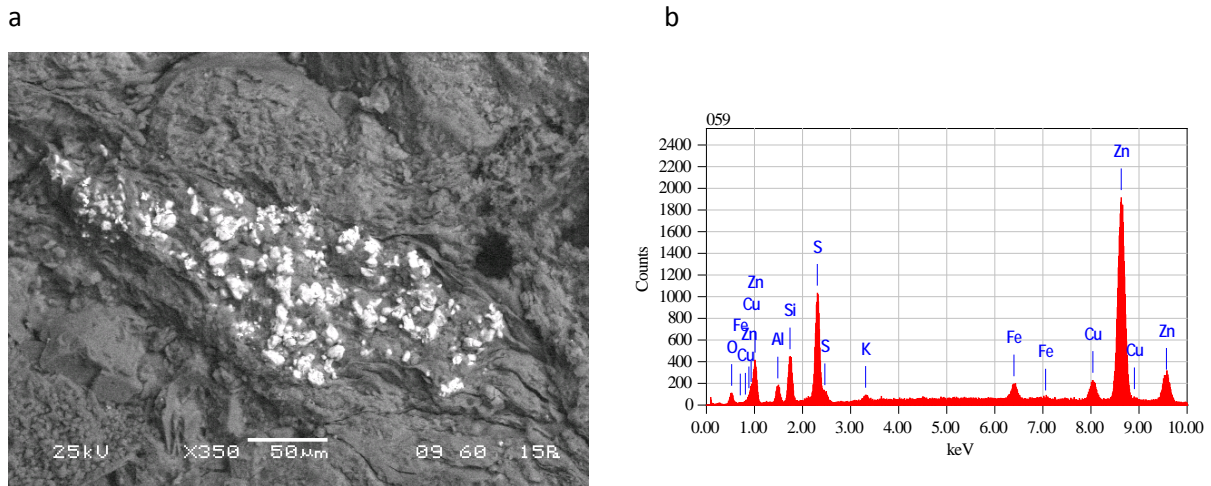


Figure 3.4-8: WW1-1056-Evergreen. a) Sphalerite and minor chalcopyrite (both white) amongst illite and other clays between quartz grains; b) EDS spectra of the sulphides and near-by minerals.

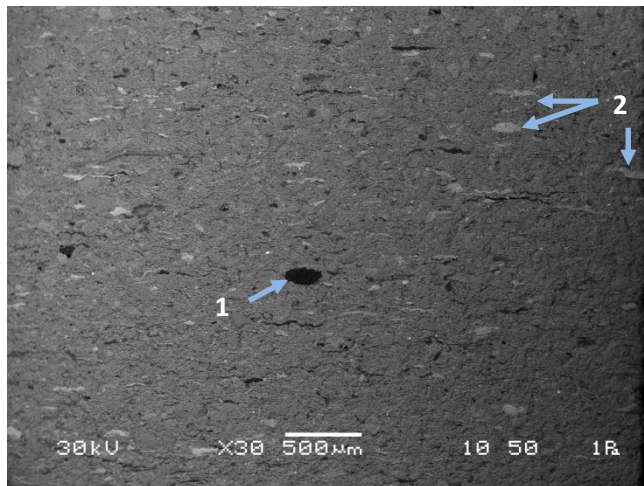


Figure 3.4-9: Chin4-897-Evergreen coalified organic matter (1) and muscovite, oxyphlogopite, and biotite mica flakes (2) are the largest common constituents of this sample.

3.4.3. Hutton Sandstone

The Hutton Sandstone samples contain similar minerals to those observed in the underlying Evergreen Formation, although reactive minerals such as amphiboles and micas (Figure 3.4-10) tend to be more altered. Pore-filling iron-oxide crystals are present and iron chlorite alteration of biotite was frequently observed (Figure 3.4-10 b). REE(+/Th, U)-monazite crystals were present in all Hutton Sandstone samples examined, but were especially large and common within the calcite-cemented quartzose samples of both Chinchilla 4 and West Wandoan 1 (Figure 3.4-11), sometimes also associated with sulphides such as pyrite and sphalerite. Significant amounts of Ca-phosphate were sometimes found in pores, and coal laminations and lenses were common in all samples (Figure 3.4-12) as were rutile and zircon crystals.

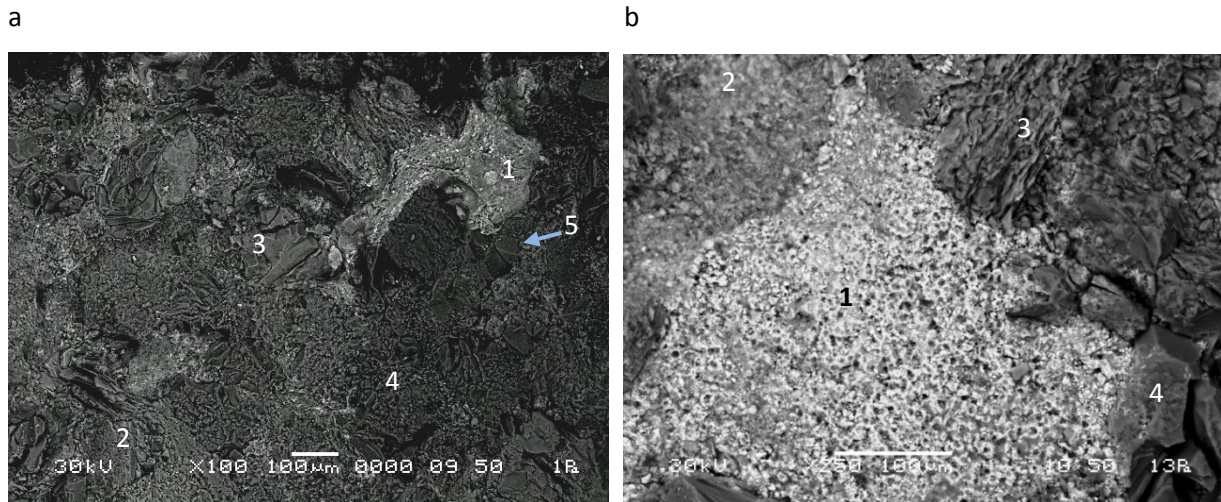


Figure 3.4-10: Chin4-868-Hutton a) Altered phlogopite containing small crystals of anatase and vermiculite/smectite (1), degraded muscovite (2), K-feldspar (3), Kaolin (4), quartz (5); b) Network of iron oxide crystals (1), Fe-chlorite (2), K-feldspar (3), Quartz (4).

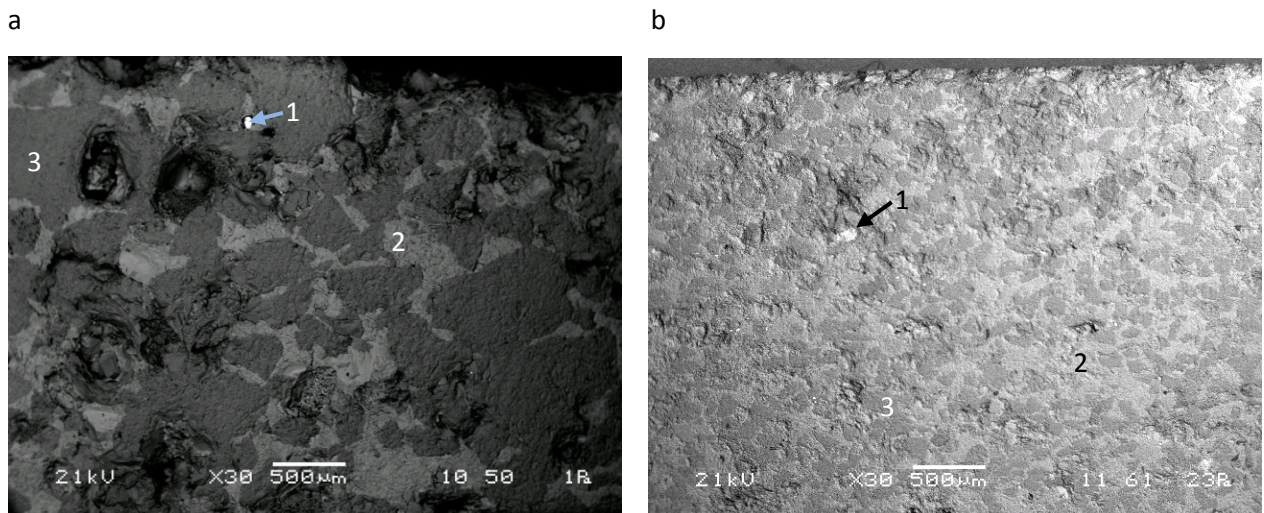


Figure 3.4-11: a) Chin4-799-Hutton. Euhedral (REE, U)-monazite (1) within calcite (2) cemented quartzose (3) sandstone; b) WW1-799-Hutton. (REE)-monazite with minor pyrite (1) in strongly calcite (2) cemented quartzose (3) sandstone.

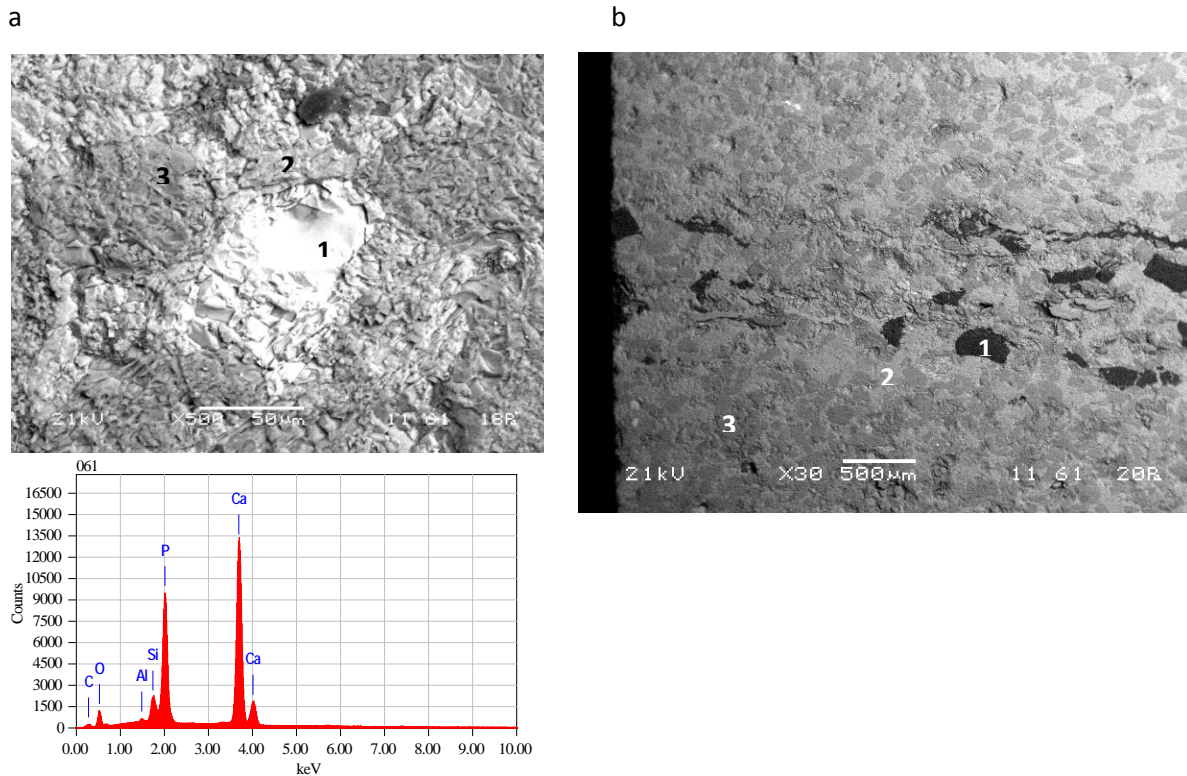


Figure 3.4-12: a) Chin4-799-Hutton. Calcium phosphate (1), calcite cement (2) and quartz (3); b) WW1-800-Hutton. Layer of coal pieces (1) in calcite (2) cemented quartzose (3) sandstone.

3.4.4. Berea Sandstone

The quartzose Berea Sandstone samples also contain K-feldspar grains (Figure 3.4-13), as well as lesser amounts of micas and alteration products such as chlorite, vermiculite, smectite and kaolinite (Figure 3.4-14a). Pore space is less abundant than in the Precipice Sandstone, being partially occluded by clays and also carbonate cement of variable Fe, Ca, Mg, Mn composition (Figure 3.4-14b). Iron oxide or possibly hydroxide also sometimes occurs together with the Fe-carbonates.

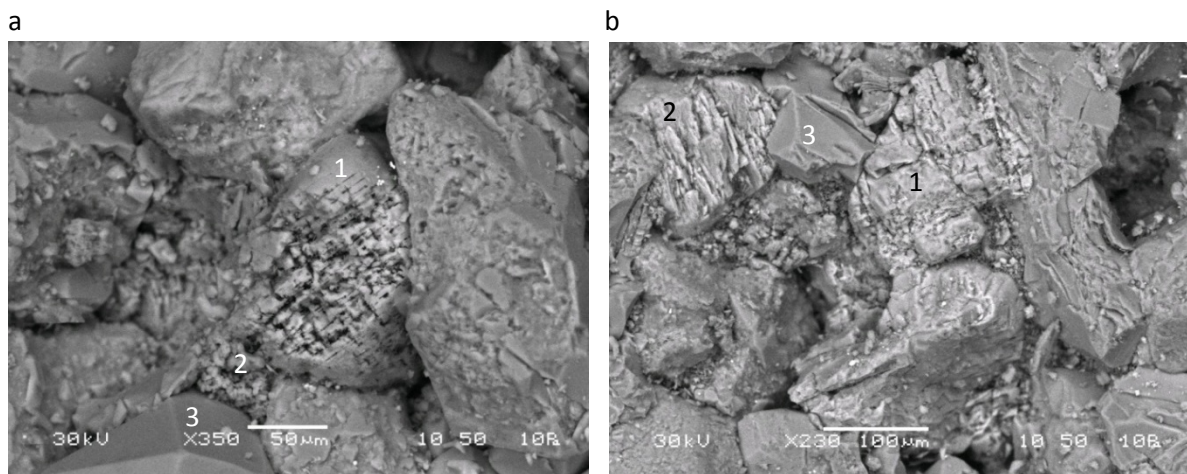
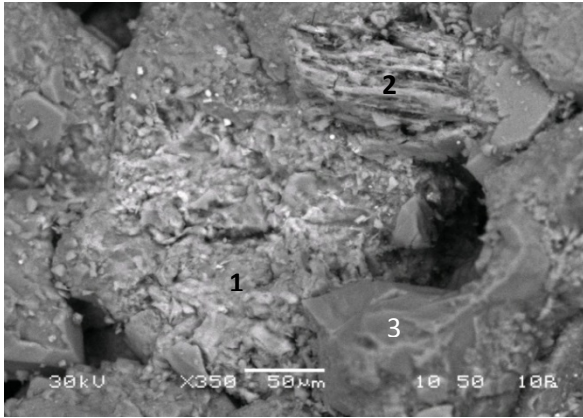


Figure 3.4-13: Berea Sandstone a) K-feldspar (1), kaolin (2), quartz (3); b) K-feldspar (1), perthitic K-feldspar (2), quartz (3).

a



b

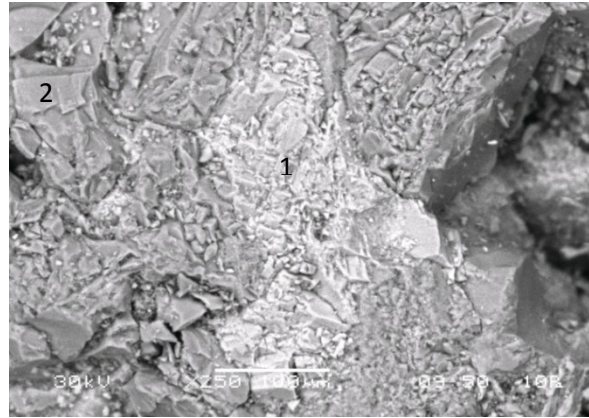


Figure 3.4-14: Berea Sandstone a) Vermiculite and chlorite (1), degraded K-feldspar (2), quartz (3); b) Ankerite (1), quartz (2).

4. Experimental Results

4.1. SEM-EDS Analysis Pre and Post Reaction

SEM surveys of the same surface positions were done before and after experiments to help show what did or did not change because of the geochemical batch reactor experiments. Unlike the QEMSCAN analyses that were not done on exactly the same surface pre and post reaction, the SEM analysis was able to directly provide visual evidence of mineral dissolution or lack of significant reaction. Examples are given for selected points of interest on the upper surface of batch reacted Chinchilla 4, West Wandoan 1, and Berea Sandstone samples. This information was used to inform interpretation of the incremental water chemistry results, and to determine which minerals to focus upon when building geochemical models of the batch reactions of each sample.

4.1.1. Precipice Sandstone

The majority of points of interest analysed via SEM pre and post reaction for the Precipice samples showed no significant changes due to batch reactor experiments (e.g. Figure 4.1-1). There was some minor physical movement of mineral fines but generally little evidence of chemical reactions having taken place. An exception to this was the sulphate salts and minor carbonate minerals observed in the WW1 Precipice samples (e.g. Figure 4.1-2). All visible sulphate and carbonate was removed from the sample surfaces during the batch reactor experiments.

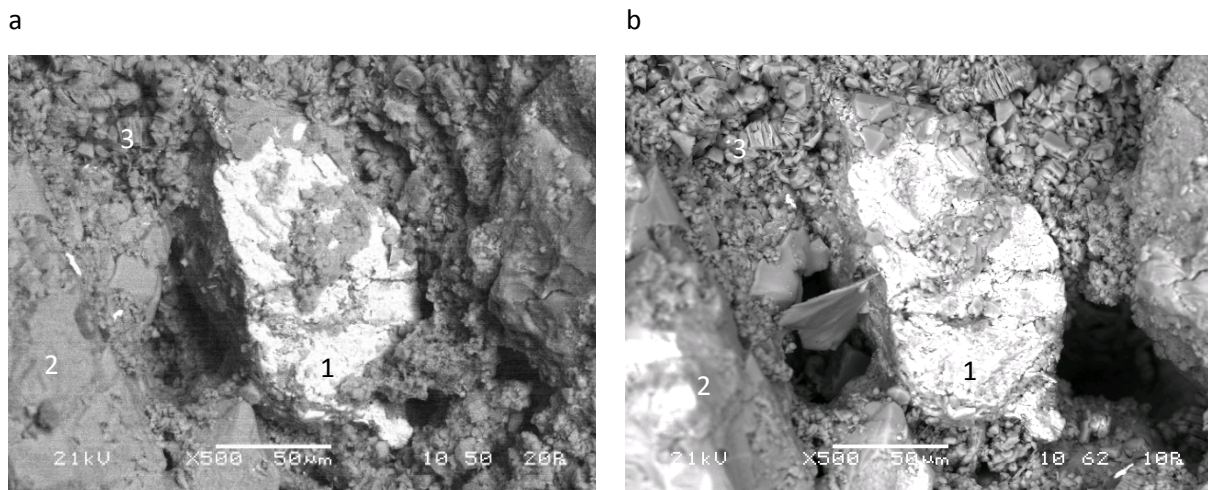


Figure 4.1-1: WW1 Upper Precipice Sandstone rutile (1), kaolin (2), and quartz (3) pre (a) and post (b) batch reaction. Although there has been some physical movement of clay fines, the clays did not show evidence of any significant chemical dissolution.

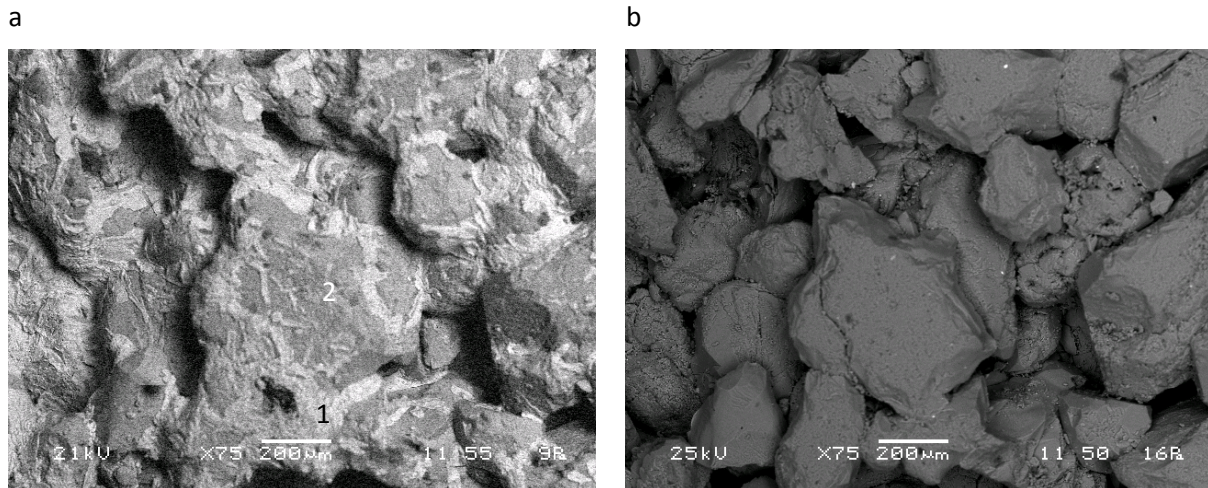


Figure 4.1-2: WW1 Lower Precipice Sandstone; (a) K-Na-sulphates (1) on and between quartz grains pre batch reactor experiment (2); (b) the sulphate minerals were removed during batch reaction.

4.1.2. Evergreen Formation

All samples taken from the Evergreen Formation contained a significant proportion of acid-reactive minerals, and pre and post reaction SEM analysis was often able to demonstrate which minerals were involved in geochemical reactions. Some minerals such as quartz, illite, mica flakes, K-feldspar and Ca-phosphate showed little change post reaction (Figure 4.1-3, -4 and -5). Other minerals such as chloritised biotite showed partial reaction (Figure 4.1-6), whereas carbonate minerals such as calcite were almost completely removed from the sample surfaces during batch reactor experiments (Figure 4.1-7).

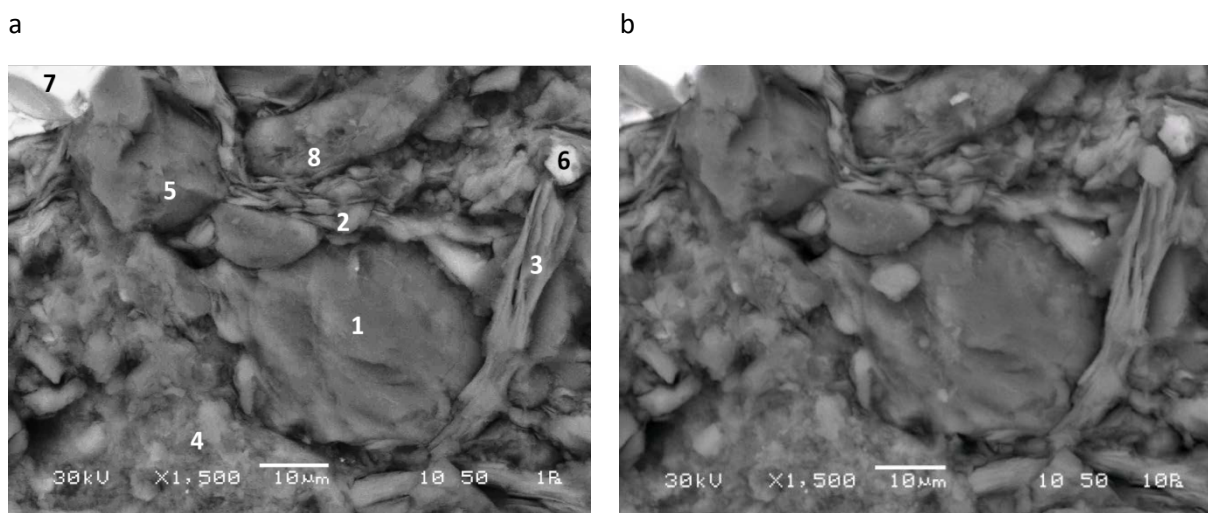


Figure 4.1-3: Chin4-897-Evergreen a) Clay altered mica (1), phlogopite (2), muscovite (3), kaolin altered K-feldspar (4), albite (5), rutile (6), zircon (7), quartz and kaolin (8); b) little obvious change occurred to these specific minerals after reaction with CO₂-water.

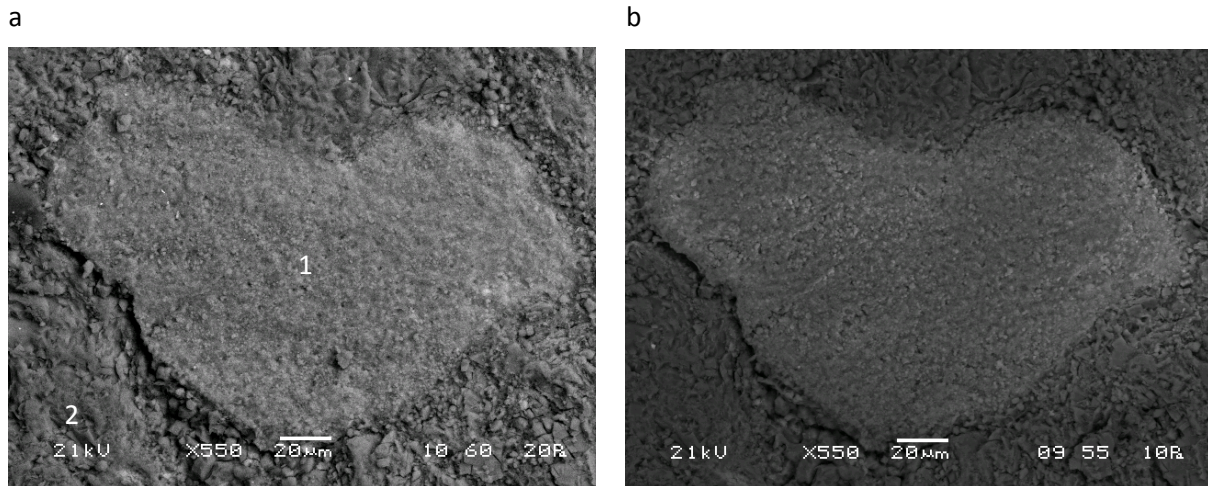


Figure 4.1-4: WW1-1043-Evergreen; Illite and fine grains of oxyphlogopite (1) between quartz grains (2) pre (a) and post reaction (b) showing little change.

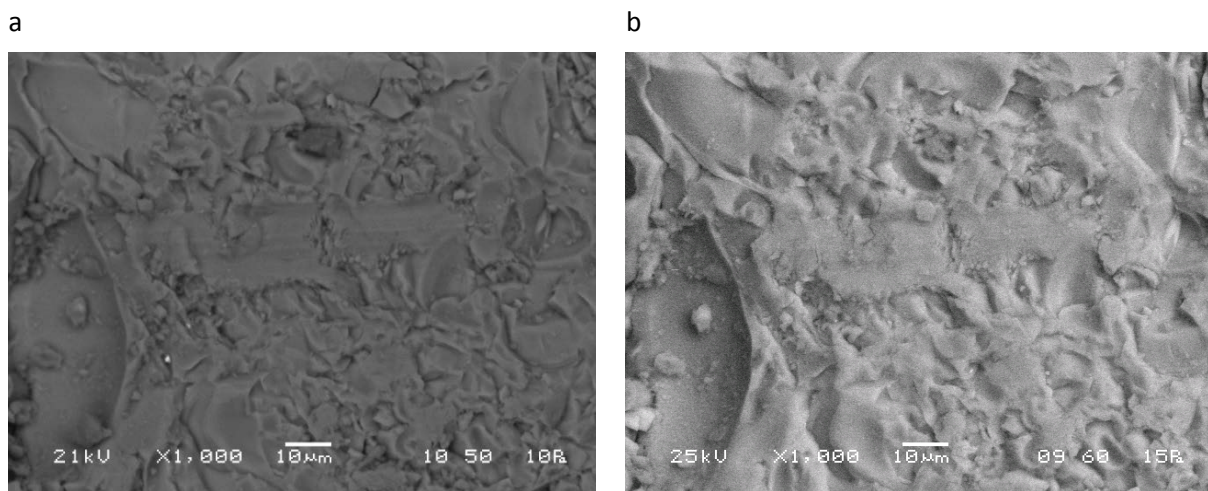


Figure 4.1-5: WW1-1056-Evergreen Ca-phosphate grain pre (a) and post (b) batch reaction showing only minor surficial changes.

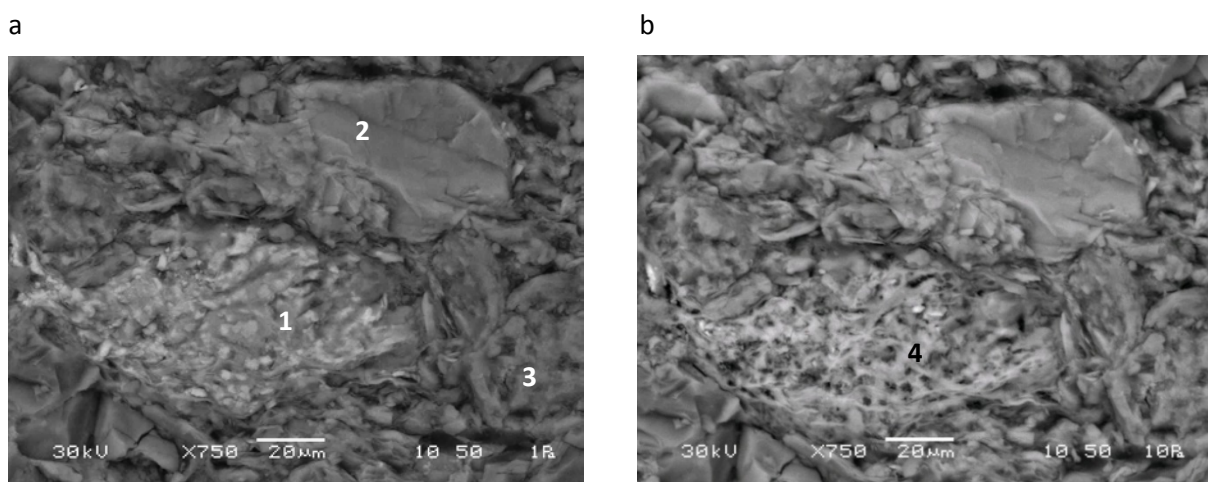


Figure 4.1-6: Chin4-897-Evergreen a) Biotite, chlorite and siderite (1); phlogopite (2), perthitic K-feldspar (3); b) siderite dissolved leaving behind remnants of the chloritised biotite framework in which it occurred (4).

Geochemical and Geomechanical Testing of Near Wellbore CO₂ Injectivity Improvement

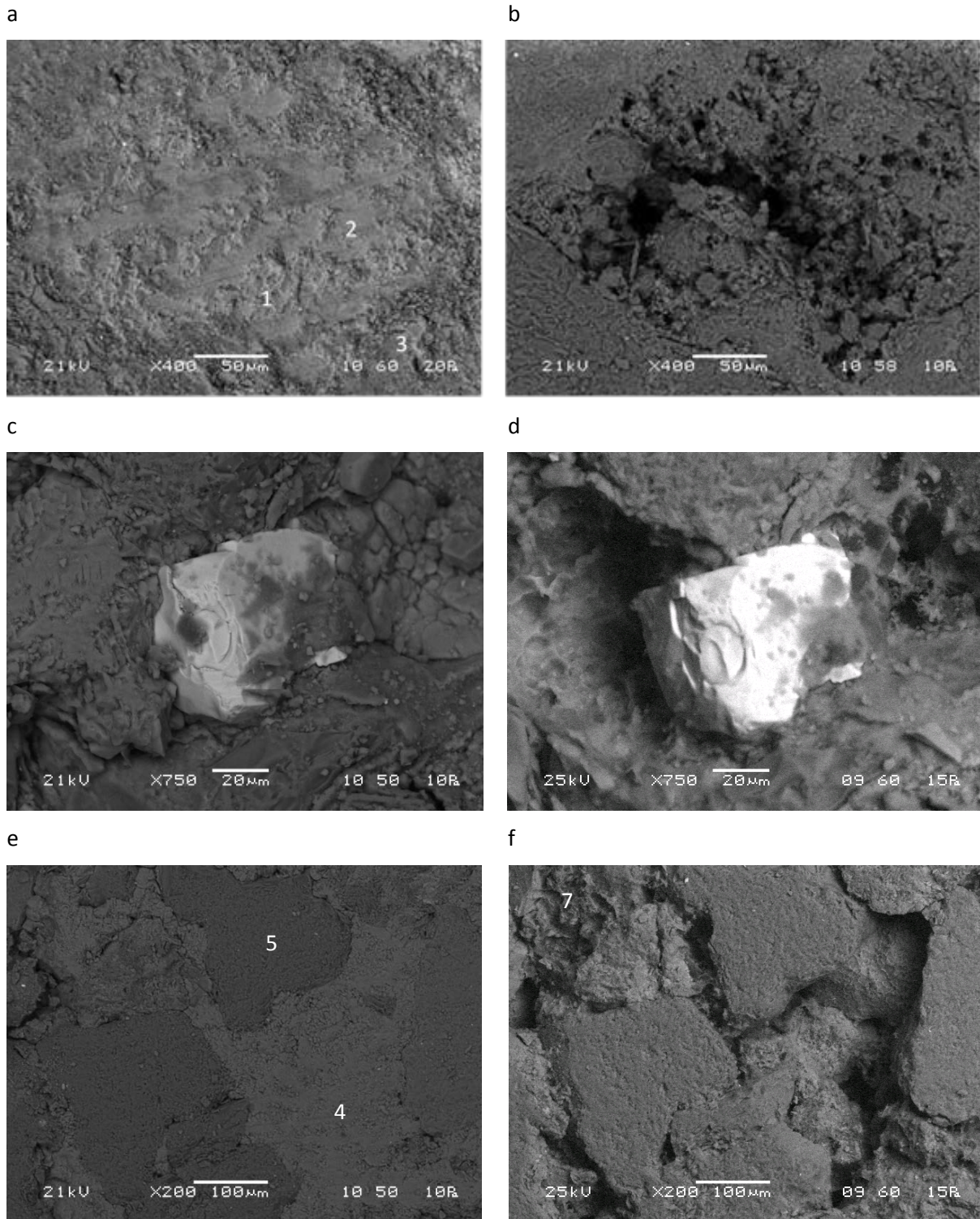


Figure 4.1-7: WW1-1043-Evergreen calcite (1) and clays (2) between quartz grains (3) pre (a) and post reaction (b); WW1-1056-Evergreen calcite (4), quartz (5), and zircon (6) grains pre (c, e) and post (d, f) reaction, with clays sometimes exposed by loss of calcite (e.g. 7 in f).

4.1.3. Hutton Sandstone

The Hutton samples behaved similarly to the Evergreen samples as expected given the similar mineralogy. A significant difference was that some remnant calcite was observed deep in the pores of the calcite cemented Hutton Sandstone samples (Figure 4.1-8). This could have been due to the generally larger grain size of the Hutton samples that correlated with larger spaces between quartz grains, and/or an overall greater abundance of calcite available for reaction near the sample surfaces. Buffering of the pH due to reaction of significant amounts of near-surface calcite early on during the batch reactor experiments most likely hindered further reaction of calcite present deeper within the samples.

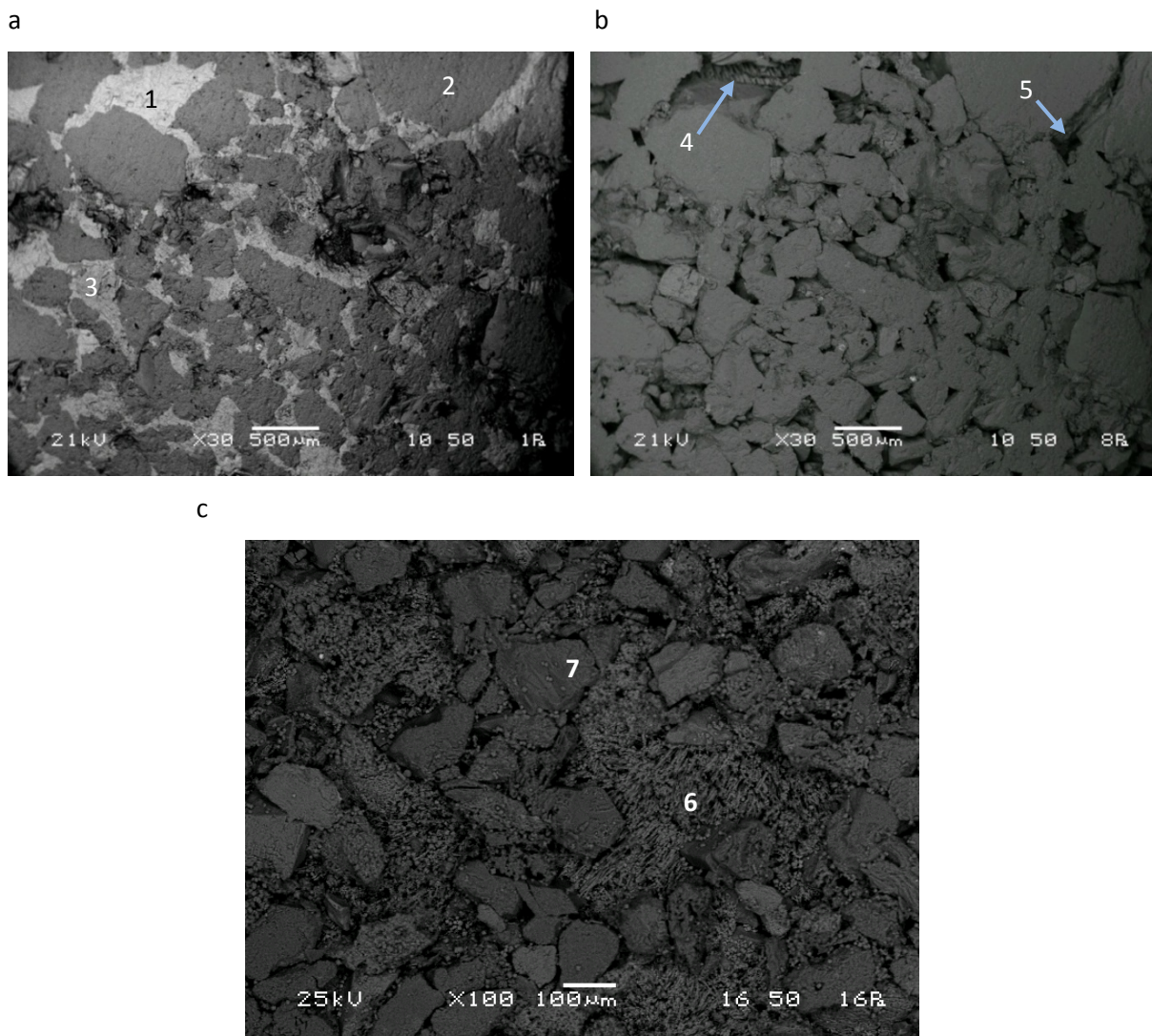


Figure 4.1-8: Chin4-799-Hutton, top of reacted sample a) Calcite cement (1) in between quartz grains (2) and minor others such as K-feldspar (3); b) Remnant calcite cement (4) and new pore-space that was previously cemented (5); c) Sample WW1-800-Hutton, base of reacted sample. Partially reacted calcite (6) remaining between quartz grains (7) was commonly observed.

4.1.4. Berea Sandstone

Similarly to the calcite cemented Hutton samples, the (Fe, Ca, Mg, Mn)-carbonate cements between quartz grains of the Berea Sandstone only partly reacted during the batch reactor experiments (Figure 4.1-9). A major difference was that unlike the Hutton samples but similarly to some Evergreen samples, the carbonate cement within the Berea samples was often associated with hematite, which did not appear to have reacted appreciably during the experiments. The mica and clay grains within the samples were too fine grained for physical mobilisation to be distinguished from chemical dissolution, but it is possible that some finer-grained, already partly altered micaceous material reacted.

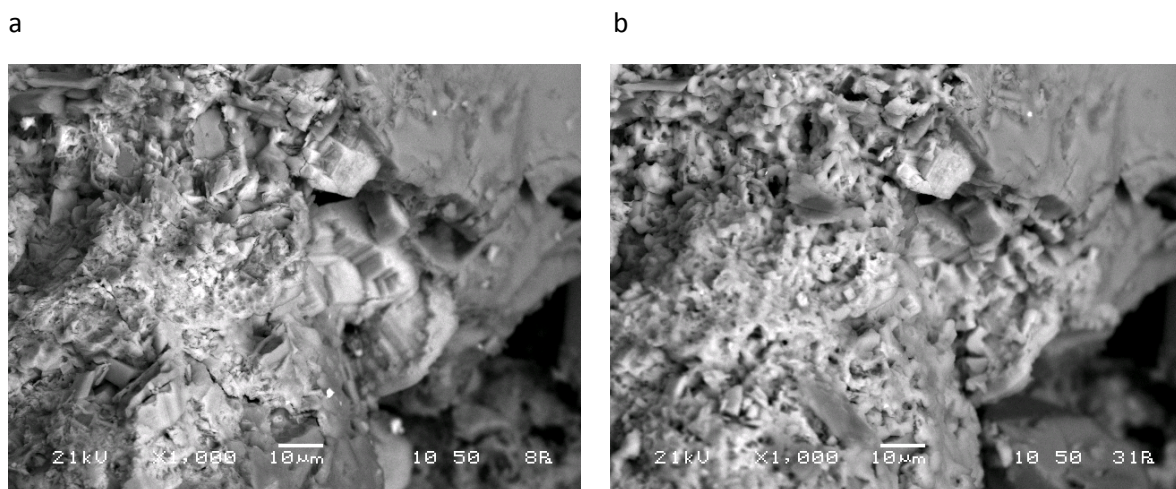


Figure 4.1-9: Berea Sandstone; Siderite and hematite (white) between quartz grains (grey) pre (a) and post (b) CO₂-brine exposure.

4.2. QEMSCAN Mineralogy and X-ray Micro-CT Results

4.2.1. Precipice Sandstone

Three sub-plug samples of the Precipice Sandstone, Chin4-1192, WW1-1217 and WW1-1165 were imaged by 3D high resolution, helical X-ray micro-CT at FEI-Lithicon Australia. The tomograms were segmented into X-ray distinct minerals and porosity components, and these were then quantified.

Chin4-1192 was mainly composed of framework grains, with 18 vol% measured resolvable porosity; this increased slightly to 18.4 vol% post- CO₂-water-rock reaction (Table 4.2-1). In each of the sub-plugs that were imaged by high resolution X-ray micro-CT, the sub-plug was cut along a plane of interest and a polished section was created. Automated, quantified SEM-EDS analysis by QEMSCAN of the polished section (performed by FEI-Lithicon) indicated this sample to mainly consist of quartz (97.8 area%, see Table 4.2-2) with 1.3 area% kaolin. Post CO₂-water-rock reaction, no significant changes were observed. This is in good agreement with SEM observations made at UQ, and water chemistry that indicated only minor geochemical changes post-reaction (Farquhar et al., 2014).

Geochemical and Geomechanical Testing of Near Wellbore CO₂ Injectivity Improvement

Table 4.2-1: Resolved mineral and porosity components from 3D tomogram segmentation of Chin-4 sub-plugs pre- and post CO₂-water-rock reactions (vol. %).

Well	Precipice Sst		Evergreen Formation				Hutton Sandstone			
	Chin4		Chin4		Chin4		Chin4		Chin4	
Depth / m	1192		1138		897		868		799	
Contents	Pre-CO ₂	Post-CO ₂								
Framework grains	78	77.4	34.4	31.8	18.9	17.5	59.4	60.6	76.3	75.9
Matrix	-	-	60.4	63.1	77.2	77.9	-	-	-	-
Clay content	7.7	7.9	-	-	-	-	35.8	33.8	5.6	6.9
Calcite cement	0.0	-	-	-	-	-	-	-	17.0	14.9
Heavy minerals	0.2	0.2	4.9	4.1	1.9	2.8	3.0	3.9	<0.1	<0.1
Resolvable porosity	18.0	18.4	-	-	-	-	1.9	1.7	1.1	2.2
Resolved porosity / organic*	-	-	0.2	1.0	2.0	1.7	-	-	-	-

*Resolvable porosity, including possible organic content. Resolved porosity indicates pores larger than 1 voxel (3D pixel) in size. See also Farquhar et al. (2014).

Table 4.2-2: Mineral assays (area %) of Chin-4 samples derived from QEMSCAN microanalysis of polished sections from sub-plugs pre- and post- CO₂-water-rock reactions.

Well	Precipice Sst		Evergreen Formation				Hutton Sandstone			
	Chin4		Chin4		Chin4		Chin4		Chin4	
Depth / m	1192		1138		897		868		799	
Minerals	Pre-CO ₂	Post-CO ₂								
Quartz	97.8	98	35.7	45.2	39.7	39.8	56.6	58.9	78.1	74.2
Alkali Feldspar	<0.1	0	26.5	20.8	5.7	6.4	7.2	6.3	1.1	3.1
Plagioclase	<0.1	<0.1	7.8	5.6	9.3	8.4	6.4	6.4	2.2	1.6
Muscovite/Illite	<0.1	0.4	1.8	1.1	10	10.6	6.0	2.9	0.2	0.2
Biotite	0	0	0.4	0.5	1.1	1.8	0.5	0.3	<0.1	<0.1
Kaolinite	1.3	1.4	12.4	10.5	19.2	20.4	6.9	10.7	2.5	3.6
Chlorite	<0.1	<0.1	3.1	3.3	3.8	3.2	8.3	8.5	0.3	0.2
Glauconite	0	0	<0.1	0.1	0.1	0.2	0.2	<0.1	<0.1	<0.1
Smectite	0	0	0.4	<0.1	<0.1	<0.1	0	<0.1	0	0
Calcite	0	0	0.2	0	0	0	0	<0.1	14.6	13.2
Siderite	0	0	0	0	<0.1	0	<0.1	0	0	0
Apatite	0	0	<0.1	<0.1	<0.1	<0.1	<0.1	<0.1	0	0
Rutile	0	0	<0.1	<0.1	0.2	0.1	0.2	<0.1	0	<0.1
Pyrite	0	0	<0.1	0	0	0	0	0	0	0
Fe-Oxides	0	0	0	0	0.2	0.2	0.1	<0.1	0	0
Zircon	<0.1	0	<0.1	0	<0.1	<0.1	0	0	0	0
Unclassified material + Trace minerals	0.8	0.2	11.4	12.8	10.6	9.0	7.6	5.9	1.0	3.8

WW1-1217 (lower Precipice) and WW1-1165 were also mainly composed of framework grains (75 vol%), with relatively high resolvable porosities of 21.5 and 18.7 vol% respectively (Figure 4.2-1a and b). WW1-1217 was mainly poorly sorted quartz grains with minor kaolinite (2.8 area%) as detailed in Table 4.2-4. QEMSCAN analysis of WW1-1165 was not available but the tomogram segmentation indicated ~ 6 vol% clay. Post CO₂-water-rock reaction, the only observable changes were dislocation of kaolin, in good agreement with SEM, and confirming the suitability of the Precipice Sandstone as a low reactivity reservoir unit.

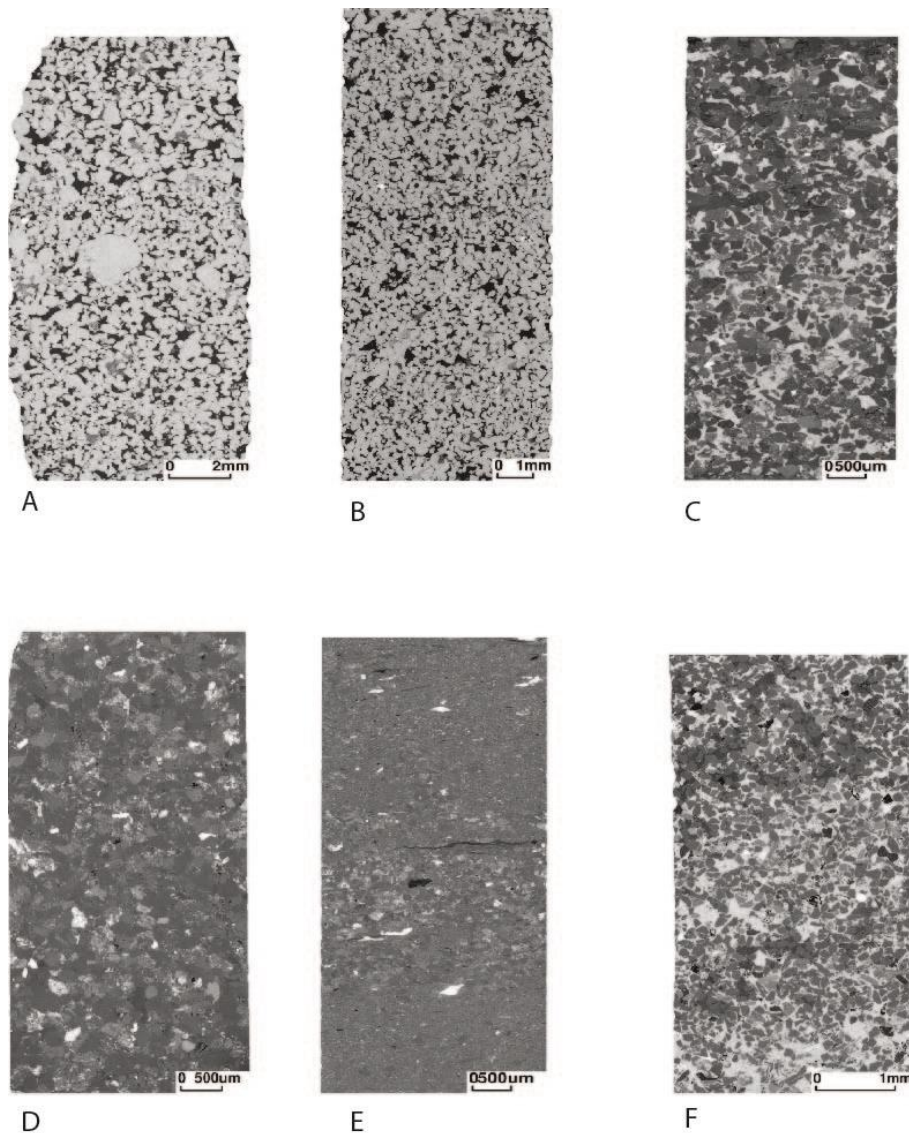


Figure 4.2-1: Vertical plane images from high resolution 3D μ CT tomograms of WW1 sub-plugs before reaction a) 1217-Precipice (WC14a), b) 1165-Precipice (WC11a), c) 1056-Evergreen (WC9a), d) 1043-Evergreen (WC8a), e) 981-Evergreen (WC3a), f) 800-Hutton (WC15a). Source: Golab et al. (2014), used with permission.

Geochemical and Geomechanical Testing of Near Wellbore CO₂ Injectivity Improvement

Table 4.2-3: Resolved mineral and porosity components from 3D tomogram segmentation of WW-1 sub-plugs pre- CO₂-brine-rock reactions (vol. %). Resolved porosity indicates pores that are larger than the elemental volume for a tomogram, i.e. 1 voxel (3D pixel) in size.

	Precipice Sandstone		Evergreen Formation			Hutton Sandstone
Well	WW1	WW1	WW1	WW1	WW1	WW1
Depth / m	1217	1165	1056	1043	981	800
Framework grain content	74.5	74.9	76.8	20.6	11.9	59.5
Matrix			22.5	73.3	84.1	32.1
Clay content	3.9	6.3				
Heavy mineral content	0.2	0.1	0.4	5.7	3.3	0.2
Resolvable porosity /organic	21.5	18.7	0.3	0.5	0.7	0.3

Table 4.2-4: Comparative mineral assays, as area percentages, of WW-1 sub-plug polished sections measured by QEMSCAN pre and post CO₂-brine-rock reactions.

	Precipice Sandstone				Evergreen Formation						Hutton Sst	
	WW1		WW1		WW1		WW1		WW1		WW1	
Depth / m	1217		1165		1056		1043		981		800	
	Pre-CO ₂	Post-CO ₂										
Quartz	96.8	na	na	96.1	21.0	24.2	57.6	56.9	37.0	na	36.5	36.3
Alkali feldspar	0.0	na	na		11.8	11.3	5.4	6.5	2.7	na	7.1	8.3
Plagioclase	0.0	na	na		21.6	23.0	26.6	26.5	12.6	na	7	8.2
Muscovite/Illite	0.2	na	na	0.3	0.2	5.7	1.7	1.6	1.1	na	2.3	3.6
Biotite	0.0	na	na		0.0	2.1	1.4	1.3	5.6	na	0.3	0.4
Illite-Smectite	0.0	na	na		9.2	8.2	0.0	0.0	15.6	na	0.0	0.0
Kaolinite	2.8	na	na	3.4	0.6	0.7	0.9	0.8	2.1	na	5.7	9.9
Chlorite	0.0	na	na		0.8	1.7	3.1	3.3	8.7	na	0.7	1.2
Calcite	0.0	na	na		30.1	19.2	0.3	0.0	0.1	na	38.4	30.1
Apatite		na	na			0.1		0.0		na		0.0
Unclassified and traces	0.2	na	na	0.1	4.7	4.0	3.0	3.0	14.3	na	0.2	2.1
Total	100	na	na	99.9	100	100	100	99.9	99.9	na	100	100.0
Total Clay/Mica	3.0	na	na	96.1	10.8	16.3	7.1	7.0	33.1	na	9.0	15.1

4.2.2. Evergreen Formation

Two samples of the Evergreen Formation from the Chinchilla 4 core, and three samples from the WW-1 core were selected for analysis pre- and post- CO₂-water-rock reaction. Chin4-1138 from the lower Evergreen and Chin4-897 from the upper Evergreen contained 34 and 19 vol% framework grains, respectively, with high matrix content (Table 4.2-1). Resolvable porosity was low for these fine-grained samples as pore-filling materials with sub-resolution porosity (pores smaller than 1 voxel in size, 2 µm) do not allow the unambiguous assignment of mineral and porosity phases using X-ray attenuation. These micropores are grouped with the clays, partly altered grains and diagenetic cements that make up the matrix material (Knackstedt et al., 2013). Chin4-1138 appeared to have a slight increase in resolvable porosity post-reaction from 0.2 to 1 vol%. Chin4-1138 and Chin4-897 contained more varied mineralogy than the Precipice samples as shown in Table 4.2-2, with chlorite and calcite potential reactive phases. There was up to 12 area% of unidentified minerals with the QEMSCAN method, some of these were identified by SEM in section 4.1. Changes in mineralogy post CO₂-water-rock reaction were not conclusive using this method (possibly due to minor rock heterogeneity). The loss of calcite from Chin4-1138 and possible increase in kaolin in Chin4-897 are indicated. This is in agreement with SEM and geochemical modelling.

The sub-plug WW1-1056 from the lower Evergreen formation contained significant calcite cement (30 area%) pre- CO₂-water-rock reaction (Fig. 4.2-1c), which was determined to be reduced to 19 area% post-reaction (Table 4.2-4). This is in good agreement with SEM, water chemistry changes and geochemical modelling. Dissolution and precipitation of other minerals was inconclusive. Resolvable porosity was very low for all WW1 Evergreen samples, indicating mainly pores below 1 µm.

WW1-1043 and WW1-981 sub-plugs had lower framework grain content (21 and 12 vol% respectively) than the other WW-1 samples (Figure 4.1-1d and e), and higher heavy mineral content. These samples also had a variable mineralogy as detailed in Table 4.2-4, with chlorite and calcite the potential reactive phases. Significant changes were not identified post CO₂-brine-rock reaction, with minor loss of material, potentially calcite, observed in WW1-1043 as shown in Figure 4.2-2c. WW1-981 sub-plug had generally fine grain size, and contained a sandy bedded section with a crack (likely from coring) pre-reaction (Figure 4.2-1e), and a relatively high proportion of chlorite (9 area%). Post-reaction this sub-plug broke in half through the existing crack, there was some minor loss of material around the edges, and a reduction in the Fe content of the chlorite observed (post-reaction QEMSCAN unavailable). Loss of Fe content was also observed in water chemical analyses and SEM.

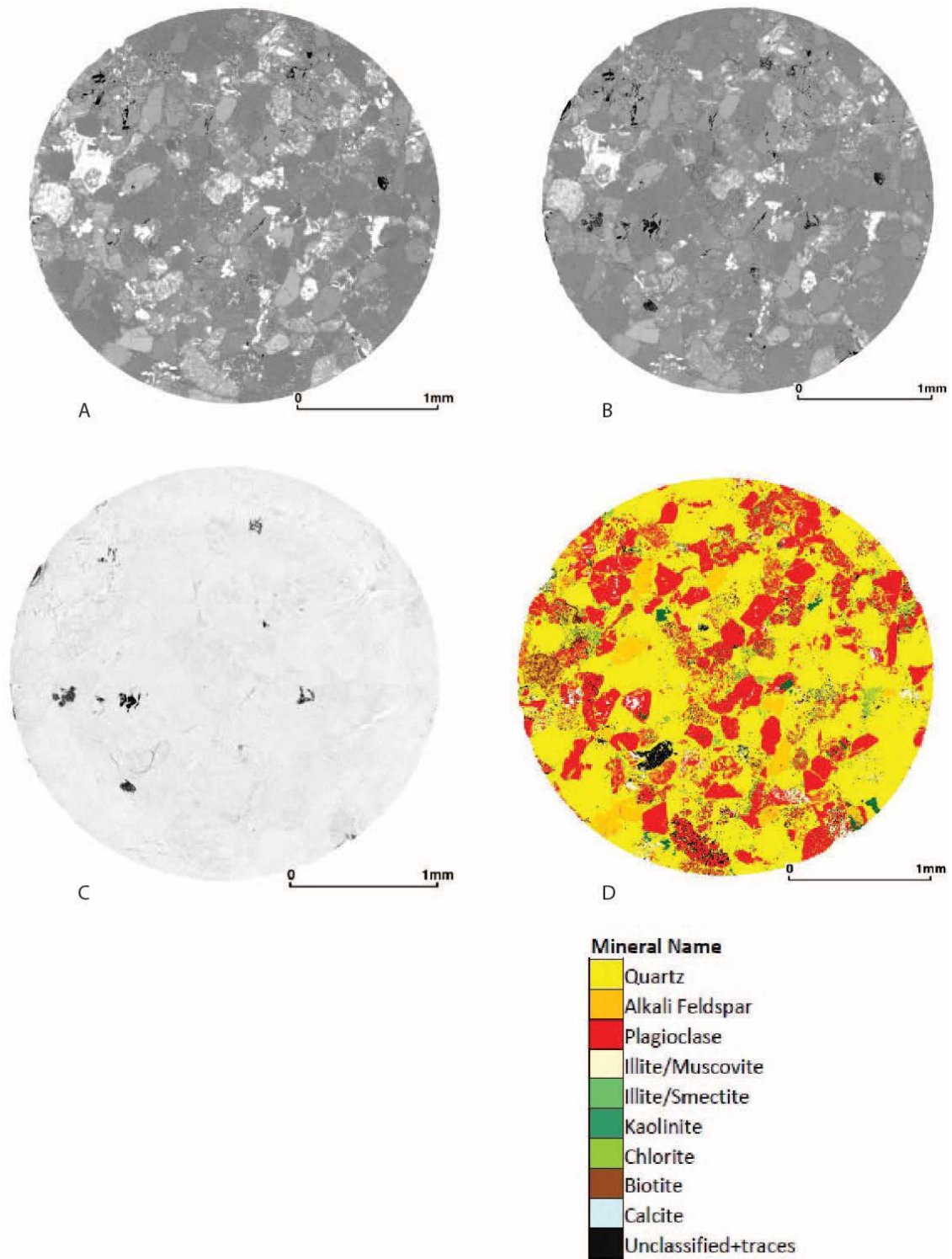


Figure 4.2-2: Registered tomogram images of WW1-1043-Evergreen sub-plug slice, a) Pre-reaction, b) post-reaction, c) difference image (dark areas = loss of material) , d) QEMSCAN after reaction with mineral key shown. Source: Golab et al. (2014), used with permission.

4.2.3. Hutton Sandstone

Sub-plugs from two sections of the Chin-4 Hutton Sandstone, and one section of the WW-1 Hutton Sandstone were tested. Significant clay content was measured in the Chin4-867 sub-plug, with a low resolvable (greater than $\sim 2 \mu\text{m}$) porosity shown in Table 4.2-1. A variable mineralogy was determined through QEMSCAN as detailed in Table 4.2-2, with 8 area% chlorite identified. Changes in mineralogy of this sample post CO₂-water-rock reaction were not conclusive using QEMSCAN; however, the increase in kaolin content post-reaction was corroborated by geochemical modelling that predicted precipitation of kaolinite (Farquhar et al., 2014). Chin4-799 was identified in 3D tomogram segmentation and QEMSCAN to be highly calcite cemented (Tables 4.2-1 and 4.2-2). Post CO₂-water-rock reaction loss of up to 2 vol% calcite was observed around the edges of the sub-plug along grain faces, cleavages and on cement boundaries (Farquhar et al., 2014). This was in excellent agreement with SEM observations, water chemistry and geochemical modelling all of which indicated calcite cement dissolution (Farquhar et al., 2014).

The WW1-800 sub-plug was observed to be significantly calcite cemented (Fig. 4.2-1f, Table 4.2-4), with 38 area% calcite content determined through QEMSCAN. Some loss of calcite around the edges of the sub-plug was observed post reaction, with up to 8 area% reduction determined by QEMSCAN. This is in excellent agreement with SEM, water chemistry and geochemical modelling observations. In general silicate dissolution was not observed, although up to ~ 4 area% kaolinite potentially precipitated.

Micro-CT imaging was noted to be a good method for visualising and quantifying porosity in reservoir rocks where the majority of porosity likely exists as pores greater than $1 \mu\text{m}$. The low portion of resolvable porosity in sealing samples indicated the use of a complementary technique such as Small Angle Neutron Scattering (SANS) could be useful in future to measure sub-micrometre scale porosity. QEMSCAN is a robust method for mapping and quantifying minerals in the rock samples measured here, and for observing major dissolution or precipitation of minerals during CO₂ reaction. However, as adjacent slices of a sub-plug are analysed pre and post-reaction, sample heterogeneity can mask minor changes through trace dissolution and precipitation. Unclassified and trace minerals were especially high in the sealing rock samples. SEM observations and water chemistry were important to determine trace mineral content and changes through CO₂ reaction.

4.3. Batch Reactor Water Chemistry Results

The incremental water chemistry results for the batch reactor experiments with WW1, Chin-4, and Berea samples are presented as figures, with concentrations in ppm normalised per gram of rock reacted. The major to minor elements that were preferentially mobilised for given samples varied depending upon the specific geological unit from which the rock samples had been taken. Relative measured dissolved ion concentrations were generally higher in the Hutton Sandstone and Evergreen Formation experiments than for the Precipice Sandstone experiments. The Precipice experiments generally had considerably less dissolved Ca, Na, Fe, Mn, Mg, and Sr than the other rocks with respect to water – rock equilibration.

The Chinchilla-4 samples were mostly reacted in fresh water, whereas the WW1 samples were primarily reacted in 1500 ppm NaCl solution. A 1% KCl solution was used for two Evergreen samples (WW1-1056 and Chin4-1138) that contained significant reactive clays as well as carbonate cement. A 1500 ppm KCl solution was used for the WW1-800-Hutton sample that had similar reactive components to a lesser extent; KCl was generally used to prevent swelling and core disintegration. The decision to use KCl was made on the basis of bench-top tests of off-cut material in solutions of pure water, NaCl, and KCl of different concentrations to test core material stability. The water-reactive Evergreen samples disintegrated in both pure water and NaCl solutions within a matter of hours, hence KCl solutions were used in subsequent pressurised experiments.

4.3.1. Precipice Sandstone

Most aqueous element concentrations remained fairly stable following CO₂ addition to the WW1 Upper Precipice experiment. Concentrations of elements in solution were generally low compared to other rocks indicating the low reactivity of this unit (Figure 4.3-1). Sulphur showed an increase in concentration; this was possibly evidence of sulphate salts observed during sample characterisation dissolving within the first two weeks of the batch reactor experiment. Trace elements such as As detected during the experiments were close to the detection limit of the ICP-OES instrument used to analyse the reaction waters.

Concentrations of dissolved elements were higher during the Lower Precipice WW1 experiment compared with the Upper Precipice, although the overall magnitude of the mobilisation was still fairly low. This implied that much of the material dissolved could have been present as salts within the sample rock pores or else released through cation-exchange from the minor clay component of the sample. Solution pH in the lower Precipice experiment decreased during the first week and then remained fairly constant at ~ pH 4 (Figure 4.3-2a). The low reactivity of the Precipice likely precluded mineral buffering of the pH.

Geochemical and Geomechanical Testing of Near Wellbore CO₂ Injectivity Improvement

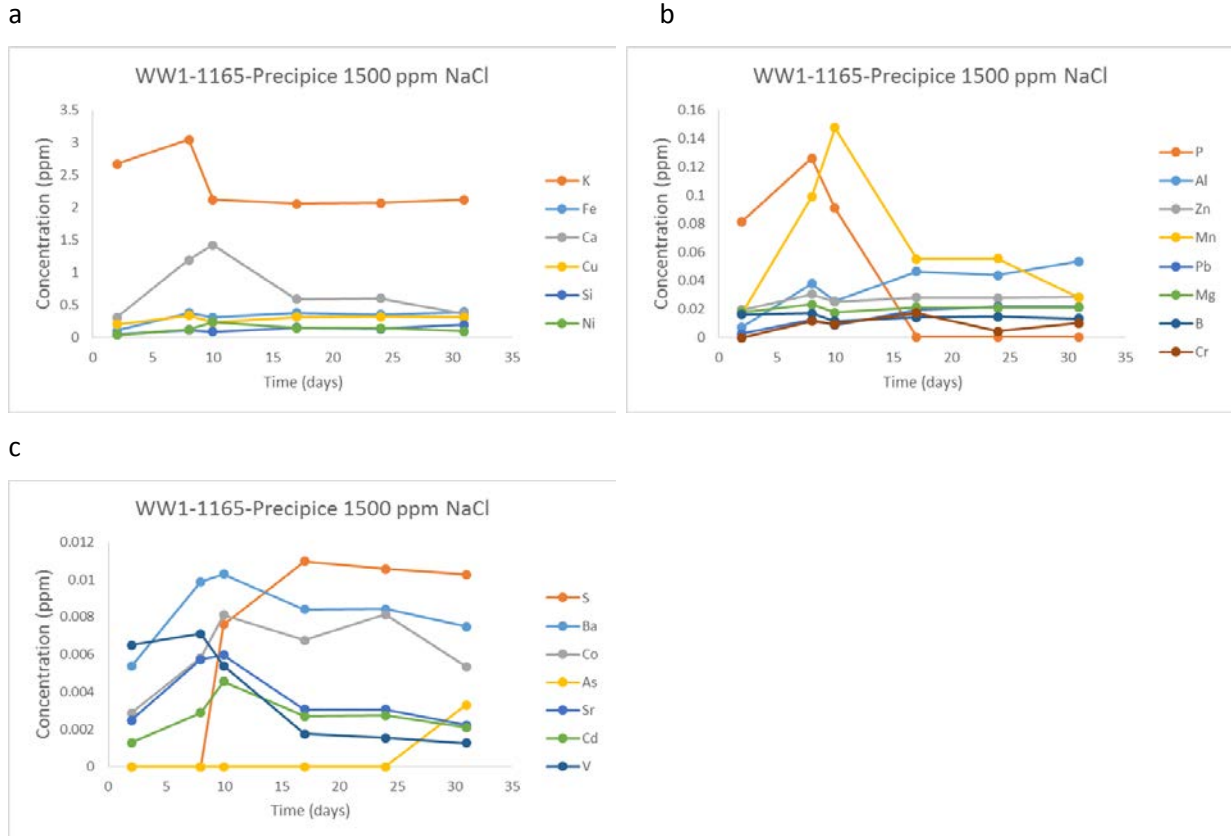


Figure 4.3-1: WW1 Upper Precipice incremental water chemistry results for batch reactor experiment.

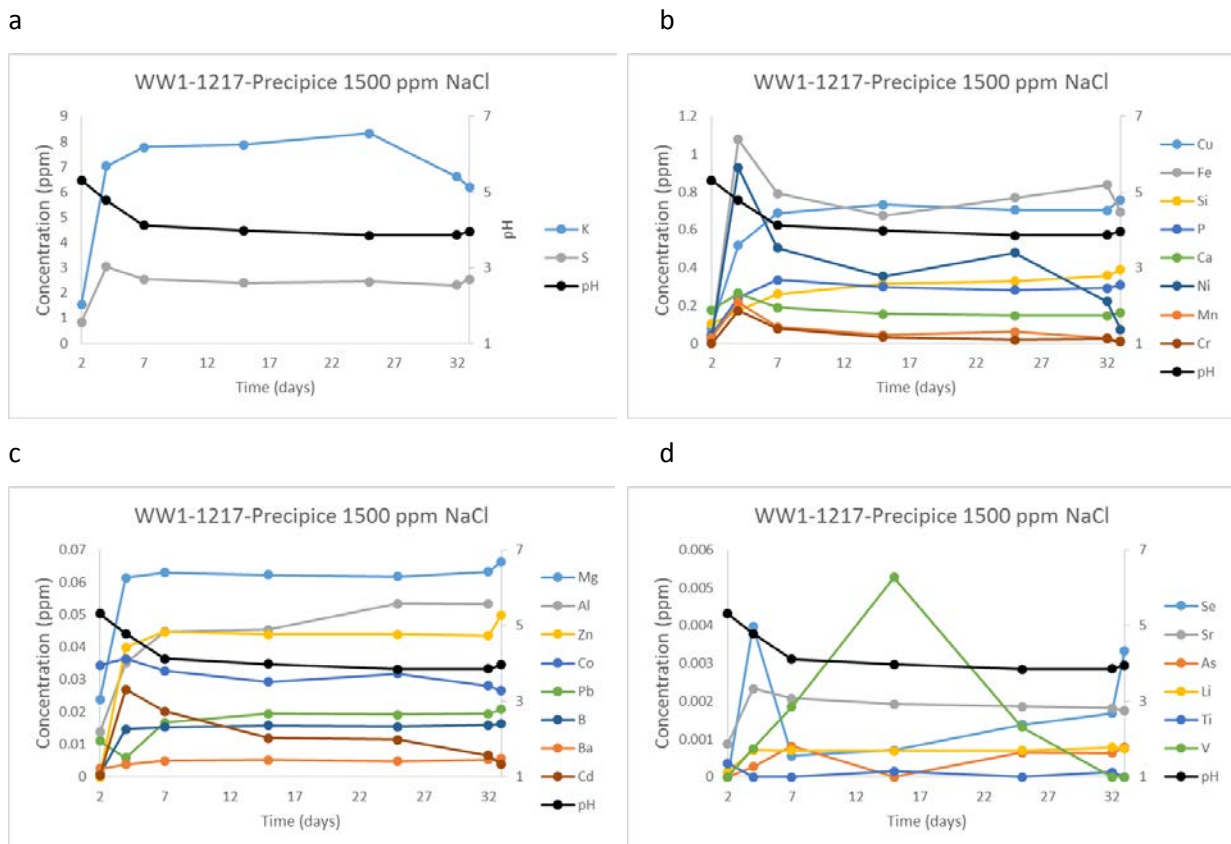


Figure 4.3-2: WW1 Lower Precipice incremental water chemistry results for batch reactor experiment.

Geochemical and Geomechanical Testing of Near Wellbore CO₂ Injectivity Improvement

The most significant elements aside from Na were K and S. These likely came from dissolution of the sulphate salts observed during characterisation of the samples. The concentration of elements such as Cd and Ni increased following CO₂ addition to the system but then decreased over time, implying that these were either initially released through surface desorption and subsequently reabsorbed or were from trace mineral dissolution and then precipitated, or were residual contamination. Anomalous V and Se trace element concentrations were likely artefacts caused by these being at levels close to the detection limit of the experiments.

The freshwater Chinchilla 4 Precipice experiment showed similar element mobilisation to that of the WW1 Upper Precipice experiment in 1500 ppm NaCl (Figure 4.3-3). A notable difference was the lack of K detected in the Chin-4 experiment and also the lower dissolved S content. Possibly there was simply a lower quantity of sulphate salts within this sample, but otherwise the mineralogy was broadly similar to that of the WW1 Upper Precipice, which is reflected by the similar major, minor, and trace element mobilisation observed.

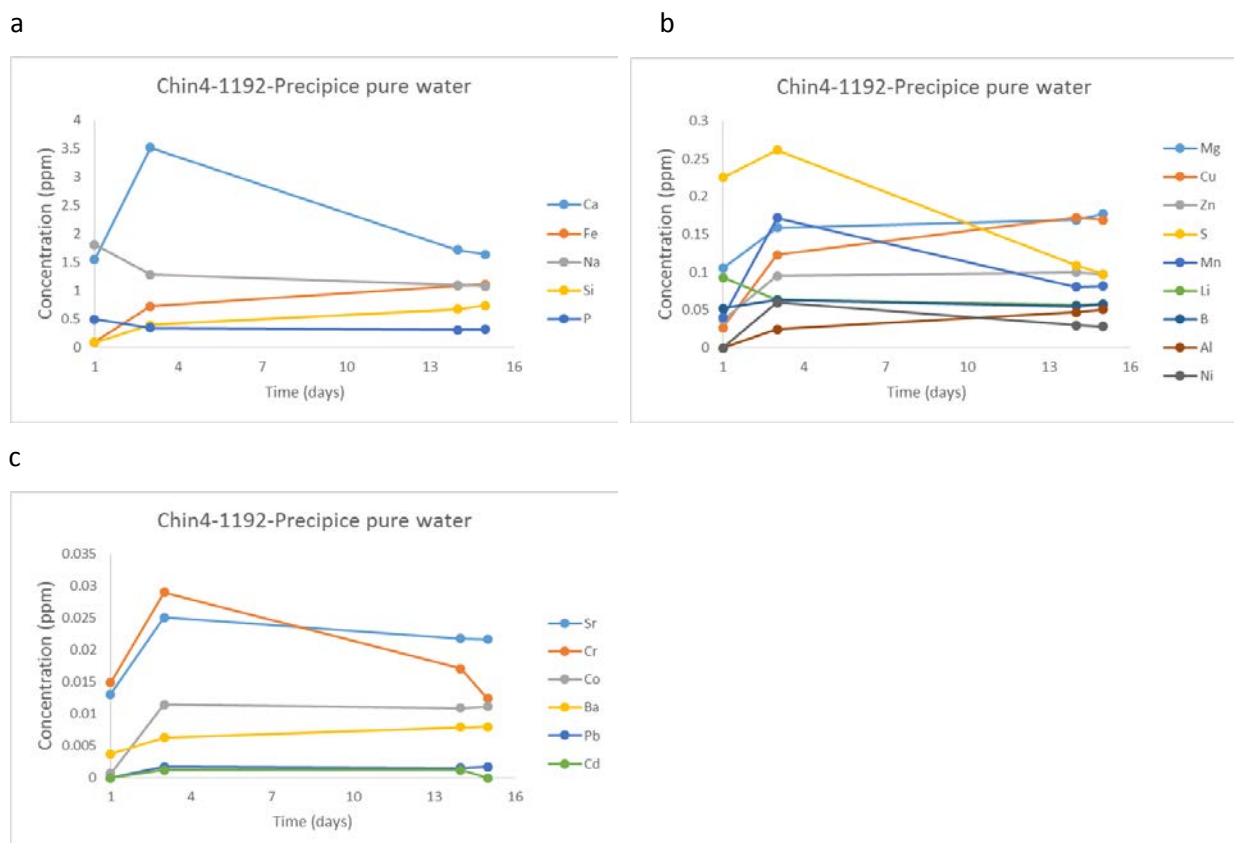


Figure 4.3-3: Chinchilla 4 Upper Precipice incremental water chemistry results for batch reactor experiment.

4.3.2. Evergreen Formation

The 981 m Evergreen WW1 sample showed slightly higher element mobilisation to solution than observed for the Precipice experiments (Figure 4.3-4). A notable difference was that carbonate dissolution likely played a greater role for this sample, given that Ca, Fe, Mg, and Mn concentrations

Geochemical and Geomechanical Testing of Near Wellbore CO₂ Injectivity Improvement

all increase and track each other over the course of the experiment, and carbonates with this composition were observed within the sample. Dissolved Si was also higher relative to the Precipice experiments, reflecting the fact that the Evergreen Formation contains a much greater quantity of reactive aluminosilicate minerals such as chlorite relative to the Precipice. This rock sample was far less permeable and had lower porosity than the Precipice samples. Hence a lower surface area of this “seal” interlaminated siltstone-sandstone material likely interacted with the reaction fluid relative to the more accessible quartzose sandstones of the underlying reservoir unit. Solution pH remained ~ 5, higher than in the Precipice experiments due to carbonate dissolution and buffering.

The WW1 Evergreen lithic sandstone sample (WW1-1043-Evergreen) was more reactive to CO₂-brine than the seal unit sample, likely due to larger grain size and greater accessibility to the minerals for reaction fluids. The increases in dissolved Ca, Mg, Mn, Fe, Sr, and Ba over time (Figure 4.3-5) are all likely due to carbonate dissolution. Ca and Mg concentrations were higher than from the WW1-981-Evergreen sample, reflecting the higher carbonate content, and also labradorite feldspar content. Accessory elements such as copper and zinc may have come from dissolution of trace minerals such as chalcopyrite and sphalerite, which were observed during SEM characterisation of some but not all samples. The reduction in dissolved Ni was likely an artefact, e.g. residual contamination gradually being removed over time. Solution pH remained ~ 5 during the experiment.

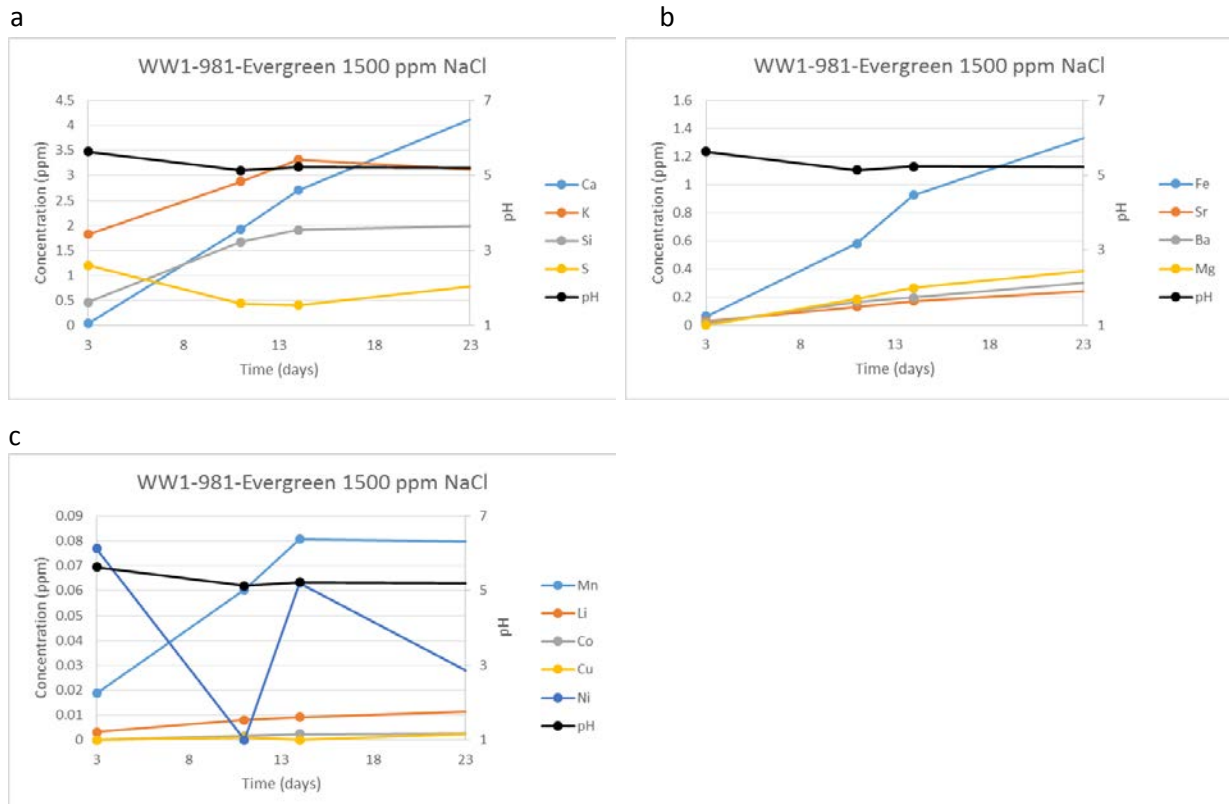


Figure 4.3-4: WW1 Upper Evergreen incremental water chemistry results for batch reactor experiment.

Geochemical and Geomechanical Testing of Near Wellbore CO₂ Injectivity Improvement

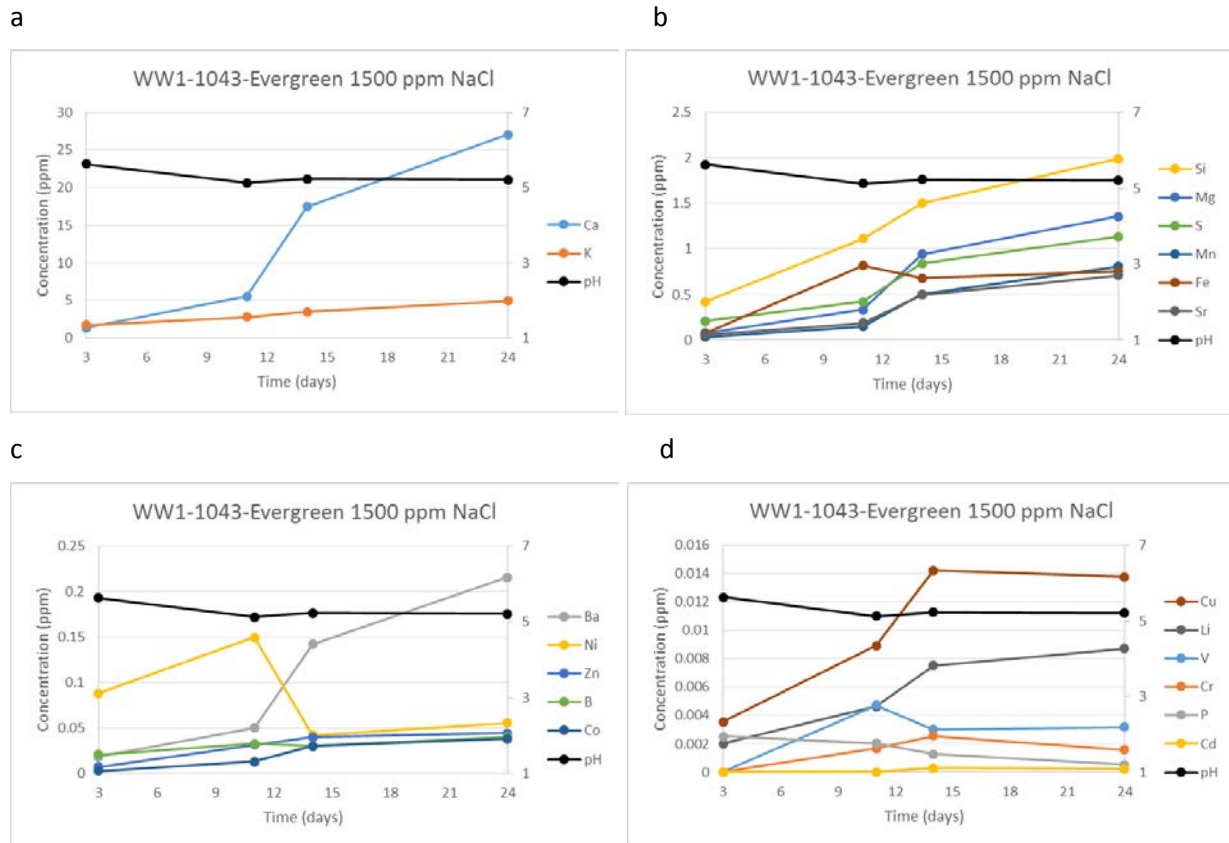


Figure 4.3-5: WW1 Lower Evergreen lithic sandstone incremental water chemistry results for batch reactor experiment.

The calcite cemented Lower Evergreen sandstone sample (WW1-1056-Evergreen) had a different response to CO₂-brine reaction relative to the other Evergreen samples (Figure 4.3-6). A high concentration of Ca up to ~1000 ppm in solution reflected calcite cement dissolution. The solution pH was also significantly buffered to ~ pH 6. Acid activated silicate dissolution was lower owing to the pH buffering, hence low concentrations of dissolved Fe and Si. The concentrations of several dissolved elements decreased following addition of CO₂ to the system, implying rapid precipitation/pacification of the sample surface due to initial rapid dissolution of calcite cement. The spike in dissolved element concentrations at the end of the experiment may reflect potential exposure of fresh surface for reaction due to removal of calcite cement.

The range and concentration of elements mobilised during the Chinchilla 4 Evergreen experiments was broadly similar to that of the WW1 samples, with any slight differences being a reflection of the different masses of individual minerals that varied between samples (Figure 4.3-7 and Figure 4.3-8). For the 1% KCl experiment it is possible that there was some contribution of elements such as Ni to the reaction water due to corrosion of batch reactor material (Figure 4.3-7). As for WW1 samples, S was a major component of the element mobilisation, indicating that sulphate salts were common for the formations sampled from both boreholes.

Geochemical and Geomechanical Testing of Near Wellbore CO₂ Injectivity Improvement

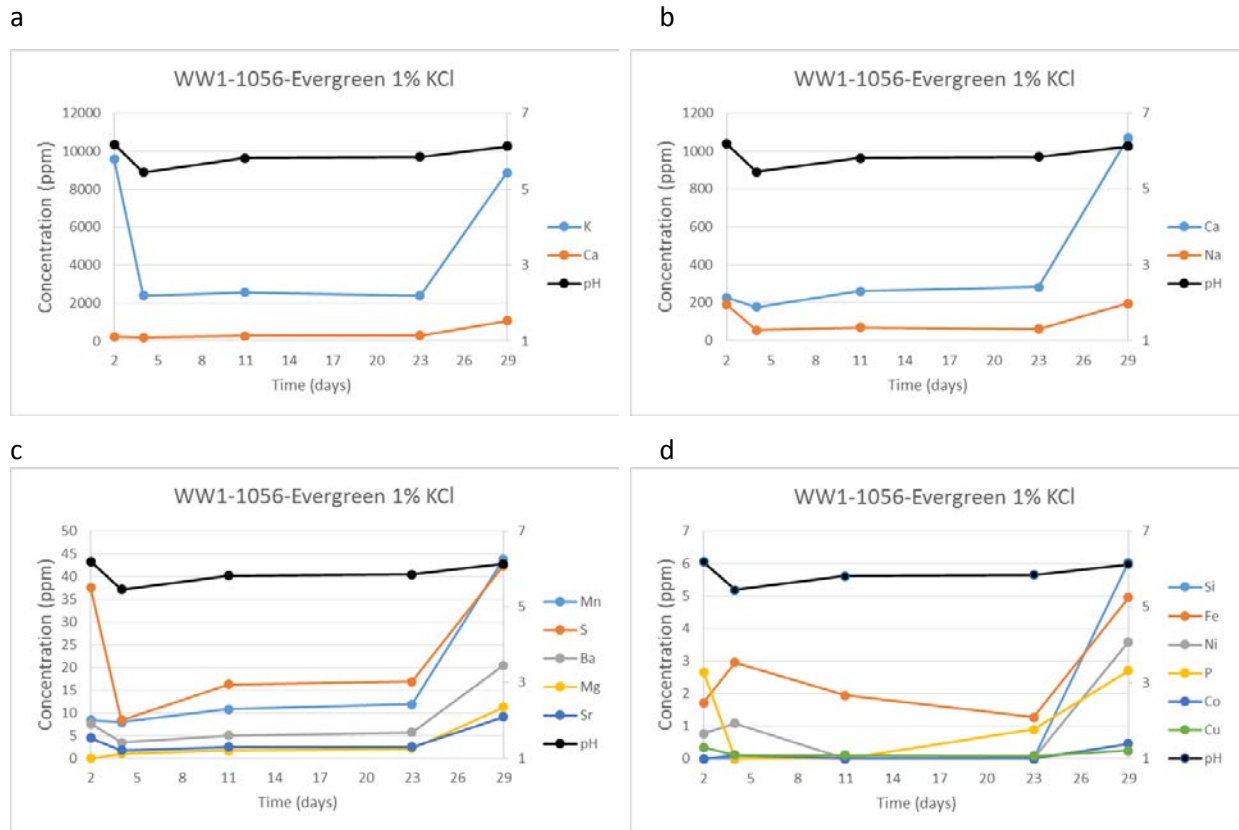


Figure 4.3-6: WW1 calcite cemented Lower Evergreen sandstone incremental water chemistry results for batch reactor experiment.

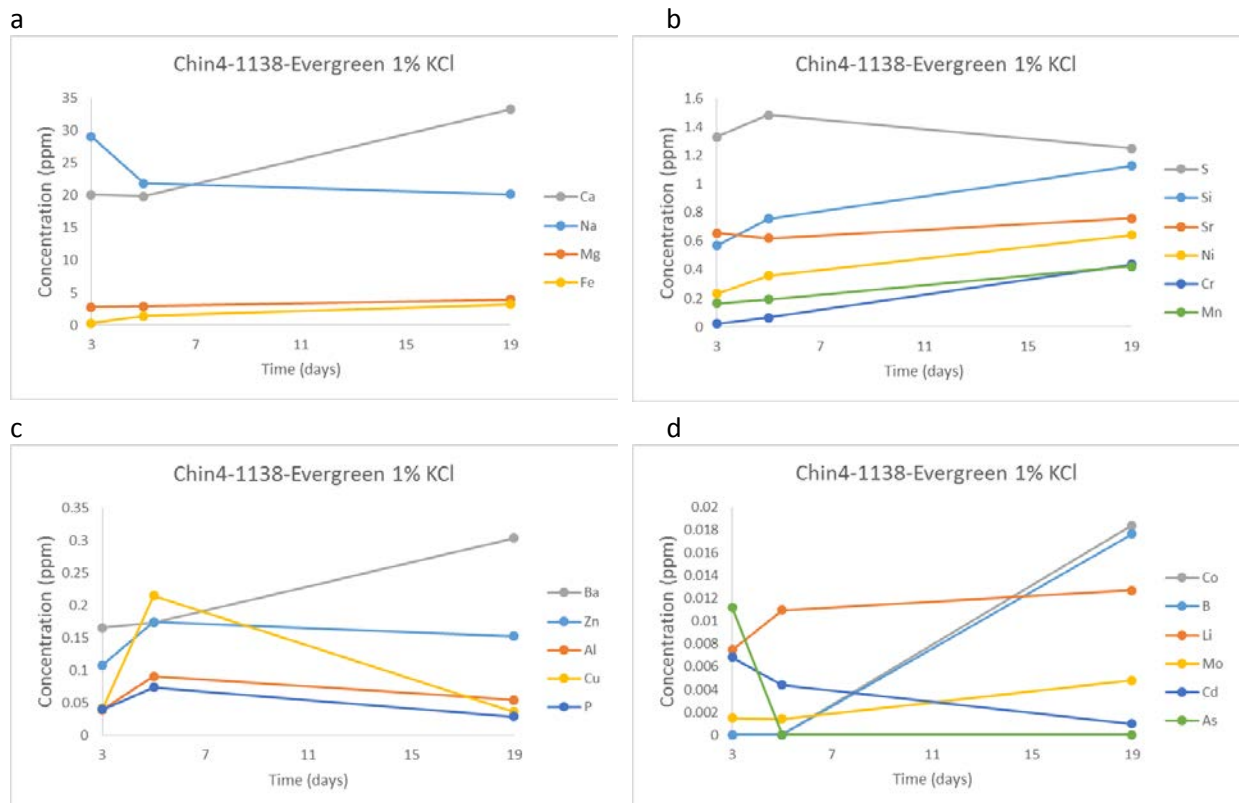


Figure 4.3-7: Chinchilla 4 Lower Evergreen sandstone incremental water chemistry results for batch reactor experiment.

Geochemical and Geomechanical Testing of Near Wellbore CO₂ Injectivity Improvement

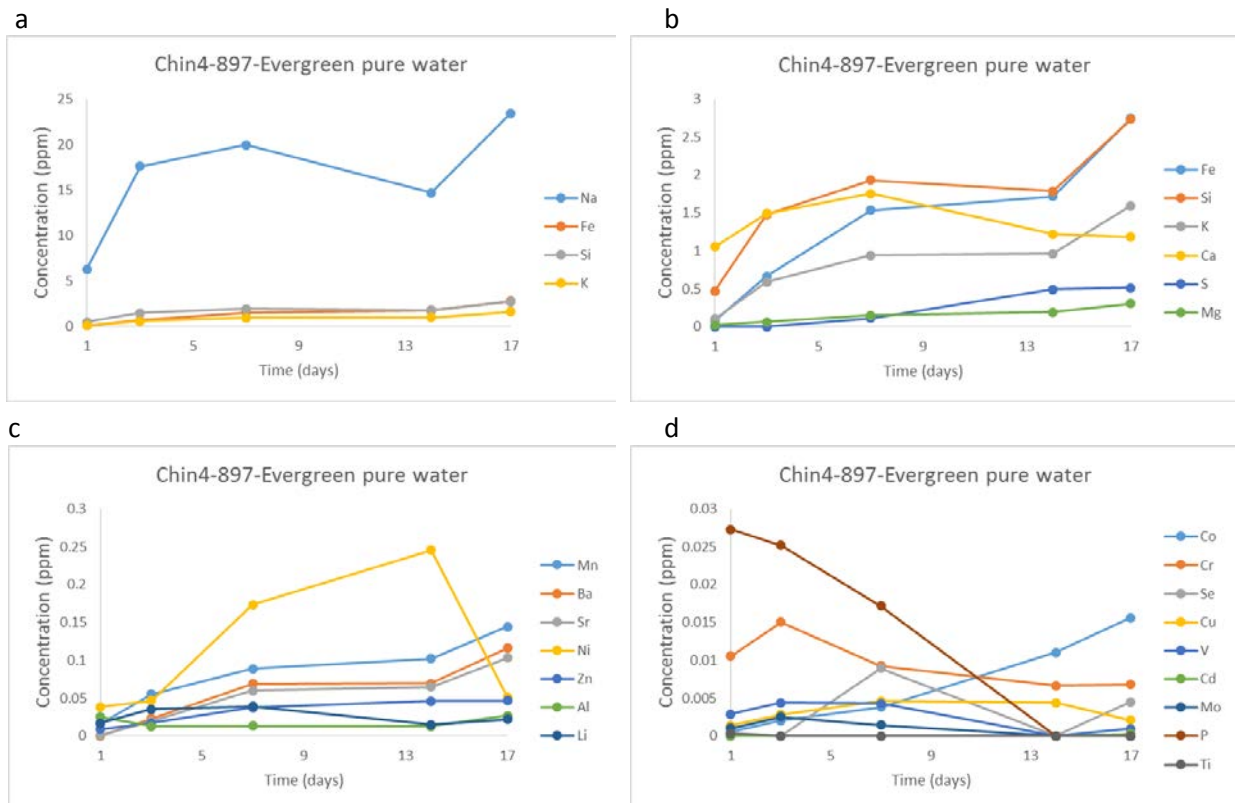


Figure 4.3-8: Chinchilla 4 Upper Evergreen interlaminated siltstone and sandstone sample incremental water chemistry results for batch reactor experiment.

4.3.3. Hutton Sandstone

The calcite cemented WW1 Hutton Sandstone sample experiment had a high concentration of dissolved Ca from calcite dissolution, and subsequently high pH (Figure 4.3-9). Other elements likely incorporated in the calcite (e.g. Mn, Mg, Sr, and Ba) also increased and were generally at relatively high dissolved concentrations. Si and Al concentration were relatively low, reflecting the low silicate dissolution. A spike in the concentrations of dissolved Na, P, Zn, Al, Cr, and Cu occurred at around 10 to 14 days followed by a decrease in these and other elements. These elements may reflect dissolution of minor phases revealed to reactive fluids by calcite cement removal that were then removed from solution via precipitation reactions within the reactor. The slight increase in S over time may have been associated with sulphate salts being sequentially exposed by dissolution of calcite cement during the course of the experiment.

Geochemical and Geomechanical Testing of Near Wellbore CO₂ Injectivity Improvement

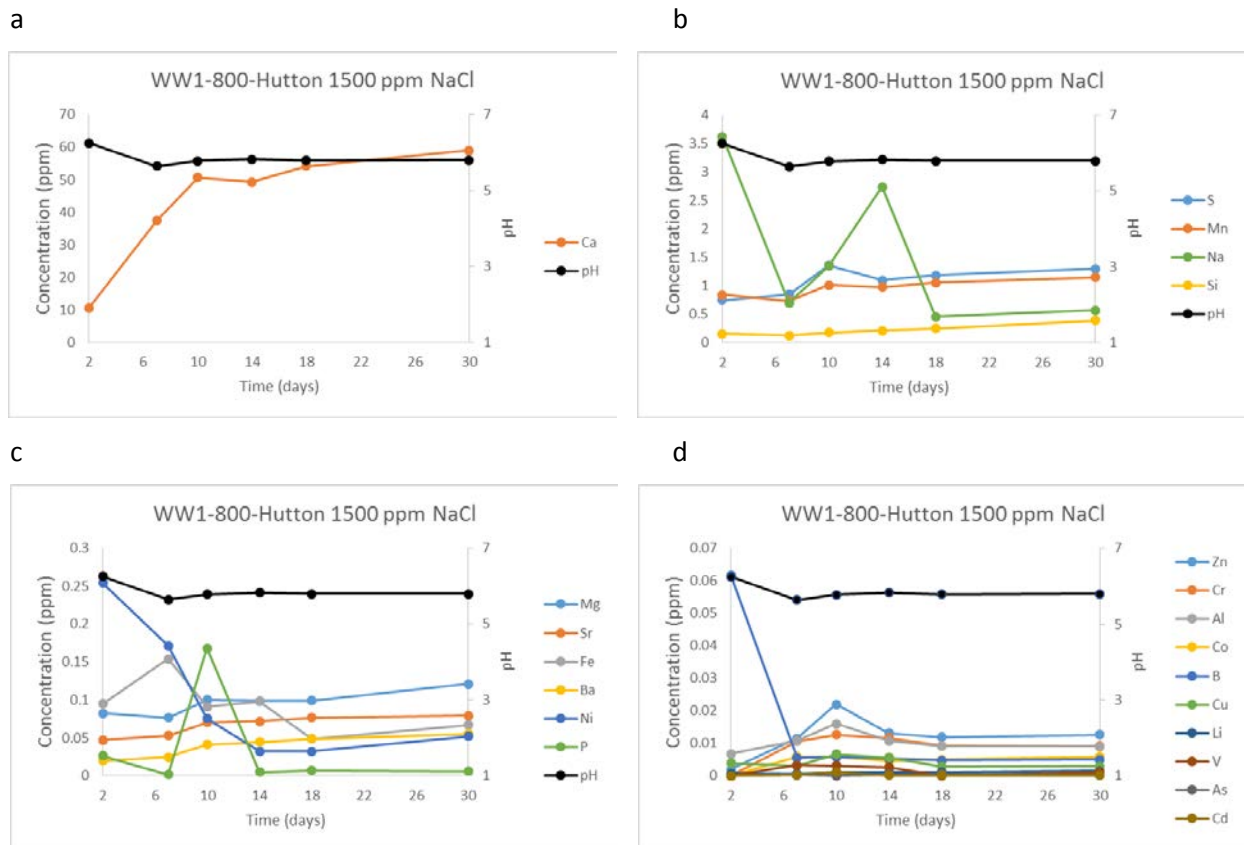


Figure 4.3-9: WW1 calcite cemented Hutton Sandstone sample incremental water chemistry results for batch reactor experiment.

Two Chinchilla 4 Hutton samples were reacted – a calcite cemented quartzose rock similar to the WW1 sample, and a lithic sandstone. The calcite cemented sample showed similar element mobilisation to that observed for the WW1 equivalent sample, though following an initial increase in most dissolved element concentrations these then either decreased or else remained fairly constant for the remainder of the experiment, reflecting pacification of the reactive fluids due to initial rapid carbonate dissolution buffering the pH of the system (Figure 4.3-10). The spike in K concentration at day 16 may have been an experimental artefact.

Zinc mobilisation tracked with Ba, Sr, Mn, Mg, and Fe mobilisation from the lithic Chin-4 Hutton Sandstone, implying that these were mobilised from the Fe-Mg carbonates observed associated with hematite in this sample, though sphalerite could also have contributed given that S was also mobilised (Figure 4.3-11). However, the S mobilisation was not linear and could have been due in part to other potential components such as sulphate salts dissolving. Significant Si was also mobilised too, so trace elements within reactive silicates could also have contributed to the reaction water chemistry.

Geochemical and Geomechanical Testing of Near Wellbore CO₂ Injectivity Improvement

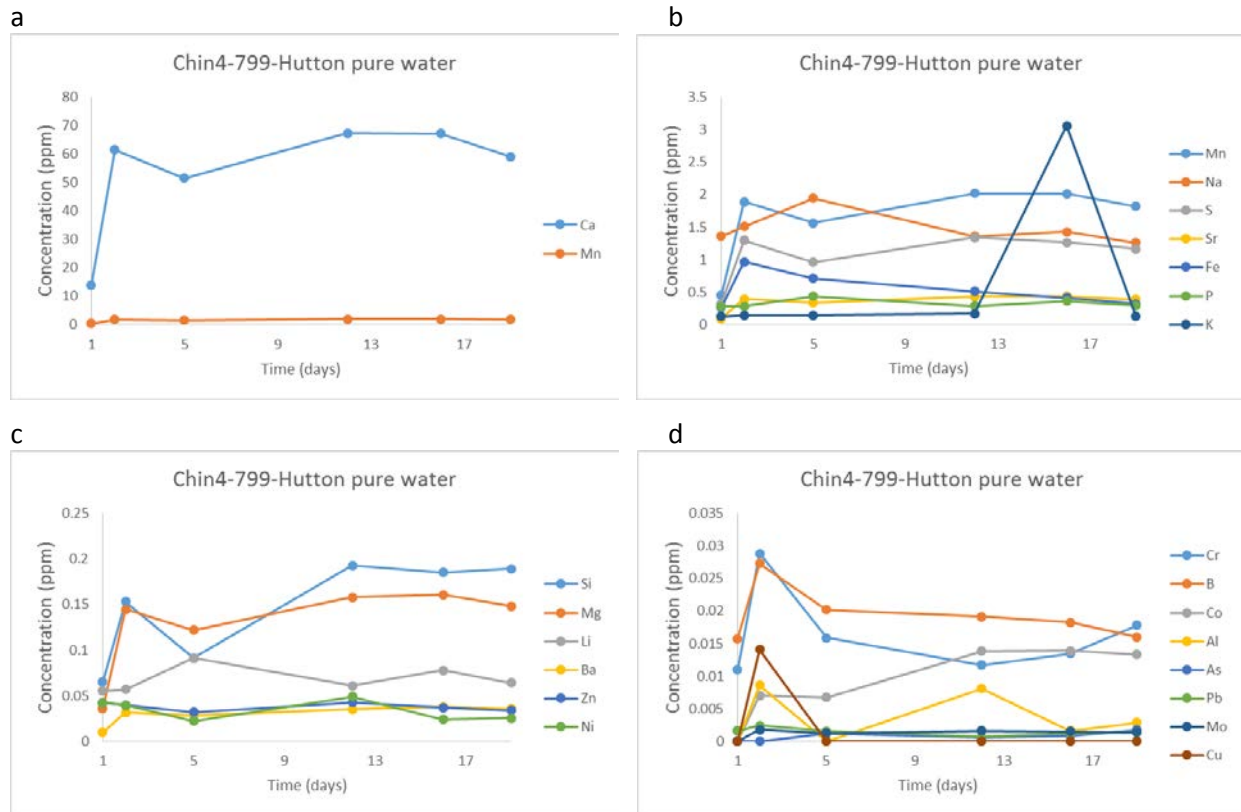


Figure 4.3-10: Chinchilla 4 calcite cemented Hutton Sandstone sample incremental water chemistry results for batch reactor experiment.

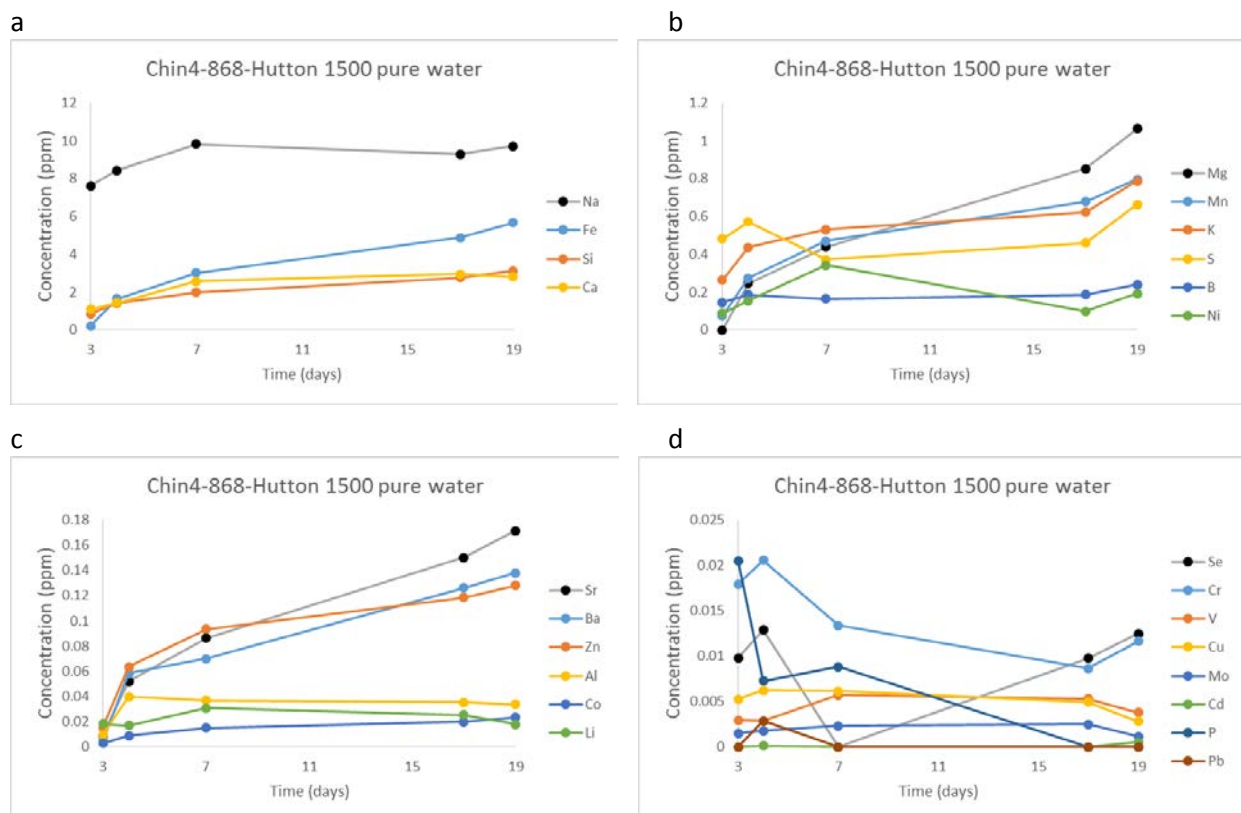


Figure 4.3-11: Chinchilla 4 lithic Hutton Sandstone sample incremental water chemistry results for batch reactor experiment.

4.3.4. Berea Sandstone

The Berea reaction water chemistry mainly reflected dissolution of Ca-Fe-Mg-Mn-carbonate cement from within pores within this quartzose sandstone (Figure 4.3-12). The concentrations of most other dissolved elements remained fairly stable over time, or even decreased in the case of Ni and Cr (Figure 4.3-12c). Al was detected, whereas Si was below detection limit, which may be indicative of incongruent dissolution of a mineral such as chlorite (e.g. Brandt et al., 2003).

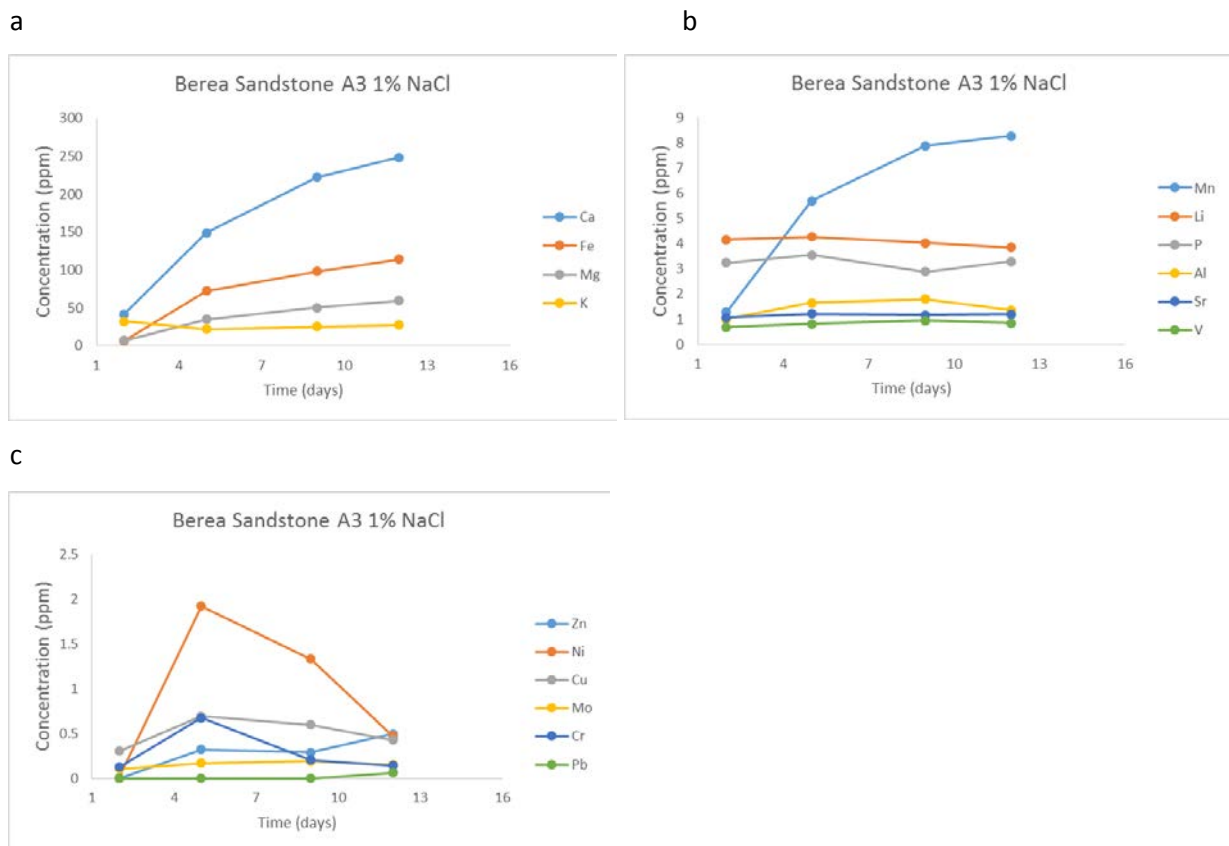


Figure 4.3-12: Berea Sandstone sample incremental water chemistry results for batch reactor experiment.

4.4. Continuous Flow Reactor Water Chemistry Results

4.4.1. Precipice Sandstone

Sample WW1-1211-Precipice was initially soaked for ~ 12 h in 500 mL of 1.5 g/L KCl solution pressurized with supercritical CO₂ at 12 MPa and 60 °C. A high concentration of aqueous sulphur was detected in the first fluid sample taken the following morning (Figure 4.4-1a), which corresponds to the sulphur minerals observed during SEM-EDS surveys of both offcuts and related Precipice Sandstone core samples. The initial flow rate of 2 L/day increased to 3 L/day on the second day, and then 4 L/day by the end of day three. Flow rates for each successive day were at least 4 L/day. The increase of most aqueous element concentrations in the fluid sample taken at the end of day 8 (198.5 hrs), relative to the preceding downwards trend for most elements, coincided with a spike in fluid discharge earlier in the day that resulted in depletion of the water reservoir. This would have

left water-saturated supercritical CO₂ in contact with the sample for a short time prior to replenishment of the water reservoir– this type of fluid has been shown in the literature to be highly corrosive (Choi et al., 2010; Choi et al., 2013; Shao et al., 2011). Alternatively, the residence time of CO₂-saturated water in contact with the sample during the few hours that the system was shut-in during replenishment of the equilibrium between water-gas reservoir and sample vessel could have been a factor. This would have been similar to having taken a sample first thing in the morning following a night of the sample batch reacting.

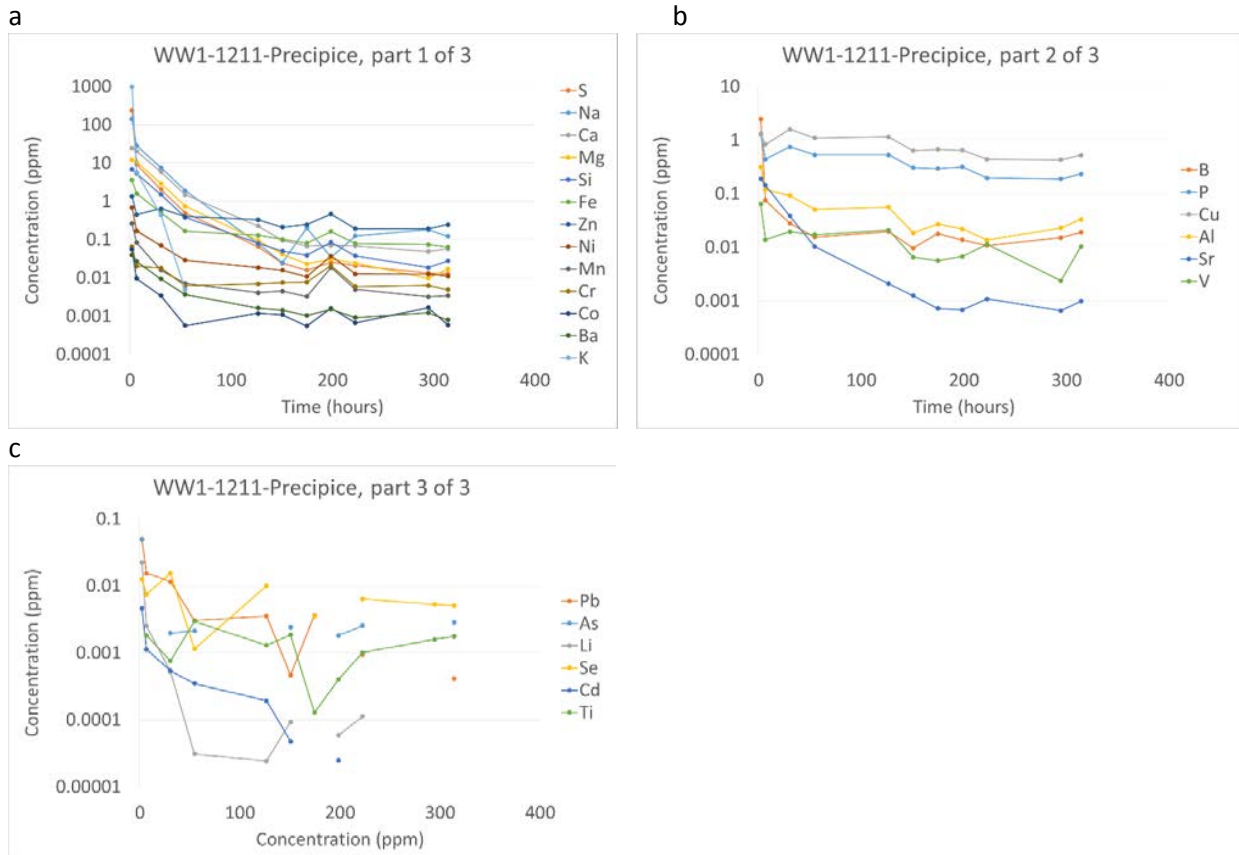


Figure 4.4-1: WW1-1211-Precipice incremental chemistry results for continuous flow reactor experiment.

4.4.2. Evergreen Formation

During pre-reaction testing, sample WW1-1056-Evergreen was found to be almost impermeable due to a combination of carbonate cement and reactive clay matrix. The smectite and other potential swelling species (possibly vermiculite) likely contributed to a NaCl brine permeability test sample disintegrating. Therefore KCl solutions were used during subsequent tests with WC9, initially 1% w/v but after further testing the salt concentration was reduced to 1.5 g/L KCl that was used during the 40 mm cube continuous flow experiment. Prior to closing the sample vessel, 500 mL of KCl solution was added to the head of the vessel early Thursday afternoon, and the system filled with CO₂ at 12 MPa and 60 °C. By the end of the work day, no water had been released from the system outlet

and so the system was shut-in and left static overnight. Upon opening the outlet tap Friday morning, reddish brown water (Figure 4.4-2) immediately discharged at a high rate of flow. This implied that sufficient carbonate cement had been dissolved throughout the entire sample overnight for liquid to now be freely able to pass through the sample, as supported by the high concentration of dissolved Ca within the first incremental water sample taken (Figure 4.4-3a), whereas no water had leaked out the open bottom of the sample vessel upon initial filling. Successive samples taken during the day had progressively higher water clarity, though this was mainly due to the fact that the flow rate initially increased over time with corresponding reduction of water-sample contact residence time. Maximum flow rate occurred during the middle of the day, which corresponds to a trough in the trend of aqueous element concentration through time; the concentrations increased again as the flow rate diminished towards the end of the day. The behaviour of the sample during the next day helps to explain why flow rate diminished.

After being shut-in overnight, the sample discharged a much smaller volume of water in comparison to the previous day even with the outlet tap fully open; 0.8 L/day as opposed to 3L/day initially. This was interpreted to be a consequence of fresh water having replaced the original KCl solution within the sample and causing cation-exchange to occur with the swelling clays in the matrix. Combined with sample dissolution during batch reaction overnight this resulted in significant fines-inhibition of permeability. The concentration of most aqueous elements apparently remained static between the fluid sampling done Thursday and Friday afternoons.

By the end of the second day, the flow rate had reduced to near-zero through the sample, and so the decision was made to interrupt the experiment and add fresh 1.5 g/L KCl solution to the head of the sampling vessel and leave that shut-in pressurized with CO₂ over the weekend to see if the sample permeability could be recovered. Monday morning reddish-brown liquid discharged at a high rate of flow from the reactor outlet just as it had done when flow had first been initialised for this experiment. The concentration of most aqueous elements within the fluid sample taken first thing Monday was also of the same order of magnitude as the first sample taken days previously, but by the afternoon the concentrations of most dissolved elements had decreased again. Exceptions to these were the concentration of aqueous Si, S, Mg, and B (Figure 4.4-3b), all of which increased during the day in spite of 3 L of water having been flushed through the rock. Most of water passed through this sample was quite clear, excepting the initial fluid samples.

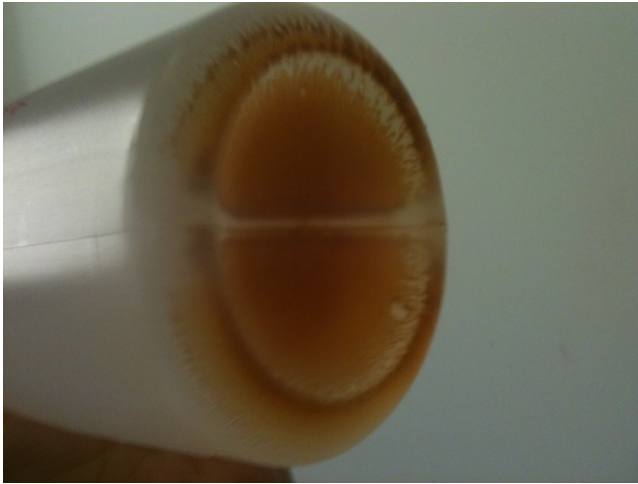


Figure 4.4-2: WW1-1056-Evergreen; reddish-brown colloidal material settling-out shortly after fluid sampling.

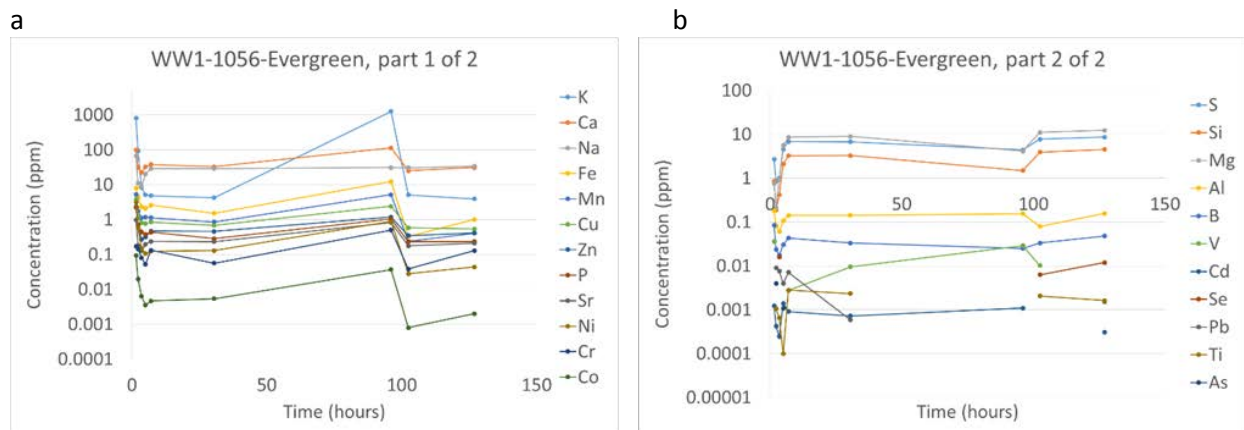


Figure 4.4-3: Incremental water chemistry for continuous flow reactor experiment with calcite cemented WW1-1056-Evergreen.

A technical problem with the CO₂ pump resulted in no fluid flow during the next day. The water ran clear at a high rate of flow on the next morning though, in spite of the sample having been sat batch reacting in pure water for over a day. This suggested that the majority of the easily reacted and accessible material within the sample had been removed or pacified. After 3L of high clarity water having been flowed through the outlet, it was decided to terminate the experiment so that the interior of the sampling vessel and the condition of the sample itself could be inspected.

Whilst the hot glue had partially foamed, the gasket was still firmly in place and well-sealed between the heat-shrink wrapped sample and the edges of the sampling vessel (Figure 4.4-4). Therefore it is unlikely that fluid bypass had been taking place. The sample itself was extremely friable with part of one end crumbling into sand as the inner part of the sampling vessel was removed from the reaction chamber. After drying with the heat-shrink left in place to preserve sample integrity as much as possible, stressed sample N₂ permeability was measured for the sample and this showed an increase of several orders of magnitude compared with pre-reaction testing (see Section 4.5.2.2).

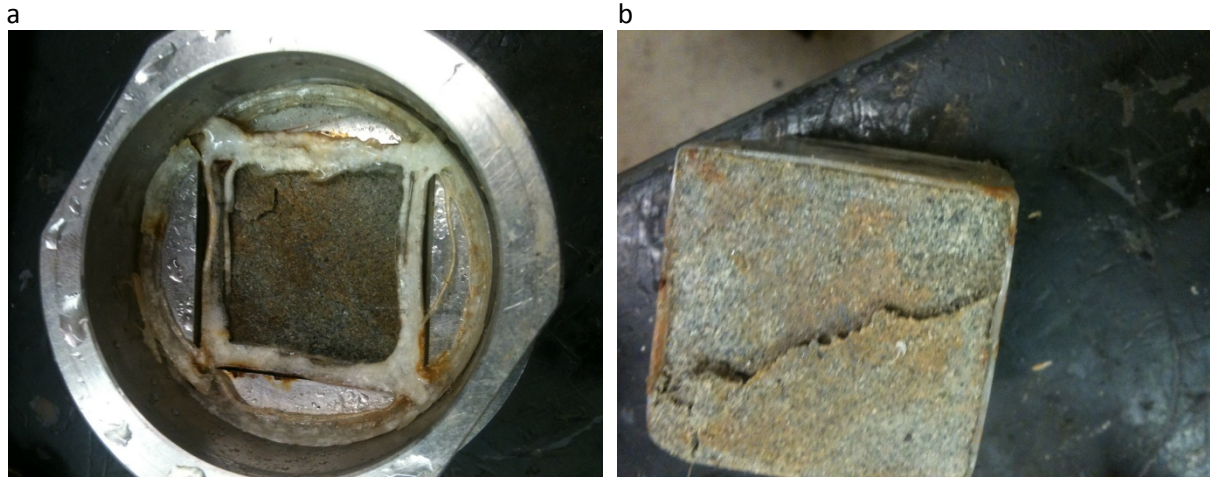


Figure 4.4-4: a) Hot glue injected into the joints between the sample and the sample holder insert foamed in response to exposure to supercritical CO₂ increasing the seal efficiency; b) the heat-shrink wrap around the sample remained firmly in place during the experiment, with the sample largely intact apart from a small sliver of rock that split off the base during removal from the chamber.

4.4.3. Berea Sandstone

The first sample used to test operation of the continuous flow reactor system was cube Berea B1. Initial outlet flow rate was ~ 0.5 L per day at maximum inlet flow rate and outlet tap openness, which increased to 1.2 L/day during the third day of operation and then afterwards increased to greater than ~ 4 L/day, at which point the outlet tap was restricted to 4 L/day. Approximately 25.5 L water in total was flowed through this sample.

The first fluid samples taken rapidly oxidised leading to significant colloidal iron precipitation, with sampled fluid progressively attaining higher clarity over successive days as the quantity of iron and other cations mobilised from the sample was reduced. Qualitatively, improved sample clarity correlated with progressive increase of the outlet fluid flow rate achieved. Once samples had been acidified with nitric acid pending ICP-OES analysis, all visible colloidal material went back into solution.

The reason why the concentrations of the aqueous elements within the final sample taken were much higher than previous days' samples (Figure 4.4-5) was due to a combination of the reactor having been shut-in over the weekend and the fact that the sample was taken in the morning at the commencement of fluid flow out of the reactor. In hindsight it would have been more consistent to always sample at the same time of day. The transient increase in the concentrations of Mn, Si, Al, Se, Cr, Ni, and Li at 342 hours before a return to the overall downward trend in concentrations over time was possibly due to a new fluid flow pathway having opened through the sample, allowing fresh reaction of material at that time.

Geochemical and Geomechanical Testing of Near Wellbore CO₂ Injectivity Improvement

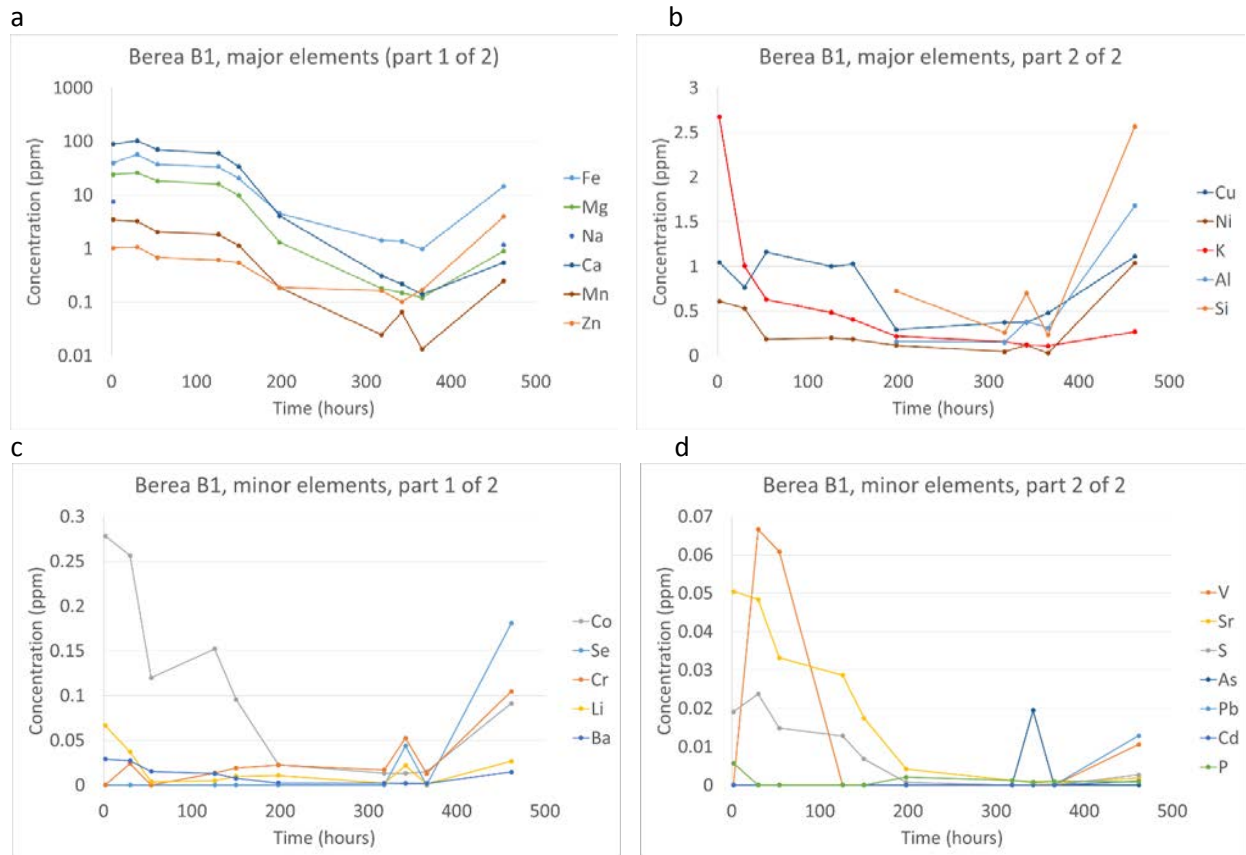


Figure 4.4-5: Major (a, b) and minor (c, d) elements measured within incremental fluid samples for the continuous flow reaction of Berea Sandstone sample B1.

4.5. Porosity and Permeability Results

4.5.1. Porosity

Porosity of sister samples pre- and post-carbonic acid reaction were tested using Hg intrusion (Table 4.5-1). Although sister samples were used for comparative purposes, the heterogeneous nature of especially the coarser-grained samples means that an undefined proportion of any difference in porosity would be due to natural pore size distribution variation between samples. The reason that the porosity test could not be performed upon the exact same sample before and after reaction is because it is a destructive test. Nevertheless, any apparent increase in porosity due to the reactor experiments performed may be expected to lead to a corresponding increase in permeability as additional space is open for flow (Table 4.5-1). A common model applied for the void-permeability relationship utilises the following equation:

$$k_1/k_{ref} = (\phi_1/\phi_{ref})^3 \quad (4.5-1)$$

Where k is the permeability and ϕ is the porosity.

Predicted porosity changes due to geochemical reactions were also able to be calculated using the results of available GWB modelling coupled with the mass and porosity of offcuts of selected samples.

Geochemical and Geomechanical Testing of Near Wellbore CO₂ Injectivity Improvement

Table 4.5-1: Porosity of sister samples pre- and post- reaction tested using Hg-intrusion.

Sample	Unreacted sample porosity (%)	Reacted sample porosity (%)		Predicted permeability improvement (eq. 4.5-1) based upon predicted (p) and measured (m) reacted block porosity ¹ relative to unreacted sister sample
		Predicted (based on section 6.1)	Measured (sister sample of unreacted block ¹)	
Berea B2	20.6		20.9	4.4% (m)
Chin4-1192-Precipice	15.2	-	14.9	-
Chin4-1138-Evergreen	8.8	-	9.3	18% (m)
Chin4-897-Evergreen	6.1	-	6.8	39% (m)
Chin4-868-Hutton	7.9	-	11.9	242% (m)
Chin4-799-Hutton	10.1	-	8.4	-
WW1-1217-Precipice (WC14)	22.0	22.16	23.2	1.9% (p), 41% (m)
WW1-1211-Precipice (WC20)	20.3	-	21.4	16.9% (m)
WW1-1165-Precipice (WC11)	18.5	18.77	21.9	4.1% (p), 66% (m)
WW1-1056-Evergreen (WC9)	8.2	14.61	7.93	473% (p), -9.6% (m)
WW1-1043-Evergreen (WC8)	5.5	6.28	9.3	52% (p), 383% (m)
WW1-981-Evergreen (WC3)	8.4	8.52	9.94	5.7% (p), 65.7% (m)
WW1-800-Hutton (WC15)	6.7	8.87	7.98	137% (p), 69.2% (m)

¹Given that sister samples were used for the destructive Hg-porosimetry tests, differences in total porosity results obtained (and discrepancies between predicted and measured post-reaction porosity) could be due to natural geological sample heterogeneity as opposed to simply being due to mineral dissolution/precipitation reactions. Similarly, calculated permeability improvement based upon difference between reacted and unreacted block porosity assumes that any apparent increase in sample porosity is due to mineral dissolution as opposed to natural sample variability.

There is some variation between the modelled predicted porosity change and the differences between measured reacted and unreacted porosities, as expected. However, the model used to calculate permeability change on the basis of porosity change provided a very large difference in results for modelled versus measured porosity differences. The predicted permeabilities calculated using the modelled porosity changes for West Wandoan 1 are probably the most realistic; for example, an increase in permeability was measured for the reacted calcite cemented WW1 Evergreen sample whereas the porosity of the reacted block was less than the unreacted block, which resulted in a prediction of permeability reduction due to the geochemical reactor experiments that is not the case (see next section). Sample heterogeneity reflecting the use of sister samples is a significant factor in the reacted versus unreacted porosity results.

4.5.2. Permeability

Permeability experiments were conducted on a variety of samples (WW1 and Berea; 15 and 40 mm cubes) to test sensitivity to fluid (gas, liquid), stress and the extent of anisotropy. The directional permeability results are reported as illustrated in Figure 2.5-1: in the bedding plane in two orthogonal directions, and perpendicular to the bedding plane (“vertical” orientation). The batch reacted 15 mm cubes had N₂ permeability measured for all three face orientations (e.g. Table 4.5-2 and Table 4.5-3), with brine permeability only measured for the vertical orientation so as to limit the influence of intra-sample fines transport upon the result. Furthermore, flow through bedding plane layer boundaries was likely to be most affected by the geochemical reactor experiments due to the presence of potentially chemically and/or physically reactive barrier elements being more commonly encountered by “vertical” fluid flow.

Table 4.5-2: Unstressed WW1 15 mm samples N₂ permeability pre and post reaction (mD)¹.

Sample	“Vertical”		Change	“Horizontal” 1		Change	“Horizontal” 2		Change
	Pre	Post		Pre	Post		Pre	Post	
WW1-1217-Precipice	168.3	236.6	+68.3 (40.6%)	245.8	233	-12.8 (-5.2%)	201.2	268.2	+67 (33.3%)
WW1-1211-Precipice	1481 ²	1452 ²	-29 (-2.0%)	-	-		-	-	
WW1-1165-Precipice	642.4	845.9	+203.5 (31.7%)	1042.3	-		893.6	-	
WW1-1056-Evergreen	0.96	16.9	+15.94 (1660%)	1.28	18.2	+16.92 (1322%)	2.55	11.3	+8.75 (343%)
WW1-1043-Evergreen	0.23	1.62	+1.39 (604%)	0.68	0.36	-0.32 (-47.1%)	0.39	3.19	+2.8 (718%)
WW1-981-Evergreen	1.68	1.28	-0.4 (-23.8%)	-	-		-	-	
WW1-800-Hutton	0.16	16.6	+16.44 (10275%)	0.27	58.2	57.9 (21456%)	0.64	52.7	52.1 (8134%)

¹Permeability measurements were over-range for the Precipice tests omitted from table. Omitted Evergreen tests were for orientations with irregular sample faces due to friability. ²WW1-1211-Precipice permeability tests were at the upper limit of analytical range, and therefore have greater error due to random fluctuations so difference in permeability pre and post experiment could be an experimental artefact.

Table 4.5-3: N₂ permeability (unstressed) of WW1 unreacted Precipice Sandstone samples (mD).

Flow orientation:	WW1-1165- Precipice (15 mm)	WW1-1165- Precipice (40 mm)	WW1-1211- Precipice (15 mm)	WW1-1211- Precipice (40 mm)	WW1-1217- Precipice (15 mm)
Perpendicular to bedding ("vertical")	642.2	624	168.3	202.6	1481
Bedding plane (1)	1042.3	591.1	201.2	240.6	1502
Bedding plane (2)	893.6	N/A (gas bypass)	245.8	244.2	1540.6

For the purpose of interpreting the significance of the results, it is important to keep in mind that small magnitude changes in permeability for the less permeable samples are sufficient to result in huge *percentage changes* in permeability for those samples, whereas the same magnitude change for initially higher permeability samples results in a much smaller *percentage change*. Furthermore, the majority of batch reactor sample dissolution reactions occurred upon the sample surfaces exposed to fluid, and especially given that the surface contacting the base of the reactor chamber tended to show little or no reaction, full penetration of the samples by the reaction fluids was unlikely to have occurred. Thus, the permeability increases observed for batch reacted samples were mainly due to surficial reactions, and possibly greater than would be observed in the field for most samples.

Changes in the physical state of the samples due to the combination of geochemical reactions, fluid-sample physical interactions and experimental procedures could also have influenced results. As the post reaction N₂ permeability was measured after the brine it is possible that this, in addition to sample drying-induced salt precipitation, may have impacted upon the results of N₂ tests for the 15 mm cubes (Tables 4.5-2 and Table 4.5-3). Similarly, as the direction of flow was through the ply of the 40 mm cubes during continuous flow reactor experiments, the post-reaction bedding plane permeability (measured orthogonal to the flow orientation during reactions) may have been deleteriously affected by intra-sample fines mobilisation blocking "horizontal" fluid flow pathways (Table 4.5-3 and Table 4.5-4). Therefore the through-the-ply ("vertical") orientation permeability tests are likely the most directly comparable pre- and post- reaction, which is why this orientation was chosen for the majority of the stressed-permeability tests.

4.5.2.1. Precipice Sandstone

The pre-reaction permeability varied widely both within and between the samples of Precipice Sandstone tested, as expected given the wide grainsize distribution and cross-laminated nature of the material (see Section 3.1). The post-reaction permeability of the 15 mm cube samples generally

Geochemical and Geomechanical Testing of Near Wellbore CO₂ Injectivity Improvement

showed little change. The N₂ permeability of very coarse-grained sample WW1-1211 perpendicular to bedding reduced slightly from 1481 to 1452 mD, but this difference was only a 2% change and so is likely within the error range of the measurement. Similarly, the 1.5 g/L NaCl brine permeability perpendicular to bedding for sample WW1-1165 also decreased slightly from 255.4 mD to 236 mD. In contrast, the 40 mm cube of sample WW1-1211 showed significant increases in permeability post continuous flow reaction (Table 4.5-4).

Table 4.5-4: WW1-1211-Precipice (40 mm) N₂ (unstressed) permeability improvement following reaction.

	Perpendicular to bedding (“vertical”)	Bedding plane (1)	Bedding plane (2)
Pre-exposure	203 mD	241 mD	244 mD
Post exposure	354 mD	337 mD	360 mD
Permeability improvement	74%	40%	48%

Before exposure, the bedding plane permeabilities of 40 mm sample WW1-1211 were quite similar indicating isotropic behaviour in these directions, whereas the vertical permeability was somewhat lower. After flushing, all the permeabilities increased by almost 50%, most significantly in the vertical direction. It is possible that the greater increase in vertical permeability may have been due in part to this being the direction of flow during the continuous flow reactor experiments (see also Section 2.5). Even so, this does not negate the fact that permeability of all three cube orientations was dramatically enhanced for this sample. The sample surface was quite friable due to the lack of bonding between sand grains, especially so post reaction that may have been due to removal of the pore-filling sulphate and minor carbonate. It is possible pore-filling sulfate salts present pre-reaction were in solid form due to sample desiccation but had been totally dissolved within groundwater in-situ. Removal of these salts during the experiments may have caused a greater increase in permeability than would have occurred in-situ due to CO₂-water-rock reactions.

The N₂ gas permeability under stressed conditions was also measured for 40 mm sample WW1-1211 before and after the carbonic acid continuous flow reactor experiment. These stressed permeability measurements were for the vertical direction (through the ply). Changes in permeability in the vertical direction are likely to be the most severely affected by mineral dissolution, and are also the most relevant for seal rock integrity. The pre-reaction permeability is shown in Figure 4.5-1. The permeability declines slightly with stress – as expected, as there is some compression of the void space and consequently less available space for fluid flow.

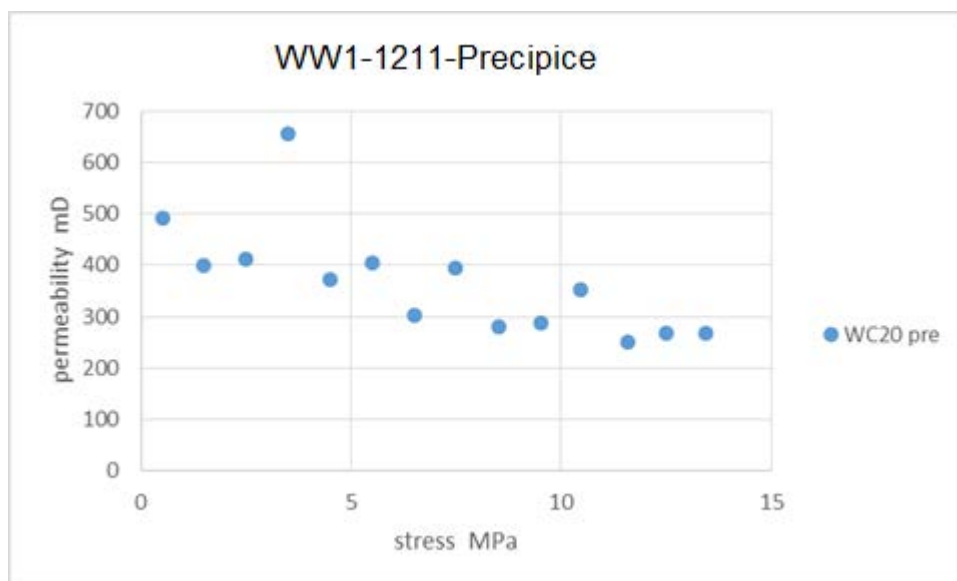


Figure 4.5-1:

Unreacted WW1-1211-Precipice (WC20) permeability vs stress.

4.5.2.2. *Evergreen Formation and Hutton Sandstone*

The pre-reaction unstressed N₂ permeabilities measured for the 15 mm cubes of the WW1 Evergreen Formation samples all ranged from 1 to 2.5 mD. Post-reaction vertical unstressed N₂ permeability was 1.6 mD for the lithic sandstone sample WW1-1043, whereas for the calcite cemented sample WW1-1056 it had increased to 16.9 mD (Table 4.5-2). However, the brine permeability for all Evergreen “seal-rock” samples pre- and post- reaction was effectively zero. Reactive clays and carbonate cement was intimately mixed in sample WW1-1056 that is likely why no water could pass vertically through this sample even following partial removal of the pore-filling cement.

Sample WW1-1043-Evergreen 40 mm cube

The pre-reaction N₂ permeability of the 40 mm sample of WW1-1043-Evergreen was extremely low, being less than 0.003 mD for all three orientations (Table 4.5-5). Transport of CO₂ saturated water could not be sustained through the sample, even with significant pressure driving force in the continuous flow reactor. Therefore, to better gauge the strain response of the sample surfaces to exposure to carbonic acid, the decision was made to remove the sample from the continuous flow reactor and place it into a batch reactor, with thin strips of thermoplastic material propping it up off the base of the reactor so as to allow fluid unhindered access to all cube faces. The unstressed N₂ permeability post reaction was still low at less than 0.3 mD, yet significantly higher than it was beforehand. It is likely that this was due simply to reaction of surficial material along the edges of the sample, as indicated by the results of the X-ray micro-CT plug sample from this interval.

Geochemical and Geomechanical Testing of Near Wellbore CO₂ Injectivity Improvement

Further evidence for the permeability increase being a surficial phenomenon is seen through comparison of the pre- and post- reaction stressed N₂ permeability (Table 4.5-5). Post-reaction, the lowest stressed permeability measurement at 0.5 MPa is twice the pre-reaction value, but after this it drops sharply to being less than half the initial permeability, indicating that any flow pathway/s opened during the unconstrained batch reactor experiment were shut under stressed conditions. The apparent significant increase in porosity for the small batch reacted sister sample relative to an unreacted sample was likely an artefact of sample heterogeneity coupled with the fact that the sample does contain highly reactive phases; however, in order for the minerals to react the acidic fluid must first be able to reach them, which the low inherent permeability of this interval severely limits.

Table 4.5-5: WW1-1043-Evergreen 40 mm cube sample unstressed N₂ permeability (mD)

	Perpendicular to bedding ("vertical")	Bedding plane (1)	Bedding plane (2)
Pre-reaction	0.0012	0.0028	0.0012
Post-reaction	0.036	0.12	0.28
Permeability improvement	30*	43*	233*

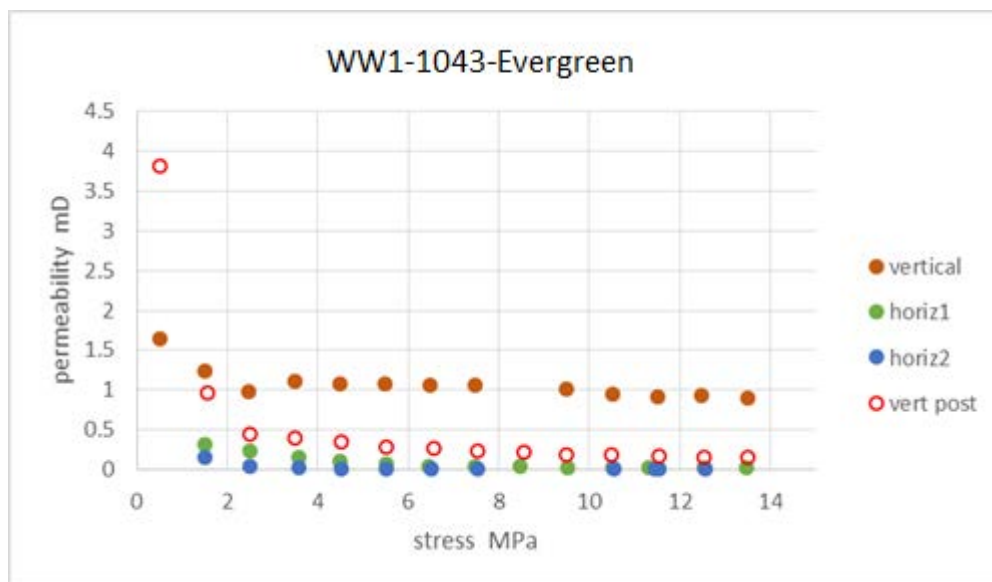


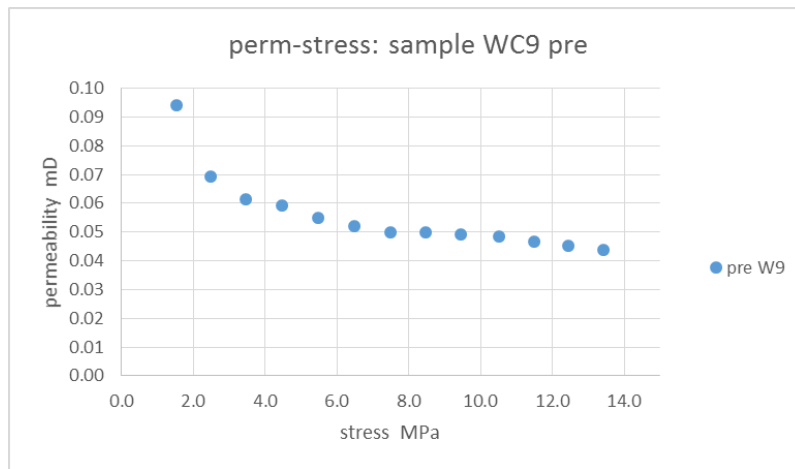
Figure 4.5-2: WW1-1043-Evergreen N₂ permeability vs stress; all three orientations pre-reaction and vertical post reaction.

Sample WW1-1056-Evergreen 40 mm cube

The vertical N₂ permeability in the virgin WW1-1056-Evergreen (WC9) calcite cemented sandstone is very low, being below detection limit for the unstressed test on both the 15 mm and 40 mm cubes,

and less than 0.1 mD for the stressed test (Figure 4.5-3a). The post-reaction permeability of the 15 mm cube was also zero; however, after flushing with the CO₂ saturated water in the continuous reactor, the vertical permeability of the 40 mm cube increased to values consistent with WW1-1211-Precipice (Figure 4.5-3b and Figure 4.5-1). This indicates that the formerly calcite cemented pores, as well as barrier layers of fines that may have been present, were breached. In a separate measurement and using a different apparatus and procedure, the unstressed vertical N₂ perm post reaction was measured at 187mD that was roughly half the low-range stressed permeability value of 300 mD.

a



b

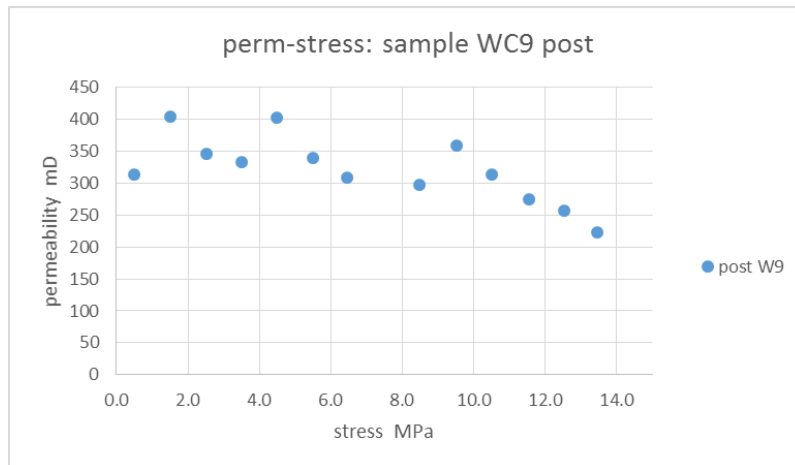


Figure 4.5-3: WW1-1056-Evergreen N₂ permeability vs stress a) pre exposure to scCO₂ saturated water during continuous flow reactor experiment; b) post exposure to scCO₂ saturated water.

4.5.2.3. Berea Sandstone

A number of Berea samples were tested with gas, fresh water and brine under unstressed conditions. These samples were for method development and evaluation purposes and for cross-laboratory comparisons. For a cleaned 15mm cube sample (lightly sonicated in ethanol to remove

surface cutting fines), the unstressed N₂ gas permeabilities were measured as: bedding1: 581mD; bedding2: 594mD and vertical: 533mD. For 40mm cubes, the unstressed N₂ permeabilities are shown in Table 4.5-6. One 15 mm sample was also tested for vertical orientation brine permeability (1%NaCl solution) before and after batch-reaction exposure to CO₂ saturated water at 10MPa and 50C for 360 hours. The results showed a 50% permeability improvement after exposure, probably due to partial dissolution of the patchy pore-filling carbonate cement.

Table 4.5-6: Directional permeability of the 40mm Berea Sandstone cube samples (unstressed, N₂).

Sample name	Bedding Plane Face-pair 1 (mD)	Bedding Plane Face-pair 2 (mD)	Perpendicular to Bedding Plane (mD)	Average (mD)
B1	666	610	404	560
B2	636	592	546	591
B3	728	718	657	701

One sample (B1, 40mm cube) was tested for compressibility (stress-strain response) pre- and post-CO₂ saturated water exposure. After stressing pre-reaction, the vertical permeability was significantly reduced, from 546mD to <100mD (Figure 4.5-4a), suggesting that the sample had undergone some damage during the stressing. This is also shown by the difference in strain behaviour during increasing and decreasing stressing (Figure 4.6-4). It is consequently likely that some fines were formed as a result of crushing and these formed barrier layers and thus reduced permeability (Figure 4.5-4b). The permeability was restored, indeed improved, after exposure to CO₂ saturated water, showing that the fines were subject to acid attack and dissolution and as such probably included particles of the patchy carbonate cement.

The unstressed vertical N₂ permeability similarly increased from 404 to 418 mD, whereas the two bedding plane orientations actually decreased to 458 mD and 434 mD respectively. This may be indicative of fines having been shifted to block some of the horizontal flow pathways during the continuous flow experiment in which the direction of flow was vertically through the bedding layers.

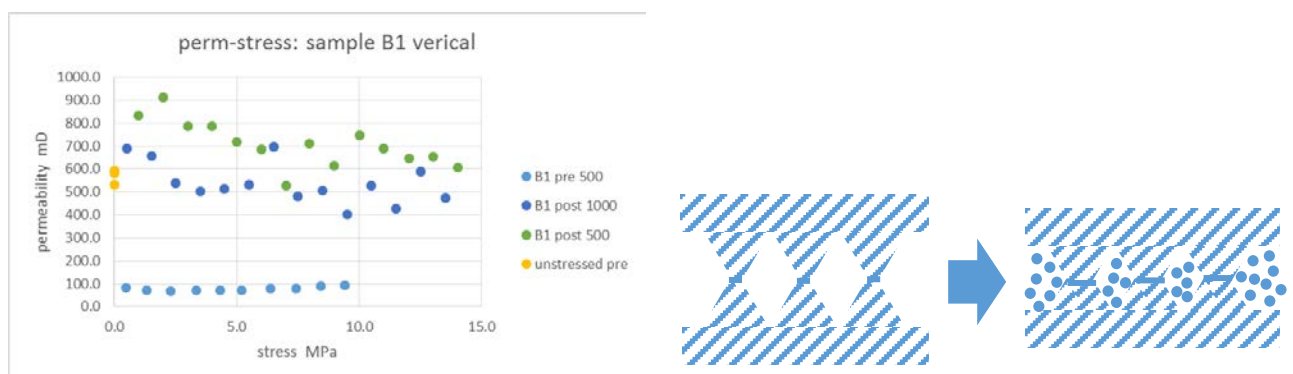


Figure 4.5-4: a) Berea Sandstone permeability vs stress; b) Conceptual cartoon of fines creation during stressing.

4.6. Geomechanical Testing

The 40 mm cube samples were also tested to determine their stress-strain response, including the extent to which this may have been affected by chemical changes from exposure to CO₂ acidified water. Testing was first performed on fresh samples, after which they were exposed to high pressure water saturated with CO₂, as described earlier. It was noted that the sample surfaces became quite friable during the continuous flushing, presumably because the inorganic cements were being dissolved and some fines were being mobilised during the water-CO₂ carbonic acid fluid flush. In some instances, this caused the strain gauges to detach during re-testing (annotated as ‘failed’ experiments). Samples WW1-1211-Precipice (WC20), WW1-1056-Evergreen (WC9), and B1 (Berea) were all flushed in the CO₂ saturated water continuous flow reactor. Sample WW1-1043-Evergreen (WC8) showed zero liquid permeability in the continuous flow reactor and experienced only minor apparent penetration by the fluid, so this sample was then exposed within a batch reactor with a view to exposing a greater face area to the carbonic acid fluid.

4.6.1. Precipice Sandstone

WW1-1211-Precipice (WC20)

Figure 4.6-1 shows the measured micro-strain (µm/m side length) for the sample before and after flushing for sample WW1-1211-Precipice (WC20). For the pre-flush sample there is a small dilation in one of the horizontal directions, and modest compression in the other directions. After exposure to carbonic acid, the sample is a little weaker (more easily compressed) that is consistent with a small amount of dissolution of minerals permitting some reorientation and closer packing of the hard quartz particles under stress. The vertical strain gauge post-exposure failed.

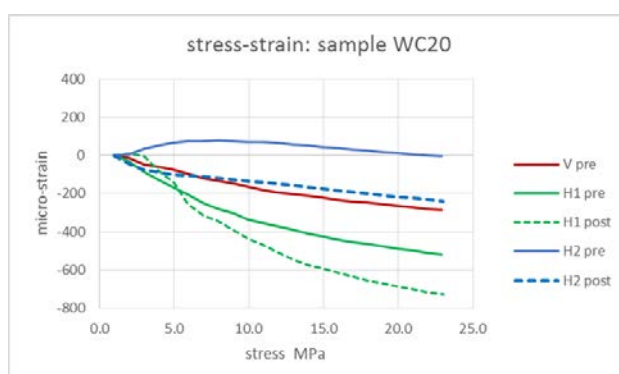


Figure 4.6-1: Directional stress-microstrain of WW1-1211-Precipice pre- and post-reaction.

4.6.2. Evergreen Formation

WW1-1056-Evergreen (WC9); WW1-1043-Evergreen (WC8)

For sample WW1-1056-Evergreen (WC9), the pre-flush response is shown (Figure 4.6-2). After exposure to the carbonic acid in the continuous flush apparatus, the sample lost integrity (the

material had essentially lost strength due to dissolution of carbonate cement and was crumbling (Figure 4.4-4). For the pre-flush sample there is some dilation in one of the horizontal directions, and modest compression in the other directions. Dilation, while possible under isotropic stress, more normally arises from shear strains: it is clearly apparent in Figure 4.4-4 that at least part of one end of this sample did experience shear.

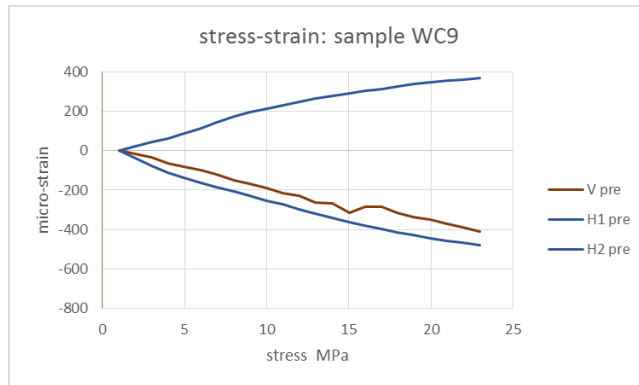


Figure 4.6-2: Directional stress-microstrain of WW1-1056-Evergreen pre- and post-reaction.

For sample WW1-1043-Evergreen (WC8), there is very little difference between the pre- and post-flush stress-strain response (Figure 4.6-3). As the sample was only peripherally subjected to carbonic acid (in a batch-soak rather than a flow through procedure, because there was no permeability for flow-through), it was presumably hardly exposed to attack. The vertical strain pre-exposure is rather higher than post, but this is likely because strain associated with particle re-orientation had already taken place in the pre-exposure test and this new closer packed arrangement persisted thereafter.

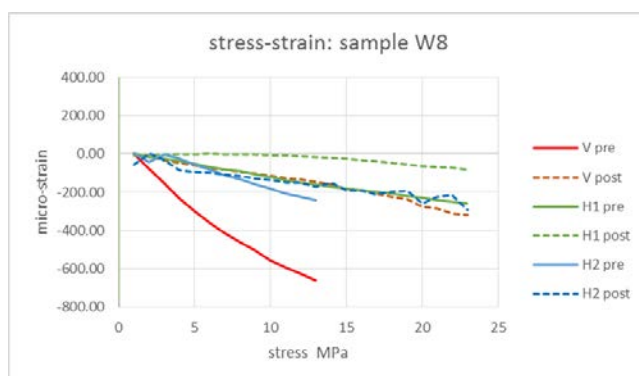


Figure 4.6-3: Directional stress-microstrain of WW1-1043-Evergreen pre- and post-reaction.

4.6.3. Berea Sandstone

The Berea sandstone sample was somewhat weaker than the Precipice and Evergreen samples, showing about double the strain for equivalent stress (Figure 4.6-4). This could partly explain why the pre-reaction stressed permeability was greatly reduced in comparison to unstressed measurements. This sample was taken from a quarry near-surface and so it is possible that it was never buried as deeply and thus naturally compacted as many of the core samples used in this study.

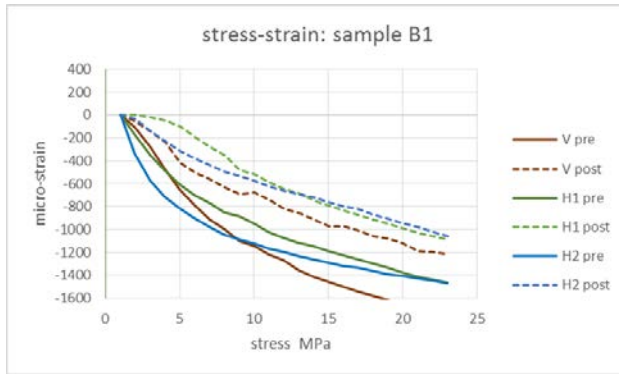


Figure 4.6-4: Directional stress-microstrain of Berea Sandstone cube B1 pre- and post-reaction.

5. Discussion of Experimental Results

5.1. Sample Mineralogy

Most of the rock samples contained similar minerals, but in differing proportions depending upon the unit facies. Carbonates, sulphates and reactive silicates such as chloritised biotite contributed the most to changes in reaction water chemistry, as demonstrated by comparison of SEM images taken before and after reactions. The behaviour of the carbonate and other cements (e.g. oxides) as well as fines observed are major factors governing rock-responses to CO₂ geosequestration. The high surface area of the fine particles observed between framework grains of all samples, coupled with the potentially reactive compositions of some (e.g. Fe-Mg-rich fines) made it likely that some of these reacted during the experiments.

Unlike the thin section petrography in which most observed feldspars appeared heavily altered, SEM analysis commonly found unaltered feldspars albeit mostly as clusters of cleavage fragments surrounded by clays or carbonate cement. The fine material around the feldspars was generally too fine-grained for SEM-EDS analysis to confirm that it did or did not originate from chemical alteration of feldspars, and general spot analysis of the fines gave a wide variety of compositions. The WW1 samples contained the widest range of feldspar compositions, with Ca-bearing feldspars being more commonly observed than for the other samples. In the medium to long term, such Ca-rich minerals are more reactive than the K and Na feldspars that were more common within the Chin4 and Berea samples, most especially the smaller sized (and therefore higher reactive surface area) cleavage fragments. Any calcium liberated from the feldspars could eventually react with dissolved CO₂ to form carbonate cement (mineral trapping of CO₂).

The potential CO₂ reservoir unit studied, the Precipice Sandstone, dominantly contains chemically unreactive minerals such as quartz as well as lesser amounts of kaolin clays that partially occlude the generally open pore space between framework grains. The combination of well-connected porosity and generally low chemical reactivity are major reasons why this formation is touted as a possible CO₂ reservoir. Minor reactive minerals such as carbonates and Fe-Mg-aluminosilicate minerals do occur throughout the Precipice Sandstone, though were more frequently observed in uppermost Precipice samples.

The baffle unit between the Upper and Lower Precipice observed within the WW1 core likely contains some chemically reactive silicates as thin micaceous and shaly layers are present. Sulphate minerals were commonly observed within the Lower Precipice WW1 samples, and were present throughout this whole unit. It is likely that the site groundwater naturally contains dissolved sulphate

that may in certain intervals be at saturation levels, given the abundance of pore-filling sulphate and its resistance to removal during washing and lubricated cutting whilst preparing samples.

The Evergreen Formation “seal-rock” samples represented a diverse range of baffled lithofacies (rock types) as well as mineral distribution, composition and particle sizes. Consequently, any potential fluid flow pathways within this formation are likely tortuous, constricted, and bounded by a variety of geochemically reactive minerals. Colloidal material and clays produced during reaction of chemically-unstable silicate minerals such as chloritized-biotite could in turn act to block pore-throats and thus restrict fluid flow, so-called “self-sealing”. Carbonate cements exposed to CO₂-rich water would initially dissolve, but then act to locally buffer the pH to near-neutral values thus retarding further potential for reaction. Units containing calcite cement are generally present in both the Evergreen Formation and overlying Hutton Sandstone, with some patchy calcite also found within an Upper Precipice Sandstone WW1 sample.

5.2. Batch and Continuous Flow Reactor Geochemistry

The Precipice Sandstone experiments showed that it is generally low in reactive material, as only low concentrations of most aqueous elements analysed for were detected. Consequently, the geochemical properties of this reservoir are likely to remain relatively stable during CO₂ injection. The Evergreen Formation seal samples contain quite geochemically reactive minerals; however, only the outer surfaces of the samples tended to be penetrated during the batch reactor experiments due to the low permeability of these materials. In the case of the continuous flow reactor experiment with the Evergreen calcite cemented sandstone, much of the pore-filling calcite did react. Even so, in order for this to occur *in situ*, there would first have to be an active fluid flow pathway leading to this material; as discussed in the next section, the virgin permeabilities of the seal samples were all extremely low. It is expected that given the combination of low permeability and high geochemical reactivity, self-sealing reactions including mineral trapping of CO₂ as carbonate minerals will occur over the long term at the interface between reservoir and seal.

The chemistry of reaction fluids from CO₂-water-rock experiments tended to be dominated by cations such as Ca, Fe, and Mg. These elements are commonly present in carbonate cement, and also can originate from dissolution of other minerals such as sulphates and reactive silicates, or even cation exchange from clays. In samples for which carbonate cement was observed, much of the Ca, Fe, Mg and Mn in solution were the result of dissolution of that cement. Some alteration of the surface of chloritised biotite (Fe-chlorite) was observed during post-reaction SEM analyses, and such minerals were likely sources for the dissolved Si and some of the Fe detected.

Relatively elevated concentrations of dissolved S were observed during some experiments, notably with the WW1 Lower Precipice samples but also others such as calcite cemented WW1 Evergreen. In the case of the Precipice, the continuous flow reactor chemistry suggests that the majority of the dissolved S originated from reaction of the pore-filling sulphates observed via SEM and also XRD analysis. Na-K-sulphates have high solubility in water and so were likely present within the groundwater of the sampled units and precipitated within the pores as the core dried out.

The continuous flow reactor experiments tended towards high sample reactivity initially, as shown by the incremental water chemistry, followed by a gradual overall decline in dissolved element concentrations as reaction flow-paths were cleared by acidic fluid-flow. Similarly, the concentrations of many dissolved elements increased sharply during the initial days of batch reactions before beginning to plateau towards the end. This may indicate reaction of predominantly fine material early on followed by lower surface area material, and/or rapid initial acidic fluid-rock equilibration leading to saturation conditions.

5.3. Porosity and Permeability

Porosity of sister reacted and unreacted samples showed that <1 % up to >4 % by volume of minerals is readily soluble in brine saturated with CO₂ at reservoir conditions. The heterogeneous nature of the coarser-grained samples means that an undefined proportion of any difference in porosity may be due to natural pore size distribution variation between samples. Nevertheless, an increase in porosity will lead to a corresponding increase in permeability as additional space is opened for flow. This was confirmed by the permeability measurements that showed a significant increase in permeability post reaction for the calcite cemented sandstones generally, and the 40 mm cubes largely independent of mineralogy or lithology.

Reasons for the difference between the post reaction permeabilities measured for Precipice 40 mm and 15 mm cubes could be partly due to scaling effects and also sample heterogeneity. The high dissolved sulphur measured during the beginning of the continuous flow reactor experiment indicated that much of the pore-filling sulphate salts within sample WW1-1211 were likely removed. Elevated dissolved sulphur was also measured during the batch reaction experiment WW1-1217, with no corresponding dramatic increase in permeability. However, sample WW1-1217 was very coarse grained and highly permeable pre-reaction, whereas sample WW1-1211 was generally much finer grained and had lower pre-reaction permeability that is likely why it was more sensitive to changes caused by experiments.

Sample WW1-1043-Evergreen was effectively impermeable prior to testing and became even more so, especially under stressed conditions, following reaction with CO₂-saturated brine. This was in

spite of the fact that the sample did contain minerals that dissolved in carbonic acid. However, due to the inherent low permeability of this clay-rich lithic sandstone, there was very poor fluid penetration beyond the surface of the sample. Sample WW1-1056-Evergreen by contrast is a calcite cemented sandstone that also had low initial permeability, but this increased significantly following geochemical reactor experiments. The difference was due to the fact that although sample WW1-1043 also contained pockets of acid-reactive carbonate cement, these were not interconnected as they were within sample WW1-1056.

The sizes of the samples used in the experiments of this study are small in comparison to the scale of geological formations. In order for any calcite cemented units of the Evergreen Formation “seal” to come into contact with a CO₂-rich fluid it would first have had to bypass units of composition similar to sample WW1-1043 (see WW1 Well Completion Report). Furthermore, following any initial dissolution of carbonate cement, the pH of the near-by groundwater would experience increased alkalinity that, in the absence of high fluid flux, would retard further mineral dissolution in that interval. By contrast, in reservoir units it is advantageous for the unit to experience increased porosity resulting from dissolution of cementing material, and the higher inherent permeability of such units means higher fluid flux to sustain dissolution reactions, which in turn increases the potential for a permeability increase to occur.

5.4. Geomechanical Testing

Geomechanical tests provide the basis for stress – permeability relationships to be described. The reservoir material *in situ* is under natural overburden and tectonic lateral stresses. Further, during injection, an overpressure – often significant – is applied in order to drive injection fluid into the subsurface. This overpressure increases the internal interstitial (pore) pressure and consequently reduces the net stress, increasing the permeability. This behaviour needs to be defined in order to predict injectivity dynamics correctly. Further, once characterised, the permeability-stress relationships allow unstressed permeability measurements (that are much easier to do) to be scaled to stressed permeabilities.

The measured strains experienced by the samples tested are quite small, and yet the permeability was still quite sensitive to any increase in stress applied irrespective of the general composition of the samples. This in turn implies that small components within the samples, be these pore throats or fine particles, may be what is most affected by the applied stress prior to any geochemical reactions taking place. However, the changes in sample strain response following geochemical reactor experiments reflect both physical (e.g. mobilisation) and chemical (dissolution/precipitation) of fines material, as well as changes in larger components such as any significant pore-filling cement and alteration of acid-reactive aluminosilicate framework grains which may have been present.

6. Modelling Methods and Results

6.1. Geochemical Modelling

The major objectives of the geochemical modelling exercise were to determine which minerals most likely reacted during experiments and to investigate the possible influence of mineral fines upon measured reaction water chemistry over time. This section is focused upon the batch reactor experiments with samples of West Wandoan 1 core material, with reference to journal papers in which modelling of the Chinchilla 4 (Farquhar et al., 2014) and Berea (Dawson et al., 2014) samples is already presented. For modelling, the actual concentrations of aqueous elements incrementally measured during batch reactor experiments were used for comparison to modelled values. The mass of minerals potentially reacted within the rock samples were directly taken into account by the models.

6.1.1. Modelling Methodology

Geochemist's Workbench (GWB) version 9 software package (Bethke and Yeakel, 2013) was used to construct models of the incrementally measured water chemistry of the batch reactor experiments. Major and minor dissolved species measured in the water-rock equilibration stage of the experiment were used as the aqueous basis components of the model, with initial input mineral masses derived from consideration of QEMSCAN, XRD, SEM-EDS and thin section petrography. In addition to minerals identified during sample characterisation, small amounts of witherite, strontianite, and rhodochrosite were also added to the models to account for Ba, Sr, and Mn mobilisation during experiments; however, these trace elements may have originated from other carbonates. Initial mineral surface areas were obtained from previous investigations of similar samples (e.g. Pearce et al., 2014). Both the surface areas and to a lesser extent the mineral masses were varied in order to achieve the best possible fit for modelled water chemistry changes over the duration of the batch reactor experiments at 60 °C, and with a CO₂ fugacity that took into account the pressure, salinity, and temperature conditions.

6.1.2. Geochemical Modelling Results

6.1.2.1. *Precipice Sandstone*

For the Upper Precipice sample WW1-1165, the main reacting minerals were trace carbonate, chlorite and muscovite to account for the Ca, SiO₂, and Fe concentrations observed experimentally (Figure 6.1-1). A lowered solution pH of 3 was predicted. The Lower Precipice sample WW1-1217 had higher release of Fe into solution from trace siderite dissolution, and also greater dissolved silica from trace silicate or amorphous silica dissolution (Figure 6.1-2). The predicted solution pH was

Geochemical and Geomechanical Testing of Near Wellbore CO₂ Injectivity Improvement

similar to the upper Precipice pH of 3, slightly lower than the experimentally measured value. Sulphate concentration in solution was predicted to be high in the lower Precipice, reflecting dissolution of sulphate minerals observed in the core.

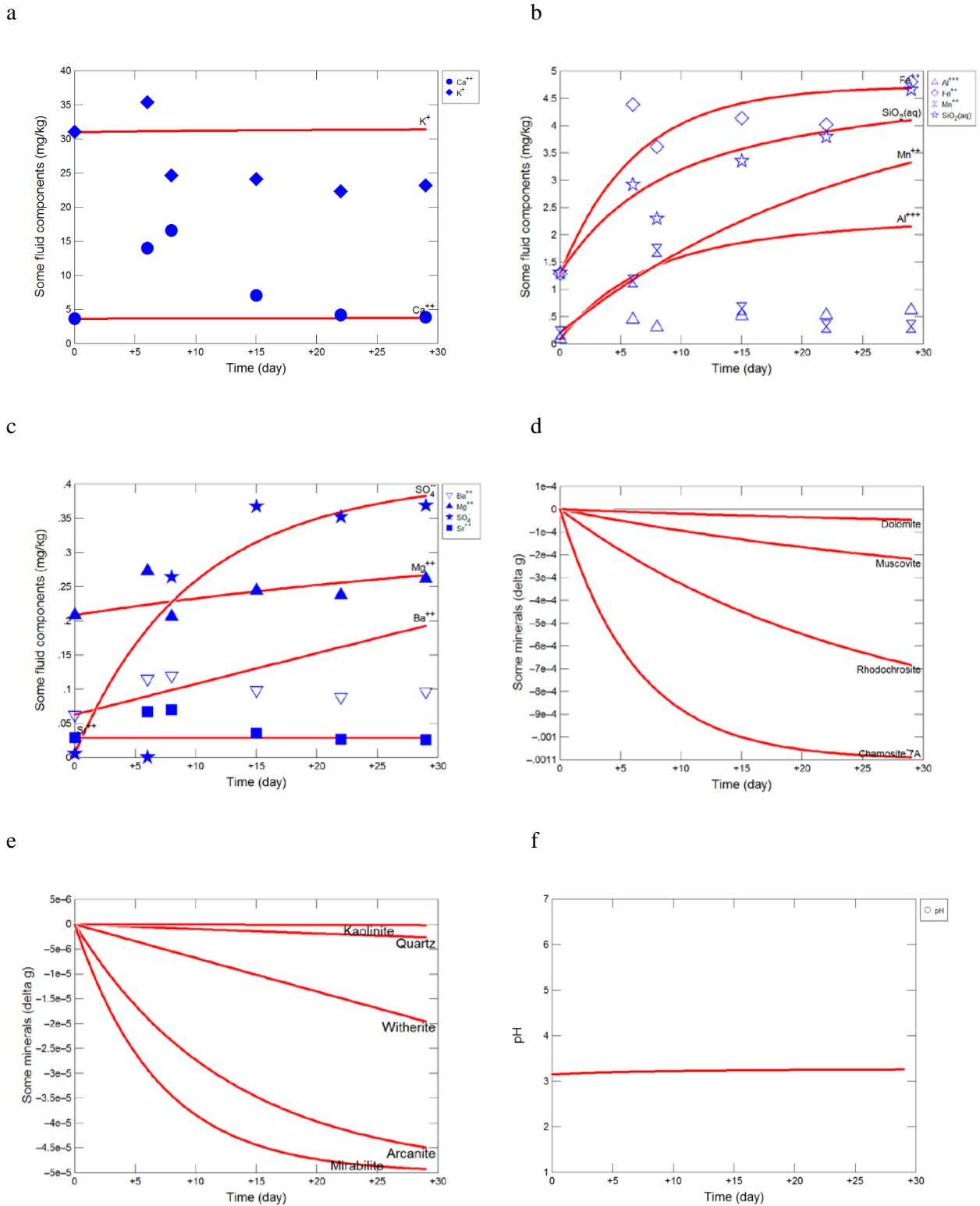


Figure 6.1-1: Geochemical modelling results for WW1-1165-Precipice batch reactor experiment.

Geochemical and Geomechanical Testing of Near Wellbore CO₂ Injectivity Improvement

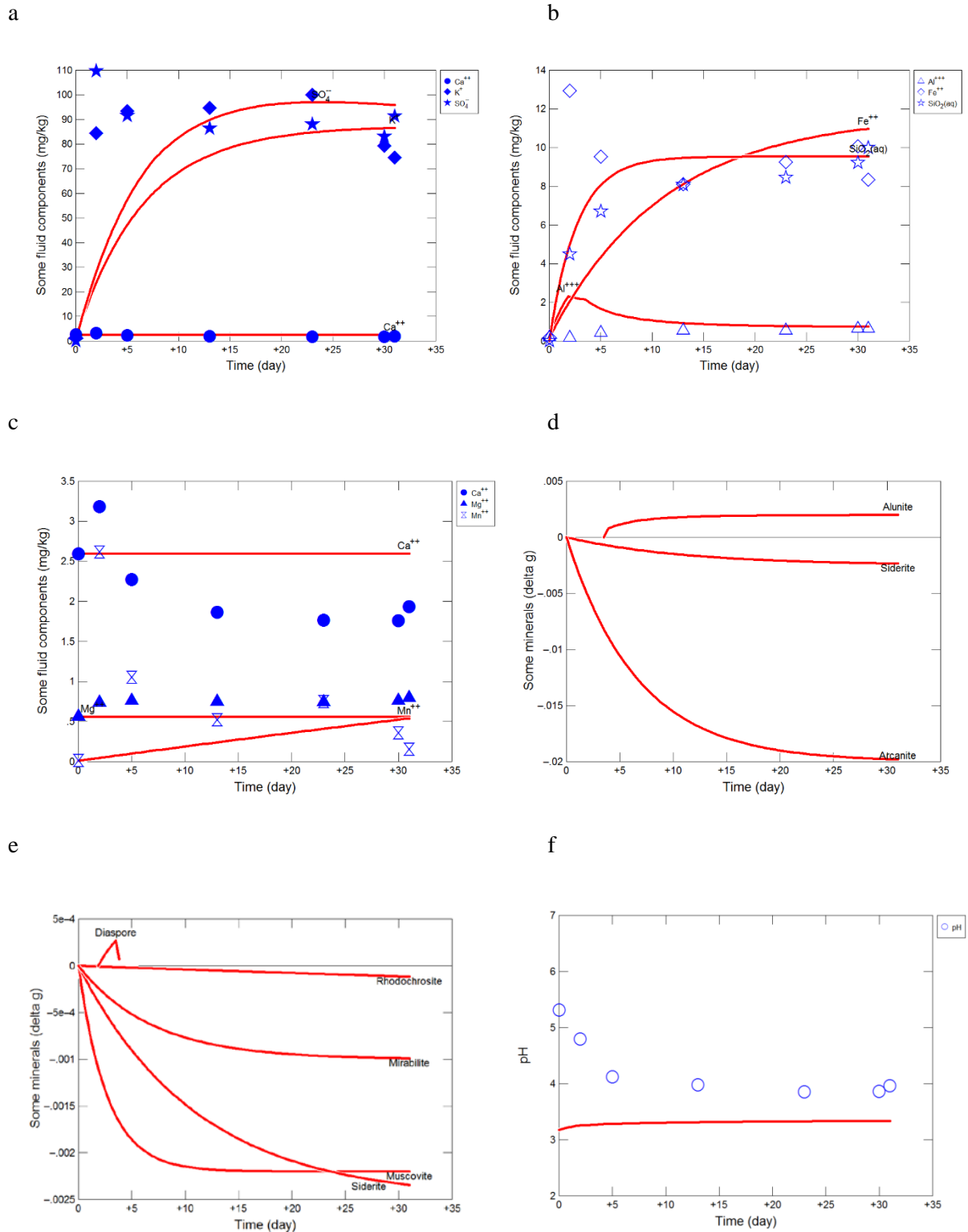


Figure 6.1-2: Geochemical modelling results for WW1-1217-Precipice batch reactor experiment. XRD and SEM-EDS analysis indicated that the significant white precipitant observed upon (and sub-sampled from) the surface of predominantly the Lower Precipice Sandstone of the WW1 core was a mixture of K and Na sulphate. The sulphate likely originated from *in situ* formation groundwater, but

it is possible that K from KCl introduced via drilling mud could have combined with the pre-existing sulphate to form K-sulphate as the core dried out in storage. Anomalously high dissolved sulphur was measured during the first incremental sample of the Lower Precipice continuous flow reactor experiment, and high aqueous sulphur was also a result of the Lower Precipice batch reactor test; orders of magnitude more so for the Lower Precipice compared with the Upper Precipice sample.

The measured drop in pH over the first week of the Lower Precipice experiment was probably due to the increase in aqueous sulphur. Accordingly, mirabilite (Na-sulphate) and arcanite (K-sulphate) were added to the Precipice models to account for the observed sulphur mobilisation and a portion of the K. To match the observed Si mobilisation and part of the K, the surface area of the muscovite was greatly increased to the point of modelling sericite that is essentially just ultra-fine-grained muscovite. However, it was not possible for the models to match the high concentrations of aqueous K and S without causing precipitation of phases such as alunite to occur in the Lower Precipice model. Barium carbonate (witherite), although not observed in any samples during characterisation tests, was added to most models in order to account for observed Ba mobilisation.

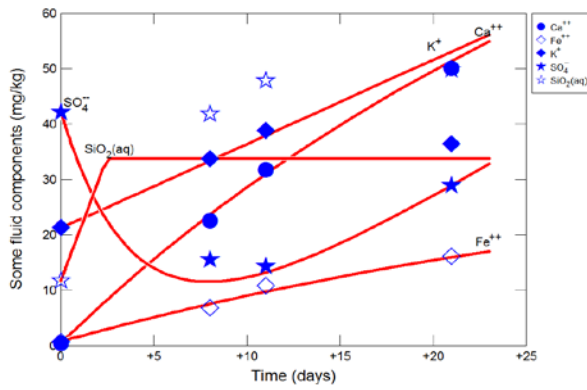
6.1.2.2. Evergreen Formation

Ca, K, SO₄ and Fe were major dissolved elements during the Evergreen experiments. For WW1-981, dissolution of carbonates including siderite, and silicates including anorthite and muscovite were predicted (Figure 6.1-3), with trace chlorite playing only a minor role. Solution pH was predicted to be buffered from 3 to 4 during the reaction. By modelling sericite dissolution the K in solution could be perfectly mirrored; however, the dissolved Si could not be matched as the model precipitated greater amounts of chalcedony whenever the surface area was further increased. Both sericite and to a lesser extent chlorite dissolution also likely contributed to the reaction water chemistry for WW1-1043-Evergreen (Figure 6.1-4).

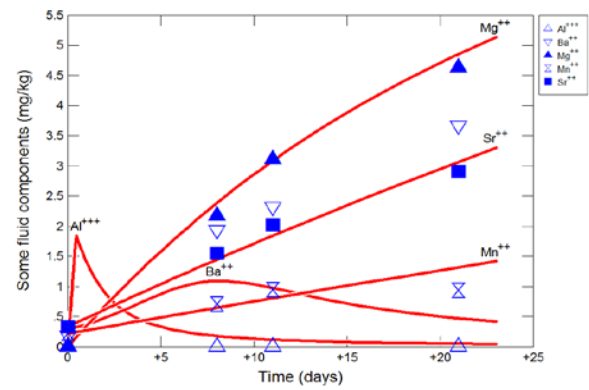
The model used assumes that precipitation rates are essentially the reverse of dissolution rates, which may not be correct given that other factors such as nucleation rates also impact upon precipitation rates. Furthermore, recent studies have found that minerals such as chlorite may undergo incongruent dissolution, preferentially losing some elements such as iron and retaining others (e.g. Black and Haese, 2014; Brandt et al., 2003). However, these studies suggested that more silicon would likely be retained by the solid mineral framework than be lost to solution. Regardless, the software used cannot account for incongruent mineral dissolution.

Geochemical and Geomechanical Testing of Near Wellbore CO₂ Injectivity Improvement

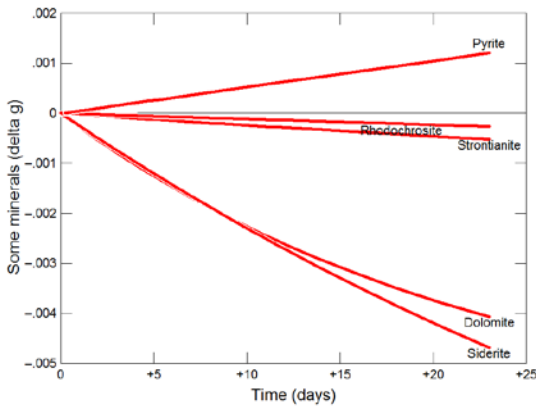
a



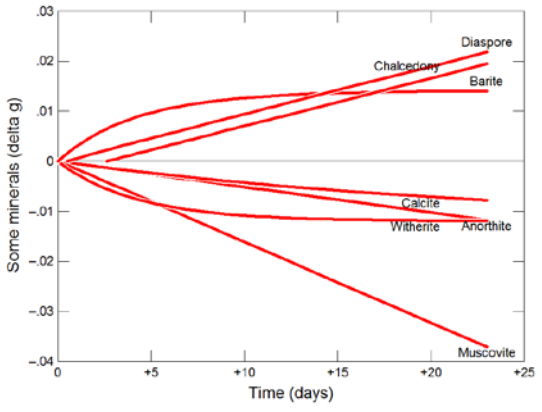
b



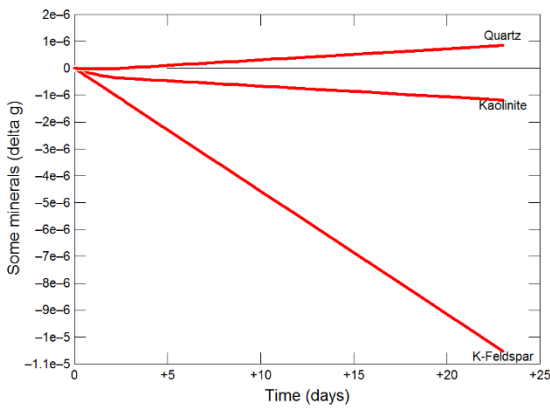
c



d



e



f

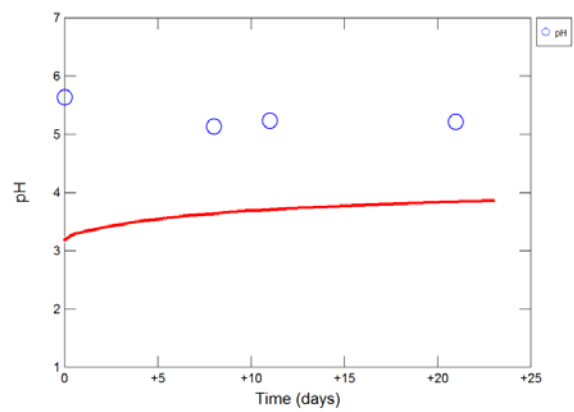


Figure 6.1-3: Geochemical modelling results for WW1-981-Evergreen batch reactor experiment.

Geochemical and Geomechanical Testing of Near Wellbore CO₂ Injectivity Improvement

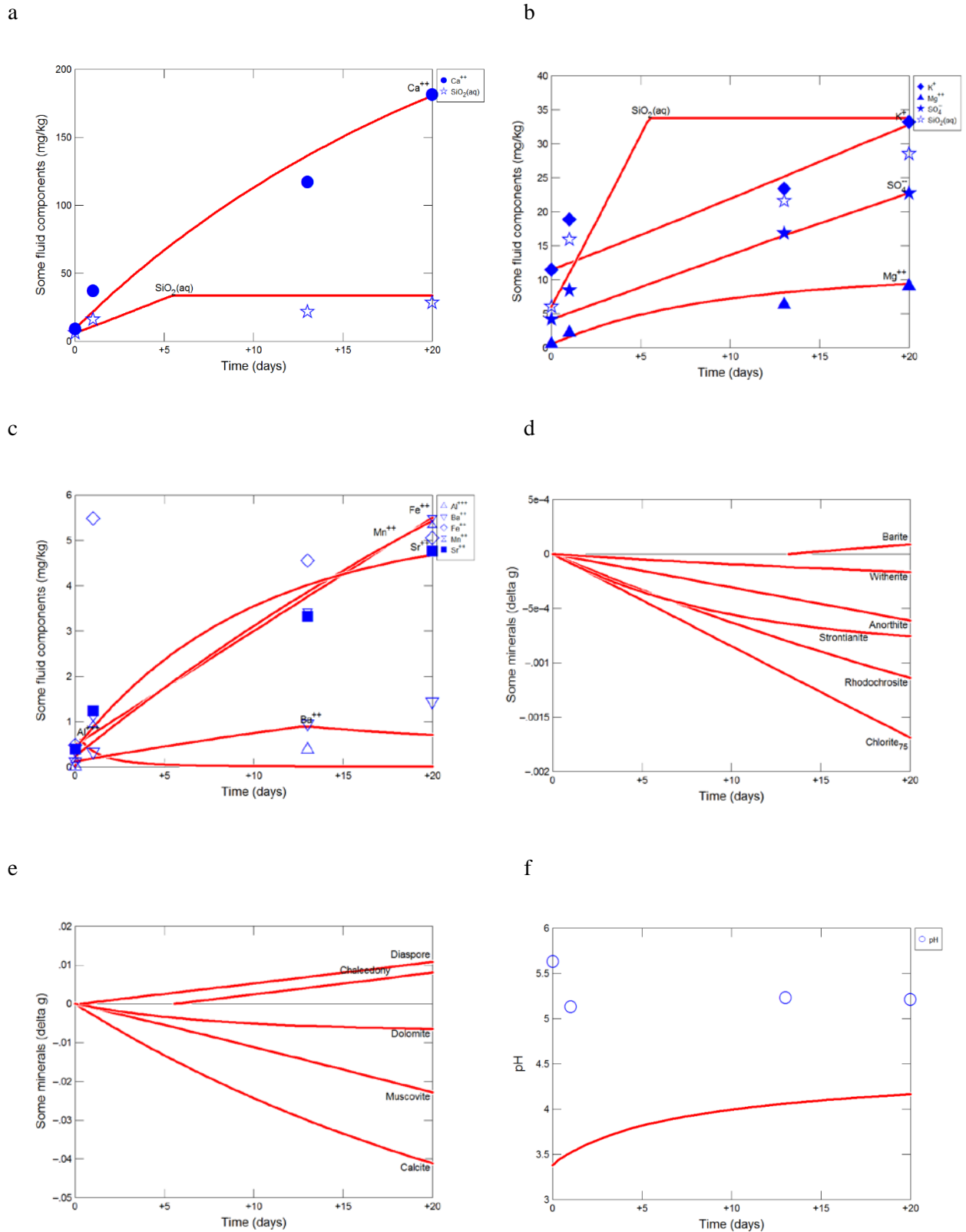


Figure 6.1-4: Geochemical modelling results for WW1-1043-Evergreen batch reactor experiment.

Trace calcite content was sufficient to produce the higher concentration of Ca in solution for WW1-1043 compared to WW1-981. The pH was predicted to be buffered during reaction through carbonate dissolution. Strontium and manganese carbonates (strontianite and rhodochrosite) were added to models as a proxy to account for observed Sr and Mn mobilisation even though these phases were never directly observed during sample characterisation tests. Other carbonates (Ca, Mg, Fe) were also major contributors to reaction water chemistry, and when observed via SEM always contained measureable accessory Mn.

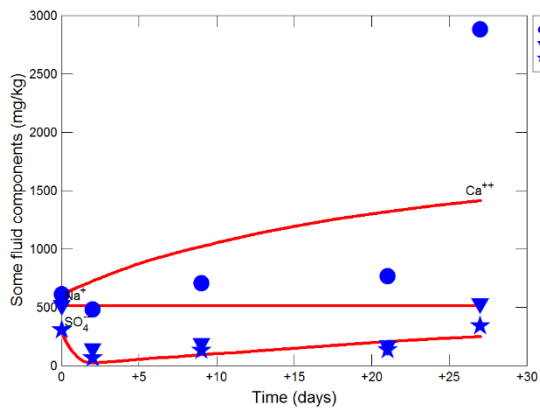
The WW1-1056-Evergreen core sample was calcite cemented and this, along with Ca-feldspar dissolution to a lesser extent, likely contributed to the very high Ca concentration in solution (Figure 6.1-5). The lack of significant increase in concentration of most other elements during the experiment was likely due to the pH buffering through significant calcite dissolution, and hence less acid activated dissolution of silicates. The sudden increase in measured dissolved concentrations at the end of the experiment may have been due to fresh material suddenly being exposed to reaction fluids potentially due to the dissolution of overlying calcite cement, or possibly turbulence caused by incremental sampling dislodging “pacified” surface material from the sample. The observed non-linearity of the experimental concentrations over time was not able to be accurately modelled with GWB. Even so, it was possible to deduce that chlorite dissolution was likely the major silicate contributing to dissolved Si and Fe. The predicted pH was buffered to ~ 4, higher than the other Evergreen sample reactions, through calcite dissolution.

6.1.2.3. Hutton Sandstone

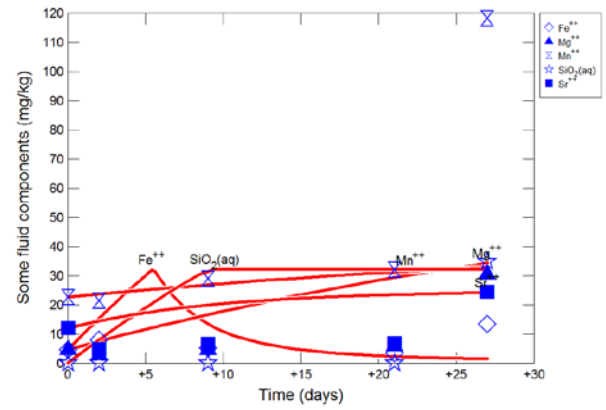
The WW1 Hutton sample was highly calcite cemented and an excellent predicted match with experimentally observed Ca mobilisation was obtained (Figure 6.1-6). Modelled sericite dissolution (fine-grained muscovite) matched the observed aqueous Si fairly well; however, dissolved K mainly reflected the 1.5 g/L KCl solution used for this experiment, masking any possible K release from sericite. Mg, Mn and Sr content in solution was relatively high and likely resulted from dissolution of calcite with a minor substituted composition. The solution pH was predicted to be buffered to the highest value of all experiments to ~ 4.5 owing to calcite dissolution.

Geochemical and Geomechanical Testing of Near Wellbore CO₂ Injectivity Improvement

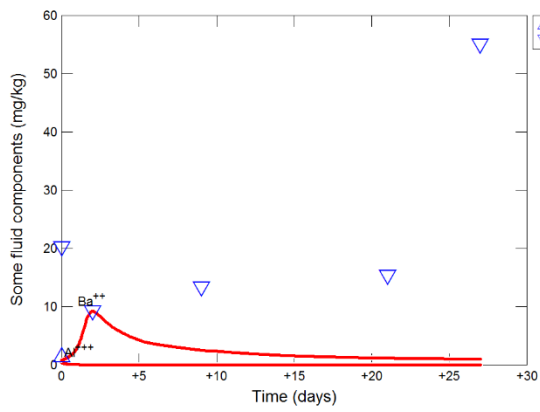
a



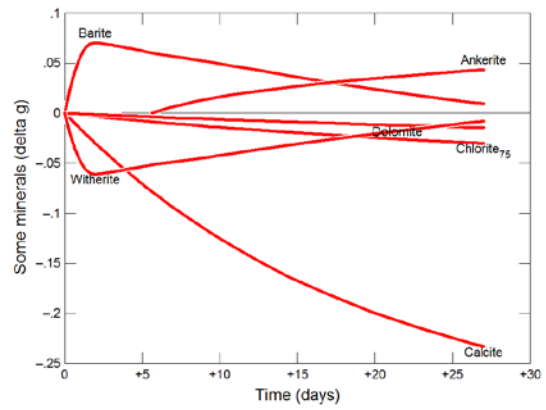
b



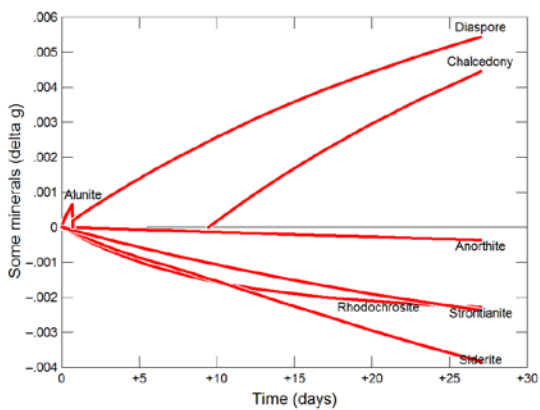
c



d



e



f

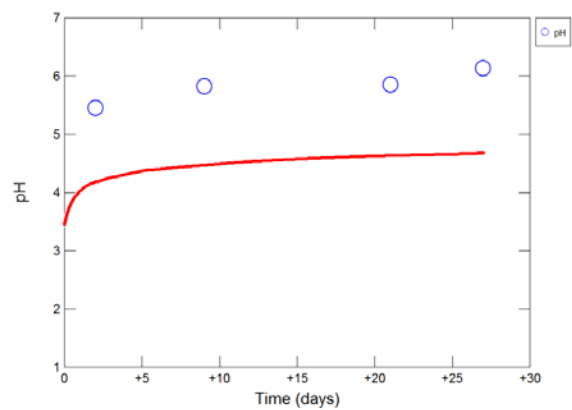


Figure 6.1-5: Geochemical modelling results for WW1-1056-Evergreen calcite cemented sandstone batch reactor experiment.

Geochemical and Geomechanical Testing of Near Wellbore CO₂ Injectivity Improvement

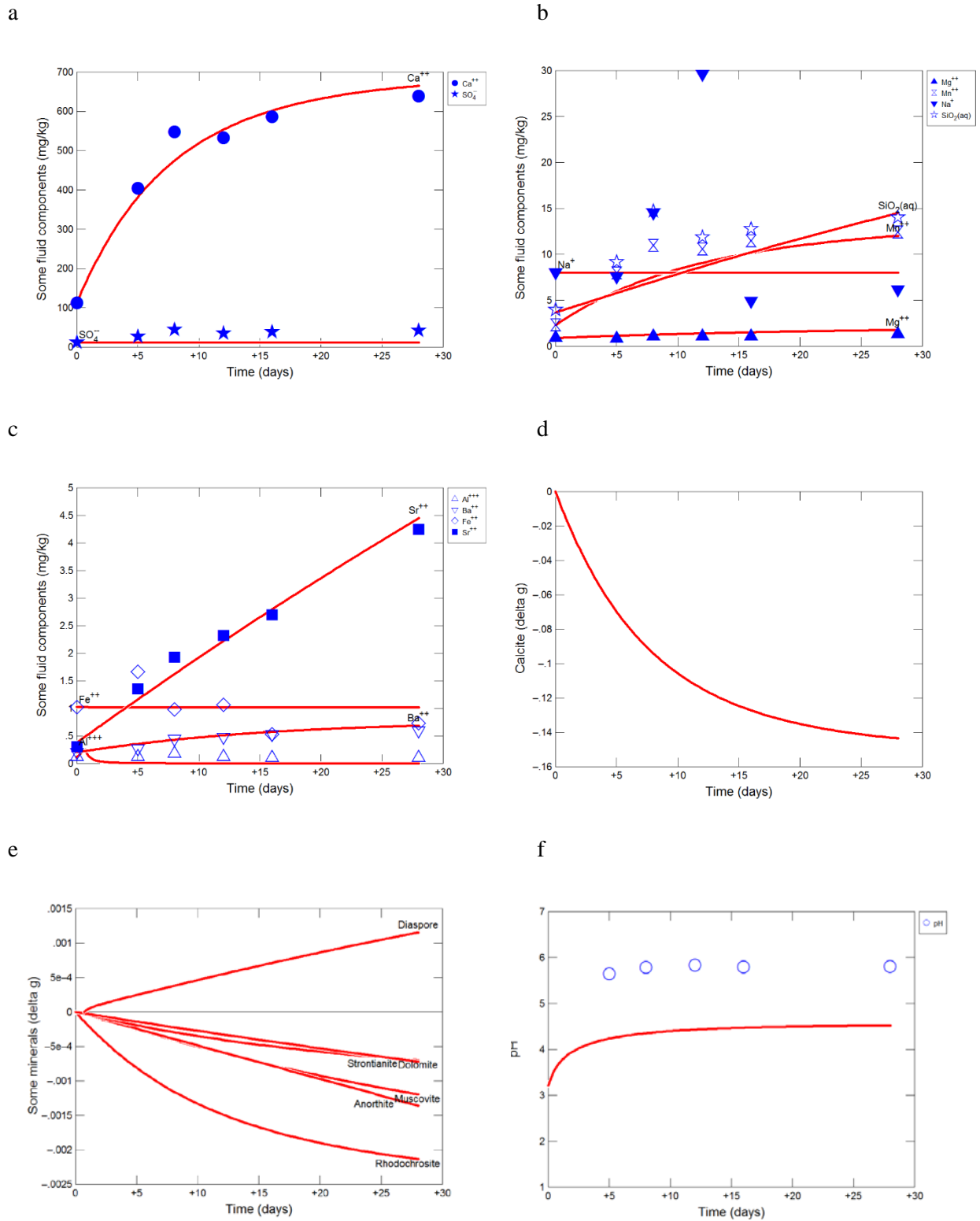


Figure 6.1-6: Geochemical modelling results for WW1-800-Hutton calcite cemented sandstone batch reactor experiment.

6.2. Mesoscale Lattice Boltzmann Modelling

In heterogeneous geomaterials, different individual components possess different porosity and permeability. Fluid transport depends not only on physical pore network arrangements and but also the properties of the confining geomaterials and the chemical interactions between them and the fluid. From a reservoir engineering perspective, for instance, an individual quartz grain is essentially impermeable whilst partly altered feldspar grains commonly have some cleavages or other internal cracks within them and consequently may allow some internal fluid flow to occur. Lithic fragments are recognisable parts of older rocks that have been eroded, transported, deposited, and incorporated into new rocks; such lithics typically have some degree of internal porosity and potentially permeability. General grain sorting variations, diverse sizes of fragments, discreet layering, and cementation may occur and all impact upon the poro-perm characteristics of a sample. Chemical fluid-rock interactions add to the dynamic complexity of fluid transport through geomaterials.

Regarding real geological systems, the main challenge for computational analysis is to account for the heterogeneity of geomaterials (including geometry, topology and the presence of multiple diverse physical and chemical components). This heterogeneity occurs at all scales, but fluid flow is most affected by variations at the pore-scale. A major issue is how to construct an appropriate model to describe pore-scale flow dynamics in sufficient detail to reflect reality. Characterisation of a real geomaterial by advanced imaging like high-resolution X-ray micro-CT/QemSCAN enables the quantification of pore-scale features, including microstructural information such as grain sizes and sorting, pores and tortuosity, as well as the distribution of multiple different geomaterial compositions. This therefore permits the construction of “digital reservoir” rocks. The lattice Boltzmann method (LBM) applied here is capable of simulating fluid flow through such complex pore networks.

The LBM works differently from the conventional macroscopic approaches (e.g. FEM, FDM or FVM) (Duguid and Lee, 1977; Huyakorn, 1983; Or and Tuller, 2000; Reichenberger et al., 2006). Instead of solving the Navier-Stokes equations or its simplified form from the macroscale view, LBM describes fluid dynamics using small cells containing fictive particles interacting through consecutive propagation and collision processes with their neighbours over discrete lattice grids. LBM uses kinetic mechanisms derived from the microscale, incorporates detailed information at the microstructure level, and therefore provides true mesoscale modelling; it is partway between full molecular dynamics simulations and conventional macroscopic depictions of reservoirs (Figure 6.2-1). It provides a means to examine viscous flow behaviours in elements with arbitrary mass (in this work,

larger than single molecules, but much smaller than the global flow field), to provide a reference base for representative parameters to then be used in macroscale models.

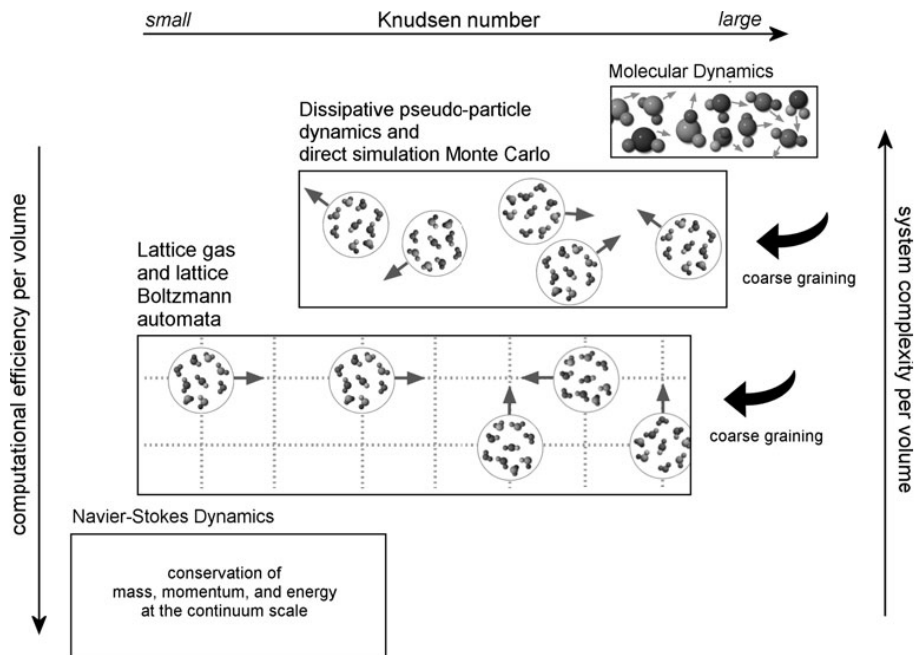


Figure 6.2-1: Multiple approaches for computational fluid dynamics with their preferred range of applicability (Raabe, 2004).

The LBM examines flow dynamics and geomaterials at the mesoscale incorporating many essential characteristics of the real processes, including accounting for fundamental flow mechanisms in real fluid transport networks having pore-scale heterogeneous structures. It also provides averaging methods for upscaling the flow physics from pore-scale to macro-scale. Moreover, it permits coupling of multiple physical processes, such as thermal and chemistry changes, fluid contact interactions with complex geomaterial surfaces, dissolution/precipitation and physical alterations to structures related to these coupled processes. Furthermore, LBM is able to use fully parallel algorithms for cases involving massive data sets, thereby making it amenable to supercomputer processing. We have developed and applied a custom eXtended LBM (XLBM) model, which furthers the conventional lattice Boltzmann method by adding material localization, multiple contact boundaries, and statistics theory, for modelling fluid flow through multiple heterogeneous geomaterials (Gao et al., 2014a, b, c).

XLBM describes the flow mechanism through cavities and multiple geomaterials containing at least some permeability, and shows the flow behaviour on the surfaces of impermeable aggregates by providing each constituent (on each lattice grid) with its own hydraulic properties. This provides a reasonable reproduction of the complex distribution of resistance forces within different mineral components (e.g. the main aggregates or permeable geomaterials), and simulates fluid flow in heterogeneous porous media having a variety of permeable and impermeable geomaterials.

6.2.1. Reconstruction of Digital Porous Media from X-ray Micro-CT/QEMSCAN Images

The micro-CT/QEMSCAN provides scanned images that need to be converted to the digital input for numerical modelling. This is done in 4 steps (Golab et al., 2013; Hou et al., 2009):

- 1) Adjusting dull and low-contrast images into high-quality;
- 2) Conducting image segmentation for clear grain contacts;
- 3) Extracting pixel data to distinguish geometric information; and
- 4) Describing material localization with impurities for further simulations using the QEMSCAN information.

The reconstructed digital porous media preserves the media characteristics along with geomaterial information that is then incorporated into each lattice node (2D pixel or 3D voxel).

6.2.2. Simulation Results and Discussion

Three application cases are illustrated here to demonstrate the capacity of the XLBM in simulating fluid flow in heterogeneous porous media with complex geometry topology and disparate geomaterials, and applications in evaluation of the representative scale permeability.

6.2.2.1. Impact of geomaterial properties on flow behaviour

The 2D porous medium represented through 315 pixels in length and 295 pixels in width includes pore spaces (in black) and a matrix material (in white) (Figure 6.2-2a). The contrast is cleaned up so that the working reconstructed image (Figure 6.2-2b) has clear pore and material boundaries. The reconstructed digital image has then been used to create two test cases with the same topology but where the solid matrix is given different material properties. For case 1, the matrix is relatively impermeable with few connected fluid flow pathways being present (Figure 6.2-3a), whereas for case 2 the matrix has an average porosity ϕ of 0.23 (Figure 6.2-3b); this is to illustrate the impact of differing material properties on the flow dynamics.

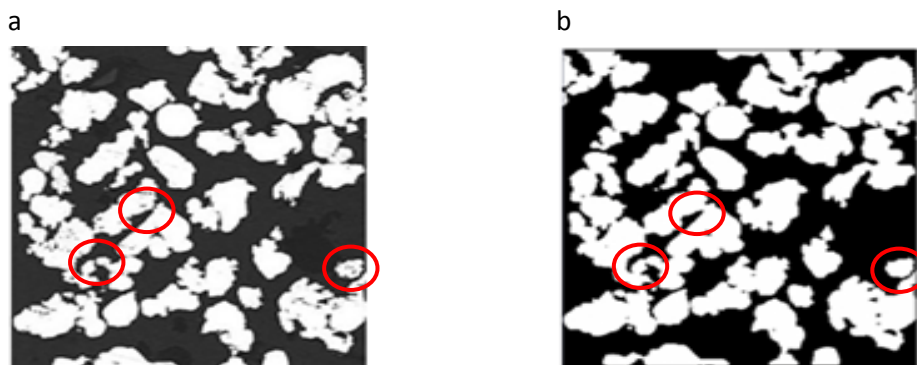


Figure 6.2-2: (a) Scan of a real porous medium section (315 × 295); (b) reconstructed digital structure, which has some slight variations compared to the original (e.g. features circled).

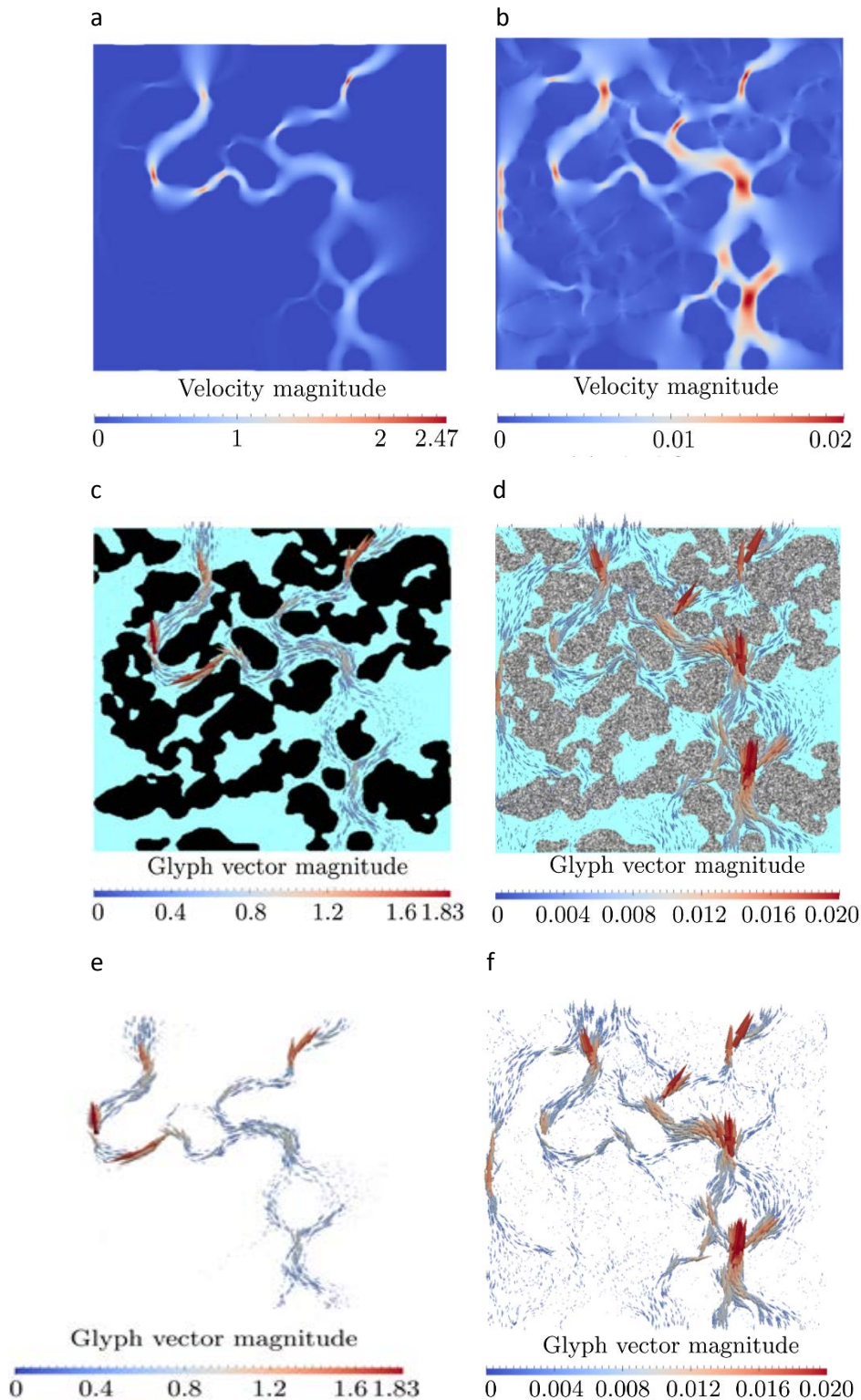


Figure 6.2-3: Fluid flow route with (a) impermeable aggregates and (b) permeable geomaterials; velocity profile of fluid flow with (c) impermeable aggregates and (d) permeable geomaterials; velocity profile (e) detached from (c), and velocity profile (f) detached from (d).

In both cases, the fluid flow is driven by fluid buoyancy from the bottom to the top and has reached steady state. The left and right side walls are no-flow non-slip boundaries. However, flow is different in the two cases, although they share the same geometry structure (topology). In case 1, (Figure 6.2-

3a, c and e), fluid only flows through the pore networks and is obstructed against impermeable aggregate surfaces. In case 2 (Figure 6.2-3b, d and f), there is seepage through the permeable matrix material and the overall resultant fluid velocity of the model is much reduced (by orders of magnitude). This clearly demonstrates that it is not only the major pore topology that governs fluid transport; if permeability of the matrix material and hence fluid flux through this material is not considered, the overall fluid flux through the modelled sample may be overestimated by the model.

6.2.2.2. *Effect of material properties on fluid transport*

This case seeks to illustrate the effect of material properties and geometric topology on pore-scale fluid flow. A 2D porous thin section is shown in Figure 6.2-4. This consists of quartz grains (impermeable), lithic fragments (relatively high permeability in this case that has a significant impact upon the outcome of this model), highly altered feldspar grains (relatively low permeability here) and pore structures. The domain grid is 201 × 201 and the relaxation time τ is defined as 0.8 for computing stability. The lithic fragments are given an average porosity of ϕ_1 ($\phi_1 = 0.5$), and the sections containing highly fractured feldspar grains have an average porosity of ϕ_2 ($\phi_2 = 0.1$). The porosity ϕ_0 for pores is 1.0. The porosity of quartz is ϕ_3 ($\phi_3 = 0$). The fluid enters from the left side and exits at the right side driven by a constant external body force $\mathbf{G} = 0.1$ with a set Reynolds number ($Re = 0.1$). The top and bottom walls are zero velocity closed boundaries. The velocity field (Figure 6.2-5) and velocity magnitude distribution (Figure 6.2-6) are at steady state.

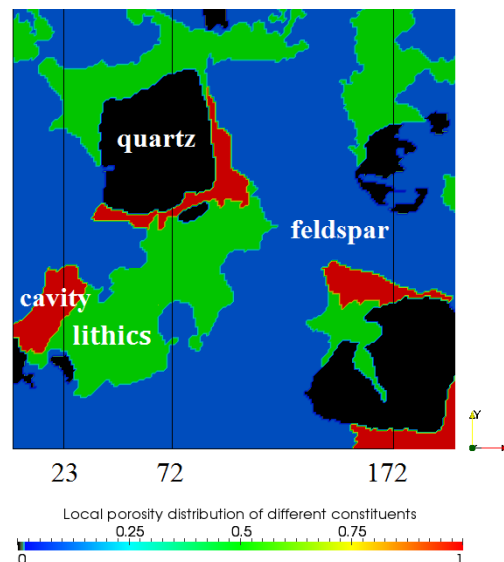


Figure 6.2-4: A thin section of porous medium involving multiple geomaterials shown in different colors (pore - red, lithic fragments - green, highly fractured feldspars - blue, quartz - black). The vertical black lines at $x = 23, 72$ and 172 indicate cross-section lines to be studied.

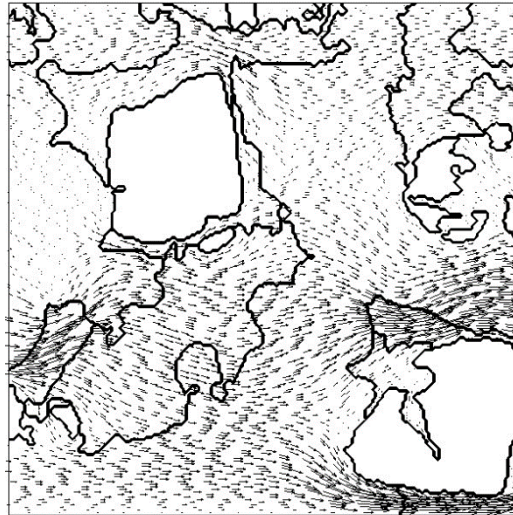


Figure 6.2-5: Outcrop of multiple geomaterials (thick black lines indicate surfaces of geomaterials), and velocity distribution of the fluid flow (arrows and length indicate the velocity direction and size, respectively).

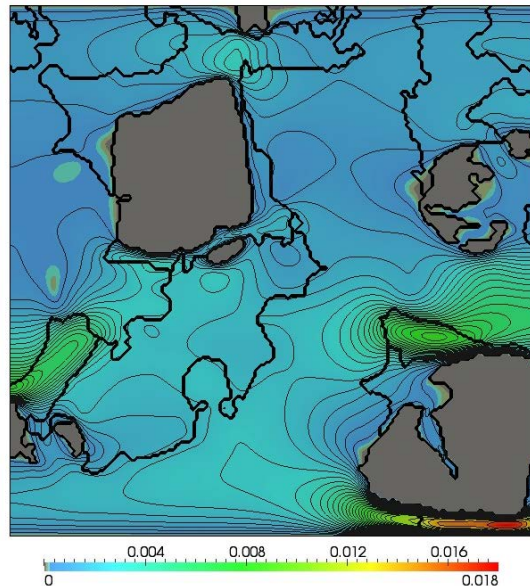


Figure 6.2-6: Outcrop of multiple geomaterials (thick black lines indicate surfaces of geomaterials), and velocity magnitude field with contours (contour step = 50).

The flow dynamics are mainly dominated by the geometric topology of the impermeable aggregates, but pore structures also greatly affect the velocity distribution. All the flow here results through matrix seepage as the pores are disconnected in the section modelled here. At a more detailed level, closure of some contours appears on the surfaces among pores, feldspar fragments, lithics and quartz, due to the disparate porosity distribution and irregular geomaterial boundaries. These material-flow effects deserve more detailed analysis, but still (as presented) serve here to illustrate how the XLBM can analyse permeable seepage phenomena in heterogeneous porous media involving multiple geomaterials.

6.2.2.3. *The 3D evolution of CO₂-induced calcite dissolution*

A CO₂-water-rock system based upon CT-scans of calcite cemented quartzose Hutton Sandstone before and after reaction is used to illustrate the ability of the model to visualise the reactive transport that took place during experiments. The model was setup to mimic the experimental conditions of sample exposure to supercritical CO₂ and water at 60°C and 12 MPa over 18-19 days (including 2-3 days N₂ blank pre-reaction at pressure and temperature), and was also extended beyond the experimental timeframe. In this case, fluid interactions with the frontier non-reactive solid surfaces, acidic fluid intrusion along the calcite-cemented cleavages, mass transport due to the calcite dissolution, generation of wormholes and highly conductive channels, and the feedback on porosity change have been studied at the pore scale.

Figure 6.2-7a and b shows the profile of the digital Hutton sample (before the acid infiltration experiment) from different angles. The 3D digital sample (with a lattice size of 1400 × 1400 × 350) was reconstructed using the X-ray micro-CT scans coupled with QEMSCAN mineral mapping data (around 3 μm voxel size). The main quartz aggregate sections (non-reactive) are shown in dark grey, which occupies most of the sample structure (76.3%); cemented calcite sections (reactive with the carbonic acid) are in light blue (17%); while most of remaining areas are filled with partly altered and fractured feldspar grains, clay and other matrix sections (dark orange) as well as other non-reactive minerals (5.6%). The pore structure only takes up around 1.1% of the whole sample, which can hardly be seen.

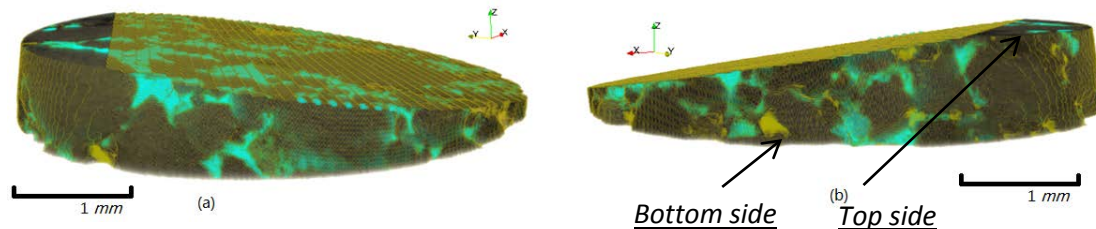


Fig. 6.2-7 (a)-(b) 3D digital Hutton Sandstone core (quartz-dark gray, cemented calcite-light blue, and other constituents such as clays, partly altered and fractured feldspars, other grains, and the matrix are dark orange).

Figure 6.2-8 compares the volume percentage of un-dissolved calcite between the experiment and modelling results (at the time step of 5×10^3) for verification: 30 cross-sections along the vertical direction (z-axis) are chosen for demonstration, where the blue line shows the experimental observation and the red line shows the modelling results. It is observed that the calcite volume at each cross-section is different due to the sample heterogeneity, and the modelling results fit the experiment observation well as a 16-day reaction outcome.

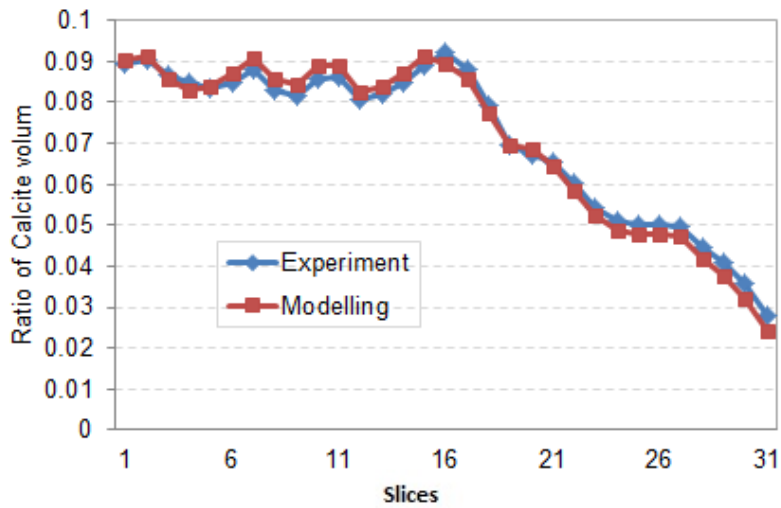


Figure 6.2-8 Comparison of the volume percentage of un-dissolved calcite at 30 different cross-sections along the vertical (z-axis) direction (sections 1 to 31 are from the bottom side to the top side marked in Figure 6.2-7 (b)): the blue line shows the experimental observation (16 days), and the red line shows the modelling results at the time step of 5×10^3 (which corresponds to 16 days).

The total calcite loss from the initial condition until the equilibrium reaction status can be seen in Figure 6.2-9, which leads to porosity enhancement in the sample. Due to this porosity improvement, more carbonic acid can penetrate into the sample core by following the calcite-dissolved pores, wormholes and channels.

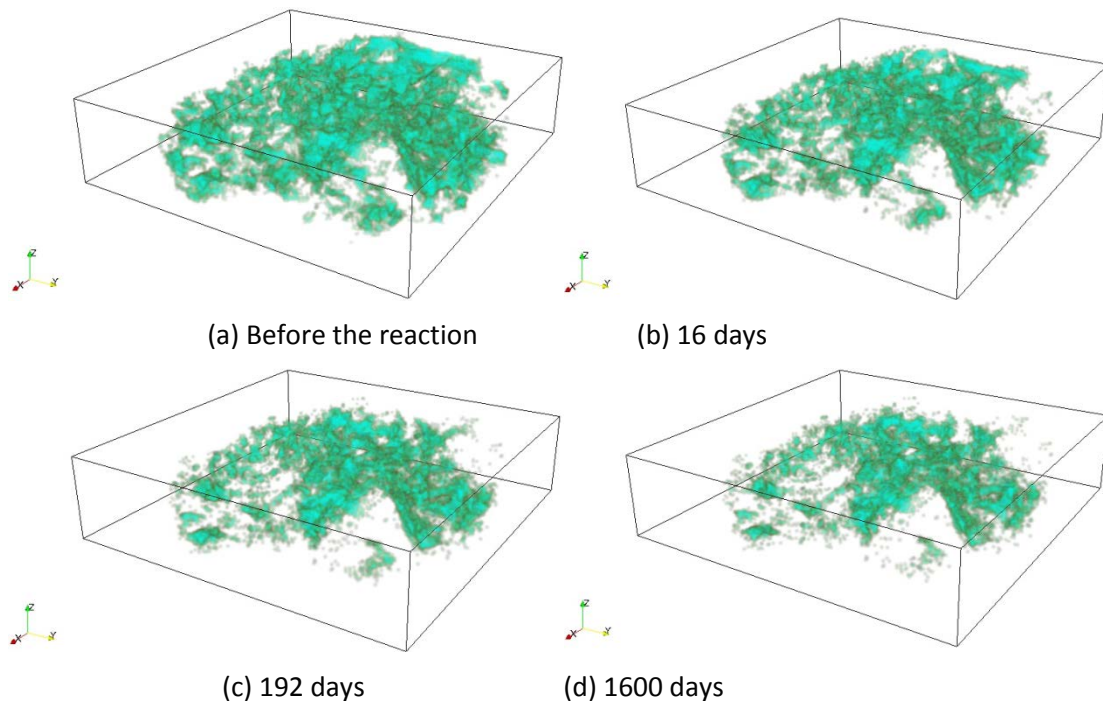


Figure 6.2-9 (a-d) Numerical simulation of acid infiltration evolution: blue color indicates the calcite distribution and loss due to the dissolution process.

Figure 6.2-10 illustrates the total volume change of calcite and pores from the beginning up until the reaction equilibrium status is attained: the blue line shows the dissolution of calcite as the reaction time increases; the red line shows the increase of pore structure and wormholes resulting from the dissolution of calcite along the cleavages planes. The calcite has been significantly dissolved in the first 30 days, leading to a calcite volume drop from around 17% to 11% of total sample volume. Around 2.3% of calcite volume has been removed and replaced by pore space in 16 days (marked as a black point), which has been verified by the experiment. The system finally reaches the reaction equilibrium status in around 1440 days, which brings an increase in porosity from initial 1.1% to a final value of 10.7%.

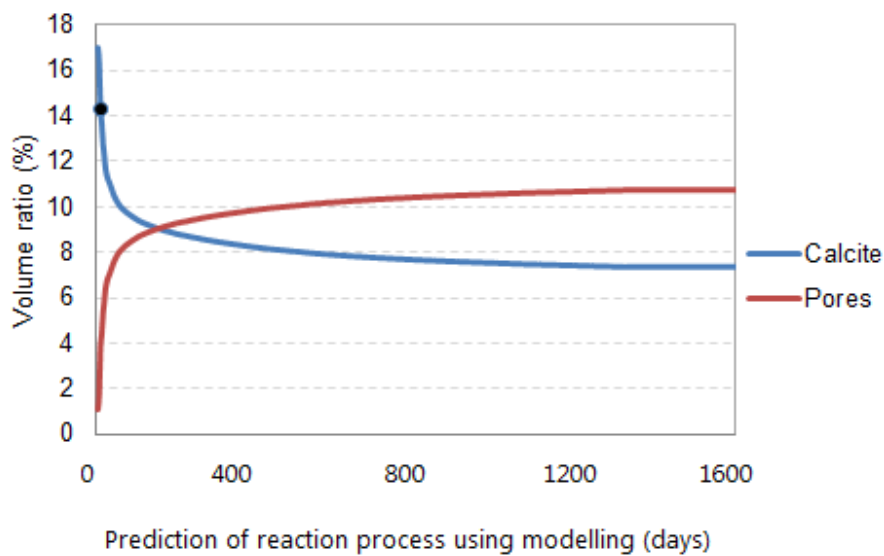


Figure 6.2-10 Total volume change of calcite and pores in the numerical simulation of acid infiltration evolution: the blue line indicates the calcite dissolution process, and red line shows the generation of wormholes (or pore structure).

6.2.2.4. Representative Scale Permeability

Upscaling from pore scale (which is physically where changes occur) to laboratory scale (where measurements of properties are typically done), and to field scale (simulations that are operationally important) remains a challenging and unsolved area of research. Conventionally, geomaterial parameters (e.g. porosity and permeability) at the representative scale are defined based on the experiments as well as statistical correlations, and then averaged and upscaled to the grid blocks used in field scale or reservoir scale simulations. Here, we consider the smallest size providing reliable and representative transport calculations (e.g. directional permeability) for upscaling purposes. This is larger than the pore scale but much smaller than the field or reservoir scales.

The sandstone sample (Figure 6.2-11) has a complicated tortuosity structure with two kinds of mineral matrices (quartz and clay). The sensitivity of (1) micro-CT voxel resolutions on the mineral compositions (e.g. relative composition ratio η_i), (2) properties of mineral components on the microscale fluid dynamics, (3) micro-CT voxel resolutions and mineral property on the directional permeability calculations, and (4) evaluation of the representative scale size of the core sample have been numerically investigated in the following four sections.

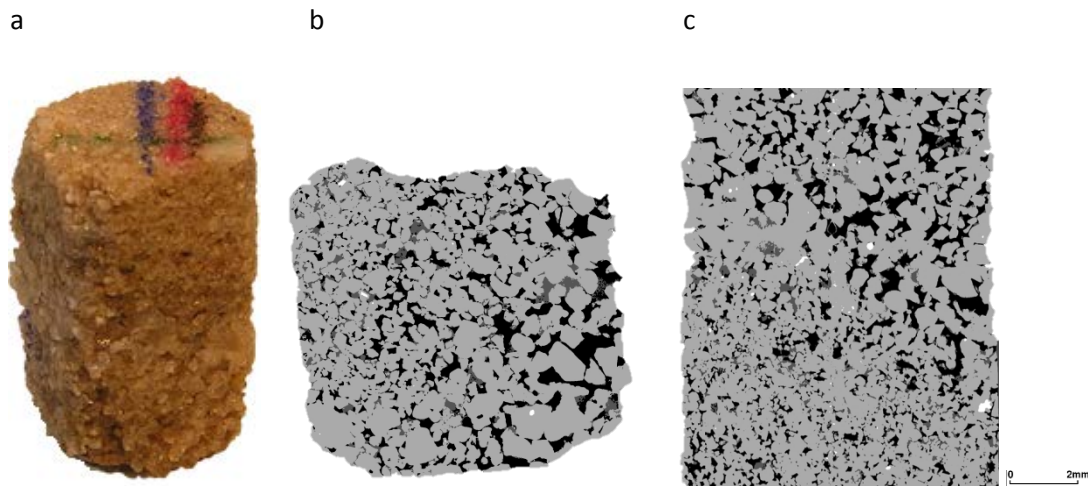


Figure 6.2-11: (a) Structure of the Precipice Sandstone sample (6.6 mm × 6.6 mm × 12.276 mm); a section of the sample along (b) the horizontal direction and (c) the vertical direction showing its anisotropy (cavity – black, quartz – light gray, clay – dark gray).

6.2.2.4.1. Sensitivity of micro-CT voxel resolutions on the core-sample compositions

The sandstone analysed here is a cuboid of 6.6 mm × 6.6 mm × 12.276 mm, which generates a digital sample with a lattice of 1000 × 1000 × 1860 at the 6.6 μm voxel size. Considering the sample anisotropy, we compare the voxel resolution effects on the physical structure fidelity (e.g. composition volume ratio) by coarsening the voxel size from 6.6 μm to 13.2 μm and 33 μm (Figure 6.2-12). The corresponding lattice size of the sample then becomes 500 × 500 × 930 and 200 × 200 × 372 (voxel size as 13.2 μm and 33 μm respectively).

Geochemical and Geomechanical Testing of Near Wellbore CO₂ Injectivity Improvement

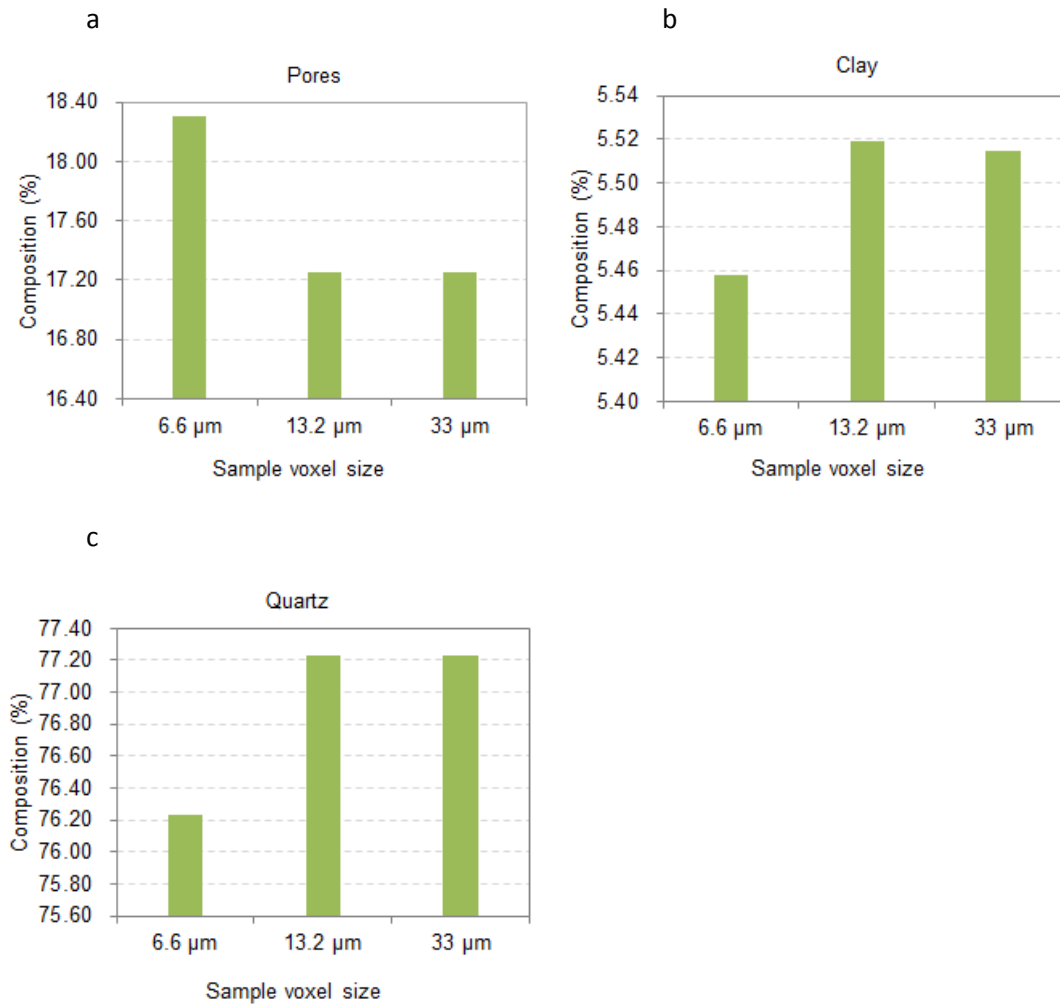


Figure 6.2-12: Composition analysis of the digital sample (6.6 mm × 6.6 mm × 12.276 mm) with different voxel sizes (6.6 μm, 13.2 μm and 33 μm): volume ratio of pores (a), clays (b) and quartz grains (c).

Figure 6.2-12 shows the variation of each composition volume ratio under different voxel resolution conditions. In all 6.6 μm, 13.2 μm and 33 μm cases, quartz takes up more than 75% of the whole sample volume (Figure 6.2-12c), pore volumes are less than 20% (Figure 6.2-12a) and clays are around 5% (Figure 6.2-12b). Clear differences in each composition ratio are observed as the voxel size is coarsened from 6.6 μm to 13.2 μm. For instance, the pore volume ratio shrinks from more than 18.2% to around 17.2%, which is due to the loss of narrow pore throats; whilst for both clay and quartz the volume ratio increases. The results have shown that around 1.0 % of pores (larger than 6.6 μm but smaller than 13.2 μm) exist between sections of clays or quartz grains. When comparing the 13.2 μm and 33 μm voxel size cases, there is no clear difference for each composition ratio due to the highly coarsened process, which also shows most of pores (99%) have a size larger than 33 μm. Similarly to these investigations of the sensitivity of pore space geometry at the coarser-scaled simulations, X-ray micro-CT scans with large voxel size (lattice resolution, larger than 6.6 μm)

could also result in loss of the detailed internal structure information (especially some narrow pore throats) of the porous media.

6.2.2.4.2. Sensitivity of mineral properties on the microscale fluid dynamics

With the aim of analyzing the sensitivity of mineral component effects on the microscale fluid dynamics, three cases are compared with different localized intrinsic clay porosities, namely 0.0 (very tight clay structure), 0.01 (low permeability) and 0.1 (some permeability). The porosity of quartz is set as 0.0, and that of pore apertures is set as 1.0. The fluid is driven under a pressure gradient of 0.1 along the positive z-axis (vertical direction), and all the side walls are set as free-slip boundaries. For XLBM calculation parameters, the relaxation time τ is defined as 1.25 and the Reynolds number (Re) is defined as 0.1 in this case for computing stability.

For clarity, the fluid flux fields are shown for a small part representing only 1.2 mm × 1.2 mm × 0.24 mm of the block. Figure 6.2-13a1, b1 and c1 have the same geometric structure and topology, but with different clay porosity: 0.0 (no flow occurring through the clays) in a1; 0.01 in b1; and 0.1 in c1. The constituents are visually distinguished through artificial colouring as: cavity – light blue, clay – light yellow and quartz – black. Clay porosity is observed as the light yellow areas in these figures. The respective fluid flux fields as shown in Figure 6.2-13a2, b2 and c2 illustrate the fact that increases in the permeability of the clay-rich areas successively contribute to these experiencing a higher proportion of the fluid transport.

6.2.2.4.3. Sensitivity of voxel resolution and mineral properties on the directional permeability

Grid independence is a basic consideration of the XLBM simulations. As mentioned in Section 6.2.2.3.1, in the case of heterogeneous sandstone considered here the sample has 1% of pore throats with a size less than 13.2 μm , whilst 99% are larger than 33 μm . Given that the narrowest pore throats (approximately around 6.9 μm) only occupy one lattice node, this portion (about 1% of the total) can be neglected here. As the sample tortuosity is quite complex, it is not feasible to define the accurate ratio of lattice nodes versus pore apertures for grid independence. Therefore, we compare these different voxel resolution and mineral component effects on the directional permeability in order to evaluate the grid independence. Through this exercise we also aim to access the representative scale size in the following section.

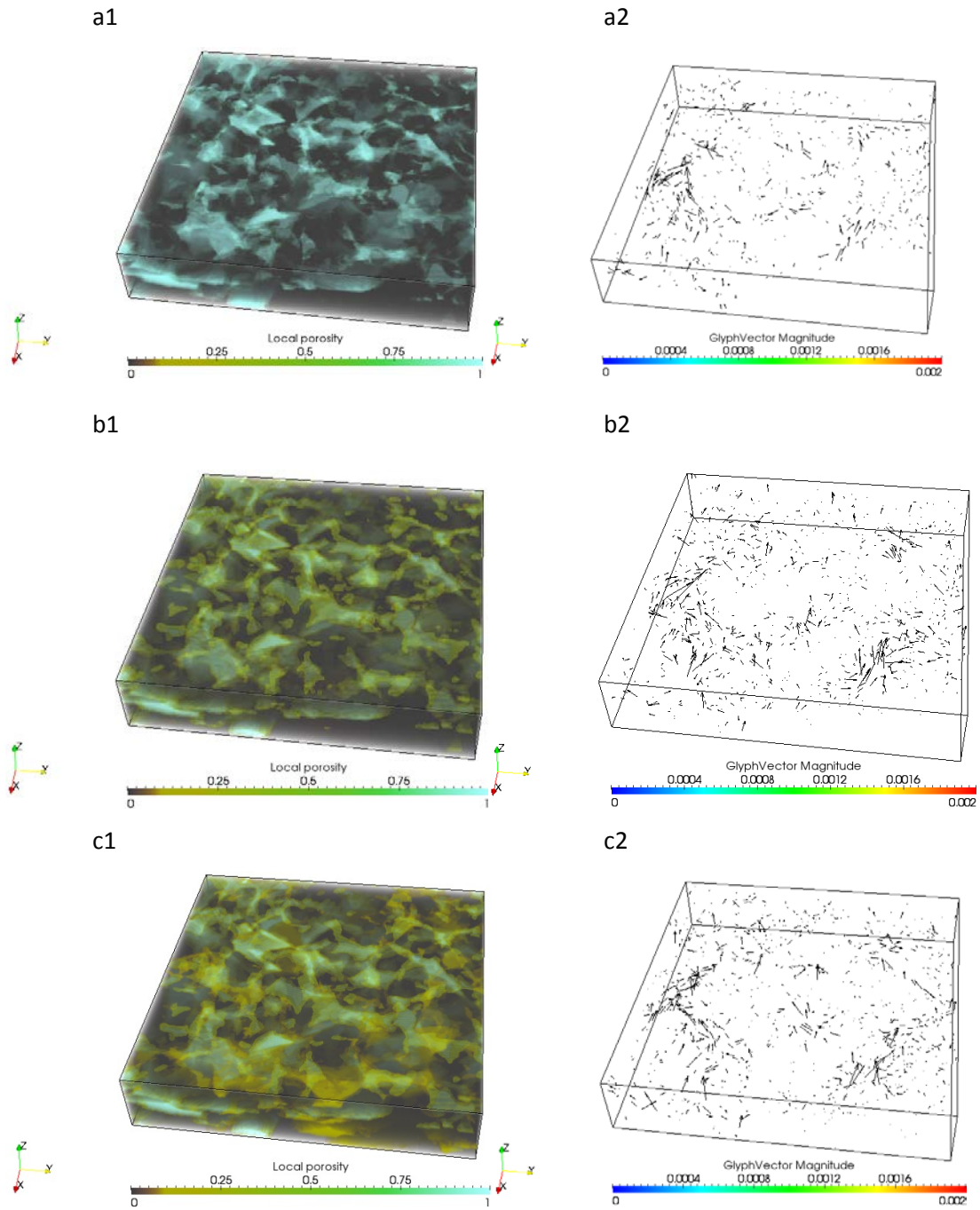


Figure 6.2-13: Digital sub block of the sample (1.2 mm × 1.2 mm × 0.24 mm, cavity – light blue, clay – light yellow and quartz – black) and its flux field distribution under intrinsic clay porosity of 0.0 (a1, a2), 0.01 (b1, b2) and 0.1 (c1, c2).

The directional permeability K is related to the fluid flux fields according to the Darcy's law (Pant et al., 2012; Whitaker, 1986):

$$K = \frac{v_e \bar{u}}{\nabla P} \quad (6.2-1)$$

Here, \bar{u} is the average velocity of the fluid flow in the porous medium and ∇P is the pressure gradient applied to the fluid flow.

The key point is that modelled vertical permeability in each voxel resolution case varies from hundreds to thousands of mD as a result of the variation of different composition volume ratios. The directional permeability goes up as the voxel resolution is coarsened (Table 6.2-1). The large difference in directional permeability among different voxel resolution cases is due to the non-fidelity of porous media information when coarsening the voxel size. Essentially, a five-fold increase in voxel size resulted in a 57% overestimation of the permeability of the modelled material in the example case for Table 6.2-1.

The problem is that in order to capture within the model the quite small pores inside the dense geomaterials a small voxel size is required, and an even smaller voxel size than that is required for building pore throats. Numerical simulations of fluid flow are quite sensitive to the geometry of pore throats.

Due to the complex sample tortuosity, the accurate ratio of lattice nodes versus pore apertures for grid independence is hard to define. Regarding the directional permeability, as high or better resolution than 1000 × 1000 × 1860 is required for achieving better grid independence where most of pore apertures at the 6.6 μm voxel resolution are at least represented by 5 lattice nodes.

Table 6.2-1: Example of voxel resolution effects on the modelled directional permeability.

Voxels	1000 × 1000 × 1860 (6.6 μm voxel size)	500 × 500 × 930 (13.2 μm voxel size)	200 × 200 × 372 (33 μm voxel size)
Vertical permeability (mD)	820	1220	1900

6.2.2.4.4. Representative scale evaluation of the core sample

The representative scale is the smallest sample size that provides reliable and representative transport calculations (e.g. directional permeability and connectivity) for upscaling reference. Because the data requirements at very fine resolution are enormous, beyond the foreseeable capacity of even the largest conventional supercomputers, it is necessary to determine the largest

voxel size (or length scale) that carries representative geometric information and fluid transport phenomena for correct macroscopic depiction. Due to the low impact of clay on the overall permeability, we only study the effect of X-ray micro-CT voxel resolutions and sample sizes (vertical length in this case) on the flow character – permeability, and then define the effective representative size for the Chinchilla 4 Precipice Sandstone sample discussed here.

Figure 6.2-14 shows the (calculated) permeability along the vertical direction. This changes with both sample size and voxel resolution: thus, for larger sample sizes, say > 10 mm, coarser voxels provide essentially the same outcome as very fine resolution, but if the sample is small, say <5 mm then much higher resolution is necessary. The obvious reason is that coarsened voxel resolution in small samples causes severe loss of the internal structure information in the porous medium. If the sample size is smaller than the representative size, even higher voxel resolution cannot retain the representative physical structure fidelity (e.g. pore size, grains of matrices and connectivity).

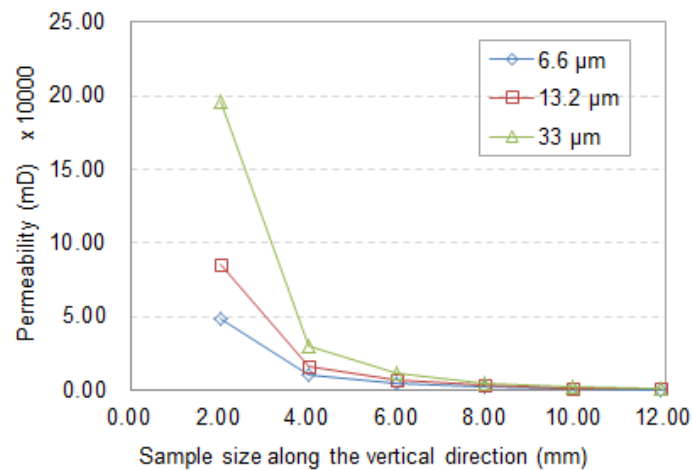


Figure 6.2-14: Permeability variation according to different sample scales (considering voxel size as 6.6 μm, 13.2 μm and 33 μm)

6.3. Near Wellbore Reservoir Modelling

6.3.1. Summary

One of the major costs of a CO₂ sequestration project is the well drilling and development. The assessment on the required number of wells is based on the estimated well injectivity, which is a function of formation porosity, permeability and the allowed overburden pressure, amongst others. However, what is often overlooked is the dynamic change in formation porosity and permeability as a result of the CO₂-water-rock interactions, which may lead to an over-conservative estimate on the required number of wells. The result of CO₂-water-rock interaction in the near-wellbore environment is potentially similar to the porosity enhancement that occurs due to conventional acid stimulation techniques. This part of the ANLEC project examines the injectivity change of a

sandstone formation during the injection of supercritical CO₂. Software (CMG-GEM) is used to simulate various case scenarios on the basis of our laboratory investigations. The reservoir stimulation studies showed, for formations with ~20% initial porosity, that every 1% porosity increase as the result of mineral dissolution would yield a 10% injectivity increase. The lower the initial porosity, the higher the percentage increases. The economic evaluation of the simulated reservoir cases suggested that costs can be saved through reducing the number of wells and injection pressure. Cost reductions through the compression element appear to be more attractive compared to that for the injection element.

6.3.2. Introduction

Economic considerations and surface impact concerns generally mean that it is desirable to drill the minimum number of wells that can accommodate the required flow of CO₂, and operating for maximum injection per well. A consequence of maximizing injection is the increased risk of pressure build-up within the reservoir causing fracture of the seal or induced seismicity. Therefore, the estimation of CO₂ injectivity, the required number of injection wells and site storage capacity are of significant importance in assessing and selecting sites for deploying CO₂ injection.

Simulation studies of CO₂ sequestration into sedimentary reservoirs have received considerable research attention with a variety of studies reported in the literature, examining different aspects and perspectives (e.g. Ghanbari et al., 2006; Ukaegbu et al., 2009; Nghiem et al., 2004; Xu et al., 2003; Izgec et al., 2008; Law et al., 1995; Kumar and Bryan 2008; Audigane et al., 2007; Ozah et al., 2005; Doughty 2006; Sifuentes et al., 2009; Juanes et al., 2006). Nevertheless, injectivity has received relatively little attention, despite being one of the most important and key aspects of the processes determining CCS viability.

Technically, the process of CO₂ injection into sedimentary formations for sequestration purposes relies in the long run mainly on hydrodynamic and mineral trapping mechanisms (Bachu 2003; IPCC, 2005). The extent of these mechanisms depends on the thermodynamic and petro-physical properties of the reservoir (Bachu 2003; Bachu 2008). During CO₂ injection, the area around the well undergoes changes in petro-physical properties due to dissolution and precipitation of minerals (Nghiem et al., 2004; Ofor and Engler 2011). Pruess et al. (2003) and Xu et al. (2003) identified that changes in porosity are a very important issue for CO₂ injection, as a small change in porosity could result in a significant change in permeability that in turn affects the injectivity (Xu et al., 2003).

The near wellbore area is the critical region during injection, as most of the resistance to flow occurs in this region. The focus of the research described here is to evaluate how permeability changes favourably as a result of mineral dissolution and the effect this has on injectivity.

Core samples from the Wandoan site, where the Precipice Sandstone has been identified as a potential injection target, show that < 1% up to 4% by volume minerals may be readily soluble in brine saturated with CO₂ at reservoir conditions depending on mineralogy. The undisturbed porosity of this formation is taken to be ~21% for this simulation. For this model, we consider changes in reservoir porosity of up to a 4% increase as a result of CO₂-water-rock interactions.

From an economic perspective, the process of CO₂ injection from the production source to the sequestration sink consists of four main elements: costs of CO₂ capture, compression, transportation and injection (IPCC, 2005). High costs associated with this process chain are one of the main hurdles for wide scale deployment of CCS (Gaspar et al., 2005). Assuming the cost of CO₂ capture per volume is fixed; this study also examines the economic and risk mitigation consequences of potential injectivity increases.

The model that is applied for CO₂ injection here utilises CMG-GEM software (CMG-GEM, 2012). The base permeability comes from experimental data (Evans, 2012) along with relative permeability information which is required for modelling. The base permeability is consistent with our own permeability measurements for Precipice Sandstone corrected for modelled stress (165mD from Evans vs 168mD from our measurement).

We then consider different case scenarios in which the near wellbore region is locally assigned different porosity (and consequently different permeability) values. The change in porosity from mineral dissolution due to CO₂ injection covers the range that we have experimentally measured. The actual chemical reactions themselves were not part of the reservoir model. Rather, on the basis of the experimental results of this study and the related GWB reaction modelling, different changes in total porosity were set in the model (at different time steps) for the purposes of assessing potential changes in injectivity due to short-term geochemical reactions expected during plume migration.

An economic assessment for the different simulation cases is obtained by adopting published cost estimates, applied to our particular process requirements and scaled to 2013 AU\$ using the Chemical Engineering plant cost index, and then converted to AU\$ at an exchange rate of 1AU\$=0.9US\$. Though crude, this serves to provide some indication of the economic consequences of not correctly accounting for chemical-dynamic changes to permeability arising from CO₂ injection.

6.3.3. Reservoir Simulation Model

This study considers a simplified reservoir geometry, which serves to afford some insight regarding the injectivity and capacity for an idealized aquifer to accept and retain large quantities of injected

CO₂ through structural and solubility trapping. The reservoir is idealized so that the important effects that are being investigated are more readily apparent.

The following cases are examined:

- Where the CO₂ injection has no effect on the porosity, permeability or mechanical properties of the injection zone. This would be the case if the reservoir rocks are inert and do not dissolve or interact at all under the changed conditions of injection.
- Where there is some interaction as a result of dissolution of mineral matter in the carbonic acid resulting from CO₂ injection. For these cases, the porosity in the immediate completion zone (to a radius of 20m) increases from an initial 21% to higher values as a result of dissolution of some mineral matter. In Case (i) porosity increases modestly (to 22 and 23%) as in a relatively unreactive sandstone unit; whereas in Case (ii) there is a higher degree of interaction and dissolution (to 23 and 25% porosity), which reflects approximately the conditions of injection into a slightly more reactive sandstone unit.

Details of the reservoir, fluid and rock properties and well properties are given in Appendix A. Details of the costing and economic evaluation are given in Appendix B.

The simulation applies a constant pressure boundary on the reservoir, i.e. the water that is initially contained in the reservoir is free to be displaced outwards. Many modelling scenarios apply a constant volume reservoir, i.e. the CO₂ that is injected is accommodated by compressing the water and the rocks. This latter assumption severely limits the injection rate since the reservoir pressure rises over time as compared to an open boundary case where the overpressure dissipates away through the edge of the reservoir. We believe open boundaries to flow more correctly represent the reality of the Precipice Formation in the Surat Basin.

6.3.4. Results and Discussion

6.3.4.1. *Process outcomes*

Figure 6.3-1 shows the extent of the plume after 2 years of injection. When injection commences, the area close to the well is quickly swept with scCO₂, displacing brine. Nevertheless, an appreciable amount of brine remains trapped in pockets within the swept zone, occupying ~45% of the pore space, the remainder being filled with scCO₂ fluid. The scCO₂ has a much lower density than the brine and rises under buoyancy up to the top seal layer. The CO₂ dissolves in the brine that it contacts, saturating the areas where CO₂ predominates (the red area in Figure 6.3-1) and migrating via viscous and diffusive mass transport at the edges of the plume. The plume spreads out beneath the seal layer away from the well, as injection proceeds. This pooling effect under the seal cap

continues throughout and after the injection period, which may last decades. (For the model, we have used only 2 years of injection, representing a proposed trial).

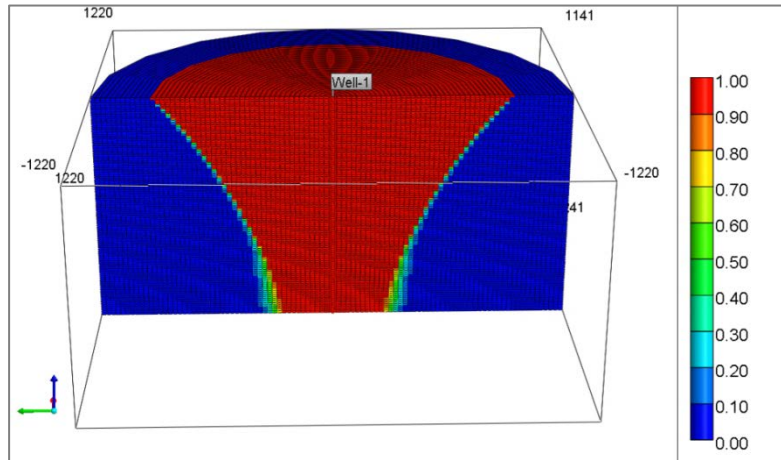


Figure 6.3-1: Plume dispersion for case 1 after 2 years of injection

When the CO₂ dissolves in brine, this is acidified resulting in a drop in pH that will cause some minerals to dissolve (e.g. Dawson et al., 2014; Farquhar et al., 2014; Nghiem et al., 2004; Xu et al., 2003). These may be carried out with brine that is displaced (in the radial direction in the simple model) into the greater reservoir, or remain within the brine trapped inside the plume zone. Dissolution of minerals removes solid material and thereby increases pore space and hence permeability. This mineral dissolution has been observed through our experimental investigation. Figure 6.3-2 and Table 6.3-1 illustrate that this increase in permeability in the near wellbore zone has a significant impact on injection: for each 1% increase in porosity, the injection rate increases by about 10%. Case 1, where porosity increases by 1% in the immediate completion zone (corresponding approximately to what might be expected in the Precipice Sandstone), predicts 12% more gas to be injected for the same bottom hole pressure, than if neglecting dissolution. In case 4, where porosity increases from 21% in the base reservoir model to 25% in the completion zone, due to mineral dissolution (a reasonable prospect in parts of the Hutton Formation and the Berea Sandstone), the injectivity is 52% greater. In a multi-well sequestration project, this corresponds to a potential capital saving of almost 1 well in 3, for the same CO₂ disposal rate.

It may be noted that the injectivity as modelled is ~2.2 million tons per year, a high rate for a single well. Comparatively, the Gorgon project proposes to inject ~500,000 tons per year per well (for each of 9 proposed wells). There are two principle reasons for this much higher injectivity: the average permeability for modelling the Gorgon reservoir is reported to be 25mD (cf. 165mD for the Precipice simulation here); and in the Gorgon project there is some pressure development during injection,

since water extraction empties only 63% of the local pore space (cf. open flow boundaries, which essentially means no pressure build up, for the Precipice simulation here).

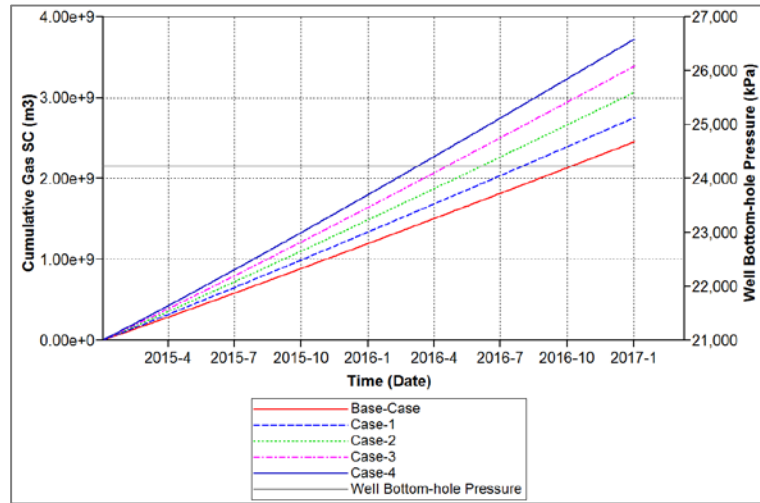


Figure 6.3-2: Injection rates for different porosities and permeabilities.

Table 6.3.1: Incremental increase of CO₂ injection for different cases.

Run	Porosity fraction	Permeability (mD)	Incremental Increase “fraction”
Case-1	0.22	195	1.12
Case-2	0.23	228	1.25
Case-3	0.24	266	1.38
Case-4	0.25	309	1.52

The simulation setup used in this report is very much simplified in order to provide an illustration only of the techno-economic impact of dissolution enhanced permeability and the importance of incorporating this process in modelling; it does not seek to represent an realistic, actual reservoir for which a more detailed static reservoir description and a much finer and more realistic gridding would be appropriate.

6.3.4.2. *Economic consequences*

This increase in permeability may be exploited to reduce costs in two ways: by reducing the (effective) number of wells – a saving in well costs, or by reducing the injection (bottom-hole) pressure, that is the compression requirements. We consider first reducing the number of wells, and take the simple approach of ratioing the cost against the base case. This has the effect of requiring a ‘fraction’ of the base case number of ‘wells’, for the same injection rate or, more realistically for a multi-well project, reducing the total number of wells that are required.

The cases that have been simulated are a base case with 21% pore volume, and four additional cases (22, 23, 24 and 25% porosity) representing injection zones with increasing amounts of soluble

Geochemical and Geomechanical Testing of Near Wellbore CO₂ Injectivity Improvement

minerals. The injection rate is taken to be 2.2 Mtpa CO₂. Table 6.3-2 shows the potential economic benefit that arises from mineral dissolution (cases 1-4) if this is realized by reducing the capital cost of the well. The total well cost for the base case is \$4,335,000.

Table 6.3-2: Incremental increase of CO₂ injection and cost saving over base case (AUD2014).

Run	Porosity fraction	Permeability mD	Fractional Perm Increase	number of wells (fraction of base case)	Cost saving (\$)
Base Case	0.21	165	1	1	\$0
Case-1	0.22	195	1.12	0.89	\$464,000
Case-2	0.23	228	1.25	0.80	\$867,000
Case-3	0.24	266	1.38	0.72	\$1,194,000
Case-4	0.25	309	1.52	0.66	\$1,483,000

Alternatively, the permeability improvement may be used to reduce the pressurization requirements, e.g. using the base case well, but with lower injection pressure. In this case the well costs are constant and the savings are made through reduced compression by way of pump capital costs and lower energy expenditure. Table 6.3-3 compares the annual cost savings from this strategy. For the base case, total compression capital and operating costs excluding power are \$51.5m and the annual compression power costs are \$54.3m. Most of these compression and power costs will in practice be incurred at the CO₂ dispatching end, e.g. at the power station where CO₂ is captured and compressed for pipeline transfer. The difference between the pump outlet pressure, the surface CO₂ pressure required, and the injection (bottom-hole) pressure, arises from the static head of the CO₂ in the injection well.

Because of the uncertainty in the actual injectivity that will be achieved in any proposed reservoir, projects generally would be obliged to drill extra wells to mitigate the risk that some wells may underperform expectations. Furthermore, the delivery pressure of CO₂ to the sequestration site may be set by a variety of considerations including amongst many others, economic optimization of the pipeline size, initial and booster compressor sizing considerations.

Geochemical and Geomechanical Testing of Near Wellbore CO₂ Injectivity Improvement

Table 6.3-3: Reduction in bottom-hole pressure for constant CO₂ injection and cost saving per year over base case (AUD2013).

Run	Average BHP (MPa)	Pump outlet pressure (MPa)	Pump saving (\$)	Power saving (\$)	Total saving (\$)
Base-Case	26,780	17.92	0	0	0
Case-1	25,269	16.66	150,000	190,000	340,000
Case-2	24,008	15.63	280,000	340,000	620,000
Case-3	22,948	14.79	330,000	470,000	850,000
Case-4	22,051	14.09	460,000	570,000	1040,000

Nevertheless, it is clear from Table 6.3-2 and Table 6.3-3 that reducing CO₂ compression is by far the more favorable strategy as opposed to reducing well numbers to take advantage of higher reservoir injectivities due to porosity enhancement derived from mineral dissolution. These cost savings are appreciable, and need to be included in economic analysis and justification for sequestration projects.

7. Discussion of Modelling Results – Outcomes and Significance

The injection of CO₂ into water bearing reservoirs in most cases will sufficiently reduce the formation water pH to cause dissolution of some minerals. Although the models indicated that some precipitation may have also taken place during the experiments, this was far outweighed by the dissolution reactions. This increases the predicted porosity in the critical near wellbore zone which in turn improves permeability and increases the CO₂ injectivity. This is usually not taken into account, but the correct assessment of injectivity is commercially important insofar as it influences the decisions about the number and size of the injection wells for a given sequestration duty, and the operation – most importantly the injection pressure, of the wells.

Near wellbore modelling even using very conservative simplifying assumptions shows substantial improvement in injectivity. More comprehensive dynamic modelling will push these predicted results to even bigger (more realistic) increases. This is shown to have significant (beneficial) design and commercial consequences.

By comparing cases where the dissolution improvement is not accounted with ones where it is, the economic consequences of using the higher injectivity for either: (i) reducing the number of injection wells that are necessary for a given CO₂ sequestration rate (thus resulting in capital cost savings), or (ii) with a fixed number of wells reducing the injection pressure necessary to infiltrate a given rate of CO₂ (reducing compression capital and operating costs), have been compared. Reducing the compression requirements leads to the better economic outcome; for the cases considered in the order of 50c per ton of CO₂ injected.

Regarding pore-scale modelling, which seeks to track more closely the actual physical transport through the porous media, XLBM modelling provides a useful tool for understanding the fluid flow and local changes to the flow architecture at the mesoscale. It provides insights regarding the impact of detailed heterogeneity and matrix properties on the fluid flow, the flow flux with respect to different sample sizes, and it illuminates sample size effects on digitally derived permeability. Once a representative scale is established that provides reliable and representative transport calculations (e.g. directional permeability) for upscaling, detailed pore scale modelling leads to suitable average characteristic parameters suitable for input for the next size scale of modelling. While the general concepts by which this upscaling may be done are known, the detailed mechanics of carrying it out require further work.

8. Recommendations for Future Work

Natural variability within the reservoir makes over-reliance on a small number of measured samples for general modelling inputs risky. Nevertheless, the measured outcomes in terms of solubilised minerals, laboratory measured porosity, well log porosity, laboratory measured permeability and permeability derived from well log grain size (the latter is currently unpublished work) are all reasonably consistent, providing a reliable basis for reservoir model development. Geological heterogeneity can only truly be addressed by a detailed survey of the subsurface structures.

Even so, further experiments on sister samples of this study could be used to investigate the impacts of a wider range of CO₂ geosequestration scenarios (including longer term reactions), comparing these with the base cases presented here. A related project (CO₂CRC 1.5; Pearce et al., 2014) has found greater mineral reactivity during reaction of fixed ratios of CO₂-SO₂ or CO₂-SO₂-O₂ dissolved in either fresh water or brine. Co-contaminants such as SO₂, O₂, and NO₂ are found in the flue gas of power stations and are costly to separate from CO₂. In some of the experiments, increased porosity was observed, whereas in others significant mineral precipitation occurred. Varying the ratios of CO₂ and co-contaminants, among other variables, for given rock compositions would be useful for determining optimal mixtures to either enhance reservoir porosity and hence permeability, or instigate mineral precipitation as a trapping mechanism for stored CO₂. Furthermore, the impact of co-contaminants such as NO₂ on geological materials has not yet received any significant level of attention.

Different ranges of salinity gave different permeabilities even using quite quartzose sandstones prior to any geochemical experiments taking place (e.g. Figure 2.5-2). It would be useful to know the differences in a given sample composition's permeability sensitivity to geochemical reactions at different salinities. Other work done for ANLEC project 7-1011-0189 has implicated mixing between CO₂-saturated, high salinity basinal brine with low salinity meteoric-derived groundwater in the formation of massively carbonate cemented zones, natural examples of so-called mineral trapping of CO₂. From a project whole-of-life perspective, it would be beneficial to have a greater understanding of the ultimate fate of injected CO₂, and how it may be possible to artificially engineer such processes as mineral trapping of the CO₂.

Permeability, which is one of the key attributes for CO₂ injection and storage, is also sensitive to relative permeability between the scCO₂ phase and the predominantly water phase. The residual (irreducible) quantities for these phases are also an important requirement of the reservoir model. Neither relative permeability nor irreducible fluid quantities are explicitly known for the Precipice, Evergreen or Hutton formations. We have applied values determined for Berea Sandstone, along

with a very simplified stratigraphy for the near wellbore and economic models, for illustrative purposes. These sample-dependent characteristics and their associated parameters are required for proper reservoir and economic model development.

Laboratory observation also indicates that fines creation and migration may considerably impair permeability. This mobilization may arise from fluid transport, from chemical composition changes in the fluids, decementing of thin barrier layers, or physical damage from local overstraining. A better understanding of fines induced permeability changes and their potential impact on reservoir flow and plume migration would provide critical injectivity risk reduction information.

The mechanical property (stress-strain) tests on some samples showed dilation in one direction under stress. While possible, dilation is an unexpected and unusual response. This underlying causes of this behaviour, whether natural or an as yet undefined experimental artefact, warrants further investigation.

Meso-scale simulation using XLBM and digitized cores shows considerable promise to build a 'bottom-up' modelling framework that provides physically realistic representation of transport processes (material and thermal flows) and material dynamics (local dissolution/precipitation, occlusion, swelling/shrinkage due to chemical or temperature changes). The massive size of data sets required for this level of detail makes rendering of more than a few cubic centimetres of rock unrealistic even using present supercomputer capabilities.

Nevertheless, properties can in principle be upscaled – for example by tessellating small detailed renditions into larger volumes - to provide key reservoir average characteristics such as directional permeability dynamics, changes to porosity and porosity distribution and material strength. The methodology for achieving this, however, needs to be developed. Also, while the mechanics for modelling multiple simultaneous and coupled physical phenomena such as material flow, chemical changes, physical changes to the flow topography *ia*, are known, encompassing them in a single simulation framework providing a high level of mathematical robustness and stability remains open. In addition, all of the detailed physical information that is necessary for modelling each step, such as reaction or solution rate equations, species and species interaction dependencies and many others, all need to be defined, collated and incorporated.

Key areas for additional work are consequently:

Laboratory:

- Extending physical and chemical characterisation to a larger sample suite and set of experimental variables (e.g. gas impurities, wet scCO₂ phase mineral interactions, temperatures, pressures, salinities, water-gas-rock ratios, longer timeframes) to provide better and more confident correlation between measured properties and properties derived from (for example) well log tools and modelling.
- The relative impact of individual properties such as sample surface area and the proportion of fines relative to large grains of the same composition upon measured and modelled geochemical reactions are still poorly defined.
- Experiments to better constrain both dissolution and precipitation rates of minerals under conditions relevant to CO₂ geosequestration (e.g. temperature, pH, salinity, ligands) would bolster the existing datasets of predominantly 'standard P-T conditions' mineral kinetic and thermodynamic data.
- There is very little information regarding relative permeability or residual fluid amounts, of CO₂ saturated water and water saturated scCO₂ phases (or more strictly, the fluid phase/solid phase surface physical and chemical interactions) that is directly applicable to the samples used in this study. No work has yet been done with the samples themselves to determine these properties.
- Fines induced blockages and their impact on permeability should be investigated.

Modelling

- At a reservoir scale, the sensitivities to input properties having significant uncertainty, e.g. barrier layers on fluid migration needs to be explored. The increase in permeability and injectivity resulting from dissolution in the CO₂ plume zone has been shown to be significant: the dynamics and sensitivities to property changes (including relative permeability and dynamic changes from fines migration) remain unexplored.
- The XLBM has been shown to be an effective tool in providing both physical insight at a scale where the major operational dynamics are governed, but which is difficult to access in the laboratory, as well as numerical values for reservoir scale average properties and their dynamic evolution. There is, however, a great deal of detailed development still to be done to fully exploit the power of this technique.
- Adding capabilities to existing geochemical modelling software, such as the ability to simultaneously model a range of surface areas and corresponding masses for individual

minerals, rather than just having single fixed values for these, would help to determine whether the non-linear trends of given dissolved elements over time during experiments were due mainly to mineral fines, strictly changes in fluid saturation state, or combinations of factors. Furthermore, for most minerals there is scant basic experimentally determined kinetic and thermodynamic data across the range of physio-chemical conditions relevant to CO₂ geosequestration. It is also difficult to fully model complex phenomenon such as incongruent mineral dissolution or mixed-species gas-aqueous reaction dynamics (e.g. CO₂-SO_x-NO_x-O₂-H₂O etc.) using GWB. The reactive transport software ToughReact may have greater potential for adaption to modelling complex real geochemical systems relevant to CO₂-sequestration, but it is not yet a substitute for existing commercial reservoir-scale modelling software. Theoretically, additions could be made to the ToughReact source-code to enable it to compete with products such as CMG, Petrel, and SKUA-GOCAD at the reservoir-scale, given that the ToughReact code is open-access. Alternatively, ToughReact could be incorporated as a sub-module of one of the existing reservoir modelling software packages and used to inform and refine models.

9. Acknowledgments

Julie Pearce acknowledges the funding provided by the Commonwealth of Australia and industry sponsors through the CO2CRC Program. We would like to acknowledge and thank FEI Lithicon Digital Rock Services for access to X-ray micro-CT and QEMSCAN data. Thanks to Dirk Kirste for providing mineral kinetic rate scripts and guidance with the geochemical modelling methods, Vince Borris for supercomputer coding, Marietjie Mostert and Guia Morelli for assistance with ICP-OES analyses, Feliz Farrajota and Gang Xia for preparation of the polished thin sections, and Anastasia Dmyterko, Hui An and Lei Ge for the Hg-porosimetry analyses. We acknowledge the facilities, and the scientific and technical assistance, of the Australian Microscopy and Microanalysis Research Facility at the Centre for Microscopy and Microanalysis, The University of Queensland.

10. References

- Advanced Resources International. (2006). Basin Oriented Strategies for CO₂ Enhanced Oil Recovery: Permian Basin. US Department of Energy: Arlington, VA. p. 117.
- Atrens, A., Gurgenci, H. and Rudolph, V. (2011). Economic optimisation of a CO₂-based EGS power plant. *Energy and Fuel*, 25(8), pp 3765-3775.
- Audigane, P., Gaus, I., Czernichowski, L.I., Pruess, K. and Xu, T. (2007). Two-dimensional reactive transport modelling of CO₂ injection in a saline aquifer at the Sleipner site, North Sea. *American Journal of Science*, 307(7), pp 974-1008.
- Bachu, S. (2003). Screening and ranking of sedimentary basins for sequestration of CO₂ in geological media in response to climate change. *Environmental Geology*, 44(3), pp 277-289.
- Bachu, S. (2008). CO₂ storage in geological media: Role, means, status and barriers to deployment. *Progress in Energy and Combustion Science*, 34(2), pp 254–273.
- Barnard, M. (2014). Wind Energy Beats Nuclear & Carbon Capture For Global Warming Mitigation. Clean Technical Retrieved July 13, 2014, from <http://cleantechnica.com/2014/07/29/wind-energy-beats-nuclear-carbon-capture-global-warming-mitigation/>
- Black, J.R. and Haese, R.R., 2014. Chlorite dissolution rates under CO₂ saturated conditions from 50 to 120°C and 120 to 200 bar CO₂. *Geochimica et Cosmochimica Acta*, 125, pp 225-240.
- Brandt, F., Bosbach, D., Krawczyk-Bärsch, E., Arnold, T., Bernhard, G., 2003. Chlorite dissolution in the acid pH-range: a combined microscopic and macroscopic approach. *Geochimica et Cosmochimica Acta*, 67, pp 1451-1461.
- Bethke, C.M., Yeakel, S. (2013). The Geochemist's Workbench Release 9.0: Reaction Modeling Guide. Aqueous Solutions, LLC, Champaign, Illinois.
- CMG-WinProp. Phase-Behaviour and Fluid Property Program. Version 2012 User's Guide. Computer Modeling Group Ltd., Calgary, Alberta.
- CMG-GEM. Advanced Compositional and Unconventional Reservoir Simulator. Version 2012 User's Guide. Computer Modeling Group Ltd., Calgary, Alberta.
- Darcy, H. (1856). Les Fontaines Publiques de la Ville de Dijon, Dalmont, Paris.
- Dawson, G. K. W., Khan, C., Farquhar, S. M., Biddle, D., Jiang, X., Pearce, J., Rudolph, V. and Golding, S. D. (2013). ANLEC R&D Project #3-1110-0101: Initial batch geochemistry and first 4D geomechanical and permeability experiment results. Edited & Externally Peer Reviewed Report, URL: <http://www.anlecrd.com.au>. Manuka, ACT, Australia, p. 45.
- Dawson, G.K.W., Pearce, J.K., Biddle, D. and Golding, S.D. (2014). Experimental mineral dissolution in Berea Sandstone reacted with CO₂ or SO₂-CO₂ in NaCl brine under CO₂ sequestration conditions. *Chemical Geology*, in press.

- Dixon, O., Draper, J.J., Grigorescu, M., Hodgkinson, J. and McKillop, M. (2010). Queensland Minerals and Energy Review, Queensland Carbon Geostorage Initiative Preliminary Report, Potential for carbon geostorage in the Taroom Trough, Roma Shelf and the Surat, Eromanga and Galilee Basins. The State of Queensland, Brisbane, Australia.
- Doughty, C. (2006). Modelling geologic storage of carbon dioxide: Comparison of non-hysteretic and hysteretic characteristic curves. In PROCEEDINGS, TOUGH Symposium, Lawrence Berkeley National Laboratory, Berkeley, California, May 15–17, 2006.
- Energy Information Administration. (1994). Costs and indices for domestic oil and gas field equipment and production operations, 1990 through 1993. DOE/EIA-TR-0568 report. U.S. Department of Energy, Washington, D.C. 20585.
- Evans, B. (2012). Predicting CO₂ injectivity properties for application at CCS sites. Report number 3-1110-0122. Curtin University, published by Global CCS Institute.
- Farquhar, S.M., Dawson, G.K.W., Esterle, J.S. and Golding, S.D. (2013). Mineralogical characterisation of a potential reservoir system for CO₂ sequestration in the Surat Basin. *Australian Journal of Earth Sciences*, 60, pp 91-110.
- Farquhar, S.M., Pearce, J.K., Dawson, G.K.W., Golab, A., Sommacal, S., Kirste, D., Biddle, D. and Golding, S.D. (2014). A fresh approach to investigating CO₂ storage: Experimental CO₂-water-rock interactions in a low-salinity reservoir system. *Chemical Geology*, in press.
- Galán, E. and Ferrell, R.E. (2013). Genesis Of Clay Minerals: In Bergaya F. and Lagaly G. (Ed.) *Developments in Clay Science, Volume 5 – Handbook of Clay Science*. Elsevier, pp 83 – 126.
- Gao, J., Xing, H., Rudolph, V., Li, Q. and Golding, S.D. (2014a). Parallel lattice Boltzmann computing and applications in core sample feature evaluation. *Transport in Porous Media*, under review.
- Gao, J., Xing, H., Rudolph, V., Li, Q., Golding, S.D. and Chi, X. (2014b). Permeability evaluation for diverse rock formation samples using parallel extended lattice Boltzmann computing. *Concurrency and Computation: Practice and Experience*, under review.
- Gao, J., Xing, H., Tian, Z. and Muhlhaus, H. (2014c). Lattice Boltzmann modeling and evaluation of fluid flow in heterogeneous porous media involving multiple matrix constituents. *Computers & Geosciences*, 62, pp 198-207.
- Gaspar, A., Lima, G. and Suslick, S. (2005). CO₂ capture and storage in mature oil reservoir: physical description, EOR and economic evaluation of a case of a Brazilian mature field. SPE paper 94181; SPE Europe/EAGE Annual Conference held in Madrid, Spain, 13-16 Jun 2005.
- Ghanbari, S., Al-Zaabi, Y., Pickup, G., Mackay, E., Gozalpour, F., and Todd, A. (2006). Simulation of CO₂ storage in saline aquifer. *Chemical Engineering Research and Design*, 48(9), pp 764-775.

- Golab, A., Knuefing, L., Goodwin, C., Sommacal, S., Carnerup, A., Dawson, G.K.W., Pearce, J.K. and Golding, S.D. (2014). Sub-project 5: Undertake time series (4D) imaging and conventional experimental studies to measure geochemical reactivity and dissolution trapping capacity of core material using supercritical CO₂. West Wandoan-1 well samples, ANLEC Project 7-0311-0128; Milestone 5.5 Report. FEI-Lithicon Digital Rock Services, Canberra, Australia, p. 61.
- Golab, A., Ward, C.R., Permana, A., Lennox, P. and Botha, P. (2013). High-resolution three-dimensional imaging of coal using microfocus X-ray computed tomography, with special reference to modes of mineral occurrence. *International Journal of Coal Geology*, 113, pp 97-108.
- Grigorescu, M. (2011a). Queensland Geological Record 2011/02, Mineralogy of the south-eastern Bowen Basin and north-eastern Surat Basin, Queensland. The State of Queensland, Brisbane, Australia.
- Grigorescu, M. (2011b). Queensland Geological Record 2011/05, Jurassic groundwater hydrochemical types, Surat Basin, Queensland - a carbon geostorage perspective. The State of Queensland, Brisbane, Australia.
- Hodgkinson, J. and Grigorescu, M. (2013). Background research for selection of potential geostorage targets—case studies from the Surat Basin, Queensland. *Australian Journal of Earth Sciences*, 60, pp 71-89.
- Hodgkinson, J., Grigorescu, M., Hortle, A., McKillop, M., Dixon, O., Foster, L. (2010). Queensland Minerals and Energy Review, The potential impact of carbon dioxide injection on freshwater aquifers: the Surat and Eromanga Basins in Queensland. The State of Queensland, Brisbane, Australia.
- Horner, K.N., Schacht, U. and Haese, R.R. (2014). Characterizing long-term CO₂–water–rock reaction pathways to identify tracers of CO₂ migration during geological storage in a low-salinity, siliciclastic reservoir system. *Chemical Geology*, in press.
- Hou, J., Li, Z., Zhang, S., Cao, X., Du, Q. and Song, X. (2009). Computerized tomography study of the microscopic flow mechanism of polymer flooding. *Transport in Porous Media*, 79, pp 407-418.
- IPCC (2005). IPCC Special Report on Carbon Dioxide Capture and Storage. Prepared by Working Group III of the Intergovernmental Panel on Climate Change [Metz, B., O. Davidson, H. C. de Coninck, M. Loos, and L. A. Meyer (eds.)]. Cambridge University Press, Cambridge, United Kingdom and New York, NY, USA, 442 pp.
- Izgec, O., Demiral, B., Bertin, H. and Akin, S. (2008). CO₂ injection into saline carbonate aquifer formations II: Comparison of numerical simulations to experiments. *Transport in Porous Media*, 73(1), pp 57–74

- Juanes, R., Spiteri, E., Orr Jr, F. and Blunt, M. (2006). Impact of relative permeability hysteresis on geological CO₂ storage. *Water Resources Research*, 42(12), pp 1-13.
- Kestin, J., Khalifa, E. and Correia, J. (1981). Tables of the dynamic and kinematic viscosity of aqueous NaCl solutions in the temperature range 20-150°C and pressure range 0.1–35 MPa. *Journal of Physical and Chemical Reference Data*, 10 (1), pp 71-87.
- Knackstedt, M., Carnerup, A., Golab, A., Sok, R., Young, B. and Riepe, L., 2013. Petrophysical characterisation of unconventional reservoir core at multiple scales. *Petrophysics*, 54, pp 216-223.
- Kumar, N., and Bryan, S. (2008). Optimizing injection intervals in vertical and horizontal wells for CO₂ sequestration. SPE paper: 116661; SPE Annual Technical Conference and Exhibition, Denver, Colorado, USA, 21-24 September 2008.
- Kaiser, M. and Rouge, B. (2014). Haynesville update-2: north Louisiana drilling costs vary slightly 2007-12. *Oil and Gas Journal*, 112(1). [online] Available at: <http://www.ogj.com/articles/print/volume-112/issue-1/exploration-development/north-louisiana-drilling-costs-vary-slightly-2007-12.html> [Accessed July 20 2014].
- Keck, R.J., Rudolph, V., Dawson, G.K.W. and Biddle, D. (2013). CHE4007: Individual Inquiry B. Simulating operational conditions for geosequestration within Hutton and Precipice Sandstones on a laboratory scale, School of Chemical Engineering. University of Queensland, Brisbane, Australia.
- Law, D., Bachu, S. and Gunter, W. (1995). CO₂ disposal into Alberta basin aquifers- Phase III: Hydrological and numerical analysis of CO₂-disposal in deep siliciclastic and carbonate aquifers in the Lake Wabamum area. Alberta Research Council, PO Box 8330, Edmonton, Alberta, Canada, T6H 5X2.
- Massarotto, P., Golding, S.D., Bae, J.S., Iyer, R. and Rudolph, V. (2010). Changes in reservoir properties from injection of supercritical CO₂ into coal seams -- A laboratory study. *International Journal of Coal Geology*, 82, pp 269-279.
- McCollum, D. and Ogden, J. M. (2006). Techno-Economic models for carbon dioxide compression, transport, and storage and correlations for estimating carbon dioxide density and viscosity. Institute of Transportation Studies, University of California, Davis.
- McCollum, D. (2006). Comparing Techno-Economic Models for Pipeline Transport of Carbon Dioxide. Institute of Transportation Studies, University of California-Davis.
- McCoy, S., and Rubin, E. (2009). The effect of high oil prices on EOR project economics. *Energy Procedia*, 1(1), pp 4143-4150.

- Nghiem, L., Sammon, P., Grabenstetter, J. and Ohkuma, H. (2004). Modelling CO₂ storage in aquifers with a fully-coupled geochemical EOS compositional simulator. SPE paper 89474; SPE/DOE Symposium on Improved Oil Recovery, Tulsa, Oklahoma, 17-21 April 2004.
- Ofori, A., and Engler, A. (2007). Effects of CO₂ sequestration on the petro-physical properties of an aquifer rock. SPE paper 147166; Canadian Unconventional Resources Conference held in Calgary, Alberta, Canada, 15-17 November 2011.
- Origin Energy. (2014). Business Electricity Tariffs Queensland - Origin Energy. [online] Available at: <http://www.originenergy.com.au/electariffqld> [Accessed 27 Jun. 2014].
- Ozah, R., Lakshminarasimhan, S., Pope, G., Sepehrnoori, K. and Bryant, S. (2005). Numerical simulation of the storage of pure CO₂ and CO₂-H₂S gas mixtures in deep saline aquifers. SPE Paper 97255; 2005 SPE Annual Technical Conference and Exhibition held in Dallas, Texas, U.S.A., 9 – 12 October 2005.
- Pant, L.M., Mitra, S.K. and Secanell, M. (2012). Absolute permeability and Knudsen diffusivity measurements in PEMFC gas diffusion layers and micro porous layers. *Journal of Power Sources*, 206, pp 153-160.
- Pearce, J.K., Kirste, D.M., Dawson, G.K.W., Farquhar, S.M., Biddle, D., Golding, S.D. and Rudolph, V., 2014. SO₂ impurity impacts on experimental and simulated CO₂-water-reservoir rock reactions at carbon storage condtions. *Chemical Geology*, in press.
- Pruess, K., Xu, T., Apps, J. and Garcia, Julio. (2003). Numerical modeling of aquifer disposal of CO₂. *SPE Journal*, 8(1), pp 49-60.
- Raabe, D. (2004). Overview of the lattice Boltzmann method for nano-and microscale fluid dynamics in materials science and engineering. *Modelling and Simulation in Materials Science and Engineering*, 12, R13.
- Reid, C., Prausnitz, M., and Sherwood, K. (1977). *The Properties of Gases and Liquids*, 3rd Edition, McGraw-Hill, New York.
- Rowe, M. and Chou, S. (1970). Pressure-Volume-Temperature-Concentration Relation of Aqueous NaCl Solutions, *Journal of Physical and Chemical Reference Data*, 15 (1), pp 61-66.
- Sifuentes, W., Giddins, M. and Blunt, M. (2009). Modeling CO₂ storage in aquifers: Assessing the key contributors to uncertainty. SPE paper 123582; SPE Offshore Europe Oil and Gas Conference Exhibition held in Aberdeen, UK, 8-11 September 2009.
- Smith, L.A. et al. (2001). Engineering and Economic Assessment of Carbon Dioxide Sequestration in Saline Formations, First National Conference on Carbon Sequestration, Washington D.C. (May 14-17, 2001). http://www.netl.doe.gov/File%20Library/Publications/Journals/vol2_no1.pdf

Geochemical and Geomechanical Testing of Near Wellbore CO₂ Injectivity Improvement

- Ukaegbu, C., Gundogan, O., Mackay, E., Pickup, G., Todd, A, and Gozalpour, F. (2009). Simulation of CO₂ storage in a heterogeneous aquifer. *Journal of Power and Energy*, 223(3), pp 249-267
- Whitaker, S. (1986). Flow in porous media I: A theoretical derivation of Darcy's law. *Transport in Porous Media*, 1, pp 3-25.
- Xu, T., Apps, J., and Pruess, K. (2003). Numerical simulation of CO₂ disposal by mineral trapping in deep aquifers. *Applied Geochemistry*, 19 (6), pp 917–936

APPENDIX A – Reservoir Model Details

Geological Model

The compositional simulator GEM from the Computer Modelling Group (CMG) suite was used for the model, applied as a simple radial (cylindrical) system (CMG-GEM, 2012). The grid system was established with 50 blocks in the radial direction, 2 blocks in the angular direction (perimeter) and 100 blocks in the vertical direction, making a total of 10,000 grid blocks. In plan view, the radial increment for each grid is 10 m in the innermost 2 rings and 25 m thereafter (for the next 48 rings). A large volume modifier (10^7) is applied to the outer boundary ring, providing a constant pressure boundary to the reservoir. This gives a total of 1220 m from the wellbore to the boundary, or a 1.22 km diameter cylindrical reservoir. This size is chosen so that the plume does not reach the outer boundary. Vertically, each grid-block is 1 m giving a total reservoir thickness of 100 m

The reservoir void space is assumed initially to be filled with water having a TDS of 1%. The reservoir operates under isothermal condition at 61 °C and has a top layer (1141m depth) pressure of 11925 kPa, which means the CO₂ is injected as a supercritical fluid (Table 3). These values are reasonably consistent with using either the Precipice or Hutton sandstones as the reservoir.

Fluid and Rock Properties

The rock property values used in the simulation study (Table A1) and the CO₂-brine relative permeability curves (Figure A1) were based on Berea Sandstone experimental measurements (Evans, 2012). These properties are similar to properties for the quartzose units of the Precipice and Hutton sandstones.

Fluid properties were calculated using CMG-WinProp (Table A2 and A3), a comprehensive equation of state module within CMG-GEM (CMG-WinProp, 2012). CO₂ solubility is modelled with Henry's Law as a function of reservoir pressure, temperature and salinity. The brine phase viscosity and density are estimated by using the Rowe and Chou (1970) correlation and the Kestin et al. (1981) correlation, respectively. The gas phase density is estimated with Peng-Robinson Equation of State (PR-EOS) and viscosity is predicted from the Jossi, Stiel and Thodos correlation (Reid et al., 1977).

Dissolution increases the porosity of the reservoir and this is correlated to an associated increase in permeability. Injectivity is directly proportional to reservoir permeability. Here, the simplified Carmen-Kozeny correlation (Nghiem et al., 2004; CMG-GEM, 2012) is used to change permeability as a function of porosity (Eq. A1)

$$K = K_0 \left(\frac{\phi}{\phi_0} \right)^3 \left(\frac{1-\phi_0}{1-\phi} \right)^2 \dots\dots\dots (Eq. A1)$$

Where; K and K₀ are current and original permeability, respectively. Similarly, φ and φ₀ are current and original porosity. The results for porosity, permeability are: [21%, 165mD]; [22%, 195mD]; [23%, 228mD]; [24%, 266mD] and [25%, 309 mD].

Table A1: Characteristics of the core sample used for the experiment

Sample ID	Lithology	Length, cm	Diameter, cm	Porosity, %	Permeability, mD
Berea B2	Sandstone	7.98	3.79	21	165

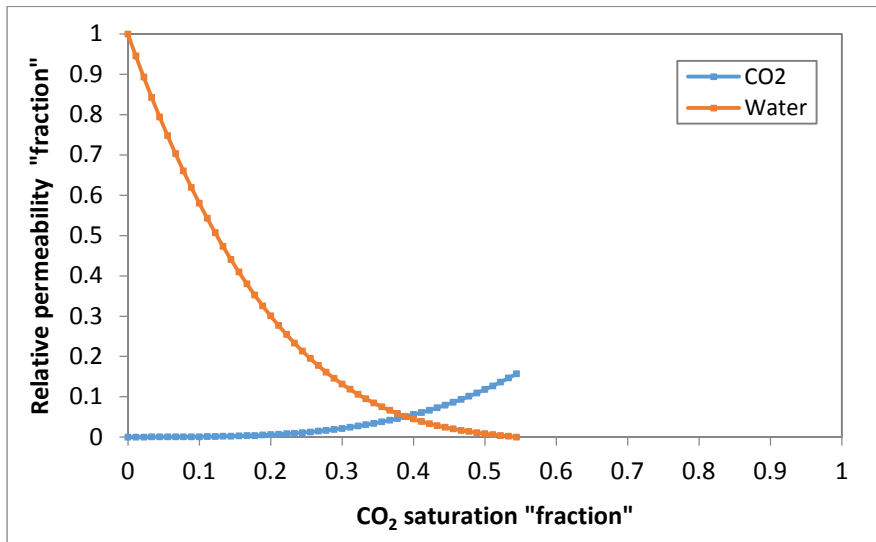


Figure A1: CO₂ and water relative permeability curves

Table A2: CO₂ standard physical properties used in the simulation

Carbon dioxide property	Value
Critical pressure (atm)	72.8
Critical temperature (K)	304.2
Critical volume (m ³ /kmol)	0.094
Molecular weight (g/gmol)	44.01
Acentric factor (dimensionless)	0.225
Boiling point (K)	211.77
Specific gravity (dimensionless)	0.818

Table A3: Base-Case properties of modelled aquifer

Aquifer Property	Value
Grid system	Radial (Cylindrical) grid
Grid number	Radial 50 grid blocks (grid increments 2×10m, 48×25m) Perimeter/angular direction 2 grid blocks Vertical 100 grid blocks (grid increments 1m)
Reservoir Depth (m)	1141
Reservoir Thickness (m)	100
Reservoir Pressure (kPa)	11925
Reservoir Temperature (°C)	61
Rock Compressibility (/kPa)	4.5×10 ⁻⁷ 1
Relative Permeability	Figure A1
Salinity	1% by weight

Well Properties

A single injection well was located in the middle of the modelled space and completed in the bottom layers over a 20m interval (Table A4). The injection well operates under one constraint (the primary constraint), which is a constant bottom-hole pressure of 24,225 kPa (almost twice initial pressure at the bottom layers of the formation). The injection is simulated for 2 years (comparable to a proposed trial injection at Wandoan) and in no case over this period does the CO₂ plume reach the modelled reservoir radial boundary.

Table A4: parameters for the injection well

Grids well completion (I, J; K)	1, 1, 80; 100
Injection duration	2 years
Well radius	0.0762 m
Skin	0
CO ₂ mole fraction	1
Maximum Bottom-hole Pressure	24,225 kPa

APPENDIX B – Economic Evaluation Details

Cost of CO₂ Compression

Cost of compression is calculated following the procedure of McCollum and Ogden (2006). In the gas phase, up to 7.4 MPa, the compression power requirement is given by equation B1:

$$W_{s,t} = \left(\frac{1000}{24 \times 3600} \right) \times \left(\frac{mZ_s RT_{in}}{M\eta_{is}} \right) \times \left(\frac{k_s}{k_s - 1} \right) \times \left[(CR)^{\frac{k_s-1}{k_s}} - 1 \right] \dots\dots\dots \text{(Eq. B1)}$$

Where ‘m’ is CO₂ flow rate (t/day), ‘Z_s’ is average CO₂ compressibility for each individual stage, ‘R’ gas constant (8.314 kJ/kmol-K), ‘T_{in}’ is CO₂ temperature at compressor stage inlet (K), ‘M’ is the molecular weight of CO₂ (44 kg/kmol), ‘η_{is}’ is isentropic efficiency of compressor, ‘k_s=(Cp/Cv)’ is average ratio of specific heats of CO₂ for each individual stage, ‘CR’ is the compression ratio of each stage.

$$CR = \left(\frac{7.38}{P_{initial}} \right)^{\left(\frac{1}{N_{stage}} \right)} \dots\dots\dots \text{(Eq. B2)}$$

Where ‘P_{initial}’ is initial pressure of CO₂ (MPa), ‘N_{stage}’ is number of compressor stages.

$$W_{total} = W_{s1} + W_{s2} + \dots\dots\dots + W_{sn} \dots\dots\dots \text{(Eq. B3)}$$

In the dense (supercritical or liquid) phase, the power calculation may be simplified to;

$$W_p = \left(\frac{1000 \times 10}{24 \times 36} \right) \times \left(\frac{m \times (P_{final} - 7.38)}{\rho\eta_p} \right) \dots\dots\dots \text{(Eq. B4)}$$

Where ‘W_p’ is pumping power requirement (kW), ‘ρ’ is the average density of CO₂ during pumping (630 kg/m³), ‘η’ is efficiency of pump.

The capital and operating costs of the compressor and pump are calculated by a model developed by McCollum and Ogden, (2006).

$$C_{comp} = m_{train} \times N_{train} \left[(0.175 \times 10^6) \times (m_{train})^{-0.71} + (1.886 \times 10^6) \times (m_{train})^{-0.6} \ln \left(\frac{P_{cut-off}}{P_{initial}} \right) \right] \dots\dots\dots \text{(Eq. B5)}$$

$$C_{pump} = \left[(1.495 \times 10^6 \times \frac{W_p}{1000}) + 0.07 \times 10^6 \right] \dots\dots\dots \text{(Eq. B6)}$$

Where ‘C_{comp}’ is capital cost of compression, ‘C_{pump}’ is capital cost of pump, ‘m_{train}’ is CO₂ mass flow rate through each compressor train (kg/s).

The total capital cost of compression is:

$$C_{total} = C_{comp} + C_{pump} \dots\dots\dots (Eq. B7)$$

The annual operating and maintenance costs are assumed proportional to the capex:

$$O \& M_{annual} = C_{total} \times O \& M_{factor} \dots\dots\dots (Eq. B8)$$

Where ‘O&M_{annual}’ is annual O&M costs (\$/year) and ‘O&M_{factor}’ is the proportionality factor.

$$E_p = P_e \times (W_{s,t} + W_p) \dots\dots\dots (Eq. B9)$$

The price of electricity price is assumed as \$ 0.142263 /kWh, based on estimates by Origin energy (2014).

Cost of CO₂ Transportation

In most cases the quantity of CO₂ to be sequestered is given by the source output, and is assumed to be a constant value in this study. Transportation cost is consequently the same for all cases examined, and shown here only for completeness. It is not used in the subsequent cost comparisons.

The model of McCollum, (2006) is used for CO₂ transportation costs.

$$C_{cap} = 13400 \times (m^{0.35}) \times (L^{0.13}) \dots\dots\dots (Eq. B10)$$

$$C_{total} = F_L \times F_T \times L \times C_{cap} \dots\dots\dots (Eq. B11)$$

Where ‘L’ is pipeline length (km), ‘F_L’ is location factor; ‘F_T’ is terrain factor.

As in equation B8, annual operating and maintenance costs are calculated by applying an O&M_{factor} factor of 0.04 to the total capital costs ‘C_{total}’.

Cost of CO₂ Injection

The further major cost elements are drilling wells, infrastructure and project management (IPCC, 2005). There have been comprehensive assessments of CO₂ injection and storage costs, for example those originally organized and published by the Energy Information Administration (1992) and Advanced Resources International (2006). These assessment costs have been updated and used by many published studies as the basis for field equipment and production operation costs (e.g. Atrens et al., 2011; McCoy and Rubin, 2009; and Kaiser and Rouge, 2014).

The costs here include initial preparatory costs of preliminary site screening (\$475,000) and candidate site evaluation (\$1,950,540) taken from Smith (2001) and scaled to 2013 AU\$. The actual

well costs including start-up costs, injection well drilling and completion cost follow Atrens et al. (2011), which reasonably matches also with the results of Kaiser and Rouge (2014).

$$C_w = 1.09^n \times \left[0.6662 \times \left(\frac{D}{D_o} \right) + 0.3338 \right] \times K e^{bd} \dots\dots\dots \text{(Eq. B12)}$$

Where 'C_w' is per well cost (2003 US\$), 'D_o' is the reference well diameter (0.23125 m), 'n' is number of years, 'D' is well diameter (m), 'd' is the well depth (m), K (0.2865) and b (6.657 × 10⁻⁴) are empirical constants.

$$\text{Injection Well Equipment} = N \times 66,586 \times \left(\frac{m}{280 \times N} \right)^{0.5} \dots\dots\dots \text{(Eq. B13)}$$

Annual operating and maintenance costs equations (Eq.'s 14 through 17) are taken from McCollum and Ogden (2006), but updated and converted to 2013 AU\$.

$$\text{Normal Annual Expenses} = N \times 10,232 \dots\dots\dots \text{(Eq. 14)}$$

$$\text{Consumables} = N \times 27,337 \dots\dots\dots \text{(Eq. 15)}$$

$$\text{Surface Maintenance} = N \times 20,770 \times \left(\frac{m}{280 \times N} \right)^{0.5} \dots\dots\dots \text{(Eq. 16)}$$

$$\text{Subsurface Maintenance} = N \times 7636 \times \frac{d}{1219} \dots\dots\dots \text{(Eq. 17)}$$

Where 'N' is number of wells, and 'd' is depth of well (m).